

Zero-dimensional, Two-dimensional Carbon Materials and their Composites: Bottom up synthesis, Properties and Applications

BY
MRIGANKA SADHUKHAN
(CHEM11201004007)

**National Institute of Science Education and Research
Bhubaneswar, Odisha**

*A thesis submitted to the
Board of Studies in Chemical Sciences
In partial fulfillment of requirements
For the degree of*

DOCTOR OF PHILOSOPHY

Of

HOMI BHABHA NATIONAL INSTITUTE

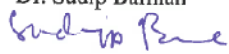
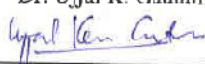
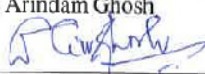


January, 2017

Homi Bhabha National Institute¹

Recommendations of the Viva Voce Committee

As members of the Viva Voce Committee, we certify that we have read the dissertation prepared by Mriganka Sadhukhan entitled "Zero-dimensional, Two-dimensional Carbon Materials and their Composites: Bottom up synthesis, Properties and Applications" and recommend that it may be accepted as fulfilling the thesis requirement for the award of Degree of Doctor of Philosophy.

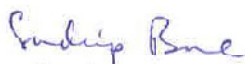
Chairman -	Prof. Alagar Srinivasan		Date: 2.6.17
Guide / Convener -	Dr. Sudip Barman		Date: 02.6.17
Examine-	Dr. Ujjal K. Gantam		Date: 2-6-17
Member 1 -	Dr. Arindam Ghosh		Date: 02/06/17
Member 2-	Dr. Prasenjit Mal		Date: 02.06.17
Member 3-	Dr. Asima Bhattacharyya		Date: 2.6.17

Final approval and acceptance of this thesis is contingent upon the candidate's submission of the final copies of the thesis to HBNI.

I/We hereby certify that I/we have read this thesis prepared under my/our direction and recommend that it may be accepted as fulfilling the thesis requirement.

Date: 02.6.17

Place: GATE


<Signature>

Guide

¹ This page is to be included only for final submission after successful completion of viva voce.

STATEMENT BY AUTHOR

This dissertation has been submitted in partial fulfillment of requirements for an advanced degree at Homi Bhabha National Institute (HBNI) and is deposited in the Library to be made available to borrowers under rules of the HBNI.

Brief quotations from this dissertation are allowable without special permission, provided that accurate acknowledgement of source is made. Requests for permission for extended quotation from or reproduction of this manuscript in whole or in part may be granted by the Competent Authority of HBNI when in his or her judgment the proposed use of the material is in the interests of scholarship. In all other instances, however, permission must be obtained from the author.

Mriganka Sadhukhan

DECLARATION

I, hereby declare that the investigation presented in the thesis has been carried out by me. The work is original and has not been submitted earlier as a whole or in part for a degree / diploma at this or any other Institution / University.

Mriganka Sadhukhan

LIST OF PUBLICATIONS

Journals

- 1)[#] Barman S.; **Sadhukhan M.** *J. Mater. Chem.*, **2012**, 22, 21832-21837.
- 2)[#] **Sadhukhan M.**; Barman S. *J. Mater. Chem. A*, **2013**, 1, 2752-2756.
- 3)[#] **Sadhukhan M.**; Bhowmik T.; Kundu M. K.; Barman S. *RSC Adv.*, **2014**, 4, 4998-5005.
- 4) Kundu M. K. [§], **Sadhukhan M.**[§]; Barman S. *J. Mater. Chem. B*, **2015**, 3, 1289-1300.
[§]These authors contributed equally
- 5)[#] **Sadhukhan M.**; Kundu M. K., Bhowmik T.; Barman S. *Int. J. Hydrogen Energy*, **2017**, 42, 9371-9383
- 6)[#] **Sadhukhan M.**; Bhowmik T.; Barman S. Fabrication of Zinc doped Hierarchical Porous Carbon nitride Microsphere for efficient removal heavy metal ions from aqueous solution. (Communicated)
- 7)[#] **Sadhukhan M.**; Bhowmik T.; Barman S. Superparamagnetic Iron oxide-carbon nitride composite for photocatalytic degradation of organic dye. (Manuscript under preparation)

Pertaining to the thesis

Conferences

1. Workshop on Electron Microscope (WEM) held on November 23-25, 2011 at IOP, Bhubaneswar.
2. 99th Indian Science Congress held on 3-7 January, 2012 hosted by KIIT University, Bhubaneswar and NISER, Bhubaneswar.

Mriganka Sadhukhan

Dedicated to.....

My Parents and Sister

ACKNOWLEDGEMENTS

My cordial gratitude goes to my supervisor, Dr. Sudip Barman, for his scientific assistance and continuous support throughout the course of this work. His broad knowledge in the field and enthusiasm for science has always been prompting me to learn and work in lab. I feel so lucky and grateful to work with him. I am also thankful to him for being patient while critically correcting this thesis.

I am highly grateful to my doctoral committee members Prof. A. Srinivasan, Dr. Asima Bhattacharyya, Dr. Prasenjit Mal and Dr. Arindam Ghosh for their help and suggestions during the course of my research work.

I wish to extend my warmest thanks to Dr. Jogendra Nath Behera (past), Dr. Sanjib Kar (past) and Dr. Nagendra Kumar Sharma (present), Chairman, Post Graduate Committee Chemical sciences (PGCS), NISER.

I also gratefully acknowledge the help rendered by all the faculty members of School of Chemical Sciences, NISER. Their fruitful advice and cooperation during my research have given a shape to my thesis.

I would like to acknowledge my past and present lab members Tanmay, Manas, Sarat, Ranjan, Amit, Dr. Susanta Kr. Bera with whom working in the lab was a pleasure. I also express my heartfelt thanks to all my friends in NISER for their numerous help, support and enjoyable company for making my life more cheerful.

I would like to extend my gratitude to Mr. Sanjay for recording the NMR of my samples.

I gratefully acknowledge the Homi Bhabha National Institute (HBNI), India for academic registration, Department of Atomic Energy (DAE), India for financial support and National

Institute of Science Education and Research (NISER), Bhubaneswar, India for research infrastructure.

I would like to express my sincere gratitude to a number of people to whom I am really indebted to for their help, support and motivation in all my endeavors.

I owe my heartfelt gratitude to my parents and my sister for their continuous support and encouragement.

At last I want to thank the God for all of these things.

Mriganka Sadhukhan

CONTENTS

	<u>Page No.</u>
Synopsis	19
List of Figures	31
List of Tables	48
List of Schemes	50
List of Abbreviation	51

Chapter 1

General Introduction

1.1. The history of Graphene	53
1.2. Different synthesis method of Graphene	54
1.2.1. Top-down fabrication method	55
1.2.1.1. Liquid exfoliation method	56
1.2.1.2. Chemical oxidation and reduction method	57
1.2.1.3. Mechanical exfoliation method	58
1.2.1.4. Electrochemical exfoliation method	59
1.2.2. Bottom up fabrication method	59
1.2.2.1. Chemical vapour deposition (CVD) method	61
1.2.2.2. Chemical synthesis method	62

1.3. Properties of Graphene	64
1.3.1 Electrical properties of Graphene	64
1.3.2. Mechanical and thermal properties of Graphene	65
1.3.3. Optical properties of Graphene	65
1.3.4. Solubility of Graphene	65
1.4. Carbon nitride as a 2D carbon material	66
1.5. History behind Carbon nitride	67
1.6. Different phases of carbon nitride and its different shape	69
1.7. Different method to synthesis of carbon nitride	71
1.7.1. Top-down fabrication method	71
1.7.1.1. Liquid exfoliation method	72
1.7.1.2. Thermal etching method	72
1.7.2. Bottom-up fabrication method	73
1.7.2.1. Laser method	73
1.7.2.2. Chemical Vapor Deposition (CVD) method	75
1.7.2.3. Template Method	76
1.7.2.4. Solid state condensation method	77
1.8. Properties of carbon nitride	78
1.8.1. Optical properties of carbon nitride	78
1.8.2. Thermal property of carbon nitride	80
1.8.3. Solubility of carbon nitride	81
1.9. Zero dimensional carbon material: graphene quantum dot	81
1.10. Graphitic carbon nitride based nanocomposite and their applications	83

1.11. Scope of this thesis	86
----------------------------	----

Chapter 2

General Experimental Methods and Techniques

2.1. Introduction	96
2.2. Instruments and Instrumental Techniques	96
2.2.1. Microwave Synthesizer	96
2.2.2. Ultrasonicator	97
2.2.3. Atomic Force Microscope (AFM)	98
2.2.4. Transmission Electron Microscope (TEM)	98
2.2.5. Powder X-ray Diffraction (p-XRD)	99
2.2.6. X-ray Photoelectron Spectroscopy (XPS)	100
2.2.7. Fourier Transform Raman Spectroscopy	101
2.2.8. Thermo Gravimetric Analysis (TGA)	102
2.2.9. Dynamic Light Scattering (DLS) analysis	102
2.2.10. Field Emission Scanning Electron Microscopy (FESEM)	103
2.2.11. UV-visible Spectrophotometer	104
2.2.12. Fluorescence Spectrometer	104
2.2.13. Time-correlated single photon counting (TCSPC) spectrometer	105
2.2.14. Nuclear Magnetic Resonance (NMR) Spectroscopy	105

2.2.15. Fourier Transform Infrared (FT-IR) Spectroscopy	106
2.2.16. Attenuated Total Reflection Fourier Transform Infrared Spectroscopy (ATR-FT-IR)	106
2.2.17. CHN Elemental Analyser	106
2.2.18. Cyclic Voltammetry	107
2.2.19. Flame atomic absorption spectrophotometer (FAAS)	108
2.2.20. Superconducting Quantum Interference Device (SQUID) magnetometer	108
2.2.21. Electron Spin Resonance Spectroscopy	109
2.3. Experimental Method	110
2.3.1. Quantum yield measurement method	110
2.3.2. Average Fluorescence life time measurement method	112
2.3.3. Fluorescence quenching Measurement	112
2.3.4. Chronoamperometry method	113
2.3.5. Differential Pulse Voltammetry	114
2.3.6. Batch Experiment	114
2.4. Chemicals	115

Chapter 3

Zero dimensional (graphitic carbon nitride and carbon) Quantum Dots: Synthesis, Properties and their Applications

Part A

Graphitic Carbon Nitride Quantum Dots

3.1. Introduction	119
3.2. Synthesis procedure of g-CNQDs	122
3.3. Characterization of g-CNQDs	123
3.3.1. Characterization of g-CNQDs by p-XRD	123
3.3.2. Characterization of g-CNQDs by UV-Visible spectroscopy	123
3.3.3. Characterization of g-CNQDs by FT-IR spectroscopy	124
3.3.4. Characterization of g-CNQDs by TEM	125
3.3.5. Characterization of g-CNQDs by AFM	126
3.3.6. Characterization of g-CNQDs by XPS	127
3.3.7. Characterization of g-CNQDs by ¹³ C NMR	129
3.3.8. Characterization of g-CNQDs by CHN elemental analysis	130
3.3.9. Characterization of g-CNQDs by TGA analysis	131
3.3.10. Characterization of g-CNQDs by Fluorescence spectroscopy	131
3.4. Properties of g-CNQDs	135
3.4.1. Solubility of g-CNQDs	135
3.4.2. Fluorescence Quantum yield measurement of g-CNQDs	136
3.4.3. Average Fluorescence lifetime measurement of g-CNQDs	136
3.4.4. Structural prediction of g-CNQDs	139
3.4.5. Room temperature ferromagnetic property of g-CNQDs	139

3.4.6. Origin of ferromagnetic property of g-CNQDs	143
3.5. Application of g-CNQDs as a sensor for mercuric and iodide ions	146
3.6. Application of g-CNQDs in the adsorptive removal of metal ions from water	158
3.6.1. Adsorption isotherm study of metal ions on g- CNQDs	158
3.6.2. Adsorption kinetic study of Cu ²⁺ ions on g-CNQDs	161
3.7. Conclusion	163

Part B

Carbon Quantum Dots

3.1. Introduction of zero dimensional carbon quantum dots (CQDs)	165
3.2. Synthesis method of CQDs	166
3.3. Characterization of CQDs	166
3.3.1. Characterization of CQDs by AFM	166
3.3.2. Characterization of CQDs by TEM	167
3.3.3. Characterization of CQDs by UV-Visible Spectroscopy	169
3.3.4. Characterization of CQDs by Fluorescence Spectroscopy	170
3.3.5. Characterization CQDs by FT-IR	175
3.4. Properties of CQDs	176
3.4.1. Quantum yield measurement of CQDs	176
3.4.2. Average life time measurement of CQDs	177
3.5. Application of CQDs as H ₂ O ₂ sensor by Fluorescence Spectroscopy	178

3.6. Conclusion	180
-----------------	-----

Chapter 4

Bottom up Fabrication of two-dimensional Carbon nitride, Graphene sheets and their applications

4.1. Introduction	187
4.2. Bottom up fabrication method to synthesis of 2D Carbon Nitride sheet	190
4.3. Characterization of 2D carbon nitride sheet	190
4.3.1. Characterization by TEM	190
4.3.2. Characterization by p-XRD	192
4.3.3. Characterization by AFM	193
4.3.4. Characterization by DLS	196
4.3.5. Characterization by SEM	197
4.3.6. Characterization by FT-IR Spectroscopy	197
4.3.7. Characterization by FT-Raman Spectroscopy	198
4.4. Electrochemical application of 2D a carbon nitride sheets	199
4.4.1. Preparation of 2D carbon nitride modified GC electrode	199
4.4.2. Determination of mercuric ions by carbon nitride modified GC electrode	199
4.4.3. Dopamine sensing by carbon nitride modified GC electrode	207
4.5. Synthesis of 2D Graphene sheets	208

4.6. Characterization of 2D graphene sheets	208
4.6.1. Characterization by AFM	209
4.6.2. Characterization by TEM	209
4.6.3. Characterization by p-XRD	212
4.6.4. Characterization by FESEM	212
4.6.5. Characterization by DLS	214
4.6.6. Characterization by XPS	215
4.7. Properties and application of 2D graphene sheets	216
4.7.1. Preparation procedure of thin graphene sheets modified glassy carbon electrode from CQDs	216
4.7.2. Fast electron transfer kinetics of thin graphene sheets	217
4.7.3. Application of 2D graphene sheets	219
4.8. Conclusion	222

Chapter 5

Iron oxide nanoparticles embedded on Carbon nitride matrix: Synthesis, magnetic property and Photocatalytic degradation of Organic dye

5.1. Introduction	228
5.2. Synthesis method of Fe ₃ O ₄ -CN _x composite	232

5.3. Characterization	232
5.4. Magnetic properties of Fe ₃ O ₄ -CN _x composite	240
5.5. Application: Photocatalytic degradation of organic dye	245
5.5.1. Method of Photocatalytic activity study	245
5.5.2. Photocatalytic degradation of RhB on Fe ₃ O ₄ -CN _x composite	246
5.5.3. Photocatalytic stability	253
5.5.4. Proposed Photocatalytic mechanism	254
5.6. Conclusion	258

Chapter 6

Highly dispersed Platinum nanoparticles on Graphitic Carbon Nitride: A Highly efficient Electrocatalyst for Oxidation of Small Organic Molecules

6.1. Introduction	263
6.2. Synthesis method of Pt/CN _x composite	267
6.3. Characterization of Pt/CN _x composite	268
6.3.1. Characterization of Pt/CN _x by p-XRD method	268
6.3.2. Characterization of Pt/CN _x by TEM analysis	269
6.3.3. Characterization of Pt/CN _x composite by FESEM analysis	271
6.3.4. Characterization of Pt/CN _x by XPS analysis	272
6.3.5. Characterization of Pt/CN _x composite by FT-IR spectroscopy	274

6.3.6. Characterization of Pt/CN _x composite by TGA, ICP-OES and CHN analysis	275
6.3.7. ECSA calculation of Pt/CN _x composite	276
6.4. Application	277
6.4.1. Electrochemical oxidation of Methanol on porous Pt/CN _x catalyst	277
6.4.2. Electrochemical oxidation of Formic acid on porous Pt/CN _x catalyst	283
6.4.3. Formaldehyde electrooxidation on porous Pt/CN _x catalyst	289
6.5. Effect of support (CN _x) in Pt/CN _x catalyst for electrooxidation of methanol, formic acid and formaldehyde	292
6.6. Conclusion	295

Chapter 7

Zinc doped Porous Carbon nitride Microspheres: Synthesis, Magnetic properties and Removal of Toxic Metal ions from water

7.1. Introduction	300
7.2. Synthesis method	304
7.2.1. Synthesis method of graphitic carbon nitride	304
7.2.2. Synthesis method of Zn-CN _x microspheres	304
7.3. Characterization of Zn-CN _x composite	304
7.3.1 Morphological characterization of Zn-CN _x composite	304
7.3.2. Structural Characterization of Zn-CN _x composite	307

7.4. Room temperature ferromagnetic property of porous Zn-CN _x microspheres	311
7.5. Adsorption of metal ions on porous Zn-CN _x microsphere	315
7.5.1. Experimental method of metal ion adsorption by Zn-CN _x microsphere	315
7.5.2. Cadmium ion adsorption study on Zn-CN _x microsphere	316
7.5.3. Copper and Lead ion adsorption studies on Zn doped CN _x microsphere	322
7.5.4. Metal ion adsorption kinetic study on Zn doped CN _x microspheres	325
7.5.5. Determination of thermodynamic parameters during cadmium adsorption process	327
7.5.6. Experimental method of Congo red adsorption on Zn-CN _x microspheres	329
7.5.7. Effect of pH on Congo Red adsorption study by Zn-CN _x microsphere	330
7.5.8. Adsorption Isotherm and kinetic study of Congo red on porous Zn-CN _x microspheres	331
7.5.9. Explanation on the adsorption by Zn-CN _x microsphere	334
7.6. Conclusion	336

SYNOPSIS

Introduction

In recent years, after the successful isolation of two dimensional (2D) graphene in 2004¹, low dimensional covalent carbon materials have attracted tremendous attention due to their unique properties and applications. Graphene is a single plane layer of honeycomb network of sp^2 hybridized carbon atoms. The unique properties of graphene² such as high thermal conductivity, high specific surface area, superior chemical stability, electron mobility etc. have made graphene and its composites extremely attractive materials for the applications in electronics, catalysis, energy storage, solar energy conversion, environmental purification and biosensing. The graphitic carbon nitride (g-C₃N₄) is another two dimensional carbon material that has similar graphene like structure. The g-C₃N₄ is one of the promising materials among different carbon based materials due to its unique structure, presence of large number of carbon-nitrogen coordination nest for stabilizing metal ions or nanoparticle. The g-C₃N₄ supported/stabilised metal nanoparticles³ have different potential applications towards electrochemical sensing, photocatalysis, electrocatalysis etc. Apart from 2D g-C₃N₄ material, graphitic carbon nitride quantum dots have attracted great attention due to its optical and biochemical properties which make them to the bioimaging and optoelectronic applications.

Organization of thesis

This thesis is divided into seven chapters and a brief description of each chapter is discussed below:

Chapter 1: General Introduction

Chapter 2: General experimental methods and techniques

Chapter 3: Zero dimensional (graphitic carbon nitride and carbon) Quantum Dots: Synthesis, Properties and their Applications

Chapter 4: Bottom up Fabrication of two-dimensional Carbon nitride, Graphene sheets and their applications

Chapter 5: Iron oxide nanoparticles embedded on Carbon nitride matrix: Synthesis, magnetic property and Photocatalytic degradation of Organic dye

Chapter 6: Highly dispersed Platinum nanoparticles on Graphitic Carbon Nitride: A Highly efficient Electrocatalyst for Oxidation of Small Organic Molecules

Chapter 7: Zinc doped Porous Carbon nitride Microspheres: Synthesis, Magnetic properties and Removal of Toxic Metal ions from water

Chapter 1: General Introduction

This chapter gives mainly a brief introduction of 2D carbon materials such as graphene and g-C₃N₄. Since the discovery of single layer sp² hybridized carbon, graphene in 2004 by A. K. Geim *et. al*¹, it has attracted enormous interest among scientific community to synthesize 2D carbon materials for their unique properties and potential applications. The top down fabrication method and bottom up fabrication method of graphene are discussed in chapter. Top down fabrication methods of graphene are generally three types such as chemical, mechanical and electrochemical exfoliation method, whereas the bottom up fabrication methods are chemical vapour deposition and chemical synthesis. In 1989 Liu and Cohen first theoretically predicted the hypothetical β-C₃N₄ compound as a superhard material⁴. Meanwhile, g-C₃N₄ got more interested in the scientific community as a 2D material due to its similar graphite like structure. The g-C₃N₄ has two building blocks such as heptazine block and triazine block and is normally synthesized from

different carbon and nitrogen based precursors via condensation at high temperature⁵. The history behind synthesis of carbon nitride, different phases of carbon nitride and different building blocks of g-C₃N₄ was discussed in this chapter. In addition, synthesis and properties of graphene quantum dots has also been discussed in this chapter.

Chapter 2: General experimental methods and techniques

This chapter provides a brief description of instrumental techniques which were used for this present investigation. Basic principle of microwave synthesizer, ultrasonicator and cyclic voltammetry used in this work, was discussed. The working principle of other instruments used in this study such as powder X-ray diffraction (p-XRD), UV-Visible spectroscopy, steady state spectrometer, Fourier transform infra-red spectroscopy (FT-IR), X-ray photoelectron spectroscopy (XPS) and microscopic techniques (TEM and SEM) are presented in this chapter. The preparation of glassy carbon modified electrode, different electrochemical methods, quantum yield measurement, average fluorescence lifetime measurement method and batch experiment method has been discussed in detail in this chapter.

Chapter 3: Zero dimensional (graphitic carbon nitride and carbon) Quantum Dots: Synthesis, Properties and their Applications

The first part of this chapter describes synthesis of graphitic carbon nitride quantum dots (g-CNQDs), their (optical, magnetic) properties and applications. The fluorescent g-CNQDs were synthesized by microwave heating of formamide (HCONH₂). These quantum dots were well characterized by p-XRD, NMR, UV-visible spectrophotometer, fluorescence spectrometer, FT-IR, XPS analysis. The fluorescence emission of g-CNQDs is strongly dependent on excitation

wavelengths and also depends on solvent, pH of the medium. The life time of the emission of g-CNQDs decreases with increasing polarity of the solvent. But the fluorescence behavior of g-CNQDs is independent of ionic strength of the medium. The quantum yield of blue fluorescent g-CNQDs is found to be ~29% whereas the highest reported quantum yield of graphene quantum dots is 28%⁶. The fluorescence emission of g-CNQDs is highly sensitive and selective towards mercuric ions in aqueous media due to the “superquenching” of fluorescence. The Stern Volmer constant of quenching of g-CNQDs by Hg²⁺ ion is $1 \times 10^7 \text{ M}^{-1}$. The g-CNQDs are an excellent fluorescence probe for selective and sensitive detection of Hg²⁺ ions in aqueous solution with the detection limit of $1 \times 10^{-9} \text{ M}$, which is below the WHO guidelines for drinking water ($\sim 10^{-8} \text{ M}$). The complex formation of Hg²⁺ ions with the CN_x sheet involving π delocalized electron moieties is responsible for the quenching of fluorescence. The addition of iodide ions abstracts the bound Hg²⁺ forming HgI₂ and gives back the fluorescence characteristic of g-CNQDs. Thus, g-CNQDs can play a dual role for selective and sensitive detection of mercuric ions as well as iodide ions in aqueous media via “ON–OFF–ON” fluorescence response (Figure 1). The magnetic property of these g-CNQDs is also discussed in this chapter. The magnetic hysteresis (M vs H) curves and Field cooled/Zero field cooled magnetization curves prove the metal free room temperature ferromagnetic property of g-CNQDs. These g-CNQDs are applied as an adsorbent for the removal of toxic metal ions from aqueous solution. The adsorption isotherms follow Langmuir adsorption isotherm model and the maximum adsorption capacity on these g-CNQDs for copper (Cu²⁺) and cadmium (Cd²⁺) ions are found to be 184 mg/gm and 425.5 mg/gm respectively. The second part of this chapter discusses the synthesis of fluorescent Carbon Quantum Dots (CQDs) from formic acid (HCOOH) by a simple microwave assisted thermal method. These CQDs show excitation wavelength, pH and solvent dependent

fluorescence behaviors. The fluorescence emission of CQDs in water can be tuned between 310 and 820 nm by changing the excitation wavelengths. These CQDs exhibit deep ultraviolet, visible and near infrared emission when it was excited from 200 to 650 nm in water solution. The CQDs were found to be an excellent fluorescence probe for determination of hydrogen peroxide (H_2O_2) in aqueous media due to quenching of fluorescence.

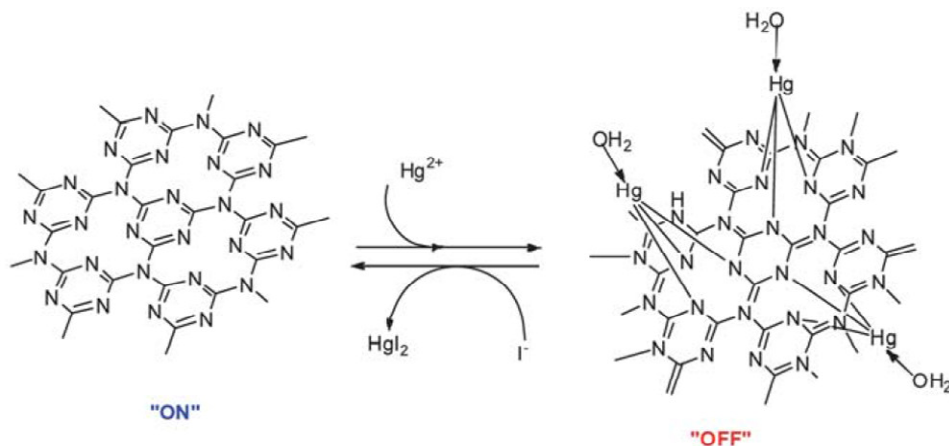


Figure 1. Schematic diagram of g-CNQDs showing its reversible binding of Hg^{2+} ions.

Chapter 4: Bottom up Fabrication of two-dimensional Carbon nitride, Graphene sheets and their applications

This chapter demonstrates the bottom-up fabrication of 2D carbon nitride, graphene sheets from their respective quantum dots for their application in non-enzymatic electrochemical detection of metal ions and hydrogen peroxide. Although several methods^{1, 7-12} are available for the production of single or few layers 2D-materials, the bottom-up fabrication of layered materials from their fundamental building blocks such as atoms, molecules, quantum dots etc. is very rare. The 2D systems have attracted a great deal of interest in both fundamental and applied scientific research for their potential applications in electronics, sensing, catalysis and energy storage. Microwave irradiation of HCONH_2 produces g-CNQDs which are used as precursors for

synthesis of 2D carbon nitride. The 2D flat carbon nitride sheets are formed by evaporation induced self-assembly and condensation of g-CNQDs on a solid substrate (Figure 2a). The drying of g-CNQDs solution generates different morphologies such as 0D carbon nitride quantum dots, 2D carbon nitride sheets and 3D carbon nitride, depending on the concentration of g-CNQDs. The g-CN_x electrode is introduced as a highly sensitive electrochemical sensor for mercuric ions (Hg²⁺) in aqueous solution. The lower detection limit of Hg²⁺ is found to be 9.1×10^{-11} M, is lower than the reported literature for Hg²⁺ detection¹³⁻¹⁵. The simultaneous electrochemical detection of lead ion (Pb²⁺), copper ion (Cu²⁺) and mercury (Hg²⁺) using a carbon nitride modified glassy carbon electrode is also described in this chapter. The second part of this chapter describes the synthesis of 2D graphene sheets from CQDs by bottom up fabrication method. The large area graphene sheets are formed on a solid substrate due to self assembly and two dimensional growth of CQDs. Graphene sheets modified glassy carbon (GS/GC) electrode showed fast electron transfer kinetics for Fe(CN)₆^{3-/4-} redox couple. Moreover, these modified electrodes are applied as a highly sensitive and selective metal free, non-enzymatic electrochemical sensor for H₂O₂ with lower detection limit of 300 nM (Figure 2b).

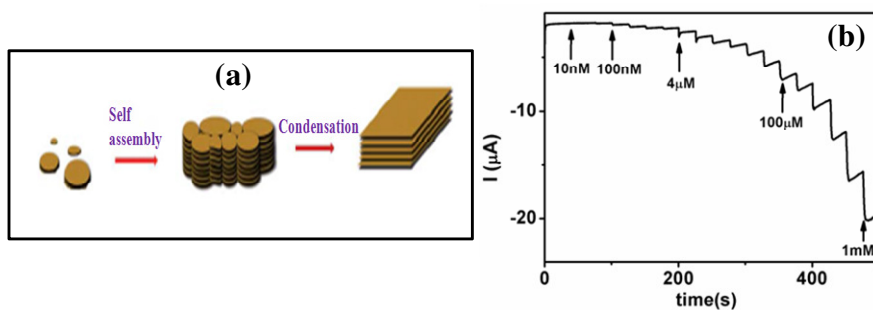


Figure 2. (a) Schematic representation of bottom-up synthesis of 2D carbon nitride sheets from its quantum dots. (b) Amperometric response of GS/GC electrode on successive addition of H₂O₂ into 0.1 M PBS.

Chapter 5: Iron oxide nanoparticles embedded on Carbon nitride matrix: Synthesis, magnetic property and Photocatalytic degradation of Organic dye

This chapter discusses a detailed synthesis, magnetic properties and application of $\text{Fe}_3\text{O}_4\text{-CN}_x$ composite. An ultrasound assisted sodium borohydride method was employed to synthesize Fe_3O_4 nanoparticles supported on carbon nitride matrix ($\text{Fe}_3\text{O}_4\text{-CN}_x$ composite). The p-XRD, XPS and TEM analysis confirmed the formation of ~5 nm sized Fe_3O_4 nanoparticles dispersed on CN_x matrix. The superparamagnetic metal or metal oxide nanoparticles¹⁶ has been a intense research subject in recent years due to their interesting physical properties and potential applications in various fields such as catalysis, drug delivery and magnetic resonance imaging.

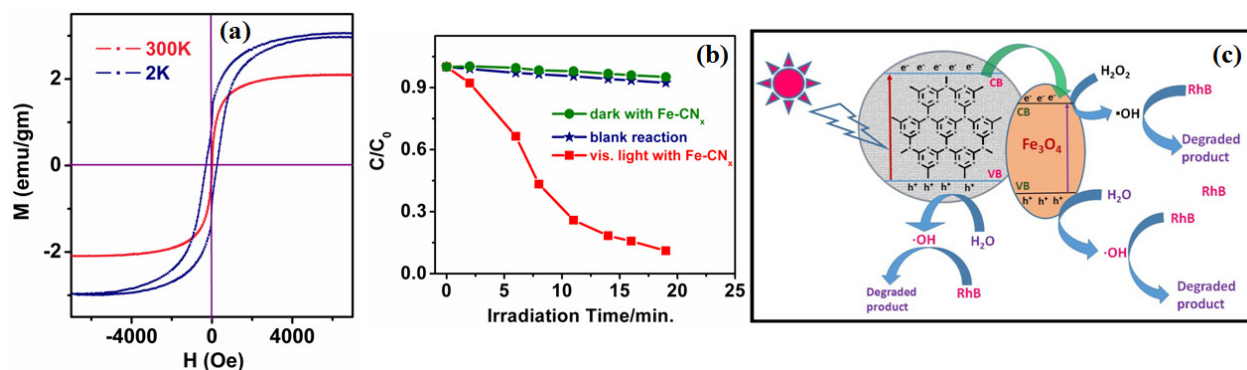


Figure 3. (a) Magnetization property of $\text{Fe}_3\text{O}_4\text{-CN}_x$ composite at 300K and 2K. (b) The photocatalytic activity of $\text{Fe}_3\text{O}_4\text{-CN}_x$ composite for RhB dye degradation under visible light irradiation. (c) Mechanism of photocatalytic degradation of RhB in presence of iron/iron oxide nanoparticles embedded CN_x matrix.

These $\text{Fe}_3\text{O}_4\text{-CN}_x$ composite exhibited superparamagnetic behavior at room temperature (Figure 3a) with low saturation field and well-defined blocking temperature (T_B) of 42K. The superior photocatalytic activity of these composite towards degradation of organic dye in aqueous media

is also discussed in this chapter. Among the different methods available to remove the dyes from waste water such as adsorption, flocculation, electrochemical oxidation, membrane filtration, photodegradation etc.; the photocatalytic degradation is considered as one of best methods for environmental pollution remediation. The $\text{Fe}_3\text{O}_4\text{-CN}_x$ composite was applied as efficient reusable photocatalyst for the degradation of Rhodamine B (RhB) dye in presence of H_2O_2 under visible/sun light (Figure 3b). The mechanism of photocatalytic degradation is also discussed at end of this chapter (Figure 3c).

Chapter 6: Highly dispersed Platinum nanoparticles on Graphitic Carbon Nitride: A Highly efficient Electrocatalyst for Oxidation of Small Organic Molecules

This chapter describes synthesis of highly dispersed platinum nanoparticles (PtNPs) on carbon nitride sheets and their application in electrochemical oxidation of small organic molecules. Highly dispersed ultra small PtNPs on CN_x sheets are synthesized by ultrasound assisted borohydride reduction method. The concern of energy shortage and environmental problem is rising due to use of fossil fuel, there is thus a need alternative and renewable energy sources.

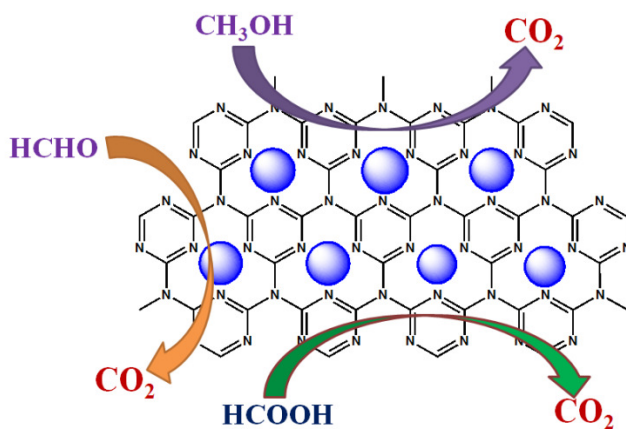


Figure 4. Schematic diagram of Pt/ CN_x composite showing oxidation of small organic molecules.

The fuel cells which are considered as an alternative energy sources, transforms the chemical energy of fuel to electrical energy due to electrochemical oxidations of fuel molecules. The main advantages of fuel cell are that it has high efficiency to produce the energy, low cost and low pollutant emission¹⁷. The electrochemical oxidation of small organic molecules such as methanol (CH₃OH), formic acid (HCOOH) and formaldehyde (HCHO) is important for the development of direct fuel cells. Electrochemical active surface area (ECSA) is an important parameter to know the electrochemical activity of the catalyst. The ECSA value of Pt/CN_x catalyst was found to be 68 m² g_{Pt}⁻¹ is 1.8 times higher than that of the commercial Pt/C catalyst (36.5 m² g_{Pt}⁻¹). Pt nanoparticles supported on g-CN_x sheets is introduced as electrocatalyst for oxidation of CH₃OH, HCOOH and HCHO in acid medium (Figure 4). The mass activity, specific activity, onset potential, tolerance to CO poisoning and long term stability for the catalytic oxidation of CH₃OH, HCOOH, HCHO on Pt/CN_x catalyst in acid media is much higher than that of commercial Pt/C catalyst. At 0.64V the mass activity of Pt/CN_x catalyst is 2.7 times higher than that of Pt/C during forward electrooxidation of methanol. The electrooxidation of HCOOH on Pt/CN_x occurs via dual mechanism with greatly enhanced oxidation through dehydrogenation pathway in comparison with commercial Pt/C. Most importantly, at 0.3V (vs. NHE), a typical working voltage in Direct Formic Acid Fuel Cell (DFAFC)¹⁸, the mass activity of Pt/CN_x composite for formic acid oxidation is 25 times higher than that of commercial Pt/C catalyst. The superior catalytic activity and durability of this Pt/CN_x catalyst can be attributed to high dispersion of PtNPs and strong metal-support interaction.

Chapter 7: Zinc doped Porous Carbon nitride Microspheres: Synthesis, Magnetic properties and Removal of Toxic Metal ions from water

This chapter demonstrates a facile synthesis of zinc doped hierarchical porous carbon nitride microspheres and their application as an effective adsorbent for removal of toxic heavy metals from aqueous solution. In recent years, industrialization and mining activities are rising all over world, water pollution due to contamination of toxic heavy metal ions is thus one of major threat to public health. Among different wastewater treatment available methods, adsorption method is most promising method due to its efficient low cost method and good removal efficiency¹⁹. Hydrothermal method was employed to synthesize of zinc doped porous carbon nitride microspheres from HCONH₂ and zinc metal.

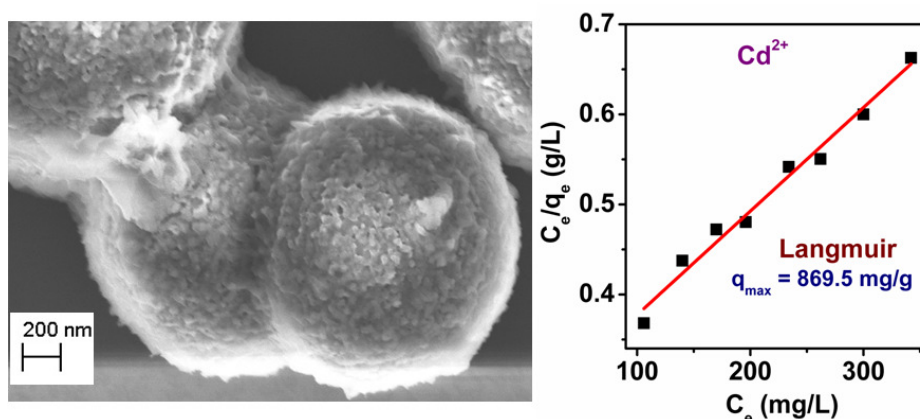


Figure 5. (a) FESEM image of Zn doped CN_x microsphere. (b) Adsorption isotherm of Cd²⁺ ions on Zn-CN_x microsphere after fitting with Langmuir adsorption isotherm model.

The electron microscopic measurements confirmed the formation of zinc doped CN_x microspheres (Figure 5a). The porous Zn-CN_x microspheres show the ferromagnetic property at room temperature (300K) with sufficient magnetization value of 0.0039 emu/gm. Therefore it can be used as a building block of future spintronic devices. These porous CN_x microspheres was applied as an adsorbent for removal of heavy metal ions (Cd²⁺, Cu²⁺, Pb²⁺) from aqueous solution.

The adsorption equilibrium, kinetics and thermodynamics of metal adsorptions on CN_x microspheres are discussed. The adsorption isotherms of these heavy metals on the CN_x microspheres are well described by Langmuir isotherm model. The temperature dependent adsorption isotherm suggests that adsorption of metal ions on these CN_x microspheres are spontaneous and endothermic process. The maximum adsorption capacities of Cd²⁺, Cu²⁺ and Pb²⁺ metal ions on Zn doped CN_x microspheres were found to be 869.5 mg/gm, 133.5 mg/gm and 446.4 mg/gm respectively. The large maximum adsorption capacities for different metal ions suggests zinc doped CN_x spheres is one of the best adsorbent for removal of metals ions from water.

References

1. Novoselov, K. S.; Geim, A. K.; Morozov, S. V.; Jiang, D.; Zhang, Y.; Dubonos, S. V.; Grigorieva, I. V.; Firsov, A. A., *Science* **2004**, *306*, 666-669.
2. Soldano, C.; Mahmood, A.; Dujardin, E., *Carbon* **2010**, *48*, 2127-2150.
3. Cheng, N.; Tian, J.; Liu, Q.; Ge, C.; Qusti, A. H.; Asiri, A. M.; Al-Youbi, A. O.; Sun, X., *ACS Appl. Mater. Interfaces* **2013**, *5*, 6815-6819.
4. Liu, A. Y.; Cohen, M. L., *Science* **1989**, *245*, 841-842.
5. Thomas, A.; Fischer, A.; Goettmann, F.; Antonietti, M.; Muller, J.-O.; Schlogl, R.; Carlsson, J. M., *J. Mater. Chem.* **2008**, *18*, 4893-4908.
6. Shen, J.; Zhu, Y.; Yang, X.; Zong, J.; Zhang, J.; Li, C., *New J. Chem.* **2012**, *36*, 97-101.
7. Lin, Y.-M.; Dimitrakopoulos, C.; Jenkins, K. A.; Farmer, D. B.; Chiu, H.-Y.; Grill, A.; Avouris, P., *Science* **2010**, *327*, 662-662.
8. Rangappa, D.; Murukanahally, K. D.; Tomai, T.; Unemoto, A.; Honma, I., *Nano Lett.* **2012**, *12*, 1146-1151.

9. Gong, K.; Du, F.; Xia, Z.; Durstock, M.; Dai, L., *Science* **2009**, *323*, 760-764.
10. Coleman, J. N.; Lotya, M.; O'Neill, A.; Bergin, S. D.; King, P. J.; Khan, U.; Young, K.; Gaucher, A.; De, S.; Smith, R. J.; Shvets, I. V.; Arora, S. K.; Stanton, G.; Kim, H.-Y.; Lee, K.; Kim, G. T.; Duesberg, G. S.; Hallam, T.; Boland, J. J.; Wang, J. J.; Donegan, J. F.; Grunlan, J. C.; Moriarty, G.; Shmeliov, A.; Nicholls, R. J.; Perkins, J. M.; Grievson, E. M.; Theuwissen, K.; McComb, D. W.; Nellist, P. D.; Nicolosi, V., *Science* **2011**, *331*, 568-571.
11. Komsa, H.-P.; Kotakoski, J.; Kurasch, S.; Lehtinen, O.; Kaiser, U.; Krasheninnikov, A. V., *Phys. Rev. Lett.* **2012**, *109*, 035503.
12. Song, L.; Ci, L.; Lu, H.; Sorokin, P. B.; Jin, C.; Ni, J.; Kvashnin, A. G.; Kvashnin, D. G.; Lou, J.; Yakobson, B. I.; Ajayan, P. M., *Nano Lett.* **2010**, *10*, 3209-3215.
13. Lee, J.-S.; Han, M. S.; Mirkin, C. A., *Angew. Chem. Int. Ed.* **2007**, *46*, 4093-4096.
14. Zhao, Z.-Q.; Chen, X.; Yang, Q.; Liu, J.-H.; Huang, X.-J., *Chem. Comm.* **2012**, *48*, 2180-2182.
15. Liu, X.; Tang, Y.; Wang, L.; Zhang, J.; Song, S.; Fan, C.; Wang, S., *Adv. Mater.* **2007**, *19*, 1471-1474.
16. Thorek, D. L. J.; Chen, A. K.; Czupryna, J.; Tsourkas, A., *Ann Biomed Eng* **2006**, *34*, 23-38.
17. Kordesch, K. V.; Simader, G. R., *Chem. Rev.* **1995**, *95*, 191-207.
18. Gong, M.; Li, F.; Yao, Z.; Zhang, S.; Dong, J.; Chen, Y.; Tang, Y., *Nanoscale* **2015**, *7*, 4894-4899.
19. Gui, C.-X.; Wang, Q.-Q.; Hao, S.-M.; Qu, J.; Huang, P.-P.; Cao, C.-Y.; Song, W.-G.; Yu, Z.-Z., *ACS Appl. Mater. Interfaces* **2014**, *6*, 14653-14659.

LIST OF FIGURES

Sl. No.	List of Figures: Figure Caption	Page No.
01	Figure 1.1. Structure of graphene	54
02	Figure 1.2. Schematic diagram of Top-Down fabrication method	56
03	Figure 1.3. Schematic diagram of Bottom-up fabrication method	60
04	Figure 1.4. Synthesis of dibenzo[bc,kl]coronene from 1,4-dimethyl-9,10-di-o-tolyl anthracene	62
05	Figure 1.5. Schematic diagrams for the formation of graphene nanoribbon from coronene and perylene	62
06	Figure 1.6. Triazine and heptazine based carbon and nitrogen containing materials: Melon, Melamine, Melam & Melem	67
07	Figure 1.7. Heptazine and triazine block of g-C ₃ N ₄	69
08	Figure 1.8. Reaction pathway of solid state condensation method starting from dicyandiamide and melamine to produce g-C ₃ N ₄	76
09	Figure 1.9. Reaction pathway of solid state condensation method starting from urea to produce g-C ₃ N ₄	76
10	Figure 1.10. Brönsted and Lewis basic sites of g-C ₃ N ₄	82
11	Figure 2.1. Photograph of microwave synthesizer	97
12	Figure 2.2. Photograph of ultrasonicator	97
13	Figure 2.3. Representation of Bragg's law	100
14	Figure 2.4. Schematic diagram of X-ray photoelectron spectroscopy	101
15	Figure 3.1. p-XRD of g-CNQDs	123
16	Figure 3.2. UV-visible spectrum for g-CNQDs in water	124
17	Figure 3.3. FT-IR spectrum of g-CNQDs	125

18	Figure 3.4.	(a) TEM image of g-CNQDs (b) Diameter distribution of g-CNQDs calculated from TEM image	126
19	Figure 3.5.	(a) AFM image of g-CNQDs taken on mica foil (b) Height distribution of g-CNQDs calculated from AFM image (c) Height profile of g-CNQDs along the line AB from Figure 3.5 (a)	127
20	Figure 3.6.	(a) The XPS survey scan of g-CNQDs showing the presence of carbon, nitrogen and oxygen	127
21	Figure 3.7.	High resolution (a) C1s and (c) N1s high resolution XPS spectra of g-CNQDs. Schematic representation of different type of (b) carbon and (d) nitrogen centered sites into the g-CNQDs moiety	128
22	Figure 3.8.	¹³ C NMR spectrum of g-CNQDs	130
23	Figure 3.9.	TGA plot of g-CNQDs	131
24	Figure 3.10.	Fluorescence spectrum for g-CNQDs in water (excitation wavelength = 340 nm)	132
25	Figure 3.11.	(a) Excitation wavelength dependent Fluorescence spectra of g-CNQDs in water solvent. (b) Normalized fluorescence spectra of g-CNQDs in water solvent at different excitation wavelengths	133
26	Figure 3.12.	Solvent dependent fluorescence emission spectra of g-CNQDs	134
27	Figure 3.13.	(a) Fluorescence spectra of g-CNQDs in water at pH 2 and 13 displaying the change of fluorescence intensity between pH 2 and 13 (b) pH dependent fluorescence intensity plot of g-CNQDs in water (Excitation wavelength =340 nm)	134
28	Figure 3.14.	Ionic strength effect on fluorescent intensity of g-CNQDs	135
29	Figure 3.15.	Fluorescence decay plots of g-CNQDs in different	136

		solvents (excitation wavelength = 330 nm, emission wavelength = 400 nm)	
30	Figure 3.16.	(a) Fluorescence decay curve and its exponential fitting curve of g-CNQDs in polar water solvent. IRF is also plotted in this graph. (b) Residual after fitting the fluorescence decay curve	137
31	Figure 3.17.	(a) Fluorescence decay curve and its exponential fitting curve of g-CNQDs in non polar toluene solvent. IRF is also plotted in this graph. (b) Residual after fitting the fluorescence decay curve	137
32	Figure 3.18.	The plausible structure of g-CNQDs	139
33	Figure 3.19.	(a) Magnetic Hysterisis loops (M-H curve) of g-CNQDs at 300K and 10K. (b) Lower magnetic field region of magnetic Hysterisis loops (M-H curve) of g-CNQDs at 300K and 10K	140
34	Figure 3.20.	Field cooled (FC) and Zero field cooled (ZFC) magnetization curves of g-CNQDs. Data measured at the external magnetic field of 1000 Oe. Inset represents the higher temperature region of FC and ZFC curves	141
35	Figure 3.21.	(a) The change of fluorescence emission intensity of g-CNQDs in water on addition of Hg ²⁺ ions. Excitation wavelength was 340 nm. (b) Stern–Volmer plot for the fluorescence quenching of g-CNQDs with Hg ²⁺ ions in water. (c) Fluorescence quenching of Hg ²⁺ ions compared to other metal ions	147
36	Figure 3.22.	Fluorescence quenching of g-CNQDs in presence of Hg ²⁺ ions and compared with other different metal ions	147
37	Figure 3.23.	(a) Fluorescence decay profiles of g-CNQDs in	148

		presence of different concentration (5-30 μM) of Hg^{2+} ions in aqueous medium (Excitation wavelength = 330 nm and Emission wavelength = 400 nm) (b) Plot shows τ/τ_0 is invariant with added Hg^{2+} ions	
38	Figure 3.24.	(a) The fluorescence enhancement of g-CNQD–(Hg^{2+}) _x complex at different concentrations of iodide ions. (b) Comparison of fluorescence enhancement ratio of g-CNQD–(Hg^{2+}) _x complex for different anions at various concentrations	150
39	Figure 3.25.	Fluorescence enhancement by iodide ions compared to other anions	150
40	Figure 3.26.	Higher ppm region of ^1H NMR spectra of (a) free g-CNQDs (4 mg/mL) (b) g-CNQDs with the presence of mercuric perchlorate salt (0.002 M) (c) g-CNQDs with the presence of mercuric perchlorate (0.002 M) and potassium iodide (0.006 M)	152
41	Figure 3.27.	Lower ppm region of ^1H NMR spectra of (a) free g-CNQDs (4 mg/mL) (b) g-CNQDs with the presence of mercuric perchlorate salt (0.002 M), (c) g-CNQDs with the presence of mercuric perchlorate salt (0.002 M) and potassium iodide (0.006 M). The values within bracket represent the area under the peak	152
42	Figure 3.28.	ATR-FTIR spectra of free g-CNQDs, g-CNQDs with the presence of Hg^{2+} ions and g-CNQDs with the presence of both Hg^{2+} and I^- ions	154
43	Figure 3.29.	UV-visible spectra of free g-CNQDs, g-CNQDs with the presence of Hg^{2+} ions and g-CNQDs with the presence of both Hg^{2+} and I^- ions	154
44	Figure 3.30.	Hg 4f XPS spectra of g-CNQDs obtained after	156

		treatment with (a) Hg^{2+} and (b) both Hg^{2+} and Γ ions	
45	Figure 3.31.	XPS spectra in the N1s region of free g-CNQDs, g-CNQDs after treatment with Hg^{2+} ion and g-CNQDs after addition of both Hg^{2+} and Γ ions	156
46	Figure 3.32.	High resolution C1s XPS spectra of free g-CNQDs, g-CNQDs after treatment with Hg^{2+} and g-CNQDs after addition of Hg^{2+} and Γ ions	157
47	Figure 3.33.	Plausible structure of $\text{g-CNQD-(Hg}^{2+})_x$ complex and regeneration of free g-CNQDs on addition of Γ ions	158
48	Figure 3.34.	Adsorption isotherm plots of Cu^{2+} ion on g-CNQDs after fitting with (a) Langmuir fitting and with (b) Freundlich fitting	160
49	Figure 3.35.	Adsorption isotherm plots of Cd^{2+} ion on g-CNQDs after fitting with (a) Langmuir fitting and with (b) Freundlich fitting	160
50	Figure 3.36.	Adsorption kinetic plot of Cu^{2+} ion on g-CNQDs with (a) pseudo-first order and (b) pseudo-second order model fitting	162
51	Figure 3.37.	(a, b) AFM images of CQDs. (c, d) are the AFM line profile along the line AB and CD on the images of (a) and (b) respectively	167
52	Figure 3.38.	TEM image of CQDs	168
53	Figure 3.39.	(a) TEM image and (b) SAED pattern of graphite nanoparticles	168
54	Figure 3.40.	UV-visible spectrum of CQDs dissolved in water	169
55	Figure 3.41.	Fluorescence emission spectrum of CQDs dissolved in water where excitation wavelength is 276 nm	171
56	Figure 3.42.	Fluorescence excitation spectrum of CQDs dissolved in water where emission wavelength was kept at 375 nm	171

57	Figure 3.43.	Fluorescence spectra of CQDs in water at different excitation wavelengths ranging from 200 to 650 nm	173
58	Figure 3.44.	Normalized FL spectra of CQDs in water at different excitation wavelengths ranging from 200 to 650 nm.	173
59	Figure 3.45.	FL spectra of CQDs in different solvents where excitation wavelength is 320 nm	174
60	Figure 3.46.	Fluorescence spectra of CQDs at different excitation wavelengths in (a) methanol, (b) cyclohexane and (c) benzene	174
61	Figure 3.47.	Fluorescence spectra of CQDs in water at different pHs where excitation wavelength was kept at 320 nm	175
62	Figure 3.48.	FT-IR spectrum of CQDs	176
63	Figure 3.49.	Fluorescence decay curves of CQDs in water, cyclohexane, THF and benzene solvents	177
64	Figure 3.50.	(a) Fluorescence decay profile of CQDs in water and its fitting curve and instrument response function (IRF) plot (excitation wavelength is 330 nm and emission wavelength is 400 nm) (b) Residual plot after fitting the fluorescence decay profile of CQDs in water	178
65	Figure 3.51.	(a) The variation of fluorescence intensity of CQDs in water in presence of different concentration of H ₂ O ₂ where excitation wavelength was kept at 320 nm (b) Fluorescence quenching plot of CQDs by H ₂ O ₂ in water	179
66	Figure 3.52.	Comparison of fluorescence intensity quenching of CQDs by H ₂ O ₂ and different metal ions and anions	180
67	Figure 4.1.	TEM images of carbon nitride sheets formed by evaporation induced condensation of g-CNQDs. The concentrations of g-CNQDs in aqueous solutions	191

		were (a) 1 mg L ⁻¹ , (b) 0.01 mg L ⁻¹ , and (c) 2 X 10 ⁻⁵ mg L ⁻¹ . (d) SAED pattern of carbon nitride sheets taken from the sheets in figure 4.1. (a)	
68	Figure 4.2.	(a, b) TEM images of carbon nitride sheets produced from a diluted, centrifuged aqueous solution of g-CNQDs.	192
69	Figure 4.3.	Powder X-ray diffraction pattern of the carbon nitride sheets	193
70	Figure 4.4.	AFM images of (a) g-CNQDs, (b) carbon nitride nanosheets and (e) micron sized carbon nitride sheets formed from different concentrations (10 ⁻⁵ , 10 ⁻⁴ and 0.1 mg L ⁻¹ respectively) of g-CNQDs solutions, (c, d and f) The line profiles along the line AB, CD and EF in image of (a), (b) and (e) respectively	194
71	Figure 4.5.	AFM image of carbon nitride sheets produced by drying a higher concentration (1mg/L) of g-CNQDs solution (b) The line profile along the line AB in image (a) indicating the presence of g-CNQDs on the surface on carbon nitride sheets	195
72	Figure 4.6.	SEM images of carbon nitride sheets prepared by evaporation of 30 mL solution of g-CNQDs (1mg/L) in air at 45 ⁰ C	197
73	Figure 4.7.	FT-IR spectrum of 2D carbon nitride sheets	198
74	Figure 4.8.	FT-Raman spectrum of 2D carbon nitride sheets	198
75	Figure 4.9.	CVs of 1.0 X 10 ⁻⁶ M Hg ²⁺ at the bare GC electrode and the carbon nitride modified GC electrode. Electrolyte: 0.02 M HCl, accumulation time: 15 min, accumulation potential: -1 V	200
76	Figure 4.10.	(a) Hg 4f XPS spectrum of carbon nitride obtained after electrochemical accumulation of Hg ²⁺ ions at	200

carbon nitride modified GC electrode. High resolution XPS spectra in the N1s region of (b) free carbon nitride sheet and (c) after electrochemical accumulation of Hg^{2+} ions. XPS spectra in the C1s region of (d) free carbon nitride sheet and (e) after accumulation of Hg^{2+} ions

- 77 **Figure 4.11.** (a) Effect of accumulation potential E_a (V) on anodic stripping cyclic voltammetric response for 1×10^{-6} M of Hg^{2+} at carbon nitride modified GC electrode. Electrolyte: 0.02 M HCl, accumulation time: 15 minutes (b) Effects of accumulation time on anodic stripping cyclic voltammetric response for 1×10^{-6} M of Hg^{2+} at carbon nitride modified GC electrode. $E_a = -1$ V. (c) Effect of pH of the solutions on anodic stripping cyclic voltammetric response for 1×10^{-6} M of Hg^{2+} at carbon nitride modified GC electrode. $E_a = -1$ V and accumulation time = 15 minutes 202
- 78 **Figure 4.12.** The anodic stripping cyclic voltammograms of different concentration of Hg^{2+} ions at carbon nitride modified GC electrode under optimum conditions 203
- 79 **Figure 4.13.** The calibration plot of voltammetric stripping current vs. the different concentration of Hg^{2+} ions: (a) full range of Hg^{2+} concentration and (b) lower Hg^{2+} concentration region 204
- 80 **Figure 4.14.** The anodic stripping voltammograms of 1×10^{-6} M Hg^{2+} ions in presence of 1×10^{-6} M each of Pb^{2+} , Cu^{2+} , Cd^{2+} , Fe^{3+} , Zn^{2+} ions at carbon nitride modified GC electrode at an accumulation potential of -1 V for accumulation time of 15 minutes and in presence of 0.02M HCl solution 205

81	Figure 4.15.	(a) Anodic stripping voltammograms for the different concentrations of Pb^{2+} , Cu^{2+} and Hg^{2+} ions at carbon nitride modified GC electrode at an accumulation potential of -1 V for accumulation time of 15 minutes and in presence of 0.02M HCl solution. (b) The calibration curve of Pb^{2+} and Cu^{2+} ions	206
82	Figure 4.16.	DPV plot of different concentration of Dopamine at the carbon nitride modified GC electrode	207
83	Figure 4.17.	a) Calibration plot of DPV current vs. concentration of dopamine (b) Calibration curve in a lower dopamine concentration region	208
84	Figure 4.18.	(a) AFM image of graphene film showing the several sheets. (b) Line profile along the AB on (a) AFM image (c) AFM image of micron sized graphene film on mica foil	209
85	Figure 4.19.	(a, c and d) TEM images of 2D graphene sheets formed from evaporation induced 2D self assembly and growth of CQDs. (b) SAED pattern taken from the sheets on TEM image of (a). (e) The HRTEM image of 2D graphene sheets	210
86	Figure 4.20.	(a) TEM image of 2D graphene sheets. A folded sheet is clearly visible. (b, c) HRTEM images of graphene sheets. 40 layers of graphene are clearly seen in TEM image of (c). (d) EDX spectrum of graphene sheets taken on TEM image of (a)	211
87	Figure 4.21.	p-XRD pattern of graphite/graphene. Sample was prepared by evaporating aqueous solution of CQDs on quartz	212
88	Figure 4.22.	FESEM images of graphene on copper foil showing (a) stacked assembly of thin graphene sheets and (b)	213

		graphene flakes. FESEM images of graphene on silicon substrate showing (c) flat graphene sheet (d) aggregated and wrinkled sheets of graphene	
89	Figure 4.23.	Change of Hydrodynamic diameter of CQDs in water with time and after ultrasonication. The whole product was dissolved in 20ml water and DLS measurements were performed at different time	214
90	Figure 4.24.	XPS survey scan of graphene sheets on silicon substrate	215
91	Figure 4.25.	C1s XPS spectrum of graphene sheets on silicon substrate	216
92	Figure 4.26.	Cyclic voltammogram of $\text{Fe}(\text{CN})_6^{3-/4-}$ at bare GC electrode and graphene sheets modified GC electrode. Electrolyte: 1 M KCl	217
93	Figure 4.27.	(a) CVs of $\text{Fe}(\text{CN})_6^{3-/4-}$ at GS/GC electrode at various scan rate ranging from 10 mV to 900 mV. (b) Cathodic and anodic peak current vs. square root of scan speed	217
94	Figure 4.28.	(a) CVs of GS/GC electrode in absence and presence of 4 mM H_2O_2 in 0.1M PBS (pH = 7) solution. (b) CVs of 4 mM H_2O_2 in 0.1M PBS at bare GC and GS/GC electrode	219
95	Figure 4.29.	Amperometric response of GS/GC electrode on successive addition of H_2O_2 into 0.1 M PBS with stirring	220
96	Figure 4.30.	Calibration plot of current vs. concentration of H_2O_2 at graphene sheets modified GC electrode (a) Full concentration region and (b) Lower concentration region	221
97	Figure 4.31.	Amperometric responses of graphene sheets modified GC electrode at a potential of -0.4V on	221

subsequent addition of dopamine (DA), ascorbic acid (AA), D-Glucose, L-Glycine, L-Cysteine, L-Tyrosine, L-Tryptophan and H_2O_2 (each concentration was $10\mu M$)

98	Figure 5.1.	p-XRD pattern of $Fe_3O_4-CN_x$ composite	233
99	Figure 5.2.	(a) TEM image of $Fe_3O_4-CN_x$ composite showing highly dispersed Fe nanoparticles on CN_x sheet. (b) Size distribution of Fe nanoparticle	234
100	Figure 5.3.	(a) HRTEM image of $Fe_3O_4-CN_x$ composite and (b) SAED pattern of $Fe_3O_4-CN_x$ composite taken from TEM image presented in Figure 5.4 (a)	235
101	Figure 5.4.	FESEM image of $Fe_3O_4-CN_x$ composite	236
102	Figure 5.5.	(a) XPS survey spectrum of $Fe_3O_4-CN_x$ composite. (b) High resolution Fe 2p XPS spectrum of $Fe_3O_4-CN_x$ composite (c) High resolution deconvoluted Fe 2p XPS spectrum of $Fe_3O_4-CN_x$ composite after fitting with Gaussian function	236
103	Figure 5.6.	(a) XPS spectra of N1s region of g- C_3N_4 and $Fe_3O_4-CN_x$ composite. (b) XPS spectra of C1s region of g- C_3N_4 and $Fe_3O_4-CN_x$ composite	237
104	Figure 5.7.	O1s XPS spectrum of $Fe_3O_4-CN_x$ composite	238
105	Figure 5.8.	FT-IR spectra of graphitic carbon nitride and $Fe_3O_4-CN_x$ composite	239
106	Figure 5.9.	M vs. H curves of $Fe_3O_4-CN_x$ at (a) 300K and (b) 2K	241
107	Figure 5.10.	Temperature dependent magnetization plot with (a) FC and (b) ZFC processes	242
108	Figure 5.11.	(a) M vs. H curves of $Fe_3O_4-CN_x$ composite below and above T_B . (b) Temperature dependence coercivity plot of $Fe_3O_4-CN_x$ composite. (c) Plot of H_c vs. $T^{1/2}$ showing the linear relationship	243

109	Figure 5.12.	Adsorption study of RhB on Fe ₃ O ₄ -CN _x catalyst by UV-visible spectroscopy	247
110	Figure 5.13.	(a) Change of UV-Visible absorption spectra of aqueous solution of RhB in presence of Fe ₃ O ₄ -CN _x composite and H ₂ O ₂ under irradiation of visible light (concentration of H ₂ O ₂ = 33mM). (b) Photocatalytic degradation of RhB dye in aqueous solution by Fe ₃ O ₄ -CN _x composite under irradiation of visible light with different concentration of H ₂ O ₂	248
111	Figure 5.14.	(a) The photocatalytic activity of Fe ₃ O ₄ -CN _x composite for RhB dye degradation under visible light irradiation. (b) The degradation kinetic of RhB on Fe ₃ O ₄ -CN _x catalyst under visible light irradiation	249
112	Figure 5.15.	Photograph showing the color of RhB solution on its photodegradation under visible light illumination by Fe ₃ O ₄ -CN _x catalyst	249
113	Figure 5.16.	(a) The photocatalytic activity of Fe ₃ O ₄ -CN _x composite for RhB dye degradation under sunlight irradiation (b) The degradation kinetics of RhB under Natural light irradiation. Conc. of H ₂ O ₂ = 33mM	251
114	Figure 5.17.	Degradation efficiency of Fe ₃ O ₄ -CN _x composite with increasing number of catalytic cycles during degradation of RhB under visible light irradiation	253
115	Figure 5.18.	Scavenger effect on the rate of RhB dye degradation under irradiation of visible light, conc. of H ₂ O ₂ = 33mM	254
116	Figure 5.19.	(a) Plausible mechanism of Fenton and Fenton like processes during photocatalytic degradation of RhB by Fe ₃ O ₄ -CN _x composite. (b) The proposed photocatalytic mechanism of RhB degradation by	256

		Fe ₃ O ₄ -CN _x composite under visible light irradiation.	
117	Figure 6.1.	p-XRD of g-C ₃ N ₄ and Pt/CN _x composite	268
118	Figure 6.2.	(a) TEM image of Pt/CN _x composite (b) PtNPs size distribution in Pt/CN _x composite (c) SAED pattern of Pt/CN _x composite showing (111), (200), (220) and (311) and (222) planes of PtNPs. (d) EDS spectrum of Pt/CN _x composite taken on the TEM image of Figure 6.2(a)	270
119	Figure 6.3.	HRTEM image of Pt/CN _x composite	271
120	Figure 6.4.	(a, b) FESEM images of Pt/CN _x composite showing porous morphology	271
121	Figure 6.5.	EDS spectrum of Pt/CN _x composite taken on the FESEM image showing the presence of C, N, O and Pt	272
122	Figure 6.6.	(a) XPS survey scan of Pt/CN _x composite. (b) XPS spectra of Pt 4f region of Pt/CN _x composite. (c) XPS spectra of C1s region of g-C ₃ N ₄ and Pt/CN _x . (d) XPS spectra of N1s region of g-C ₃ N ₄ and Pt/CN _x	273
123	Figure 6.7.	FT-IR spectra of g-C ₃ N ₄ and Pt/CN _x composite	274
124	Figure 6.8.	TGA plots of Pt/CN _x composite and g-C ₃ N ₄ in N ₂ atmosphere	275
125	Figure 6.9.	Cyclic Voltammograms of Pt/CN _x and Pt/C in 1(M) H ₂ SO ₄ at the scan rate of 50 mV/sec N ₂ atmosphere	276
126	Figure 6.10.	(a) Cyclic Voltammograms of methanol oxidation of Pt/CN _x and Pt/C catalysts in 1(M) CH ₃ OH + 1(M) H ₂ SO ₄ solution at scan rate of 50 mV/sec (b) The comparison of the onset potential of Pt/CN _x and Pt/C catalysts for methanol oxidation	278
127	Figure 6.11.	(a) CVs of Pt/CN _x of 1 (M) CH ₃ OH + 1 (M) H ₂ SO ₄ solution at different scan rates ranging from 10 mV/sec to 200 mV/sec. (b) Plot of forward peak	279

		current densities vs. square root of scan rates	
128	Figure 6.12.	Chronoamperometry curves of Pt/CN _x and Pt/C catalysts of methanol oxidation in 1(M) CH ₃ OH + 1(M) H ₂ SO ₄ solution at constant potential of 0.7V	281
129	Figure 6.13.	Change of forward current density of Pt/CN _x and Pt/C catalysts with the number cycle for methanol oxidation in 1(M) methanol + 1(M) H ₂ SO ₄ solution	282
130	Figure 6.14.	CV curves of Pt/CN _x and Pt/C catalyst in N ₂ saturated 1(M) H ₂ SO ₄ solution containing 1(M) HCOOH at the scan rate of 50 mV/sec	284
131	Figure 6.15.	CVs of 1 st cycle, 5 th cycle, 30 th and 50 th cycle of Pt/CN _x catalyst of formic acid oxidation in 1(M) H ₂ SO ₄ solution at the scan rate of 50 mV/sec	284
132	Figure 6.16.	(a) CVs of Pt/CN _x in 1(M) HCOOH + 1(M) H ₂ SO ₄ solution at different scan rates ranging from 30 mV/sec to 200 mV/sec. (b) Plot of forward current densities of first (P ₁) and second peak (P ₂) vs. square root of scan rates of Pt/CN _x catalyst for HCOOH oxidation	286
133	Figure 6.17.	Chronoamperometry curves of Pt/CN _x and Pt/C catalysts in N ₂ saturated 1(M) H ₂ SO ₄ solution containing 1(M) HCOOH at a constant voltage of 0.3V	287
134	Figure 6.18.	Change of backward current density with the number of cycle of Pt/CN _x and Pt/C catalyst during 1(M) formic acid oxidation in 1(M) H ₂ SO ₄ medium	288
135	Figure 6.19.	(a) CVs of Pt/CN _x and Pt/C catalysts of formaldehyde oxidation in N ₂ saturated 1(M) H ₂ SO ₄ solution containing 1(M) HCHO at scan rate is 50 mV/sec. (b) Comparison of onset potentials of	290

		Pt/CN _x and Pt/C catalysts for formaldehyde oxidation	
136	Figure 6.20.	(a) CVs of Pt/CN _x catalyst in 1(M) H ₂ SO ₄ + 1(M) HCHO solution at different scan rates starting from 30 mV/sec to 200 mV/sec. (b) Forward current densities vs. square root of scan rates of Pt/CN _x catalyst during HCHO oxidation in 1(M) HCHO + 1(M) H ₂ SO ₄ solution	291
137	Figure 6.21.	Cronoamperometry curves of Pt/CN _x and Pt/C catalysts in N ₂ saturated 1(M) formaldehyde + 1(M) H ₂ SO ₄ solution at constant voltage of 0.8V	292
138	Figure 7.1.	(a, b and c) FESEM images of Zn-CN _x composite confirming its 3D porous microsphere morphology	305
139	Figure 7.2.	(a) FESEM image of Zn doped g-CN _x microsphere and its mapping images showing the homogeneous distribution of (b) carbon (c) nitrogen (d) zinc on Zn doped g-CN _x microsphere	305
140	Figure 7.3.	(a, b) TEM images of Zn-CN _x composite. (c) HRTEM image of Zn-CN _x composite. (d) EDS spectrum of Zn-CN _x composite taken on the TEM image showing the presence of Zn, C, N and O	306
141	Figure 7.4.	p-XRD of g-C ₃ N ₄ and Zn-CN _x microsphere	307
142	Figure 7.5.	FT-IR spectra of g-C ₃ N ₄ and Zn-CN _x microsphere	308
143	Figure 7.6.	(a) XPS survey scan of Zn-CN _x microsphere. (b) XPS spectra of Zn in Zn-CN _x microsphere. (c) C1s XPS spectra of g-C ₃ N ₄ and Zn-CN _x microsphere. (d) N1s XPS spectra of g-C ₃ N ₄ and Zn-CN _x microsphere	309
144	Figure 7.7.	(a) Magnetic Hysterisis loops (M-H curve) of Zn-CN _x microsphere at 300K and 10K. (b) Magnetic Hysterisis loops (M-H curve) of Zn-CN _x	312

		microsphere at 300K and 10K at the lower magnetic field region	
145	Figure 7.8.	Field cooled (FC) – Zero field cooled (ZFC) magnetization curve of Zn-CN _x composite. Data measured at the external magnetic field of 1000 Oe. Insets represent the higher temperature region	313
146	Figure 7.9.	(a) Contact time effect on the adsorption of Cd ²⁺ ion on Zn doped g-CN _x microsphere. (b) The effect the pH of Cd ²⁺ adsorption on Zn doped g-CN _x microsphere. Adsorption isotherm of Cd ²⁺ ion on Zn doped g-CN _x microsphere after fitting with (c) Langmuir and (d) Freundlich adsorption isotherm model	317
147	Figure 7.10.	Zeta potentials of Zn-CN _x microspheres at different pH	318
148	Figure 7.11.	(a) Langmuir and (b) Freundlich adsorption isotherm model fitting of Cu ²⁺ ion on Zn doped g-CN _x microsphere. (c) Langmuir and (d) Freundlich adsorption isotherm fitting of Pb ²⁺ ion on Zn doped g-CN _x microsphere	322
149	Figure 7.12.	Adsorption kinetic study of Cd ²⁺ ion on Zn doped g-CN _x microsphere with fitting of (a) pseudo-first order and (b) pseudo-second order kinetic model equations. Adsorption kinetic study of Pb ²⁺ ion on Zn doped g-CN _x microsphere with fitting of (c) pseudo-first order and (d) pseudo-second order kinetic model equations	326
150	Figure 7.13.	(a) Langmuir adsorption isotherm of Cd ²⁺ on Zn doped g-CN _x microsphere at different temperatures. (b) van't Hoff plot of Cd ²⁺ ion adsorption on Zn doped g-CN _x microsphere for the calculation of	328

		thermodynamic parameters	
151	Figure 7.14.	(a) Langmuir and (b) Freundlich adsorption isotherm model fitting of CR dye on Zn doped g-CN _x microsphere	331
152	Figure 7.15.	Pseudo-second order adsorption kinetics of CR dye onto Zn-CN _x composite	333
153	Figure 7.16.	FT-IR spectra of Zn-CN _x after (a) Cd ²⁺ ion adsorption (b) Cu ²⁺ ion adsorption and these are compared with FT-IR spectrum of Zn-CN _x	334

LIST OF TABLES

Sl. No.	List of Table: Table Caption	Page No.
01	Table 3.1. Fluorescence decay time (τ) and its corresponding pre-exponential factor (A), average life time (τ_{avg}) of g-CNQDs in various solvents	138
02	Table 3.2. Magnetic parameters of the g-CNQDs	141
03	Table 3.3. Comparison of Magnetic parameters of the g-CNQDs with other compounds	142
04	Table 3.4. Elemental content in g-CNQDs	145
05	Table 3.5. Relative parameters of adsorption isotherm of different metal ions after fitting with Langmuir and Freundlich adsorption isotherm model	161
06	Table 3.6. The adsorption kinetic model parameters of Cu^{2+} ion after fitting with pseudo-second order kinetic models	163
07	Table 3.7. Fluorescence decay time (τ) and its corresponding pre-exponential factor (A) of CQDs in different solvents	177
08	Table 4.1. Average size of g-CNQDs in aqueous solution measured by dynamic light scattering measurement at different concentrations of g-CNQDs.	197
09	Table 5.1. Magnetic characterization of various sample derived from magnetic measurement	244
10	Table 5.2. Comparison of rate constant for photocatalytic degradation of RhB dye by different photocatalyst under visible light irradiation	252
11	Table 6.1. Summary of methanol oxidation on Pt/CN_x and commercial Pt/C electro catalyst	280
12	Table 6.2. Summary of electrochemical performance of	282

		methanol oxidation on various electro-catalysts	
13	Table 6.3.	Comparison of different electrochemical performance during formic acid oxidation of Pt/CN _x with Pt/C catalyst	285
14	Table 6.4.	Summary of electrochemical performance for formic acid oxidation on reported electro-catalysts	289
15	Table 6.5.	Comparison of electrochemical performance parameters for formaldehyde oxidation	292
16	Table 7.1.	Detailed CHN analysis of g-C ₃ N ₄ and porous Zn-CN _x microspheres	310
17	Table 7.2.	Magnetic parameters of Zn-CN _x microspheres	313
18	Table 7.3.	Elemental content in Zn-CN _x microspheres	313
19	Table 7.4.	Relative parameters of adsorption isotherm of Cd ²⁺ ions after fitting with Langmuir and Freundlich adsorption isotherm model	320
20	Table 7.5.	Comparison of maximum adsorption capacities of Cd ²⁺ metal ion adsorption with different adsorbent	320
21	Table 7.6.	Relative parameters of adsorption isotherm of Cu ²⁺ and Pb ²⁺ metal ions after fitting with Langmuir and Freundlich adsorption isotherm model	323
22	Table 7.7.	Comparison of maximum adsorption capacities of Cu ²⁺ metal ion adsorption with different adsorbent	323
23	Table 7.8.	Comparison of maximum adsorption capacities of Pb ²⁺ metal ion adsorption with different adsorbent	324
24	Table 7.9.	The adsorption kinetics model parameters of metal ions after fitting with pseudo-first order and pseudo-second order kinetic model	326
25	Table 7.10.	Thermodynamic parameters of the adsorption of Cd ²⁺ ions on Zn-CN _x	329
26	Table 7.11.	Relative parameters of adsorption isotherm of CR dye after fitting with Langmuir and Freundlich	332

		adsorption isotherm model	
27	Table 7.12.	Comparison of maximum adsorption capacities of CR adsorption with different adsorbents	333
28	Table 7.13.	The adsorption kinetics model parameters of CR dye after fitting with pseudo-second order kinetic model	333

LIST OF SCHEMES

Sl. No.	List of Schemed: Scheme Caption	Page No.
01	Scheme 3.1 Schematic diagram for electronic transitions of CQDs during fluorescence emission.	172
02	Scheme 4.1. Schematic diagram for the formation of 2D carbon nitride sheets from g-CNQDs and 2D graphene sheets from CQDs.	223

LIST OF ABBREVIATIONS

EDTA	Ethylenediaminetetracetic acid
HCl	Hydrochloric acid
H ₂ SO ₄	Sulfuric acid
GQD	Graphene quantum dot
CQD	Carbon quantum dot
NaClO	Sodium hypochlorite
g-CNQDs	Graphitic carbon nitride quantum dots
H ₂ O ₂	Hydrogen Peroxide
g-C ₃ N ₄	Graphitic carbon nitride
ppm	parts per million
NIR	Near Infrared
DMSO	Dimethyl Sulfoxide
HOMO	Highest occupied molecular orbital
LUMO	Lowest unoccupied molecular orbital
τ_{avg}	Average life time
IRF	Instrument response function
CVD	Chemical vapour deposition
T _B	Blocking temperature

CHAPTER 1

General introduction

Graphene is single two-dimensional (2D) layer of sp^2 hybridized carbon. The sp^2 carbon atoms are covalently bonded with three other carbon atoms to form honeycomb network which is the basic building block of other allotropes such as 3D graphite, 1D carbon nanotube and 0D fullerene. Because of its unique physical and chemical properties such as very high electrical¹ and thermal conductivity², mechanical stiffness³ etc., graphene is considered as a next generation materials for various applications. After successful isolation of graphene by exfoliation of graphite (by Geim and Novoselov in 2004¹), graphene and other single or few layer(s) of 2D materials has attracted enormous interests to the scientific community. The single layer of graphene has been extensively studied for fundamental research and R&D applications due to its interesting properties such as quantum hall effect, unique electronic structure, extremely high carrier mobility and high current density. On the other hand graphitic carbon nitride has similar graphene like structure. Among other 2D materials, graphitic carbon nitride (g-C₃N₄) is considered as a one of most promising material due to its high chemical stability, tuneable electronic structure, large surface area, metal free catalytic and photo-catalytic activities etc. In 2006, g-C₃N₄ was first used as a metal-free heterogeneous catalyst – mesoporous C₃N₄ used as a catalyst for Friedel-Craft reaction⁴. The discovery of visible light induced photocatalytic hydrogen evolution of g-C₃N₄ (metal free photo-catalysis) was reported by F. Goettmann *et. al.* in 2009⁵. After this discovery, enormous work on the catalytic, photocatalytic and electrocatalytic activities of graphitic carbon nitride has reported. The photocatalytic hydrogen evolution from water⁶, photocatalytic degradation of various organic dye⁷, photochemical CO₂

reduction⁸, photoelectric sensing⁹ and important organic catalytic reactions¹⁰ using graphitic carbon nitride has been reported by several groups. The lack of band gap of graphene has one of main limitation of graphene for its electronic and opto-electronic applications. The zero-dimensional graphene quantum dots (GQDs) in contrast to graphene show non-zero band gap due to quantum size and edge effects. The band gap of GQDs can be tuned by changing the size and modifying the surface of it¹¹. GQDs exhibits strong photoluminescence property over a wide range at room temperature. Most works have been done on GQDs on the basis of theoretical prediction¹². Experimental synthesis and applications of GQDs are recently focused in the research field. GQDs has more interest compare to other semiconductor quantum dots since GQDs has high intrinsic non toxicity, photo stability and much wider photoluminescence bandwidth.

1.1. The history of Graphene

Graphene, a 2D carbon material is a single atomic layer of graphite which is made of hexagonal network of sp^2 hybridized carbon atoms. In 1947 P. R. Wallace theoretically studied the properties of graphene¹³, after this graphene has got interest in science. In 1948 Ruess and Vogt were first published the transmission electron micrograph of isolated graphene sheet. In 1962 Hoffmann and his co-workers synthesized graphene by chemical reduction method from graphene oxide¹⁴. In 1987 the actual name “graphene” was given by Mouras *et. al.*¹⁵ In 2004 Geim and Novoselov discovered the single layer graphene from highly oriented pyrolytic graphite (HOPG)¹ and in 2010 they got Nobel prize in physics due to discovery of a simple method for isolating the single layer of graphite. After this discovery, research work on graphene started to rise rapidly due to its unique physical, thermal, mechanical and electronic properties.

In graphene carbon atoms are tightly packed into honeycomb lattice. It is a basic building block of three dimensional type of graphite. The structure of graphene is shown in Figure 1.1. It may be single layer, few layers (two to nine layers) or multiple layers (more than ten layers). Single layer or few layer graphenes show high optical transparency, high charge carrier ability at room temperature, high theoretical specific surface area and high thermal conductivity.

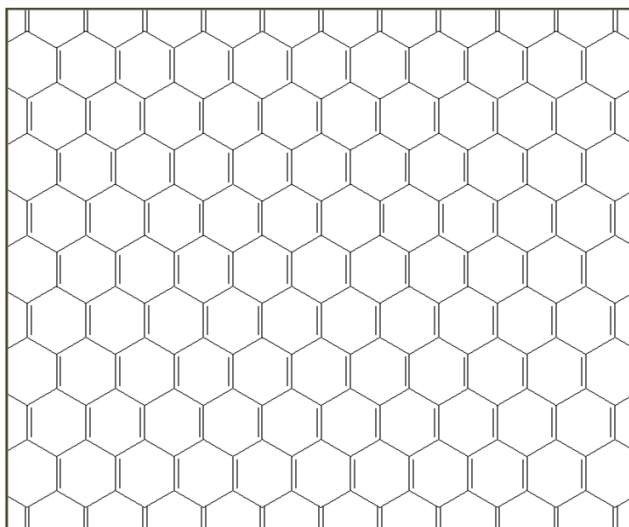


Figure 1.1. Structure of graphene.

1.2. Different synthesis method of Graphene

After the discovery of thin layer graphene and because of its unique physical, chemical, mechanical and thermal properties different groups started to synthesis of graphene by using different methods. On the basis of literature fabrication method of graphene can be classified in two different approaches one is (i) top-down fabrication method and another one is (ii) bottom-up fabrication method. The top-down fabrication method includes liquid exfoliation method, chemical oxidation and reduction method, mechanical exfoliation method and electrochemical

exfoliation method whereas the bottom-up fabrication method includes chemical vapour deposition method and chemical synthesis method.

1.2.1. Top-Down fabrication method

The top-down fabrication method means starting from large piece of material to produce small piece of material by chemical or mechanical methods. The schematic diagram of the top-down fabrication method is shown in the Figure 1.2. Building block units are removed from the substrate to form nanostructure in the top-down fabrication method. In the powder production method the crushing and the milling of the chunks represents the top-down fabrication method. Synthesis of ultrathin 2D nanomaterials has done through exfoliation from its bulk material is one of the example of the top-down fabrication method.

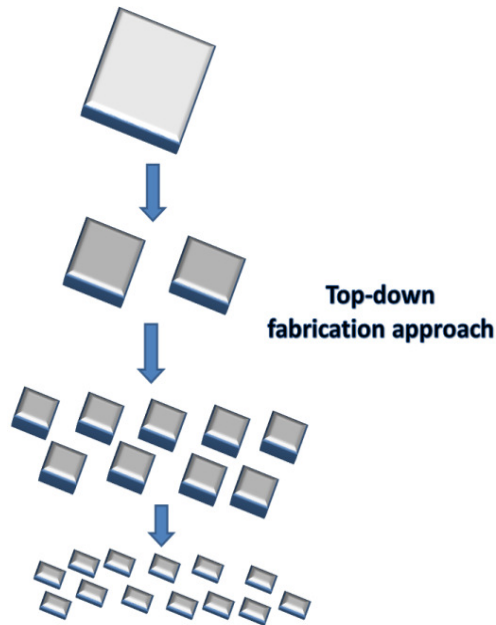


Figure 1.2. Schematic diagram of Top-Down fabrication method.

Similarly, graphene can be synthesized from graphite by different types of exfoliation methods such as liquid, mechanical and electrochemical exfoliation methods. Top-down fabrication method includes synthesis of graphene from graphene oxide (GO) by chemical oxidation and reduction method. A large quantity can be produced by top-down fabrication method. In nanolithography, top-down fabrication method is vigorously used. In the nanolithography method the required material is protected by a mask and the base material was etched by using acids or ultraviolet light or X-ray or electron beams. By using a specific pattern of mask the placement and position of the material can be monitored on a substrate which helps to produce different nanoelectronic devices; this is the greatest advantage of the top down fabrication method. During the preparation of nanoelectronic devices by top down fabrication method the internal stress, defects on the surface and crystallographic damage are forming into the material; this imperfection into the device is the main disadvantage of this method.

1.2.1.1. Liquid exfoliation method

Graphene can be obtained by exfoliation of graphite in different organic solvents. Graphite was dispersed into organic solvents by ultrasonication method to get single layer or few layer graphene in organic solution. This method is called liquid exfoliation method. The ultrasonication helps to overcome the strong van der Waals interaction between the graphene planes of the graphite material. Highly oriented pyrolytic graphite (HOPG) has been used as precursor in the solution based liquid exfoliation method to get high quality single layer graphene¹⁶. Different organic solvents such as N-methylpyrrolidone (NMP)¹⁷⁻¹⁸, N,N-dimethylformamide (DMF)¹⁹ etc. has been used for the solution based liquid exfoliation method. Starting materials and synthesized graphene both have strong interaction and high dispersion

property in NMP and DMF solvents. Exfoliation method in aqueous solution has also been used for the preparation of graphene from graphite in presence of surfactant for example sodium dodecyl benzenesulfonate (SDBS)²⁰, sodium cholate²¹ etc. The surfactants serve to stabilize the exfoliated single layer or few layer graphene sheets by preventing the π - π stacking interaction. The advantage of liquid exfoliation method is that by this synthesis method good quality of graphene can be obtained. It is low cost method with high scalability. But this method has several disadvantages such as it has no control on the sizes of graphene flakes during synthesis method. This is the main drawback to the application in the field of nanotechnology. Sometimes the liquid exfoliation method damages the graphene sheet that lead to change the physical and chemical properties of graphene. Obtaining a single layer of graphene sheet is also a challenging work by the liquid exfoliation method. In the solution phase they always try to form multilayer graphene sheets due to van der Waals interaction whose further exfoliation is very much difficult. The Low yield and poor electrical properties of the synthesized graphene by this method are the other disadvantages of this method.

1.2.1.2. Chemical oxidation and reduction method

Graphene oxide (GO) can be obtained by exfoliation of graphite after its oxidation. Oxidation of graphite increases the interlayer spacing of the successive layers of graphite. After oxidation, ultrasonication of the graphite oxide was applied into water or organic solvent or mixture of both to get single layer or few layers of graphene oxide. The exfoliated graphene oxide was reduced to obtain single layer or few layers graphene. This method is called chemical oxidation and reduction method. In 1958 W. S. Hummer and R. E. Offeman synthesized the GO from graphite by using strong oxidizing solution of concentrated sulphuric acid, sodium nitrate and potassium

permanganate²². GO contains hydroxyl group, carboxylic group and epoxide functional group in the basal plane of carbon. Reduction with hydrazine or thermal reduction of GO can form graphene into the solution. The high scalability and the low cost are the advantages of this method. The main drawback of this method the synthesized graphene has large number of defects²³. Low purity and low electrical conductivity of graphene are also the disadvantages of this method.

1.2.1.3. Mechanical exfoliation method

Mechanical exfoliation involves the synthesis of graphene directly from graphite by mechanical force. The acting forces between the layers of graphite are the van der Waals force which can overcome by applying mechanical forces. Single or few layers graphene can be obtained from highly oriented pyrolytic graphite (HOPG) or natural graphite by applying mechanical force through atomic force microscopy (AFM) or scanning tunnelling microscopy (STM) tips. Changing the bias voltage and distance between the tip and the sample one can exfoliate the graphene layer from graphite. Line defects in the graphene layer have been generally observed in this method²⁴. One of the extremely simple mechanical exfoliation methods is Scotch tape method. This method follows the micromechanical exfoliation of graphene from HOPG using adhesive tape. By doing repeated peeling it off the single atomic layer of graphene has been cleaved on the adhesive tape. The most important thing is that the cleaved single atomic layer graphene by this method shows extraordinary high electrical conductivity at room temperature. This experiment is first discovered by A. K. Geim and K. S. Novoselov in 2004¹ and they got Noble prize in physics. High quality of graphene can be produced by mechanical exfoliation

method. Large scale production of graphene cannot be produced and this method and it has lack of reproducibility.

1.2.1.4. Electrochemical exfoliation method

In the electrochemical exfoliation method highly oriented pyrolytic graphite (HOPG) is used as working electrode, platinum is used as a counter electrode and Ag/AgCl or saturated calomel electrode (SCE) is used as a reference electrode. Different electrolyte solutions such as sulphuric acid, sodium dodecyl sulphate (SDS)²⁵, poly(sodium-4-styrenesulphonate) (PSS)²⁶ etc. are generally used in the electrochemical exfoliation method. During the electrochemical process positive potential is applied, the working electrode is oxidised and started to intercalate by electrolyte molecules and the negative potential is applied for exfoliation process. By this method graphene flake can be synthesized successfully. This method is environmental friendly method, it can be performed at ambient condition and it follows first kinetic method compare to other methods. The electrochemical exfoliation method has disadvantage of inhomogeneous prepared graphene solution, it consists of different sizes and layers of graphene flakes. Sometimes during this method unwanted oxidation of graphene happens which introduces the oxygen functional group onto the surface of graphene layers and decreases the electrical conductivity of the graphene.

1.2.2. Bottom-up fabrication method

Building a brick house from bricks is the simple example of bottom up fabrication method. It is an assembly method like forming a molecule from its atoms or forming a cluster from molecules. When cluster is forming from molecule by bottom up fabrication method then the molecule is

called the building block of that cluster. Atoms or molecules are used as the building blocks for the formation of nanomaterials, nanotube, nanorod, thin films and layered structures. Self assembly process is introduced into the bottom up fabrication method where the building blocks are arranged themselves. Therefore, self assembly process helps to decrease the fabrication time of the bottom up fabrication method.

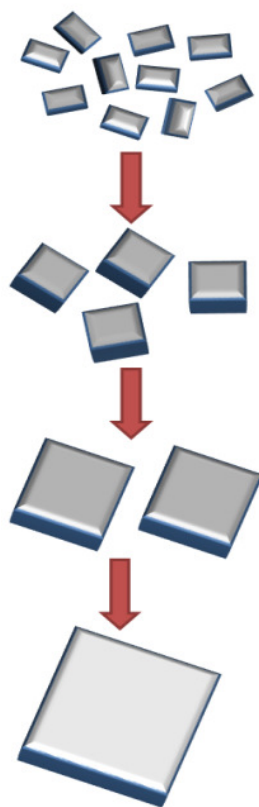


Figure 1.3. Schematic diagram of Bottom-up fabrication method.

The schematic diagram of the bottom up fabrication method is shown in Figure 1.3. Graphene quantum dot can be synthesized from different carbon based materials by bottom up fabrication method²⁷. Bottom up fabrication method are generally used for the synthesis of the nanomaterials with less defects and homogeneous chemical composition. High precession with control

resolution in the atomic level can be obtained by this method. As configuration at the atomic level can be controlled by this method therefore graphene nanoribbons with zigzag and arm chair configuration can be synthesized and distinguished. The synthesis way of graphene by bottom up fabrication method can be divided in two methods, one is chemical vapour deposition (CVD) method and another one is chemical synthesis method which is discussed below.

1.2.2.1. Chemical vapour deposition (CVD) method

CVD method is a well-known method involves deposition of gasses reactants onto a substrate. It is mostly applicable in the thin film technology. In reaction procedure the hydrocarbons are heated at high temperature where it decomposes on the substrate and then it was cooled that helps to deposit the carbon atoms on the substrate whereas the by-products evaporate out from the system chamber. High quality graphene with a large scale and large area can be synthesized by CVD method. By this method we can synthesis highly crystalline graphene. Grain boundary and several defects are formed into the graphene sheets during the synthesis by the CVD method. In this method hydrocarbon, ethylene, acetylene, benzene and methane are used as the source of carbon and different metals such as copper²⁸, nickel²⁹, platinum³⁰, ruthenium³¹ etc. are used as substrates to synthesis of graphene. Silicon and quartz are also used as a substrate to grow the graphene layer(s) on it by CVD method³⁰. Due to high availability and low cost nickel and copper metals has been used extensively as a substrate to synthesis the graphene by CVD method. The number of graphene layers deposited on substrate depends on the nature of hydrocarbon and different reaction parameters. By changing the pattern of the substrate the shape of the synthesized graphene can be altered. Transfer process of graphene layer synthesized by

CVD method from one substrate to another substrate or removal from the substrate is the difficult procedure which is the limitation of this process.

1.2.2.2. Chemical synthesis method

This method involves synthesis of graphene from different organic compounds using as precursor. For example Müllen and co-workers have synthesized graphene nanoribbons using 1,4-diiodo-2,3,5,6-tetraphenylbenzene and 4-bromophenylboronic acid as organic precursors by chemical synthesis method³². Polycyclic aromatic hydrocarbons are also used to synthesis the graphene molecule having less crystal defect and less grain boundaries. The chemically synthesized polycyclic aromatic hydrocarbon was heated on copper foil to synthesize high quality graphene. During synthesis of graphene from polycyclic aromatic hydrocarbon on copper foil the heating temperature depends on type of different polycyclic aromatic hydrocarbons. Polycyclic aromatic hydrocarbons such as coronene, pentacene, rubrene etc. are synthesized by chemical synthesis method.

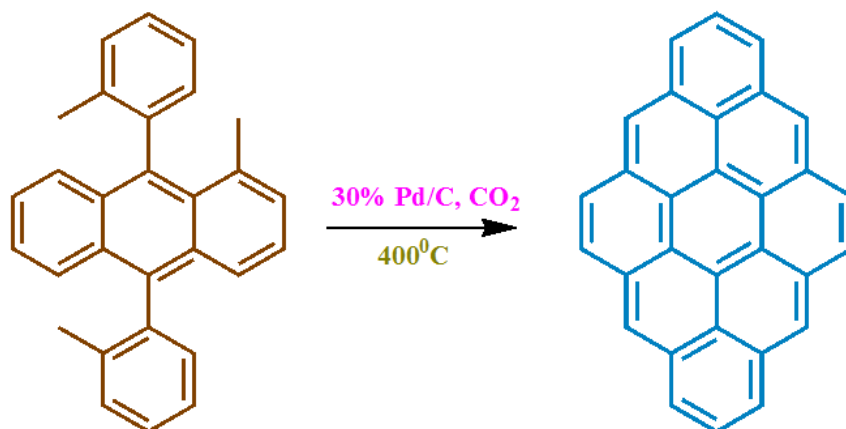


Figure 1.4. Synthesis of dibenzo[bc,kl]coronene from 1,4-dimethyl-9,10-di-o-tolyl anthracene.

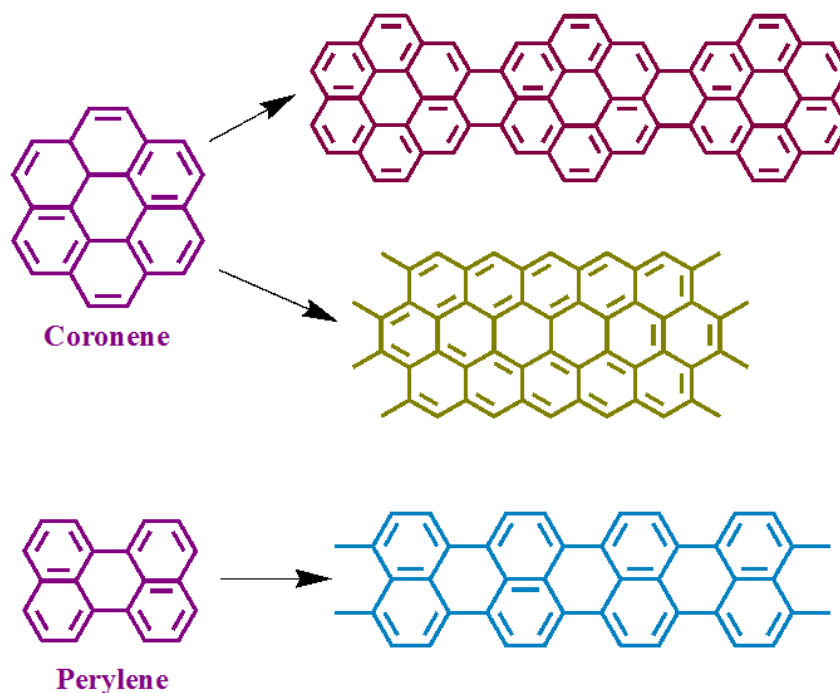


Figure 1.5. Schematic diagrams for the formation of graphene nanoribbon from coronene and perylene.

For example dibenzo[bc,kl]coronene has been synthesized from 1,4-dimethyl-9,10-di-o-tolyl anthracene shown in Figure 1.4. Graphene with imposing the geometrical restriction for example graphene nanoribbons can be synthesized from polycyclic aromatic hydrocarbons. Single walled carbon nanotube has been used as a one dimensional reactor where coronene and perylene has been used as polycyclic aromatic hydrocarbon and it is fused to synthesize the graphene nanoribbons. The schematic diagram is shown Figure 1.5. During the synthesis method of larger graphene flake from coronene molecules several polymers are formed, among them only trimer and tetramer were detected by the mass spectroscopy. The main drawback to synthesis of graphene from polycyclic aromatic hydrocarbon is that with increasing the molecular size the

synthesis procedure become difficult due to solubility problem of the intermediated compound in organic solvents.

1.3. Properties of Graphene

Graphene has unique electrical, mechanical, thermal and optical properties which are discussed below.

1.3.1 Electrical properties of Graphene

It has been observed that the electronic properties of graphene depend on the number of 2D layers of graphene. The two layers graphene behaves as a semiconductor with zero band-gap which consists of one electron and one hole. From three layers or more than three layers the number of charge carrier started to increase and the conduction and valence band started to overlap. Quantum Hall effect is an important property in electrical properties of a material. Quantum Hall effect has been observed into the graphene structure for both electron and holes due to exceptional mobility of electron and hole at low temperature and high magnetic field. This property has been observed for single layer or few layer graphene due to its low scattering effect whereas it is not sufficient in case of multiple layer of graphene. At room temperature the electron mobility of graphene is $15000 \text{ cm}^2 \text{ V}^{-1} \text{ s}^{-1}$, is too much high compare to other materials³³. In most of the materials the electron mobility does not depend on at low temperature, but graphene shows exception in this case which proves that electron movement hindered from defect scattering, not from photon scattering. In terms of resistivity it has low resistivity ($10^{-6} \Omega \text{ cm}$) at room temperature compare to other materials³⁴.

1.3.2. Mechanical and thermal properties of Graphene

J. Hone *et. al.* measured the mechanical properties of monolayer graphene by using atomic force microscope (AFM) nanoindentation method³. They have shown single layer graphene has high Young modulus like around 1TPa with breaking strength of 42 N/m. This data concluded that single layer graphene is strongest but thinnest material. The strength of the synthesized graphene depends on presence of dislocation and grain boundaries presence in the polycrystalline graphene. Experimentally A. A. Balandin and his coworkers have measured the thermal conductivity of suspended single layer graphene using non contact optical based method. At room temperature it shows extraordinary high value of thermal conductivity up to $(5.3 \pm 0.48) \times 10^3 \text{ W/mk}^2$.

1.3.3. Optical properties of Graphene

Graphene has excellent light transmittance property where it can absorb only 2.3% light and it can reflect only 0.2% light³⁵. Monolayer and bi-layer graphene can show completely transparent property when optical energy is smaller than double of its Fermi level³⁶. It can absorb light of wide wavelength starting from ultraviolet to ending at infrared including visible light. Therefore, it can be used in different photonic devices. It has large number of application in the field of optical modulator due to its ability to absorb a very small amount of light with wide range of wavelengths can open up its application in the field of optical modulator. It is using to make high speed data communication device due to its high bandwidth structure³⁷.

1.3.4. Solubility of Graphene

Graphene oxide contains different functional group for example carboxylic acid group, hydroxyl group, epoxide group. The different oxygenated functional groups in graphene help to soluble in water. Due to this hydrophilic nature of graphene oxide and presence of negative charge on its surface; GO has high dispersion ability in water without aggregation of the graphene layers whereas graphene or reduced graphene oxide has hydrophobic nature due to absence of such polar groups. Therefore graphene is not soluble; it is dispersed in the solvents. The aqueous solution of pure graphene is not stable due to its aggregation property which can be prevented by adding various surfactants. For example, J. N. Coleman *et. al.*²¹ have presented a method by which graphene dispersion in water can be stabilized in water by using sodium cholate as a surfactant of concentration upto 0.3 mg/mL. In this method sonication and followed by centrifugation produces the dispersed solution of graphene in water. Herein, the quality of the graphene depends on the power and time of the sonication and the centrifugation rate. Apart from the use of water as a solvent for stable dispersion of reduced graphene oxide or graphene; they are insoluble in different organic solvents like toluene, chloroform, dichloromethane etc. due to its strong aggregation property, but it can be dispersed in organic solvents by using ball milling method³⁸.

1.4. Carbon nitride as a 2D carbon material

Nitrogen rich carbon nitride generally represented as CN_x where $x > 1$, though during synthesis of carbon nitride hydrogen is often observed. So most appropriate representation should be CN_xH_y . s-triazine ring is basic building block unit of carbon nitride. As s-triazine is aromatic in nature so the two dimensional polymer of s-triazine ring will be also aromatic in long range with 2D planar structures like graphite. Most of the carbon nitrides which are produced from triazine

ring by solid state thermolysis are disorder structure in long range. Heptazine can be another building block for CN_xH_y product. Edward G. Gillan *et al.* have shown that heptazine can also be a building block of carbon nitride which they have proved by taking ^{13}C solid state NMR and by isolating the stable heptazine molecular anions after corrosive base hydrolysis of CN_xH_y product³⁹. Therefore, thermally unstable triazine and heptazine rings can produce nitrogen rich carbon nitride. The high degree of condensation with tri-s-triazine unit makes the carbon nitride to be highly stable with respect to chemical and thermal with medium bandgap and indirect semiconductor⁴⁰.

1.5. History behind Carbon nitride

Jöns Jakob Berzelius, father of modern chemistry first synthesized the carbon nitride polymer from mercuric thiocyanate $[Hg(SCN)_2]$ by heating and its name was given by Justus von Liebig in 1834⁴¹. “Melon” is the name of that synthetic polymer and its formula is $(C_6N_9H_3)_n$ (Figure 1.6). Justus von Liebig synthesized the melon based compound on the pyrolysis of ammonium chloride with potassium thiocyanate. The colour of melon is yellow and it is amorphous, insoluble and highly pure compound. He characterized several triazine and heptazine/tri-s-triazine based molecular compounds such as melamine, melam, melem, and melon (Figure 1.6). After these different scientists discovered different carbon-nitrogen compounds. For example in 1835 Leopold Gmelin discovered the potassium hydromelonate $[K_3C_6N_7(NCN)]$ and in 1855 Hennenberg discovered the cyameluric acid $(H_3C_6N_7O_3)$. First, Cohen theoretically predicted the carbon nitride compounds in 1985. The ab-initio calculation shows that carbon nitride has five different phases such as cubic, pseudocubic, alpha, beta and graphitic carbon nitride. In 1922 Edward C. Franklin observed melon derivatives has empirical composition which he have

synthesized from mercuric thiocyanate and hydrogen content varied from 1.1 to 2 wt% with varying the preparation method⁴². It proves that melon has no single crystalline structure; it has mixture of polymers of different sizes. He proposed the formula as $(C_3N_4)_x$ in his review paper. In 1933 Linus Pauling analyzed the structure of $C_6N_7O_3Na_3 \cdot 3H_2O$ and some related compounds by X-Ray study and expected the structure is coplanar arrangement of three fused rings. In 1982, Leonard and coworkers proved the prediction by Pauling after discovering the crystal structure of a cyameluric derivative, after successfully synthesizing the unsubstituted cyameluric nucleus,

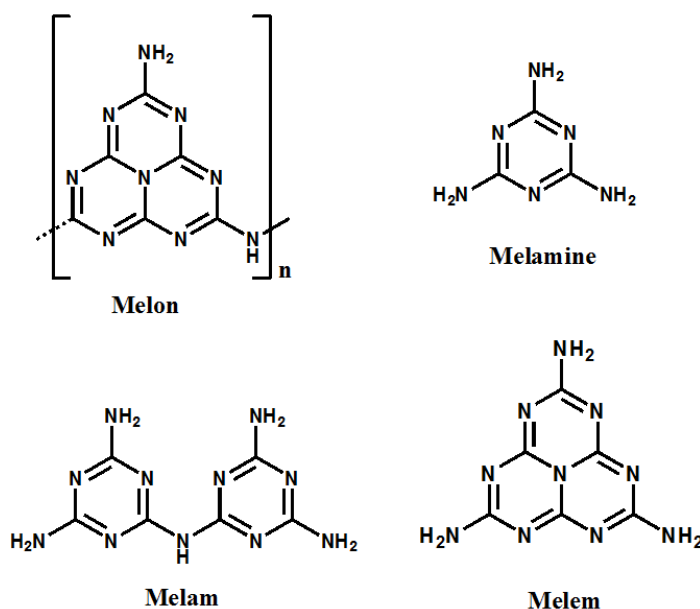


Figure 1.6. Triazine and heptazine based carbon and nitrogen containing materials: Melon, Melamine, Melam & Melem.

$C_6N_7H_3$, by a bottom-up assembly starting from 2,4-diamino-1,3,5-triazine and methyl *N*-cyanomethanimidate⁴³. In 1940 Redemann and Lucas told that melon and graphite are having resemblance where both are infinitely large and planar. They have shown that the Edward C.

Franklin's carbon nitride structure is the condensation product of 21 molecules of 2,5,8-triamino-tris-s-triazine, $C_{126}H_{21}N_{175}$. After 50 years at 1990 when it was discovered that β - C_3N_4 with highly dense sp^3 bonded C_3N_4 phase is having extremely high bulk modulus and hardness which is comparable with diamond then researchers are interested to synthesis and characterize the β - C_3N_4 molecule. Due to thermal instability of β - C_3N_4 molecule it is very much difficult to synthesize. Later theoretical study proves that g - C_3N_4 is the most stable allotrope of carbon nitride at ambient condition.

1.6. Different phases of carbon nitride and its different shape

Mainly, there are five different structural forms of carbon nitride which are β - C_3N_4 , α - C_3N_4 , cubic- C_3N_4 , pseudocubic- C_3N_4 and g - C_3N_4 . They are either two dimensional or three dimensional polymorphs. Among different structural forms of carbon nitride α - C_3N_4 , β - C_3N_4 and g - C_3N_4 are most energetically stable phases which are theoretically predicted. Experimentally it has been observed that at ambient condition g - C_3N_4 is most stable allotrope. β - C_3N_4 phase is the polymorph among different carbon nitride structures which is isostructural with β - Si_3N_4 . β - C_3N_4 is a metastable phase of carbon nitride. It is a hexagonal network of tetrahedral bonded (sp^3) carbon and sp^2 bonded nitrogen in trigonal planar geometry. It has either $P3$ or $P6_{3/m}$ space group. Structural features of β -carbon nitride includes high number of atoms make it high density as well as hardness like diamond. In 1989 Liu and Cohen have done local density approximation calculation which suggests that β -carbon nitride have bulk modulus 427 GPa which is comparable with diamond (440 GPa)⁴⁴. Similar way, α - C_3N_4 is isostructural with α - Si_3N_4 . In α - C_3N_4 carbon and nitrogen atoms are adopting sp^3 and sp^2 hybridization respectively. The structure of α - C_3N_4 consists ABAB stacking sequence where 'A' and 'B' layers are having

mirror image relationship. Here 'A' layer is the unit cell of β - C_3N_4 and then the B layer is the mirror image of the unit cell of β - C_3N_4 . The c parameter of α - C_3N_4 structure is then twice c of β - C_3N_4 polymorph. The unit cell of α - C_3N_4 has $P3_{1c}$ symmetry. α - C_3N_4 has unique feature of negative Poisson ratio in all directions which is a unique property among different carbon nitrides. Cubic C_3N_4 is isostructural with Zn_2SiO_4 . In 1996 J. Hemley *et. al.* have done local density approximation calculation of cubic C_3N_4 structure with stoichiometry C_3N_4 have a bulk modulus 496 GPa significantly larger than that of diamond⁴⁵. Cubic C_3N_4 is a network structure where the corners are linked by CN_4 tetrahedrons consists of CNC angle of 109° . Two space groups of I-43d and F43m has been proposed for cubic C_3N_4 structure. The structure of g- C_3N_4 also exhibits ABAB stacking sequence with planar structure. The unit cell of g- C_3N_4 has $P6^-m2$ symmetry.

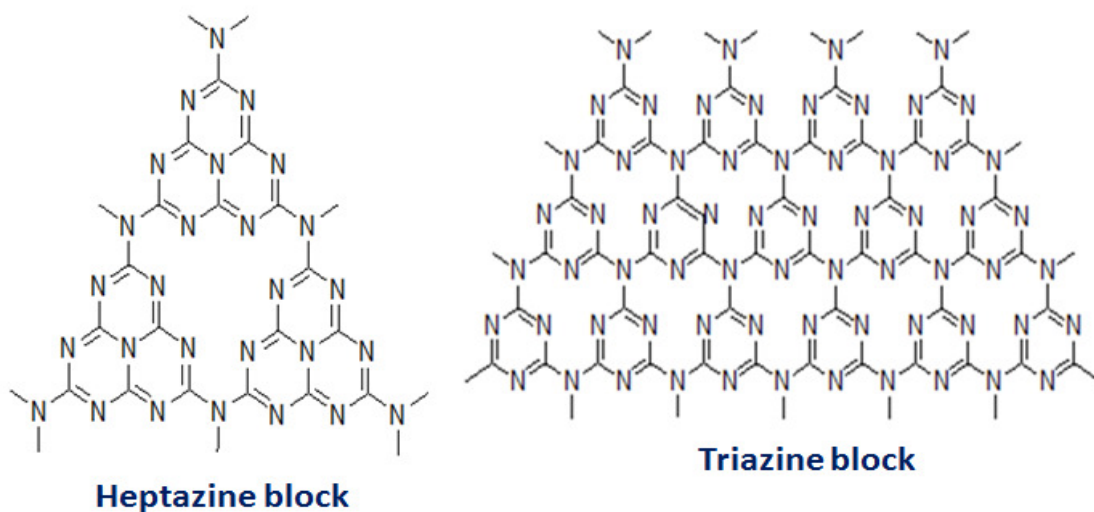


Figure 1.7. Heptazine and triazine block of g- C_3N_4 .

There are two types of $g\text{-C}_3\text{N}_4$ possible which are heptazine block based $g\text{-C}_3\text{N}_4$ and triazine block based $g\text{-C}_3\text{N}_4$ shown in Figure 1.7. Pseudocubic- C_3N_4 structure has defective zinc blende structure and it has $P42m$ symmetry. Beside of this different phases of carbon nitride it can be in different shaped such as microfiber carbon nitride with large length-diameter ratio⁴⁶, nanorod⁹, tubular graphitic carbon nitride⁴⁷, hollow vessel graphitic carbon nitride⁴⁸, leaf like carbon nitride nanostructure⁴⁹ etc. Different shaped carbon nitride has different properties with specific application. For example, ribbon like $g\text{-C}_3\text{N}_4$ can be synthesized from dicyandiamide using sodium chloride as template. The importance of this ribbon like $g\text{-C}_3\text{N}_4$ microstructure is that it has high solubility in water with high stability and it has high photoluminescence property⁵⁰.

1.7. Different method to synthesis of carbon nitride

On the basis of literature study fabrication method of carbon nitride can be classified in two different approaches top-down fabrication method and bottom-up fabrication method. The top-down approached includes liquid exfoliation method and thermal etching method whereas the bottom-up fabrication method includes laser method, CVD method, template method and solid state condensation method. By bottom-up fabrication method carbon nitride can be produced in large scale.

1.7.1. Top-Down fabrication method

Top-Down fabrication method involves the exfoliation of bulk solid to its reduced dimensional form. Top-Down fabrication method of carbon nitride is two types, namely liquid exfoliation method and thermal etching method.

1.7.1.1. Liquid exfoliation method

Liquid exfoliation method is generally developed to synthesis of 2D carbon nitride nanosheets.

The exfoliation process depends on the enthalpy of mixing of the nanosheets. To increase the efficiency of the exfoliation process enthalpy of mixing should be minimized. The enthalpy of mixing depends on the surface energy of the solvent and the thickness and volume fraction of the nanosheets⁵¹. Firsttime, X. Zhang *et. al.* demonstrated that ultrathin 2D g-C₃N₄ nanosheets can be synthesized from bulk g-C₃N₄ by ultrasound method in water named as green liquid exfoliation method⁵². In 2014, K. Schwinghammer *et. al.* demonstrated that the synthesis of 1-2 nm thickness of carbon nitride nanosheet by liquid exfoliation of poly(triazine imide) in water by sonication method⁵³. To improve efficiency and as well as to synthesis the uniform size of carbon nitride nanosheets researchers are used mixed solvents for example mixture of ethanol-water, dimethylformamide-water, tetrahydrofuran-water, isopropanol-water etc⁵⁴⁻⁵⁵. Further improvement has done by intercalation method followed by liquid exfoliation method. Intercalation of the metal into the g-C₃N₄ sheet can overcome the van der Waals interaction force between the carbon nitride layers which helps to produce the g-C₃N₄ layers. Mineral acids for example HCl and H₂SO₄ are used for intercalation into the graphitic carbon nitride sheet. The nitrogen of the carbon nitride is the binding site of the mineral acids which helps the intercalation process. Due to small size of lithium ion it can also be intercalated to exfoliate the carbon nitride layers producing high quality few layer carbon nitride sheets⁵⁶.

1.7.1.2. Thermal etching method

Weak van der Waals forces are acting between the layers of bulk carbon nitride like graphite. Therefore, thermal treatment can delaminate the 2D carbon nitride nanosheets from bulk carbon

nitride material. The thickness of the carbon nitride layers can be decreased by layer by layer thermal etching of the bulk carbon nitride. For example, P. Niu *et. al.* demonstrated that 2 nm thickness of g-C₃N₄ nanosheet can be obtained by thermal etching of bulk g-C₃N₄⁵⁷. Thermal etching method have disadvantages like the defects are forming into the thin carbon nitride layers during the thermal etching process and yield of this method is also very low.

1.7.2. Bottom-up fabrication method

1.7.2.1. Laser method

Synthesis of carbon nitride by laser method can be divided into two ways one is synthesis of carbon nitride by laser ablation method and another is synthesis of carbon nitride by laser induced chemical reaction method. Laser ablation method is the process to remove materials from a solid substrate using a high energy laser source. In laser ablation technique graphite substrate is used as source of carbon. During ablation on the graphite surface nitrogen or ammonia has been used as the source of nitrogen atoms. The carbon atoms into the graphite surface are the ablated species and the nitrogen or ammonia molecules are adsorbed on the graphite surface. Due to laser radiation the nitrogen or ammonia molecules decomposes to nitrogen atoms on the surface of graphite and it increases the amount of nitrogen content on the graphite source. The ablation of carbon atoms from the graphite surface can decrease the carbon content on its surface. The relative quantity of carbon and nitrogen of the as synthesized carbon nitride depends on the pressure of nitrogen or ammonia or mixed gas and the wavelength of using laser as well as power of it. Generally, Nd:YAG or CO₂ laser has been used in the laser ablation technique. In laser ablation technique nitrogen atom bombardment with high energy has

been used to get nitrogen rich carbon nitride compound. To synthesis the exact ratio of nitrogen and carbon ($N/C = 1.33$) in C_3N_4 is very much difficult by this method. Additionally, the synthesized carbon nitride by laser ablation method is contaminated by $-C\equiv N$, $-C_2N$, $-CH$ and $-NH$ groups which is proved by XPS and FT-IR spectroscopy. There are very few reports where crystalline carbon nitride has been synthesized by laser ablation technique. In some cases the crystalline pattern is not matching completely with the carbon nitride, some peaks are missing, some peaks are very low intense which is not matching with theoretical values. Zhong-Min Ren *et. al.*⁵⁸.synthesized the carbon nitride films on the (100) plane of silicon substrate by laser ablation of graphite in presence of low energy nitrogen ion beam bombardment. High energy back scattering spectroscopy study has shown that 40% nitrogen is there in the carbon nitride film. The TEM and electron diffraction pattern proves the predominant amorphous nature of the carbon nitride film. The time of flight (TOF) measurement of the synthesized amorphous carbon nitride film suggests the existence of paracyanogen like material such as $(CN)_n$ ⁵⁸. Generally, CO_2 or KrF lasers have been used to synthesis the carbon nitride by laser induced chemical method. Crystalline C_3N_4 film is possible to synthesize by pulsed laser induced reactive quenching at the liquid-solid interface of tungsten substrate and hexamethylenetetramine compound. Hexamine ($C_6H_{12}N_4$) dissolved in liquid ammonia at -60^0C and decomposition of the mixture was done by ArF excimer laser. The synthesized carbon nitride was deposited on tungsten and mixture of α and β phases of carbon nitride have been observed⁵⁹. Crystalline carbon nitride can be synthesized by using laser ablation method. Li Yang and his coworkers successfully synthesized the crystalline carbon nitride nanopowder and nanorod by using pulsed laser ablation technique of a graphite surface in liquid ammonia solution at room temperature and pressure. By using

short laser pulse length nanopowder carbon nitride can be obtained whereas by using long laser pulse length gives nanorod carbon nitride⁶⁰.

1.7.2.2. Chemical Vapor Deposition method

Generally chemical vapor deposition (CVD) method is used to prepare thin film of carbon nitride on various substrates. There are different types of CVD method. On the (100) plane of silicon crystalline carbon nitride were prepared by microwave plasma chemical vapor deposition method (MPCVD) where CH_4 and N_2 are used as precursor gases⁶¹. By this CVD method carbon nitride nanotube can also be fabricated from the polymerization of carbon nitride nanobells⁶². Amorphous carbon nitride thin film was prepared by plasma enhanced chemical deposition (PECVD) method using high purity NH_3 and CH_4 as the source of nitrogen and carbon respectively by using radio frequency⁶³. Uniform deposition of the carbon nitride over large area of substrate is the advantage of PECVD method. Laser CVD method is another CVD method to synthesis of carbon nitride material⁶⁴. The main advantage of this method is that one can selectively deposit the compound on the substrate by controlling the laser pathway. Selective phase growth of carbon nitride film can be prepared by bias-assisted hot filament chemical vapor deposition (HFCVD) method controlling mixture of N_2 , H_2 and CH_4 gases⁶⁵. $\beta\text{-C}_3\text{N}_4$ film was prepared on nickel substrate by magnetically rotated arc plasma jet chemical vapor deposition method⁶⁶. The main advantage of all types of the CVD method is that there is less deposition of waste material with the synthesized compound on the substrate because only the heated samples are deposited on the surface of the substrate.

1.7.2.3. Template Method

The most common way to increase the surface area of carbon nitride is to make it porous which is possible by simple template method using silica nanoparticle or mesoporous silica. 3D Cubic mesoporous carbon nitride was synthesized from ordered mesoporous silica KIT-6 as hard template⁶⁷. Mesoporous carbon nitride was synthesized from SBA-15ht as template where mesoporous silica SBA-15ht was synthesized with tetraethyl orthosilicate as a silica source and Pluronic P123 ((EO)20(PO)70(EO)20) as a structure-directing agent⁶⁸. In most of the cases the mesoporous carbon nitride was synthesized by using silica template as hard template. After formation of mesoporous structure the silica matrices were removed by aqueous ammonium bifluoride (NH_4HF_2) or hydrogen fluoride (HF) which is hazardous and not environmentally friendly. Due to hazardous and environmental issue researchers are started to synthesis of mesoporous carbon nitride from soft template like block polymers and surfactants. Graphitic carbon nitride with nanoporous structure has been synthesized by using different soft and direct templates for example different ionic and non ionic surfactant and different ionic liquids through the self-polymerization reaction of dicyandiamide⁶⁹. Though there are very few reports to synthesis of porous⁷⁰ and mesoporous⁷¹ g-C₃N₄ by template free method. Generally hazardous chemicals are used to remove the template. M. Wu *et al.* demonstrated that without using any hazardous chemicals soft template can be removed after synthesis of carbon nitride nanosheet. It can be synthesized from melamine and potassium chloride (KCl) at an elevated temperature of 550⁰C. Here, KCl is used a soft template and acts as a preventer of recombination rate between light induced electrons and holes. The residual KCl can be removed by simply washing with water. Therefore this potassium modified g-C₃N₄ can be used efficiently in the photocatalytic H₂ evolution reaction⁷².

1.7.2.4. Solid state condensation method

Solid state condensation method involves the polymerization of different precursors at high temperature and pressure. $g\text{-C}_3\text{N}_4$ can be prepared by one step polymerization method from different precursors such as dicyandiamide⁷³, urea⁷⁴ and melamine⁷⁵ compounds. The formation pathway of $g\text{-C}_3\text{N}_4$ from dicyandiamide, melamine and urea via solid state condensation method has shown in Figure 1.8 and 1.9.

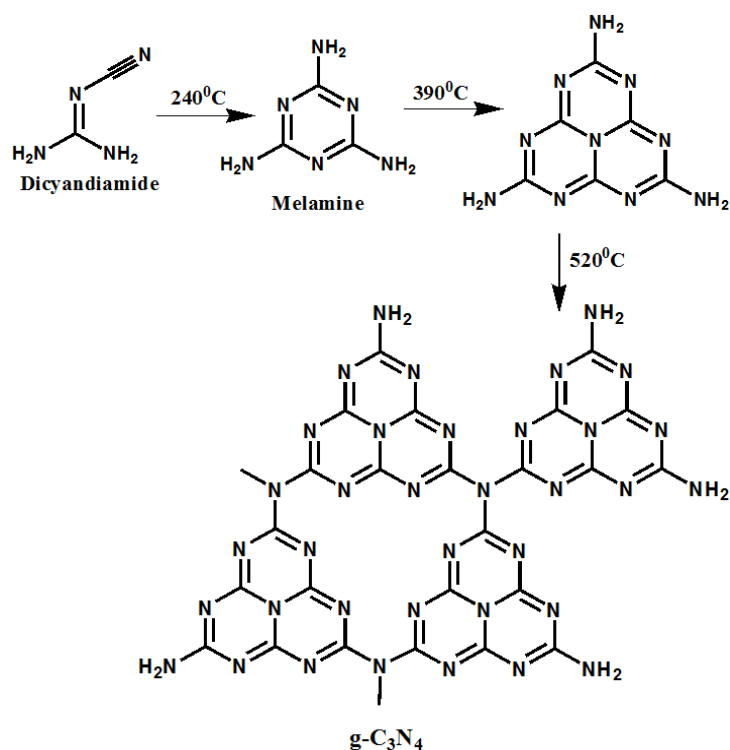


Figure 1.8. Reaction pathway of solid state condensation method starting from dicyandiamide and melamine to produce $g\text{-C}_3\text{N}_4$.

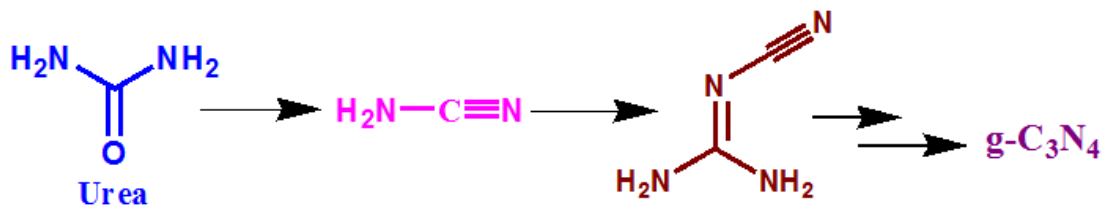


Figure 1.9. Reaction pathway of solid state condensation method starting from urea to produce g-C₃N₄.

g-C₃N₄ was obtained from temperature induced condensation of dicyandiamide by using eutectic mixture of lithium chloride and potassium chloride as solvent. From urea yellow colored g-C₃N₄ can be synthesized on a large scale by the simple pyrolysis of urea under ambient pressure. First, the urea was dried at 80⁰C for 24 hours, and then it was put in a covered crucible and heated at 550⁰C for 3 hours to obtained g-C₃N₄. Instead of using toxic dicyandiamide compound nitrogen rich g-C₃N₄ can be synthesized from thiourea by solid state condensation method⁷⁶. Formation of disorganized 2D agglomerate by solid state condensation makes the compound small surface area with low catalytic activity which is the main drawback of solid state condensation method.

1.8. Properties of carbon nitride

1.8.1. Optical properties of carbon nitride

Optical band gap is an important term to the optical properties measurement of semiconductor materials. Optical band gap of a semiconductor material is the energy difference between valence band and conduction band. It is closely related to the energy gap between HOMO and LUMO levels. Materials having large optical band gap called insulator whereas materials having

medium band gap is called semiconductor and materials having low or no band is called conductors. Optical band gap can give also the idea of electrical conductivity. Optical properties of carbon nitride were performed by doing UV-visible diffuse reflectance spectroscopy and photoluminescence measurement. By doing diffuse reflectance spectroscopy one can find out the optical band gap of the semiconductor materials. Different carbon nitride materials has different optical band gap and it depends on synthesis method and the amount of nitrogen content into the carbon nitride compound. Electronic structure of amorphous carbon nitride can be changed by increasing amount of hydrogen gas during ion beam assisted deposition method. So it will increase the degree of polymerization by forming terminal NH and CH bonds which will increase the optical band gap of amorphous carbon nitride material⁷⁷. Carbon nitride film has different band gap from bulk carbon nitride material. Generally optical band gap of carbon nitride film varies from 0 eV to 3 eV⁷⁸. S. E. Rodil *et. al.*⁷⁸ have observed that the optical band gap of the synthesized sp^2 bonded carbon nitride by DC magnetron sputtering system increases with the nitrogen content in the film. They have also synthesized carbon nitride film by filtered cathodic vacuum arc in presence of low pressure N_2 plasma. For this carbon nitride they have observed that optical band gap initially decreases with increase of the nitrogen content but after a certain amount of nitrogen content the band gap remain constant. The increase of nitrogen content to the carbon nitride film can increase the porosity of the film which is the cause of strong luminescent property of this film. This observation proves that the incorporation of amount of nitrogen can change the optical band gap of this carbon nitride film and its optical property depends on the synthesis method of the film preparation. With increase the amount of nitrogen content into the carbon nitride material the sp^2 domain increases into the film; therefore the distribution of sp^2 domain and local bonding of this domain can change the optical band

gap⁷⁹. Optical band gap of synthesized carbon nitride by CVD method varies with the nitrogen ion energy and composition of the reactants. Optical band gap of bulk carbon nitride material depends on degree of condensation of the material at different temperatures and nature of the starting materials⁸⁰. g-C₃N₄ observed optical band gap of 2.7 eV where the positions of conduction band and the valence band are -1.1 eV and +1.6 eV which originates from the sp² hybridized carbon and nitrogen atoms in g-C₃N₄ structure⁴⁰. Modification of shape of g-C₃N₄ can increase the band gap from 2.7 eV to 3.0 eV⁵⁰. Optical band gap of g-C₃N₄ can be modified by doping the heteroatoms into its framework structure. The optical band gap of fluorine doped carbon nitride decreases compare to undoped g-C₃N₄. After doped with fluorine the band gap shifted from 2.7 eV to 2.63 eV which proves that fluorine is not bounded as a counter ion, it is doped into the g-C₃N₄ framework⁸¹. Z. Ding *et. al.*¹⁰ showed that the different transition metals such as Co, Ni, Mn, Zn modified carbon nitride has lower energy band gap compare to the undoped g-C₃N₄¹⁰. Different metal doped g-C₃N₄ has different color which proves that they have high power to absorb the light. Usually g-C₃N₄ shows strong blue photoluminescence property at room temperature over a wide range of wavelength. Two-photon absorbance and chemiluminescence properties have been observed by g-C₃N₄ material.

1.8.2. Thermal property of carbon nitride

The high nitrogen concentration into the carbon nitride increases the thermal stability of amorphous carbon nitride material. The graphitic carbon nitride thermally can suffer up to temperature 600⁰C which was analyzed by TGA analysis. The complete decomposition of graphitic carbon nitride started from temperature at 750⁰C⁴⁰.

1.8.3. Solubility of carbon nitride

There is no detectable standard solubility of carbon nitride in conventional solvents such as alcohol, dimethyl formamide (DMF), tetrahydrofuran (THF), toluene, ether and water⁸². Carbon nitride synthesized from different precursors and by different synthesis methods has different solubility for a specific solvent. Generally, carbon nitride is more soluble in polar solvents like formamide, DMF and water than non polar solvent which is may be presence of hydrogen bonding between carbon nitride and polar solvent. Ultrathin g-C₃N₄ has more solubility than bulk due to presence of van der Waal interaction between the carbon nitride layers in the bulk sample⁸³.

1.9. Zero dimensional carbon material: graphene quantum dot

Quantum dots are fluorescent semiconductor nanocrystals, few nanometer size contain hundred to a few thousand atoms and shows quantum confinement effect. The size of the quantum dot can change the electronic properties of it; the size of the quantum dot is inversely proportional to the band gap of it. Among different quantum dots, graphene quantum dot (GQD) has got great attention into the scientific community due its large application in the field of biomedicine, photovoltaic cell and microelectronics with low toxicity. Graphene quantum dots have strong fluorescence emission property with high quantum yield and it has tunable emission property over the entire wavelength range from ultraviolet to infrared including visible range. The quantum confinement and the edge effect are responsible to induce its photoluminescence property. The fluorescence quantum yield of GQD can be increased by doing oxidation of it by acid treatment or by doing surface passivation of it during synthesis method of it. Additionally, fluorescent carbon nitride quantum dots have also excellent properties such as low toxicity, high

stability, easy biological labelling. Therefore, fluorescent graphene and carbon nitride quantum dots can be used in bioimaging and biosensing application fields. Both graphene and carbon nitride quantum dots are better material than semiconductor metal oxide quantum dots in the biological application field because into the semiconductor metal oxide quantum dots metal oxide can creates high toxicity which is unfavorable to study the bioimaging and biosensing. GQD can be synthesized from graphene or graphite by top down fabrication method which involves the breaking the carbon-carbon bonds of graphene or graphite. GQD can be synthesized from organic molecule which is known as bottom up fabrication method. The main advantage of this method is that we can control the size of GQDs. Multistep and the purification of each step is the main problem of this method. First, in 2004, Xu *et. al.*⁸⁴ discovered the carbon quantum dot during the purification of single walled carbon nanotube from arc discharge method. Among different carbon quantum dots graphene and carbon nitride quantum dots has got more attention into scientific community due to its great potential application in different fields. Micrometer sized graphene sheets have limitation in the application field of nanodevices. When lateral dimension of the graphene sheet became below 100 nm they are called graphene quantum dot (GQD) and it shows properties such as quantum confinement effect and edge effect which changes its physical properties⁸⁵. First time in 2011 X. Sun *et. al.*⁸⁶ have represented that photoluminscent carbon nitride dot can be synthesized by simple heat treatment method. They demonstrate that photoluminscent carbon nitride dot can be synthesized by polymerization of 1,2-ethylenediamine and carbon tetrachloride (CCl₄) under reflux or microwave or solvothermal heating. In the same year again X. Sun *et. al.*⁸⁷ have reported the synthesize of photoluminscent carbon nitride by microwave irradiation method of N,N-dimethylformamide in presence of acids such as H₂SO₄, chlorosulfonic acid, HNO₃ or HCl. Again in 2012 X. Sun *et. al.*⁸⁸ have

demonstrated the synthesized photoluminescent carbon nitride dots by polymerization of carbon tetrachloride (CCl_4) and using different organic amines such as dimethylamine, ethylamine or tripropylamine in presence of acids such as sulfuric acid (H_2SO_4), nitric acid (HNO_3), chlorosulfonic acid and hydrochloric acid (HCl) separately under microwave heat treatment. Most of the cases during the synthesis method of carbon nitride dot high temperature have been used. A low temperature was used to synthesis of highly fluorescent carbon nitride dot by using sodium citrate and urea as starting materials⁸⁹. Strong fluorescent zero dimensional carbon nitride quantum dot was synthesized from guanidine hydrochloride and EDTA by microwave heating method and it shows the chemiluminescence feature with NaClO^{90} .

1.10. Graphitic carbon nitride based nanocomposite and their applications

Synthesis of nanostructured composite material became more interesting into the scientific community due to its improved and large area of application in different fields. Now days, the graphitic carbon nitride material has been used to prepare different composite materials with different metal or metal oxide nanoparticles or with other semiconductor materials. Due to the presence of 2D flat surface with high surface area and presence of Brönsted and Lewis basic sites into the $\text{g-C}_3\text{N}_4$ moiety (Figure 1.10) it can make a good potential junction into the composite material. Due to large energy demand and to protect the environment from the pollution renewable energy technology started to develop in rapid way. Renewable energy technology produces sustainable energy from sources like wind, sunlight, water, plants. Renewable energy technology can produce large amount of energy by keeping the environment clean. Fuel cells and water splitting cells are considered the renewable energy source. Oxygen reduction reaction,

hydrogen evolution and oxygen evolution reaction have vital role in the fuel cell and water splitting technology.

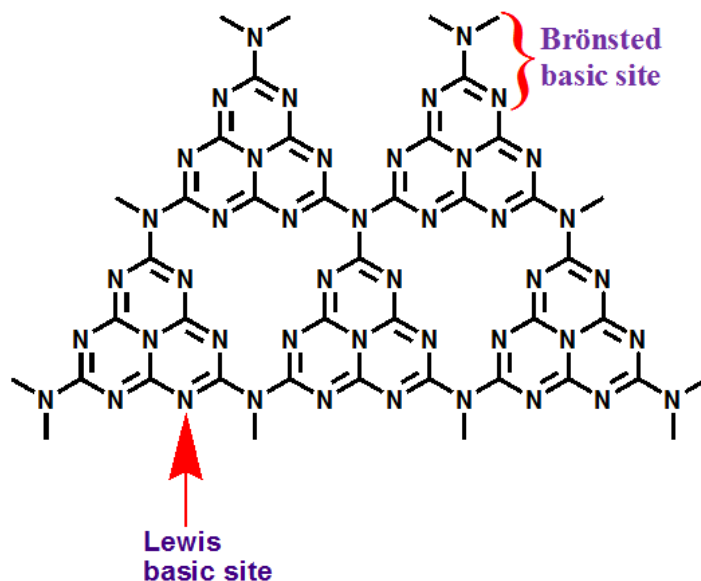


Figure 1.10. Brønsted and Lewis basic sites of g-C₃N₄.

Different graphitic carbon nitride based composite materials are used as electrocatalysts into the oxygen reduction reaction and hydrogen evolution reaction and oxygen evolution reaction. As a renewable energy technology in solar energy technology semiconductor materials have been used as a photocatalyst material to convert solar light to solar energy. A traditional semiconductor photocatalyst material is TiO₂. But in terms of solar energy conversion efficiency it has poor performance due to its wide band gap. Additionally it has poor efficiency as a photocatalyst into the visible light driven energy conversion. Therefore, different TiO₂ modified photocatalyst, TiO₂ alternative photocatalyst has been used to get improved solar energy conversion efficiency. Now a day it is still challenging to fabricate in a facile way which can be used a highly efficient visible light driven photocatalyst. Recently, g-C₃N₄ has got more attention

in the research field and has been used as a promising photocatalyst in the solar energy conversion study due to its tunable electronic structure. During the photocatalysis process under the visible light illumination the electron from the valence band of $g\text{-C}_3\text{N}_4$ is excited to conduction band and hole is created into the valence band. The electron presence into the conduction band is responsible to carry out the photocatalytic process. But the recombination process between electron and hole during the photocatalysis decreases the efficiency of the process. The main drawback to use the $g\text{-C}_3\text{N}_4$ as a photocatalyst is it has high rate to recombine the electron and hole during the photocatalytic study. Therefore, instead of use of $g\text{-C}_3\text{N}_4$ scientists starts to use different composite material of $g\text{-C}_3\text{N}_4$ which has very less probability of recombination process between electron and hole. Heterojunction formation into the $g\text{-C}_3\text{N}_4$ based composite is very much important due to its high efficiency into the photocatalytic study. In this type of composite the charge carriers are transferred through the heterojunction of the composite which decreases the recombination rate. For example Li *et. al.* have demonstrated that $g\text{-C}_3\text{N}_4/\text{rGO}$ nanocomposite shows enhanced visible light photocatalytic degradation of 4-nitrophenol and RhB dye by forming metal free heterojunction⁹¹. Apart from this heterojunction composite material of $g\text{-C}_3\text{N}_4$ metal or metal oxide embedded $g\text{-C}_3\text{N}_4$ composite can also change the photocatalytic activity by changing the band gap of its. Particularly the metal/metal oxide-carbon nitride composite material reduces the band gap and can absorb the light in visible region which increases its efficiency in the application of water splitting by using solar energy⁹², photocatalytic hydrogen production⁹³ and dye degradation⁷ by using visible light. Though $g\text{-C}_3\text{N}_4$ has potential power as a photocatalyst for hydrogen evolution reaction and water splitting, the quantum efficiency is very low whereas the metal doped carbon nitride composite can fill up that inability with high efficiency⁶. Fuel cell development is gradually increasing due to large

energy demand and decreasing the amount of fossil fuel in the earth. Most operating fuel cell involves polymer electrolyte membrane (PEM) fuel cell which converts the chemical energy of hydrogen fuel to electrical energy. The catalysts used in the fuel cell are generally high surface area metal nanoparticles with narrow size distribution and well dispersed on the supporting material. Different carbon materials like carbon black are used as support material into the catalyst of the PEM fuel cell. It is challenging to maintain the narrow size distribution with high surface area of metal nanoparticles on the supporting material during the electrocatalytic activity into the fuel cell. Therefore, there is need to develop the support material which have strong interaction with the metal nanoparticles with high durability and stability. Among different carbon based support materials graphitic carbon nitride has got more interest as a support material of the electrode into fuel cell due to its high surface area and presence of heteroatom nitrogen which helps to bind the metal nanoparticles strongly⁹⁴⁻⁹⁵.

1.11. Scope of this thesis

On the basis of literature study of different carbon materials graphene and carbon nitride material has reached as a most interesting material in the research area. The goal of this thesis is to synthesis, property studies and application of graphene, carbon nitride and its composite material.

Synthesis of different dimensional carbon nanomaterials like 0D, 1D, 2D and 3D is very much important due to its unique properties and different properties varies from one dimension to other dimension. Zero dimensional quantum dots have unique optical properties due to its quantum confinement effect which open up biological application like bioimaging, drug delivery etc. In the third chapter synthesis of zero dimensional graphitic carbon nitride quantum dots and

zero dimensional carbon quantum dots has been discussed. Different groups have synthesized carbon nitride material from different carbon and nitrogen containing precursors for example dicyanamide, urea etc. In the third chapter formamide has been used as the precursor to synthesis the graphitic carbon nitride quantum dots (g-CNQDs) by microwave mediated synthesis method. g-CNQDs has excitation wavelength dependent emission property, pH dependent fluorescence property, high ionic strength, high quantum yield. Additionally as g-CNQDs is a metal free material therefore it has low toxicity towards the different biological cells. Therefore, g-CNQDs can be used in different biological applications. g-CNQDs shows ferromagnetic behavior as a metal free 2D carbon material at room temperature, therefore it can be used in spintronic devices and memory devices. Mercury is one of the toxic heavy metals present in the environment which can contaminate the drinking water. Therefore, sensing Hg^{2+} ion in water is very much important. This synthesized g-CNQDs can bind Hg^{2+} ion selectively and shows superquenching property by decreasing its fluorescence intensity. Therefore, g-CNQDs can be used as a probe of Hg^{2+} sensing material. g-CNQDs has high efficiency to remove Cu^{2+} and Pb^{2+} ions from water with high adsorption capacity, therefore it can be used as a waste water treatment material. This chapter also demonstrates the synthesis of carbon quantum dot (CQDs) from formic acid by microwave mediated method which shows excitation wavelength dependent emission property where the emission is covering from the UV region to near IR region, will show a good cell imaging application.

Bottom up fabrication method can be used to synthesis of 2D nanomaterial from its zero dimensional quantum dots which are highlighted in chapter 4. Here 2D carbon nitride and 2D graphene sheets are synthesized from g-CNQDs and CQDs as building blocks respectively by bottom up fabrication method. 2D carbon nitride sheet modified glassy carbon electrode has been

used as an electrochemical sensor of Hg^{2+} ions in water. 2D graphene self assembled from CQDs can be used as an electrochemical sensor of H_2O_2 . Therefore, in future 2D carbon nitride sheets and 2D graphene due to its high surface area and fast electron transfer it can be used as a probe in electrochemical sensing technology or devices.

Different synthesis method of carbon nitride based composite for example iron oxide nanoparticles embedded on carbon nitride matrix ($\text{Fe}_3\text{O}_4\text{-CN}_x$ composite), platinum nanoparticles dispersed-carbon nitride (Pt-CN_x) composite and zinc doped carbon nitride (Zn-CN_x) microspheres has been shown in chapter 5, 6 and 7 respectively. Each composite has different applications. The $\text{Fe}_3\text{O}_4\text{-CN}_x$ composite has superparamagnetic property at room temperature which can be used in magnetic resonance imaging. RhB dye degradation study by this composite has done. The Pt-CN_x composite is shown higher electrochemical oxidation efficiency of small organic molecule like methanol, formic acid and formaldehyde in acidic medium than commercial Pt/C catalyst, so this composite can be used in fuel cell devices. The Zn-CN_x microspheres can be used as waste water treatment as it can remove Cd^{2+} , Cu^{2+} and Pb^{2+} ions from water with high adsorption capacity.

Chapter References

1. Novoselov, K. S.; Geim, A. K.; Morozov, S. V.; Jiang, D.; Zhang, Y.; Dubonos, S. V.; Grigorieva, I. V.; Firsov, A. A., *Science* **2004**, *306*, 666-669.
2. Balandin, A. A.; Ghosh, S.; Bao, W.; Calizo, I.; Teweldebrhan, D.; Miao, F.; Lau, C. N., *Nano Lett.* **2008**, *8*, 902-907.
3. Lee, C.; Wei, X.; Kysar, J. W.; Hone, J., *Science* **2008**, *321*, 385-388.

4. Goettmann, F.; Fischer, A.; Antonietti, M.; Thomas, A., *Angew. Chem. In. Ed.* **2006**, *45*, 4467-4471.
5. Wang, X.; Maeda, K.; Thomas, A.; Takanabe, K.; Xin, G.; Carlsson, J. M.; Domen, K.; Antonietti, M., *Nat Mater* **2009**, *8*, 76-80.
6. Maeda, K.; Wang, X.; Nishihara, Y.; Lu, D.; Antonietti, M.; Domen, K., *J. Phys. Chem. C* **2009**, *113*, 4940-4947.
7. Cheng, N.; Tian, J.; Liu, Q.; Ge, C.; Qusti, A. H.; Asiri, A. M.; Al-Youbi, A. O.; Sun, X., *ACS Appl. Mater. Interfaces* **2013**, *5*, 6815-6819.
8. Lin, J.; Pan, Z.; Wang, X., *ACS Sustainable Chem. Eng.* **2014**, *2*, 353-358.
9. Xu, L.; Xia, J.; Wang, L.; Ji, H.; Qian, J.; Xu, H.; Wang, K.; Li, H., *Eur. J. Inorg. Chem.* **2014**, *2014*, 3665-3673.
10. Ding, Z.; Chen, X.; Antonietti, M.; Wang, X., *ChemSusChem* **2011**, *4*, 274-281.
11. Kim, S.; Hwang, S. W.; Kim, M.-K.; Shin, D. Y.; Shin, D. H.; Kim, C. O.; Yang, S. B.; Park, J. H.; Hwang, E.; Choi, S.-H.; Ko, G.; Sim, S.; Sone, C.; Choi, H. J.; Bae, S.; Hong, B. H., *ACS Nano* **2012**, *6*, 8203-8208.
12. Li, L.-s.; Yan, X., *J. Phys. Chem. Lett.* **2010**, *1*, 2572-2576.
13. Wallace, P. R., *Phys. Rev.* **1947**, *71*, 622-634.
14. Boehm, H. P.; Clauss, A.; Fischer, G. O.; Hofmann, U., *Z. Anorg. Allg. Chem.* **1962**, *316*, 119-127.
15. Mouras, S.; Hamwi, A.; Djurado, D.; Cousseins, J. C., *Rev. Chim. Miner.* **1987**, *24*, 572-588.

16. Behabtu, N.; Lomeda, J. R.; Green, M. J.; Higginbotham, A. L.; Sinitskii, A.; Kosynkin, D. V.; Tsentelovich, D.; Parra-Vasquez, A. N. G.; Schmidt, J.; Kesselman, E.; Cohen, Y.; Talmon, Y.; Tour, J. M.; Pasquali, M., *Nat. Nanotechnol.* **2010**, *5*, 406-411.
17. Hernandez, Y.; Nicolosi, V.; Lotya, M.; Blighe, F. M.; Sun, Z.; De, S.; McGovern, I. T.; Holland, B.; Byrne, M.; Gun'Ko, Y. K.; Boland, J. J.; Niraj, P.; Duesberg, G.; Krishnamurthy, S.; Goodhue, R.; Hutchison, J.; Scardaci, V.; Ferrari, A. C.; Coleman, J. N., *Nat. Nanotechnol.* **2008**, *3*, 563-568.
18. Vallés, C.; Drummond, C.; Saadaoui, H.; Furtado, C. A.; He, M.; Roubeau, O.; Ortolani, L.; Monthieux, M.; Pénicaud, A., *J. Am. Chem. Soc.* **2008**, *130*, 15802-15804.
19. Blake, P.; Brimicombe, P. D.; Nair, R. R.; Booth, T. J.; Jiang, D.; Schedin, F.; Ponomarenko, L. A.; Morozov, S. V.; Gleeson, H. F.; Hill, E. W.; Geim, A. K.; Novoselov, K. S., *Nano Lett.* **2008**, *8*, 1704-1708.
20. Lotya, M.; Hernandez, Y.; King, P. J.; Smith, R. J.; Nicolosi, V.; Karlsson, L. S.; Blighe, F. M.; De, S.; Wang, Z.; McGovern, I. T.; Duesberg, G. S.; Coleman, J. N., *J. Am. Chem. Soc.* **2009**, *131*, 3611-3620.
21. Lotya, M.; King, P. J.; Khan, U.; De, S.; Coleman, J. N., *ACS Nano* **2010**, *4*, 3155-3162.
22. Hummers, W. S.; Offeman, R. E., *J. Am. Chem. Soc.* **1958**, *80*, 1339-1339.
23. Tung, V. C.; Allen, M. J.; Yang, Y.; Kaner, R. B., *Nat Nano* **2009**, *4*, 25-29.
24. Rao, C. N. R.; Maitra, U.; Matte, H. S. S. R., Synthesis, Characterization, and Selected Properties of Graphene. In *Graphene*, Wiley-VCH Verlag GmbH & Co. KGaA: 2012; pp 1-47.
25. Alanyalıoğlu, M.; Segura, J. J.; Oró-Solè, J.; Casañ-Pastor, N., *Carbon* **2012**, *50*, 142-152.

26. Wang, G.; Wang, B.; Park, J.; Wang, Y.; Sun, B.; Yao, J., *Carbon* **2009**, *47*, 3242-3246.
27. Liu, R.; Wu, D.; Feng, X.; Müllen, K., *J. Am. Chem. Soc.* **2011**, *133*, 15221-15223.
28. Li, X.; Cai, W.; An, J.; Kim, S.; Nah, J.; Yang, D.; Piner, R.; Velamakanni, A.; Jung, I.; Tutuc, E.; Banerjee, S. K.; Colombo, L.; Ruoff, R. S., *Science* **2009**, *324*, 1312-1314.
29. Reina, A.; Jia, X.; Ho, J.; Nezich, D.; Son, H.; Bulovic, V.; Dresselhaus, M. S.; Kong, J., *Nano Lett.* **2009**, *9*, 30-35.
30. Roumen, V.; Alexander, M.; Roumen, H. P.; Raymond, K.; Myrjam, M.; Annick, V.; Chris Van, H., *Nanotechnology* **2010**, *21*, 095602.
31. Sutter, P. W.; Flege, J.-I.; Sutter, E. A., *Nat. Mater.* **2008**, *7*, 406-411.
32. Yang, X.; Dou, X.; Rouhanipour, A.; Zhi, L.; Räder, H. J.; Müllen, K., *J. Am. Chem. Soc.* **2008**, *130*, 4216-4217.
33. Geim, A. K.; Novoselov, K. S., *Nat Mater* **2007**, *6*, 183-191.
34. Chen, J.-H.; Jang, C.; Xiao, S.; Ishigami, M.; Fuhrer, M. S., *Nat Nano* **2008**, *3*, 206-209.
35. Nair, R. R.; Blake, P.; Grigorenko, A. N.; Novoselov, K. S.; Booth, T. J.; Stauber, T.; Peres, N. M. R.; Geim, A. K., *Science* **2008**, *320*, 1308-1308.
36. Li, Z. Q.; Henriksen, E. A.; Jiang, Z.; Hao, Z.; Martin, M. C.; Kim, P.; Stormer, H. L.; Basov, D. N., *Nat. Phys.* **2008**, *4*, 532-535.
37. Novoselov, K. S.; Falko, V. I.; Colombo, L.; Gellert, P. R.; Schwab, M. G.; Kim, K., *Nature* **2012**, *490*, 192-200.
38. Zhao, W.; Wu, F.; Wu, H.; Chen, G., *J. Nanomaterials* **2010**, *2010*, 1-4.
39. Holst, J. R.; Gillan, E. G., *J. Am. Chem. Soc.* **2008**, *130*, 7373-7379.
40. Liu, J.; Wang, H.; Antonietti, M., *Chem. Soc. Rev.* **2016**, *45*, 2308-2326.
41. Liebig, J., *Annalen der Pharmacie* **1834**, *10*, 1-47.

42. Franklin, E. C., *J. Am. Chem. Soc.* **1922**, *44*, 486-509.
43. Hosmane, R. S.; Rossman, M. A.; Leonard, N. J., *J. Am. Chem. Soc.* **1982**, *104*, 5497-5499.
44. Liu, A. Y.; Cohen, M. L., *Phys. Rev. B* **1990**, *41*, 10727-10734.
45. Teter, D. M.; Hemley, R. J., *Science* **1996**, *271*, 53-55.
46. Zhao, Y.; Liu, Z.; Chu, W.; Song, L.; Zhang, Z.; Yu, D.; Tian, Y.; Xie, S.; Sun, L., *Adv. Mater.* **2008**, *20*, 1777-1781.
47. Tahir, M.; Cao, C.; Butt, F. K.; Idrees, F.; Mahmood, N.; Ali, Z.; Aslam, I.; Tanveer, M.; Rizwan, M.; Mahmood, T., *J. Mater. Chem. A* **2013**, *1*, 13949-13955.
48. Li, Y.; Zhang, J.; Wang, Q.; Jin, Y.; Huang, D.; Cui, Q.; Zou, G., *J. Phys. Chem. B* **2010**, *114*, 9429-9434.
49. Li, Y.; Paul, W. M.; Lei, Y.; Tom, B. S.; James, A. S.; Keith, N. R., *Nanotechnology* **2006**, *17*, 5798.
50. Yuan, B.; Chu, Z.; Li, G.; Jiang, Z.; Hu, T.; Wang, Q.; Wang, C., *J. Mater. Chem. C* **2014**, *2*, 8212-8215.
51. Zhang, J.; Chen, Y.; Wang, X., *Energy Environ. Sci.* **2015**, *8*, 3092-3108.
52. Zhang, X.; Xie, X.; Wang, H.; Zhang, J.; Pan, B.; Xie, Y., *J. Am. Chem. Soc.* **2013**, *135*, 18-21.
53. Schwinghammer, K.; Mesch, M. B.; Duppel, V.; Ziegler, C.; Senker, J.; Lotsch, B. V., *J. Am. Chem. Soc.* **2014**, *136*, 1730-1733.
54. Chen, H.-Y.; Ruan, L.-W.; Jiang, X.; Qiu, L.-G., *Analyst* **2015**, *140*, 637-643.
55. Lin, Q.; Li, L.; Liang, S.; Liu, M.; Bi, J.; Wu, L., *Appl. Catal., B* **2015**, *163*, 135-142.

56. Yin, Y.; Han, J.; Zhang, X.; Zhang, Y.; Zhou, J.; Muir, D.; Sutarto, R.; Zhang, Z.; Liu, S.; Song, B., *RSC Adv.* **2014**, *4*, 32690-32697.
57. Niu, P.; Zhang, L.; Liu, G.; Cheng, H.-M., *Adv. Funct. Mater.* **2012**, *22*, 4763-4770.
58. Ren, Z. M.; Du, Y. C.; Ying, Z. F.; Qiu, Y. x.; Xiong, X. X.; Wu, J. D.; Li, F. M., *Appl. Phys. Lett.* **1994**, *65*, 1361-1363.
59. Sharma, A. K.; Ayyub, P.; Multani, M. S.; Adhi, K. P.; Ogale, S. B.; Sunderaraman, M.; Upadhyay, D. D.; Banerjee, S., *Appl. Phys. Lett.* **1996**, *69*, 3489-3491.
60. Yang, L.; May, P. W.; Yin, L.; Smith, J. A.; Rosser, K. N., *J. Nanopart. Res.* **2007**, *9*, 1181-1185.
61. Zhang, Y. P.; Gu, Y. S.; Chang, X. R.; Tian, Z. Z.; Shi, D. X.; Zhang, X. F., *Mater. Sci. Eng., B* **2000**, *78*, 11-15.
62. Zhang, G. Y.; Ma, X. C.; Zhong, D. Y.; Wang, E. G., *J. Appl. Phys.* **2002**, *91*, 9324-9332.
63. Yu, G. Q.; Lee, S. H.; Lee, D. G.; Na, H. D.; Park, H. S.; Lee, J. J., *Surf. Coat. Technol.* **2002**, *154*, 68-74.
64. Falk, F.; Meinschien, J.; Schuster, K.; Stafast, H., *Carbon* **1998**, *36*, 765-769.
65. Chen, Y.; Guo, L.; Wang, E. G., *J. Mater. Sci. Lett.* **1997**, *16*, 594-597.
66. Yen, T. Y.; Chou, C. P., *Appl. Phys. Lett.* **1995**, *67*, 2801-2803.
67. Zheng, Y.; Lin, L.; Ye, X.; Guo, F.; Wang, X., *Angew. Chem. Int. Ed.* **2014**, *53*, 11926-11930.
68. Jun, Y.-S.; Hong, W. H.; Antonietti, M.; Thomas, A., *Adv. Mater.* **2009**, *21*, 4270-4274.
69. Wang, Y.; Wang, X.; Antonietti, M.; Zhang, Y., *ChemSusChem* **2010**, *3*, 435-439.
70. Zhang, Y.; Liu, J.; Wu, G.; Chen, W., *Nanoscale* **2012**, *4*, 5300-5303.

71. Kumar, S.; Surendar, T.; Kumar, B.; Baruah, A.; Shanker, V., *RSC Adv.* **2014**, *4*, 8132-8137.
72. Wu, M.; Yan, J.-M.; Tang, X.-n.; Zhao, M.; Jiang, Q., *ChemSusChem* **2014**, *7*, 2654-2658.
73. Bojdys, M. J.; Müller, J.-O.; Antonietti, M.; Thomas, A., *Chem. Eur. J.* **2008**, *14*, 8177-8182.
74. Liu, J.; Zhang, T.; Wang, Z.; Dawson, G.; Chen, W., *J. Mater. Chem.* **2011**, *21*, 14398-14401.
75. Liao, G.; Chen, S.; Quan, X.; Yu, H.; Zhao, H., *J. Mater. Chem.* **2012**, *22*, 2721-2726.
76. Dong, F.; Sun, Y.; Wu, L.; Fu, M.; Wu, Z., *Catal. Sci. Technol.* **2012**, *2*, 1332-1335.
77. Hammer, P.; Victoria, N. M.; Alvarez, F., *J. Vac. Sci. Technol., A* **1998**, *16*, 2941-2949.
78. Rodil, S. E.; Muhl, S.; Maca, S.; Ferrari, A. C., *Thin Solid Films* **2003**, *433*, 119-125.
79. Lejeune, M.; Durand-Drouhin, O.; Zellama, K.; Benlahsen, M., *Solid State Commun.* **2001**, *120*, 337-342.
80. Zheng, Y.; Liu, J.; Liang, J.; Jaroniec, M.; Qiao, S. Z., *Energy Environ. Sci.* **2012**, *5*, 6717-6731.
81. Wang, Y.; Di, Y.; Antonietti, M.; Li, H.; Chen, X.; Wang, X., *Chem. Mater.* **2010**, *22*, 5119-5121.
82. Gillan, E. G., *Chem. Mater.* **2000**, *12*, 3906-3912.
83. Wang, Y.; Wang, X.; Antonietti, M., *Angew. Chem. Int. Ed.* **2012**, *51*, 68-89.
84. Xu, X.; Ray, R.; Gu, Y.; Ploehn, H. J.; Gearheart, L.; Raker, K.; Scrivens, W. A., *J. Am. Chem. Soc.* **2004**, *126*, 12736-12737.
85. Buzaglo, M.; Shtein, M.; Regev, O., *Chem. Mater.* **2016**, *28*, 21-24.

86. Liu, S.; Tian, J.; Wang, L.; Luo, Y.; Zhai, J.; Sun, X., *J. Mater. Chem.* **2011**, *21*, 11726-11729.
87. Liu, S.; Wang, L.; Tian, J.; Zhai, J.; Luo, Y.; Lu, W.; Sun, X., *RSC Adv.* **2011**, *1*, 951-953.
88. Liu, S.; Tian, J.; Wang, L.; Luo, Y.; Sun, X., *RSC Adv.* **2012**, *2*, 411-413.
89. Zhou, J.; Yang, Y.; Zhang, C. Y., *Chem. Commun.* **2013**, *49*, 8605-7.
90. Tang, Y.; Su, Y.; Yang, N.; Zhang, L.; Lv, Y., *Anal. Chem.* **2014**, *86*, 4528-4535.
91. Li, Y.; Zhang, H.; Liu, P.; Wang, D.; Li, Y.; Zhao, H., *Small* **2013**, *9*, 3336-3344.
92. Liu, J.; Zhang, Y.; Lu, L.; Wu, G.; Chen, W., *Chem. Commun.* **2012**, *48*, 8826-8828.
93. Li, X.; Hartley, G.; Ward, A. J.; Young, P. A.; Masters, A. F.; Maschmeyer, T., *J. Phys. Chem. C* **2015**, *119*, 14938-14946.
94. Di Noto, V.; Negro, E., *Fuel Cells* **2010**, *10*, 234-244.
95. Di Noto, V.; Negro, E., *Electrochim. Acta* **2010**, *55*, 7564-7574.

Chapter 2

General Experimental Methods and Techniques

2.1. Introduction

This chapter describes the basic principle of various instruments which are used in this thesis work and their maker name. The experimental methods which are involved in this thesis work are also discussed in this chapter.

2.2. Instruments and Instrumental Techniques

2.2.1. Microwave Synthesizer

Synthesis the graphite carbon nitride quantum dots (g-CNQDs) from formamide and synthesis of carbon quantum dots (CQDs) from formic acid was done by using MAS-II microwave synthesizer which is from Sineo Microwave Chemistry Technology Company (Shanghai, China) picture shown in Figure 2.1. In microwave synthesizer microwave radiation is used as the source of energy and it transferred to heat energy through space and medium. Microwave is an electromagnetic wave of 1 mm to 1m wavelength range. Microwave heating is different from conventional heating because heating effect in microwave heating is due to dielectric loss of the material in the presence of electromagnetic field whereas heating effect in conventional heating is due to heat radiation from outside to inside by external heat source. Microwave absorption by substances produces heat energy and transmitted to the surrounding environment which depends on dielectric constant, specific heat and shape of substances.



Figure 2.1. Photograph of microwave synthesizer.

2.2.2. Ultrasonicator

Synthesis of Pt/CN_x and $\text{Fe}_3\text{O}_4\text{-CN}_x$ composite has been done by ultrasound method using ultrasonicator. Ultrasound was performed in SINEO UWave-1000 (Shanghai, China) machine



Figure 2.2. Photograph of ultrasonicator.

at 28 kHz frequency and 400W power whose picture is shown in Figure 2.2. In ultrasonicator machine an ultrasonic probe is used to create sound energy by using ultrasonic frequency (more than 20 kHz). Ultrasonic frequency is creating by longitudinal movement of the ultrasonic probe's tip. During the ultrasound method ultrasonic power can be adjusted according to the reaction condition.

2.2.3. Atomic Force Microscope (AFM)

The characterizations of g-CNQDs, 2D carbon nitride sheets, carbon quantum dots (CQDs) and 2D graphene sheets were done using tapping mode of AFM (Asylum MFP-3D Atomic Force Microscope). Generally, there are three primary modes of AFM which are contact mode, non-contact mode and trapping mode. In most of the cases trapping mode is used to get the topography image by trapping the surface by the oscillating probe. According to the surface morphology the amplitude of the cantilevers oscillation is changed. Therefore, topography image can be obtained by maintaining the amplitude of the cantilever's oscillation. The main advantages of trapping mode are that it damage less portion of the sample due to its lower force and it has higher lateral resolution.

2.2.4. Transmission Electron Microscope (TEM)

The characterizations of all the materials were done by using transmission electron microscopy JEOL, JEM2010, operated at 200 kV and transmission Electron Microscopy FEI, Technai G2 2010, operated at 200 kV. The transmission electron microscope is powerful instrument which can characterize the materials at nanoscale label which is important in nanoscience and technology field. This is a microscopic technique where the electron beam is transmitted through an ultra film sample specimen. The first TEM was built by M. Knoll and E. Ruska, in 1932¹.

There are two types of imaging in the TEM instrument which are bright field imaging and dark field imaging. Transmitted beam is used for bright field imaging whereas the diffracted beam is used for dark field imaging. Bright field imaging was done by placing the suitable aperture below the back focal plane of the objective lens by which transmitted beam is collected and the diffracted beam is eliminated. Dark field imaging was done either by using movable aperture or by shifting the incident electron beam by keeping the aperture position fixed. By this instrument we can also measure imaging, dark selected area electron diffraction (SAED) pattern and high resolution transmission electron microscope (HRTEM). Bright field and dark field imaging are used to analyze the domain and defect structure of the sample on the atomic scale. The SAED pattern can give the information about the crystalline nature of the compound as well as the information about the phase of the sample.

2.2.5. Powder X-ray Diffraction (p-XRD)

Powder X-ray diffraction (p-XRD) measurement were performed on a Bruker DAVINCI D8 ADVANCE diffractometer equipped with Cu K_{α} radiation ($\lambda = 0.15406$ nm). Powder X ray diffraction pattern is a tool to measure the crystalline phase of the materials. Cu-source was used as an X-ray source which generates Cu K_{α} radiation. Lynx-Eye high resolution energy dispersive detector was used which allows a range of scattering angle which is scattered from the sample. It is sensitive because it can simultaneously increase the intensity of the signal, increasing the peak to background ratio and decreasing the number of scan. The X-ray source is essentially monochromatic. So the K_{β} line in the X-ray spectrum is removed by using Nickel filter. The absorption edge of nickel metal is at 1.488 \AA which lies between the K_{α} ($\lambda = 1.5406 \text{ \AA}$) and K_{β} ($\lambda = 1.392 \text{ \AA}$) of copper-X-ray source. Hence nickel foil of an appropriate thickness is used to reduce the K_{β} line intensity. The basic principle is that the X-ray will fall on the sample and it

will scatter from the plane of the sample's crystal and will fall in detector. The scattering pattern will depend on the crystal structure of the sample. It follows the Bragg's law which is

$$2d\sin\theta = n\lambda$$

where d is the spacing between the layers of the atom, λ is the wavelength of the X-ray, θ is the angle between incident rays and the surface of the layer, n is an integer. The diagram is shown in Figure 2.1.

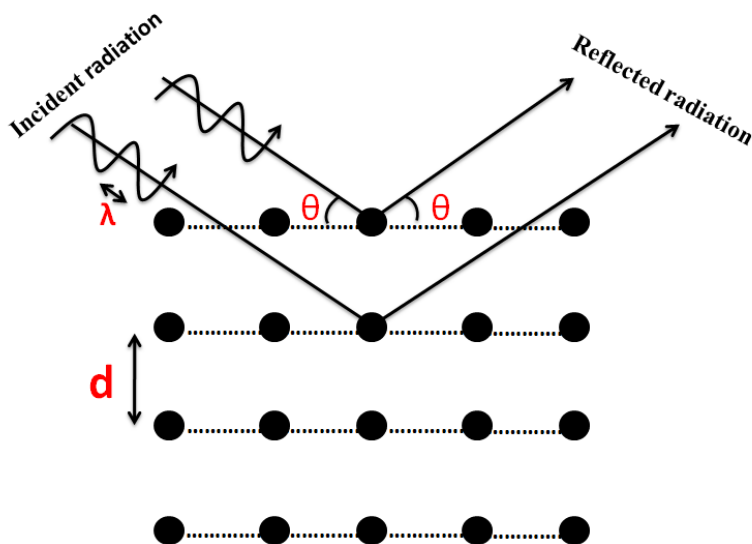


Figure 2.3. Representation of Bragg's law.

2.2.6. X-ray Photoelectron Spectroscopy (XPS)

Surface composition of various materials and oxidation state of the corresponding element can be obtained by XPS measurement. Surface atomic percentage of the element can be obtained from area calculation of the corresponding peak in XPS spectra. XPS measurements on the

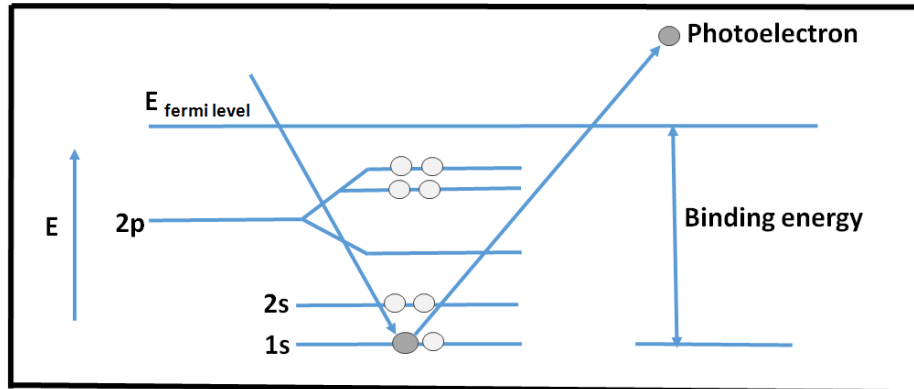


Figure 2.4. Schematic diagram of X-ray photoelectron spectroscopy.

sample were done using a monochromatic Mg K_{α} X-ray source (XPS, VG Microtech). X-ray electromagnetic wave was irradiated on the sample. The electron will escape from the atom if the X-ray is sufficiently high energy to overcome the binding energy of electron. The schematic diagram of XPS spectroscopy is shown in Figure 2.4. From the principle of conservation of energy the following equation can be written where $h\nu$ is energy of the X-ray².

$$h\nu = \text{binding energy (BE)} + \text{kinetic energy (KE)}$$

From this equation we can find out the binding energy of the element in the analysed sample. Ultra high vacuum is one of the experimental conditions during XPS measurement.

2.2.7. Fourier Transform Raman Spectroscopy

In Raman spectroscopy monochromatic light is used which will interact with the molecular vibrational modes of the analyzed sample, resulting the scattered light with the shifting to lower

or higher energy level compare to initial laser light energy. Usually as a source laser light of near ultra-violet, near infrared or visible region has been used in Raman spectroscopy studies. Raman spectroscopy is an inelastic scattering and interacts with the polarisable electron density of the analyzed molecule. FT-Raman spectrum of 2D carbon nitride sheet was measured on Micro Raman (Model: STR 500; Seki Technotron, Japan) spectrometer using 488 nm laser.

2.2.8. Thermo Gravimetric Analysis (TGA)

TGA is the measurement of the change of weight percentage of materials with temperature due to change physical or chemical properties of the material. TGA can give the idea of thermal stability, volatility, adsorption property, decomposition nature of the material; proves the presence of some special group to predict the structure of the analysed compound. The TGA of carbon nitride dots was done using Mettler Toledo 851e TGA/DTA (Mettler Toledo, Switzerland).

2.2.9. Dynamic Light Scattering (DLS) analysis

From dynamic light scattering (DLS) study we can measure the particle size distribution. There are two parameters which are hydrodynamic diameter and Z-average mean correspond to particle size in the DLS study. Hydrodynamic diameter is the size of hydration layer surrounding particle which is determined from diffusion coefficient of the particle in the solution by using Stokes-Einstein equation and Z-average mean means cumulative mean which is calculated from autocorrelation function generated during DLS measurement. Hydrodynamic diameter of CQDs in solutions was measured at 25⁰C by DLS using the Malvern Zetasizer Nano ZS instrument.

2.2.10. Field Emission Scanning Electron Microscopy (FESEM)

SEM images of 2D carbon nitride sheet were obtained using field emission scanning electron microscope (FESEM) system of Zeiss, Germany make, Model: Supra 55. SEM images of other compounds and the composites were obtained using FESEM system of Carl Zeiss, Germany make, Model: Sigma. The large depth of field of the SEM instrument allows a large amount of the sample to be in focus at one time and produces an image which can represent the sample in the 3D way. SEM has advantages like combination of higher magnification, larger depth of field, greater resolution. Topography, morphology, compositional and crystallographic information we can know from SEM analysis. The main instrumental parts of the SEM instrument are virtual source, first condenser lens, condenser aperture, second condenser lens, objective aperture, scan coil, objective lens and detector. The Virtual Source is the electron gun which is generating monochromatic electrons. The electrons are condensed by the first condenser lens. This lens is used to form the beam and as well as it limits the amount of current in the beam. Condenser aperture is used to eliminate the high-angle electrons from the beam. The second condenser lens changes the upcoming electrons into a coherent beam and it is usually controlled by the fine probe current knob. Again the objective aperture further eliminates the high-angle electrons from the electron beam to make it more fine and tight. Then the scan coils sweep the beam in a grid fashion dwelling on points for a period of time determined by the scan speed which is usually in the microsecond order. The final lens is the objective lens which focuses the scanning beam onto the part of the specimen. After scanning onto the specimen the signal is coming to the detector and then electronic part which can produce image from the signal. In field emission scanning electron microscopy (FESEM) field emission gun is used which is a sharp tip of tungsten needle. Due to sharpness of the tip the electric field at the tip is

very strong. Electron probe diameter is less than 1nm is possible by FESEM, so it can go higher resolution than normal SEM. Ultra-high vacuum is the necessary condition for imaging to avoid ion bombardment to the tip from the residual gas in the chamber.

2.2.11. UV-visible Spectrophotometer

The optical absorbance of the synthesized compounds was studied using Varian Cary 100 Bio UV-visible Spectrophotometer. The minimum wavelength resolution of this instrument is 0.2 nm. It follows Lambert Beer's law which is

$$A = \log \frac{I_0}{I} = \epsilon c l$$

where A is the optical density or absorbance, I_0 is the incident light intensity and I is the transmitted light, ϵ is the molar absorption coefficient, c is the concentration of the solution and l is the path length of light beam passing through the solution.

2.2.12. Fluorescence Spectrometer

Steady state fluorescence measurement was done by fluorescence spectrophotometer. Fluorescence studies of the synthesized compounds were carried out using a Perkin Elmer, LS 55 spectrometer. Xeon lamp (150 Watt) is the excitation source of this machine and R-928F (Hamamatsu) is the photomultiplier tube which is used as photodetector. During measurement temperature was maintain by using Perkin Elmer peltier system. In fluorescence spectra the intensity, emission wavelength maxima, area of the spectra all are important parameters to analyse the optical characteristic of the compounds. The fluorescence light was measured in a perpendicular with respect to the direction of excitation light.

2.2.13. Time-correlated single photon counting (TCSPC) spectrometer

Time resolved fluorescence life time measurements were performed using a time-correlated single photon counting (TCSPC) spectrometer (Edinburgh, OB920). Fluorescence life time measurement is very much important to study the dynamic and static quenching of the fluorophore molecules. In static quenching there is no change of life time of fluorophore after adding the quencher to the fluorophore but in case of collision quenching there is change of life time after addition of quencher to the fluorophore. It is also used in different study of photophysical and photochemical processes. The important components of the TCSPC machine are pulsed excitation source, delay line, time-to-amplitude converter, multichannel analyzer, START and STOP PMTs, constant fraction discriminator. Different diode lasers and LED have been used as pulsed excitation source. The instrument response function (IRF) was measured from IRF pulse by taking the full width at half maxima and it varies source to source.

2.2.14. Nuclear Magnetic Resonance (NMR) Spectroscopy

^{13}C and ^1H NMR spectra were recorded using a NMR Spectrometer (400MHz) which is from Bruker biospin. NMR is a property of a nucleus in an atom. Every nucleus in an atom acts as a tiny bar magnet with its nuclear spin (I). In many atoms for example ^{12}C these nuclear spins are paired against each other, such that the nucleus of the atom has no overall spin i.e. $I = 0$. ^{13}C and ^1H both have nuclear spin $I = 1/2$. In presence of external magnetic field the two spin states exist such as $I = +1/2$ and $I = -1/2$ with two different energy levels; one spin is align with the external magnetic field and another one is opposite to the external magnetic field. The difference in energy is depending on the strength of the external magnetic field. We can observe the transition of nucleus either the absorption of energy or the subsequent release of energy as the nucleus relaxes

back to the lower energy ground state. Traditionally this was done by scanning slowly by the faster Fourier transform method where one big, broad pulse of radio waves is used to excite all nuclei, and then the results are analyzed by computer.

2.2.15. Fourier Transform Infrared (FT-IR) Spectroscopy

FT-IR spectra were recorded by using infrared region electromagnetic radiation. FT-IR spectroscopy or vibration spectroscopy can give the confirmation of presence of different functional group in the samples. The main advantages of FT-IR spectroscopy are by this method very less amount of sample is needed and it is very much sensitive method. FT-IR measurements of all the compounds were performed using a Perkin-Elmer spectrum RXI FT-IR spectrophotometer.

2.2.16. Attenuated Total Reflection Fourier Transform Infrared Spectroscopy (ATR-FTIR)

ATR-FTIR measurements of aqueous solution of g-CNQDs were performed using a Perkin-Elmer Spectrum RXI FT-IR spectrophotometer equipped with a ZnSe crystal. The ATR-FTIR spectrum of g-CNQDs was determined by using few drops of aqueous solution of g-CNQDs on the ZnSe ATR surface. For ATR-FTIR titration measurements, aqueous solution of g-CNQDs was prepared by sonicating 5mg of g-CNQDs with 10 ml of water for 1hr. The concentration of mercuric and iodide ions in the aqueous solution of g-CNQDs for the ATR-FTIR titration were 0.002 (M) and 0.004 (M) respectively.

2.2.17. CHN Elemental Analyser

The CHN analysis of different samples was recorded using TruSpec CHNS analyzer. The methodology includes combustion of the sample at high temperature, removal of byproduct,

ballast collection, sampling of the combustion gases, measurement, gas isolation, signal processing and operating controls. Combustion of the sample was done at high temperature in presence of ultra high pure oxygen; it is an oxidative reductive process. After combustion the carbon, hydrogen and nitrogen of the sample are converted into the corresponding gases. Those combustion gases are isolated and equilibrated in ballast which is called ballast collation. Then sampling of the combustion gas was done and measured the carbon and hydrogen by infrared spectroscopy. Then the gases swept into flow stream which is called gas isolation. Thermal conductivity cell was used to determine the nitrogen amount. Operating control includes sample amount, combustion temperature, ballast equilibrate time, ballast aliquot fill time, ballast pressure stabilization time, IR pressure stabilizer, IR stop flow time etc.

2.2.18. Cyclic Voltammeter

Electrochemical measurements have been done by a cyclic voltammeter where three standard conventional electrodes were used at room temperature (25⁰C). Ag/AgCl (in saturated KCl solution) was used as reference electrode, platinum was used as counter electrode and glassy carbon (GC) was used as working electrode. In the electrochemical measurement the potential applied to the working electrode and measured the current passing through the electrochemical cell and the applied potential was measured with respect to the reference electrode. The Ag/AgCl (in saturated KCl solution) reference electrode was made of silver wire that has been coated with solid silver chloride and that wire is immersed into the saturated KCl solution. The half cell reaction of this electrode is



The role of counter electrode is to provide the pathway to flow the current through the electrochemical cell without passing significant current to the reference electrode. If the reduction occurs during the electrochemical cycle on the working electrode surface then oxidation will be there at the counter electrode. Commercial glassy carbon electrode was polished with 1.0, 0.3 and 0.05- μm alumina slurry sequentially on Buehler microcloth polishing clothes. After cleaning the electrode it was mild sonicated in de-ionized water for about 10 minutes. The cleaned GC electrode was used to modify by the catalyst or composite materials and used for electrochemical analysis. All the Electrochemical measurements were performed with a conventional three electrode cell using an electrochemical workstation (CH Instrument, Model: 1100A).

2.2.19. Flame atomic absorption spectrophotometer (FAAS)

It is an analytical technique by which we can quantitatively determine the concentration of the different metal ions into the solution. In FAAS liquid sample is used to analyze aspirated and is introduced into flame, where atomization of the sample occur. In this method to determine the concentration of different metal ions in the sample solution different flame for different metal ion has been used and a calibration plot has done with the known metal ion concentration. The advantages of FAAS are high precession, fast analysis and low cost method.

2.2.20. Superconducting Quantum Interference Device (SQUID) magnetometer

Magnetic property measurement was done by using SQUID-VSM System (Quantum Design-make). Magnetic property measurements include study of hysteresis loop, field cooled and zero field cooled measurement, magnetic susceptibility measurement etc. It is a very sensitive

magnetometer which can detect very weak magnetic signal. Its sensitivity is too much high that it can measure magnetic field which is coming from human heart and brain. Josephson junction is used into the SQUID magnetometer which can detect a very small change of energy even weaker than electromagnetic energy. Josephson junction is made off two superconductor materials which is separated by very thin insulating material so that electron and pass through the insulating material. The electrical current density through the Josephson junction depends upon the phase difference across the junction of the two superconducting wave functions. The phase difference is influenced by the external magnetic field i.e. magnetic flux into the superconducting material and it can convert to electrical voltage. This is the basic principle of SQUID magnetometer. Mainly there are two types of SQUID, radio frequency SQUID and direct current SQUID. Direct current SQUID, made off two Josephson junctions is more sensitive than radio frequency SQUID which is made of one Josephson junction. In direct current SQUID the two Josephson junctions are placed parallel to each other and electrons are tunneled through the junctions and quantum interference phenomenon has been observed.

2.2.21. Electron Spin Resonance Spectroscopy

Electron Spin Resonance (ESR) spectroscopy has been used to study the paramagnetic species and Zeeman effect is the origin of the ESR spectroscopy. Every spin have magnetic moment and in present of external magnetic field it splits and creates different energy levels. The splitting energy gap is proportional to applied magnetic field. Now if we applied photons i.e. energy same with the Zeeman splitting there will be transition between spin up and spin down state. During sweeping the external magnetic field microwave region electron magnetic radiation adsorbed by the system falls in the microwave region. The first derivative of these absorption spectra is

represented in the ESR spectroscopy. The simplest system of ESR study is free electron with spin of $1/2$. In presence of external magnetic field the Hamiltonian of the system is

$$\hat{H} = g \cdot \mu_B \cdot \hat{S} \cdot B_{\text{ext}}$$

where g is electron g factor, μ_B is Bohr magneton, \hat{S} is spin operator vector, B_{ext} is the external magnetic field. Therefore, in presence of external magnetic field there will be two energy states which are

$$E_{S=+1/2} = +1/2 g \cdot \mu_B \cdot B_{\text{ext}}$$

$$E_{S=-1/2} = -1/2 g \cdot \mu_B \cdot B_{\text{ext}}$$

Therefore, the energy difference between the energy states is

$$\Delta E = g \cdot \mu_B \cdot B_{\text{ext}} \cdot \Delta m_s = h \gamma_{\text{mw}}$$

where Δm_s is $+1$ which is the transition selection rule of ESR spectroscopy³.

2.3. Experimental Methods

2.3.1. Quantum yield measurement method

Quantum yield (QY), the most important characteristic of the fluorophore is an intrinsic property and it is necessary to know as its efficiency to be use as a fluorescence probe in the different

applications. QY is a dimensionless quantity. The fluorescence quantum yield is the ratio of number of photons emitted to the number of photons absorbed during fluorescence process. In other way the fluorescence quantum yield is the ratio fluorophore's emissive rate (K_f) to non-radiative decay rate (K_{nr}) plus fluorophore's emissive rate which is expressed as

$$QY = K_f / (K_f + K_{nr})$$

Higher quantum yield means brighter emission of the fluorophore. There are two methods for relative quantum yield measurements one is a single-point method and another one is comparative method. The quantum yield is calculated using the integrated emission intensities from a single sample and reference pair at identical concentration which is represents the single point method. Therefore this method is fast and easy method. It is not always reliable due to the inaccurate measurement of the absorbance of the fluorophores. In the comparative method well characterized reference with known fluorescence quantum yield has been used. In this method multiple concentrations of fluorophore has been prepared and its absorbance and fluorescence has been measured. By calculating the slope of the line generated by plotting the integrated fluorescence intensity against the absorption for multiple concentrations of fluorophore the quantum yield has been calculated. Therefore, it is more time consuming but provides much higher accuracy compare to the single point method. Quantum yield of g-CNQDs in different solvents and CQDs in water were calculated by the comparative method and used the following equation²

$$\varphi_S = \varphi_R \times (I_S/I_R) \times (\eta_S^2/\eta_R^2) \times (A_R/A_S)$$

where the ϕ is the quantum yield, I is the integrated photoluminescence intensity (excitation wavelength is 340 nm), A is the optical density and η is the refractive index of the solvent. The subscript “S” refers to the sample, g-CNQDs and “R” for reference. Quinine sulfate in 0.1M H₂SO₄ was taken as a reference. It is known from literature that quantum yield of Quinine sulfate in 0.1M H₂SO₄ is 54%.

2.3.2. Average Fluorescence life time measurement method

Fluorescence life time is another important characteristic property of the fluorophore. Fluorescence life time is the life time of the excited state. Fluorescence life times were determined using time correlated single photon counting technique. Decay curves were fitted using multi exponential model using the following:

$$I(t) = \sum_0^n A_i \exp\left(\frac{-t}{\tau_i}\right)$$

Where I(t) is the intensity usually assumed to decay as the sum of individual single exponential decays, A_i are the pre-exponential factors, τ_i are the decay times. The fluorescence decay curves are fitted to triple exponential functions. The average life time (τ_{avg}) were determined by

$$\tau_{avg} = \frac{\sum_i A_i \tau_i^2}{\sum_i A_i \tau_i}$$

2.3.3. Fluorescence quenching measurement method

The quenching can easily be understood by a Stern-Volmer analysis. The Stern-Volmer constant, K_{SV} is related to fluorescence intensities by the following Stern-Volmer equation⁴:

$$F_0/F = 1 + K_{SV} [Q]$$

Where F_0 and F are the fluorescence intensities in absence and presence of quencher, respectively and $[Q]$ is the concentration of quencher. The Stern-Volmer plot is the F_0/F versus $[Q]$ plot which should be straight line. The slope of the straight line is the value of K_{SV} .

2.3.4. Chronoamperometry method

Chronoamperometry method is an electrochemical method where current is measured with time at constant potential applied on working electrode. Therefore, in this method the output is current whose nature depends on the time. For short time capacitive current is dominant which decreases exponentially with time at constant potential. For short time into the current there is large contribution of non-Faradaic current. For long time Faradic current is dominant and it follows Cottrell equation. For long time into the current there is large contribution from the diffusion limited faradic current. The capacitive current (I_{cap}) follows the following equation:

$$I_{cap} = \frac{E}{R_u} e^{-t/R_u C_d}$$

where R_u is the uncompensated resistance and C_u is the double layer capacitance. The Cottrell equation is as follows:

$$I_{cott} = \frac{nF\sqrt{D_0}}{\sqrt{\pi t}} C_0^\alpha$$

where F is Faraday constant, D_0 is diffusion coefficient. From the Cottrell equation if we plot I_{cott} vs. $t^{-1/2}$ then from the slope diffusion coefficient can be calculated. This method has lot of

application in electrochemical sensing field. Apart from this by this method we can get preliminary idea of nucleation and growth of a system.

2.3.5. Differential Pulse Voltammetry

Differential pulse voltammetry (DPV) is an electrochemical method where potential was applied as a series of regular voltage pulses. The DPV current was measured before change the potential and the difference of current are plotted against the potential. The DPV is the derivative of linear sweep voltammetry. In the differential pulse voltammogram, the height of the current peak is directly proportional to the concentration of corresponding analyte. Different analytes has different and specific peak potential. The sensitivity of the detection of this analyte DPV can not only help improve the sensitivity of the detection of an analyte is high and the resolution of the voltammogram, but also provide information about the chemical form of the analytes, such as oxidation and complexation status, which is very important for an analysis.

2.3.6. Batch Experiment

Adsorption of toxic metal ions has been studied by batch adsorption technique. Batch experiment has done to determine the adsorption isotherm on the adsorbent and we can find out the adsorption capacity. In the chapter 7 batch experiment have done to study the Cd^{2+} , Pb^{2+} and Cu^{2+} ions adsorption on the Zn doped g-CN_x microsphere composite. In the batch experiment for a particular metal ion adsorption study different initial concentration of that metal ion was prepared in separate glass vials. For each different initial concentration of metal ion solution 10.0 ml aqueous solution was prepared and was stirred with 5.0 mg of Zn doped g-CN_x microsphere for sufficient time to reach the adsorption equilibrium. The mixture was stirred with stirring bead

throughout the adsorption process to ensure the sufficient contact between metal ions and the Zn doped g-CN_x microsphere. After reach at equilibrium the Zn doped g-CN_x microsphere was separated from the solution by centrifugation with 16,000 rpm speed and the remaining metal ion concentration into the solution was measured by flame atomic absorption spectrophotometer (FAAS). The adsorbed metal ion on the Zn doped g-CN_x microsphere per unit mass was calculated by the following equation:

$$q_e = \frac{(C_0 - C_e) \times V}{m}$$

where q_e (mg g⁻¹) is the amount of adsorbed metal ion per unit mass of adsorbent after complete adsorption, C_0 and C_e are the initial and equilibrium concentration of metal ions respectively (mg L⁻¹), m is the weight of adsorbent (g) and V is the volume of solution (L).

2.4. Chemicals

Formamide (HPLC grade) was purchased from Merck (Darmstadt, Germany) and used as received without any further purification. Formic acid (HCOOH) was used as a precursor for microwave assisted synthesis of carbon quantum dots (CQDs). Formic acid (HPLC grade) was purchased from Merck (Darmstadt, Germany) and used as received without any further purification. Formamide (HCONH₂), chloroplatinic acid hexahydrate (H₂PtCl₆ · 6H₂O), sodium borohydride (NaBH₄) and Vulcan XC-72 carbon black (10 wt% Pt) and methanol (CH₃OH) were all purchased from Sigma Aldrich. Formic acid, formaldehyde and sulphuric acid (H₂SO₄) were purchased from Merck. All chemicals were used without further purification

Chapter References

1. Knoll M.; E. Ruska E., *Z. Physik*. **1932**, 78, 318-339.
2. Hollas J. M., *Modern Spectroscopy*, **2003**, Wiley, Fourth Edition.
3. Weil J. A.; J. R. Bolton J. R., *Electron Paramagnetic Resonance. Elementary Theory and Practical Applications*. **2008**, Wiley-Interscience, Second Edition.
4. Lakowicz J. R., *Principles of Fluorescence Spectroscopy*. **1999**, Springer, Third Edition.

CHAPTER 3

Zero dimensional (graphitic carbon nitride and carbon) Quantum Dots: Synthesis, Properties and their Applications

The graphene has attracted so much attention to scientific community because graphene is a promising two dimensional material for its future applications in nanotechnology due to its superior electronic, thermal, mechanical properties as well as its chemical stability¹⁻². Since graphene is zero band gap material, it has thus limitation for its electronic and opto-electronic applications. The zero dimensional quantum dots are the nanometer-sized semiconductor materials where excitons are confined in all three special dimensions. Zero dimensional graphene quantum dots (GQDs) are small graphene fragments where electronic transport is confined in all three special dimensions and a band gap is developed in GODs due to its quantum confinement and edge effects. The most of the work on GQDs was focused mainly on theoretical studies; however, synthesis and study of their optical properties are only a recent effort. Several methods has been developed for the preparation of GQDs such as electron beam lithography³, hydrothermal cutting of graphene sheets⁴, bottom-up approach⁵, electrochemical⁶ and solvothermal cutting⁷, metal catalysed approach⁸, chemical synthesis⁹ etc. Since the excitons in graphene have an infinite Bohr diameter, any sized graphene fragments will show quantum confinement effect. However, typically GQDs have dimension in size below 20 nm diameter. This band gap of GODs can also be tuned by modifying size and surface chemistry of GQDs. The absorption spectra of GQDs show a peak at ~ 230nm due to π - π^* excitation of π bonds¹⁰. The functional group in GQDs can change the adsorption features of GODs and can significantly modify the photo-luminescence behaviour (edge effect). The different photo-luminescence quantum yield is reported for various GODs and the highest reported value is 28%¹¹. It is reported by several groups that optical properties of GQDs may vary depending on the method of synthesis and functional group at the edges GQDs. It is interesting that several groups have reported up-conversion luminescence of GQDs¹¹⁻¹². Although several groups observed the up-

conversion phenomena of GQDs, the actual mechanism for up-conversion of GQDs is not clearly understood. The doping the graphene with hetero-atoms can effectively alter their intrinsic properties – for example N heteroatom doping in graphene could effectively induce band gap in graphene leading to introduce new properties for device applications. One of the most important properties of GQDs is highly soluble in various solvent including water, showing low toxicity and edges can be easily modified with functional groups. These properties of GQDs make them attractive materials for various applications such as electrochemical capacitor¹³, lithium ion battery¹⁴, solar cell¹⁵, bioimaging¹⁶ etc.

Part A

Graphitic Carbon Nitride Quantum Dots

3.1. Introduction

GQDs are one of the most important classes of carbon nanomaterials. In 1989 Liu and Cohen¹⁷ first predicted the hypothetical beta carbon nitride (β -C₃N₄) material. By using a theoretical empirical model they have shown its bulk modulus is comparable or greater than diamond material proving its super hard property which is an important property to be an applicable material in technology. After this discovery different scientific communities are started to synthesize such super hard material practically in laboratory. In addition cohesive energy calculation of β -C₃N₄ material proves that it is a metastable state. According to theoretical calculation mainly, there are five different phases of carbon nitride¹⁸⁻¹⁹ which are α -C₃N₄, β -

C_3N_4 , graphitic carbon nitride (g- C_3N_4), pseudocubic C_3N_4 and cubic C_3N_4 . The g- C_3N_4 is the stable allotrope²⁰ among them and the scientific community has found it has unique properties due to its graphite like structure. Several methods such as reactive sputtering, laser ablation and chemical vapour deposition (CVD) have been used for the formation of amorphous carbon nitride²¹⁻²³. Several groups^{19, 24-27} have synthesized g- C_3N_4 from carbon, nitrogen and hydrogen precursors via condensation reactions at high temperature. However, no effort has been made to synthesize graphitic carbon nitride quantum dots (g-CNQDs), which are similar to graphene quantum dots. Noticeably, a few reports on the synthesis of amorphous carbon nitride nanomaterials have appeared in the literature recently²⁸⁻²⁹.

Selective and sensitive detection of heavy metal ions and anions in aqueous media are important since they play an active role in different biological and environmental processes. Mercury is one of the most toxic heavy metals that exist in the environment and it forms a large number of binary compounds of which many of them are toxic. The oxidized form of mercury, Hg^{2+} , is the source of contamination. In the aquatic ecosystem microorganisms transform mercuric ions into methyl mercury, which is neurotoxic³⁰. Thus, there is a need to develop a simple method to detect mercuric ions at a very low concentration in water. The fluorescence based organic molecules acting as sensors for the detection of mercuric ions are reported in the literature³¹⁻³⁴. Most of these fluorescence Hg^{2+} sensors are effective in organic solvents as they form complexes with Hg^{2+} but reports on sensors that can detect mercuric ions in aqueous media are very few³³⁻³⁴. On the other hand, there is no report in the literature of the application of carbon based nano materials for the detection of mercuric ions. In addition, the selective sensing of iodide anions is also important because it plays an important role in biological as well as environmental processes. The thyroid has a plasma membrane glycoprotein Na^+/I^- symporter that

facilitates active iodide (I⁻) transport in the thyroid, which is the initial step in thyroid hormone biogenesis³⁵. However, only a few reports³⁶⁻³⁷ are available for iodide sensing. So, there is a need to have selective and sensitive iodide sensor(s) to detect thyroid disorders for clinical purposes.

With gradually increasing the industries and population the toxic metals are adding into the water which is a worldwide problem. The toxic metals are non-biodegradable which create difficulties to remove from environment. Copper is an essential metal ion in human body which helps to form red blood cell and also keep the blood vessels active in the body. But excess of copper in the human body is harmful and creates its Toxicity property. The excess copper in the human body can damage the nervous system and liver of the body³⁸. The main source of excess copper in human body is from drinking water and food. Sometimes the excess copper of the human body can create eye problem by deposition of it in the cornea of the eye. 2.5 ppm is the permissible limit of copper³⁹. Cadmium is one highly toxic metal among different heavy metals. It is well known that the toxic effect of cadmium is the cause of Itai-Itai disease in Japan. Different chronic disorder in human body can be created by the toxicity of cadmium⁴⁰. Cadmium can also damage the kidney, liver, gastrointestinal tract, lungs in human body⁴¹. Therefore, it is important to remove toxic metals from waste water. Among different methods adsorption method is most promising method to remove the metal ions from waste water due to its low cost with good removal efficiency. For adsorption process there is necessary to choose a proper adsorbent material such as clay⁴², polymer⁴³, carbon nanotube⁴⁴, biomaterial⁴⁵ etc. Apart from this carbon nitride is also a promising adsorbent material in the adsorption study due to its high stability and presence of heteroatom which helps to interact with the metal ions.

Spintronics also known as spin electronics are the study of coupling of spin of electron with its associated magnetic property in solid state devices. Now a day, production of spintronic

devices is a very much rapidly expanding area in research of the technological development. Spintronic materials are used in the field of non volatile memory devices, spin light emitting diodes, non volatile logic components etc. Room temperature ferromagnetic materials are used as the spintronic materials. Materials which are used in spintronic devices should be room temperature magnetic semiconductor. Recently, researchers are focused on the ferromagnetic property study of carbon based materials due to its application in the field of metal free room temperature magnets. Conventionally, d and f electrons are the source to generate the magnetic property into the magnetic material compounds. Carbon based materials containing p electrons have weak spin orbit coupling and large spin relaxation time which helps to create magnetic properties into the materials and can be used in spintronic devices. To the best of my knowledge there is no report of room temperature ferromagnetic graphitic carbon nitride quantum dots (g-CNQDs) which is one of the carbon based material. The magnetic property of the g-CNQDs material can open in new promising application site such as spintronic devices.

3.2. Synthesis procedure of g-CNQDs

Microwave synthesis method has been used to synthesize the g-CNQDs using Formamide (HCONH_2) as a precursor. In a typical synthesis method, 10 mL of formamide was heated by a microwave synthesizer at 180°C for 30 minutes. The colorless solution started to change to brown color solution during microwave heating. The resulting brown color solution was evaporated in a rotary evaporator by applying vacuum at 180°C to produce black solids on a large scale. Finally, these black solids were washed with de-ionized water and dried under vacuum. However, no g-CNQDs have been obtained under similar experimental conditions using dimethyl formamide (DMF) as a precursor instead of formamide.

3.3. Characterization of g-CNQDs

3.3.1. Characterization of g-CNQDs by p-XRD

Figure 3.1 represents the powder X-ray diffraction (p-XRD) pattern of g-CNQDs. The strongest peak at 2θ value of 27.2° corresponds to the (002) plane with interlayer d-spacing of 3.3\AA , which

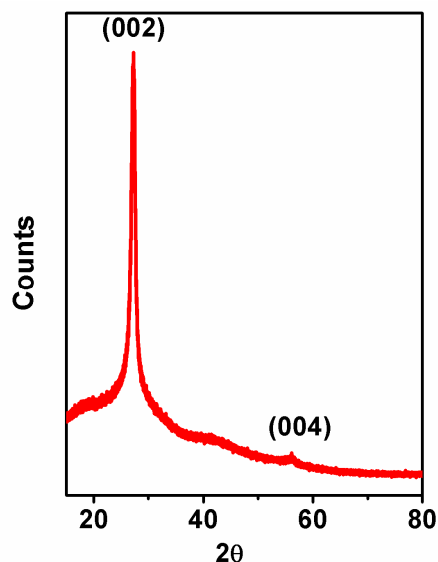


Figure 3.1. p-XRD of g-CNQDs

is close to that reported for graphitic carbon nitride compound in literature(3.26\AA)⁴⁶. The low intense peak at 2θ value of 56.2° corresponds to the (004) plane with interlayer d-spacing of 1.63\AA , which is also close to that reported for graphitic carbon nitride compound⁴⁷.

3.3.2. Characterization of g-CNQDs by UV-visible spectroscopy

The UV-visible spectrum of g-CNQDs was done in its aqueous solution. The UV-Visible spectrum of g-CNQDs is represented in Figure 3.2. There are two peaks at 260 nm and 340 nm

in the UV-Visible spectrum of g-CNQDs. It is already reported that a peak at ~250 nm is due to $\pi \rightarrow \pi^*$ electronic transitions of carbon nitriles containing s-triazine rings⁴⁸. Thus, the presence of s-triazine rings in the synthesized g-CNQDs is confirmed by UV-Visible spectroscopy study. Additionally, the UV-Visible spectrum of g-CNQDs showed a peak centered at 340 nm which is similar to the absorption peak at 320 nm for graphene quantum dots⁴⁹.

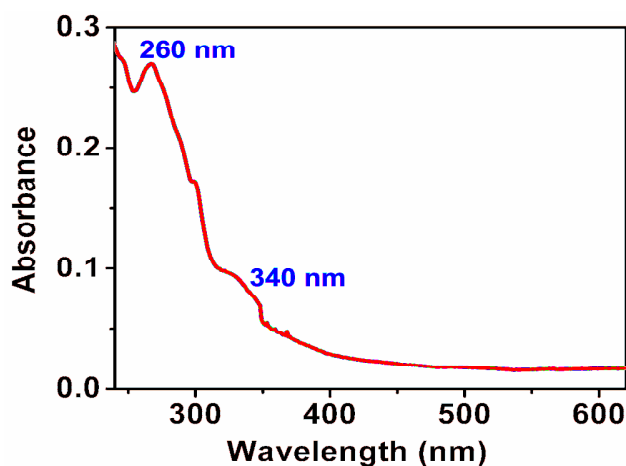


Figure 3.2. UV-visible spectrum of g-CNQDs in water.

3.3.3. Characterization of g-CNQDs by FT-IR spectroscopy

FT-IR spectroscopy of g-CNQDs has been done to prove the existence of graphite like sp^2 bonding in g-CNQDs and to prove the presence of s-triazine ring into the moiety (Figure 3.3). The FT-IR spectroscopy has done in the solid state using a pellet made of pinch of solid g-CNQDs and solid anhydrous potassium bromide (KBr). The intense bands at 1213, 1317 and 1408 cm^{-1} correspond to aromatic C=N stretches whereas bands at 1559 and 1616 cm^{-1} can be assigned to C=N stretches into the carbon nitride moiety. The two bands at 1213 and 1317 cm^{-1} can be attributed to the secondary and tertiary amines into the g-CNQDs respectively⁵⁰.

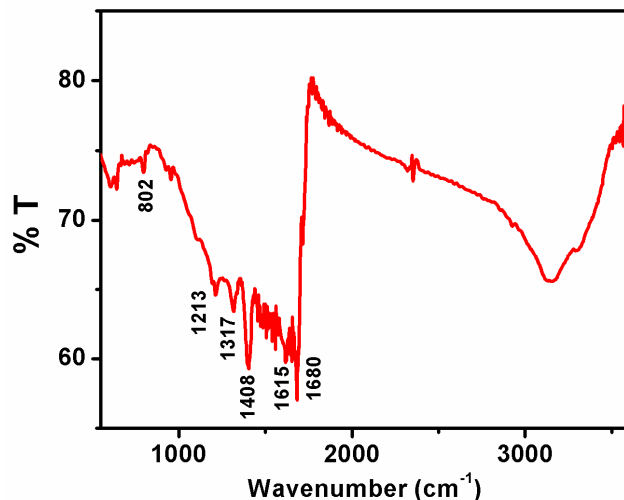


Figure 3.3. FT-IR spectrum of g-CNQDs

The characteristic peak at 800 cm^{-1} is assigned to the breathing mode of s-triazine rings and a broad band at 3100 cm^{-1} to 3400 cm^{-1} corresponds to the stretching mode of $-\text{NH}_x$ groups. Therefore, FT-IR spectrum proves the formation of g-CNQDs containing s-triazine rings into the carbon nitride moiety.

3.3.4. Characterization of g-CNQDs by TEM

Transmission electron microscopy (TEM) measurement have done to know the particle size of the g-CNQDs. Figure 3.4 (a) represents the TEM image of g-CNQDs and its size distribution is represented in Figure 3.4 (b). The TEM image has taken on carbon coated copper grid (200 meshes). The g-CNQDs were dispersed in de-ionized water by sonication and were drop casted on the grid and dried at 45°C . This grid was used for TEM measurement. Their sizes (diameter) are mostly distributed in the range 2–15 nm with average diameter of 7 nm.

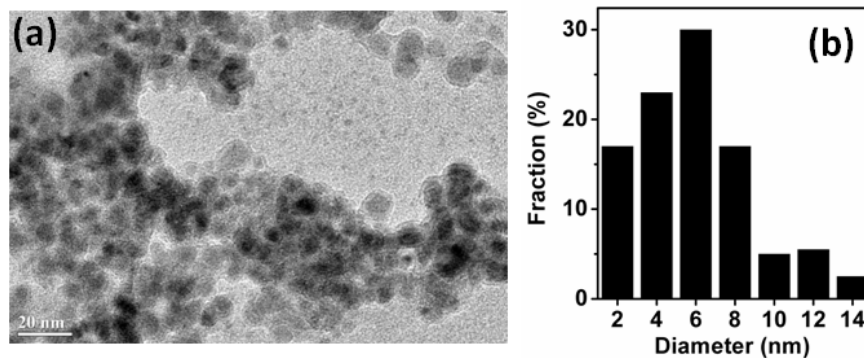


Figure 3.4. (a) TEM image of g-CNQDs (b) Diameter distribution of g-CNQDs calculated from the TEM image.

3.3.5. Characterization of g-CNQDs by AFM

AFM image represents the topographic height of the material and its size. Figure 3.5 (a, b and c) represent AFM study of g-CNQDs. AFM image have taken on mica foil. Initially, mica foil was cleaned with water, acetone, and isopropyl alcohol and again with water followed by dried under nitrogen gas flow. The g-CNQDs were dispersed in water by sonication. The well dispersed g-CNQDs were drop casted on cleaned mica foil and dried at 45⁰C. A thin layer of the compound will be coated on the cleaned mica foil and it is used for AFM study. Figure 3.5 (a) is the AFM image of the g-CNQDs on mica foil where the particles are well distributed all over on the mica foil. The height distribution and height profile of g-CNQDs has been represented in Figure 3.5 (b and c) respectively where height of g-CNQDs are in the range between 0.3 nm and 2.1 nm with average height is about 1.1 nm, suggesting that g-CNQDs consist of either a single layer or a few layers of carbon nitride sheets.

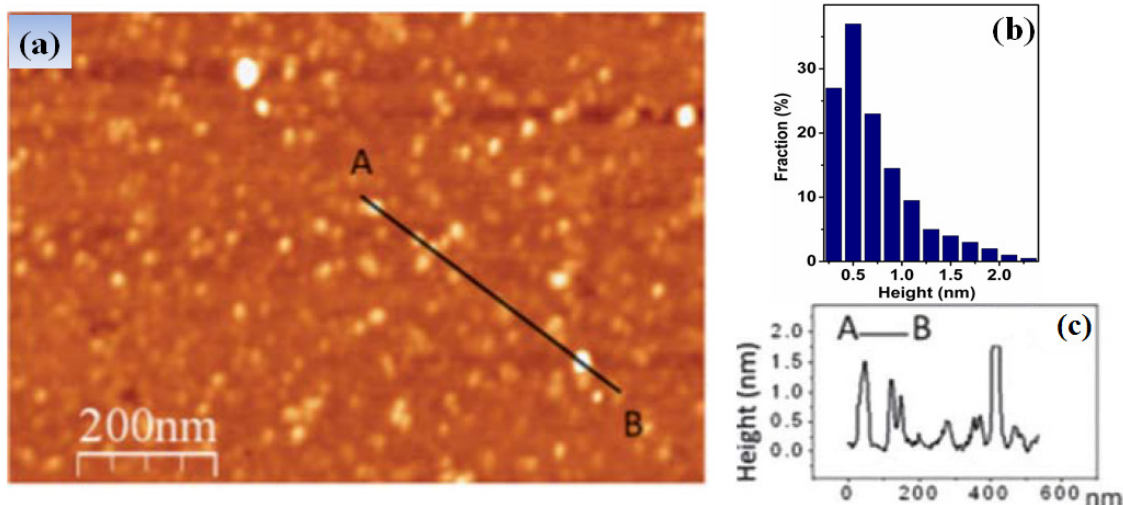


Figure 3.5. (a) AFM image of g-CNQDs taken on mica foil. (b) Height distribution of g-CNQDs calculated from the AFM image. (c) Height profile of g-CNQDs along the line AB from Figure 3.5 (a).

3.3.6. Characterization of g-CNQDs by XPS

XPS measurements were carried out to know the building block and the chemical environment of carbon and nitrogen atoms in g-CNQDs. Figure 3.6 shows the survey scan of the XPS spectrum

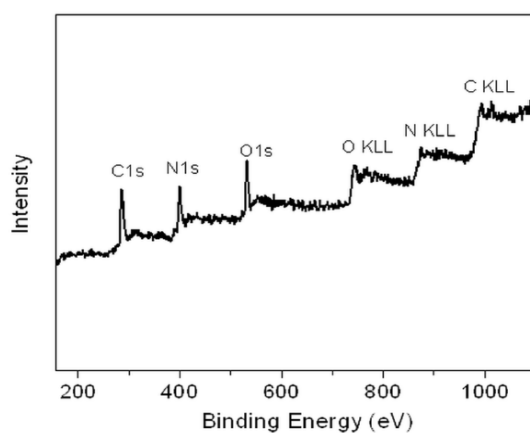


Figure 3.6. (a) The XPS survey scan of g-CNQDs showing the presence of carbon, nitrogen and oxygen.

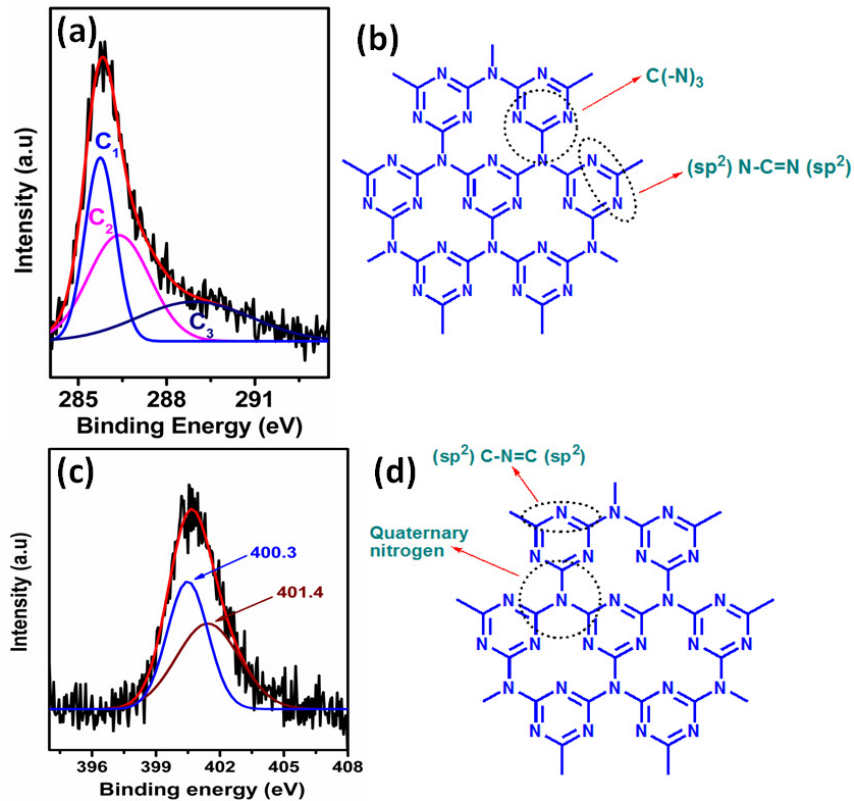


Figure 3.7. High resolution (a) C1s and (c) N1s high resolution XPS spectra of g-CNQDs. Schematic representation of different type of (b) carbon and (d) nitrogen centered sites into the g-CNQDs moiety.

where carbon1s (C1s), nitrogen1s (N1s) and oxygen1s (O1s) with their respective auger peaks (CKLL, NKLL and OKLL) are observed which indicates the presence of carbon, nitrogen and oxygen atoms into the g-CNQDs. The high resolution XPS spectra of C1s and N1s has been shown in Figure 3.7 which were analyzed by deconvoluting the peaks to different contributions by fitting with Gaussian function. It is well known from C1s XPS spectra⁵¹ of CN_x a peak at 284.0 eV is attributed to a C–C bonding environment, peaks in the range 285–287 eV are due to

the C–N bonding and the peaks due to CO_x are in the range of 288–290 eV. Figure 3.7 (a) shows the XPS spectrum of C1s region of g-CNQDs, which was deconvoluted to three main Gaussian peaks (C₁, C₂, and C₃). The binding energies of 285.45 eV (C₁) and 286.35 eV (C₂) are attributed to the presence of (sp²) N–C=N (sp²) (carbon bonded to two nitrogen atoms) and C(–N)₃ (planar trigonal carbon geometry) respectively,⁵¹⁻⁵²(shown in Figure 3.7 (b)) whereas the peak at 290.05 eV (C₃) is attributed to CO_x. The presence of CO_x in the g-CNQDs is probably due to presence of oxygen containing functional groups at the edge of g-CNQDs. The N1s XPS spectrum of g-CNQDs (Figure 3.7 (b)) was deconvoluted into two Gaussian peaks (N₁ and N₂) indicates the presence of two different types of nitrogen in g-CNQDs. The peak at 400.3 eV refers to the presence of (sp²) C–N=C (sp²), nitrogen bonded to two carbon atoms or pyridine moiety⁵³⁻⁵⁴(shown in Figure 3.7 (d)). The second peak in this region at 401.4 eV corresponds to quaternary nitrogen which is bonded to three sp² carbon atoms, known as graphitic nitrogen⁵³⁻⁵⁴. The area ratio of these two peaks is 1.40, which is close to that of triazine based graphitic C₃N₄ moiety. The weak component at 293.2 eV in C1s XPS spectrum corresponds to the π electron delocalization in C₃N₃ hetero-cycles⁵⁵. Thus, XPS studies provided us with proof of the existence of s-triazine based graphitic-C₃N₄ structure into the g-CNQDs.

3.3.7. Characterization of g-CNQDs by ¹³C NMR

¹³C NMR experiments have been carried out to obtain the carbon environments in g-CNQDs. Teter and Hemley¹⁸ theoretically predicted that the characteristic peak in ¹³C magic angle spinning (MAS) NMR for ideal hexagonal graphitic material should appear at ~150 ppm. Figure 3.8 shows the ¹³C NMR spectrum of g-CNQDs dissolved in DMSO-d₆ solvent. The characteristic peak at 151 ppm of g-CNQDs can be attributed to the CN₃ group of the hexagonal

graphitic C₃N₄ moiety. The peak at 161.2 ppm can be assigned to the sp² hybridized carbon of s-triazine rings whereas peaks in the range 163–166 ppm are attributed to the protonated forms⁵⁶ of g-CNQDs or its complex structural forms⁴⁸.

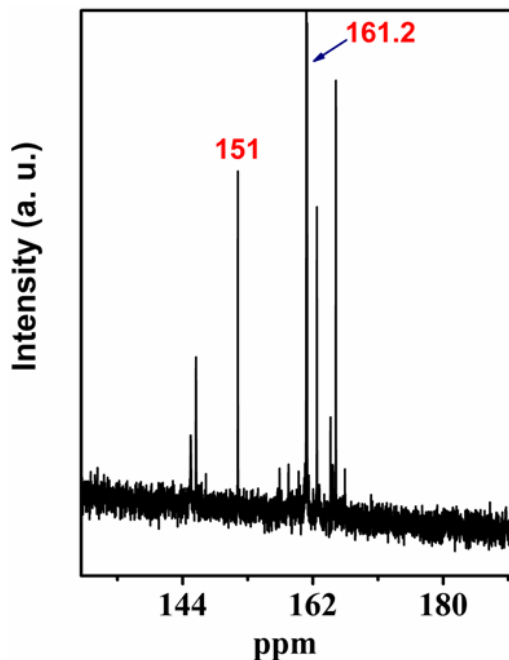


Figure 3.8. ¹³C NMR spectrum of g-CNQDs.

3.3.8. Characterization of g-CNQDs by CHN elemental analysis

CHN elemental analysis was done to know the elemental composition of g-CNQDs. CHN elemental analysis of g-CNQDs was obtained from CHN elemental analysis by weight as carbon (C) 43.13%, nitrogen (N) 47.3%, hydrogen (H) 3.79% and oxygen (O) 5.78%. This suggests the average composition of g-CNQDs is C₃N_{3.3}O_{0.4}H_{0.26} and proves the presence of more amount of nitrogen compare to carbon into g-CNQDs. The presence of little amount of oxygen is probably due to presence of oxygen containing functional groups in the edge of g-CNQDs.

3.3.9. Characterization of g-CNQDs by TGA analysis

The thermal stability study of g-CNQDs was done by thermo gravimetric analysis (TGA). The decomposition temperature of g-CNQDs is very close to the reported bulk carbon nitride material. Figure 3.9 shows the TGA plot of g-CNQDs. It shows the little quantity of weight loss

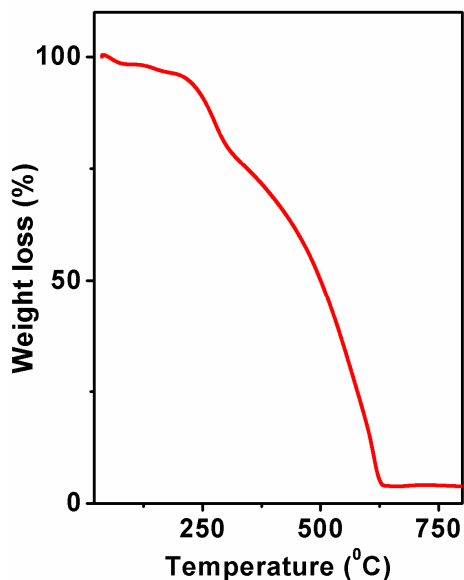


Figure 3.9. TGA plot of g-CNQDs.

at 250°C and then gradual decrease of weight till 640°C. The decomposition of edge groups can be attributed for 1st weight loss and then slowly decomposition of s-triazine ring from the sample. This indicates the synthesized g-CNQDs from formamide have thermal stability over a wide temperature range and nature is similar to reported bulk carbon nitride.

3.3.10. Characterization of g-CNQDs by Fluorescence spectroscopy

Figure 3.10 represents the fluorescence spectrum of g-CNQDs in water. A strong fluorescence emission peak centered at 405 nm was observed when the aqueous solution of g-CNQDs was

excited at the wavelength of 340 nm (Figure 3.10). Figure 3.11 (a) shows the fluorescence emission spectra of g-CNQDs at different excitation wavelengths and Figure 3.11 (b) shows the normalized emission spectra of g-CNQDs at different excitation wavelengths. The fluorescence emission of g-CNQDs is excitation dependent when the excitation wavelength is higher than 340 nm.

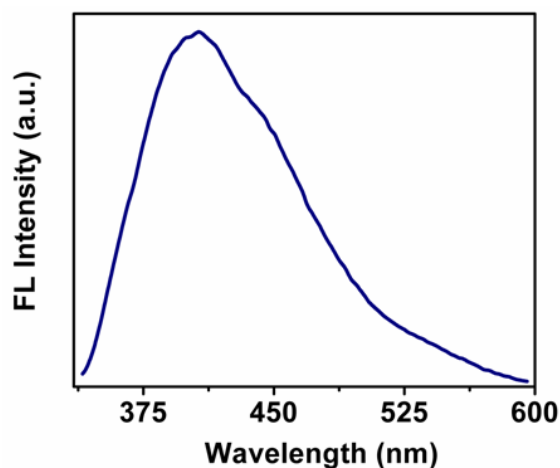


Figure 3.10. Fluorescence spectrum for g-CNQDs in water (excitation wavelength = 340 nm).

The fluorescence peak shifted from 405 nm to 580 nm and its intensity decreased remarkably when the aqueous solution of g-CNQDs was excited at a wavelength ranging between 340 nm and 560 nm. Similar excitation dependent behavior is reported in the literature for graphene quantum dots⁴ and carbon quantum dots⁵⁷. Strong solvent dependent fluorescence emission behavior of g-CNQDs was found and shown in Figure 3.12 where the excitation wavelength was kept at 330 nm. In the solvent dependent study of g-CNQDs the changes in maximum intense peak position with variation of solvent follows the trend such as for benzene, tetra hydro furan

(THF), dimethyl formamide (DMF), water, formamide and chloroform (CHCl_3) the maximum intense peaks are 385, 400, 402, 404, 405 and 420 nm respectively. In addition to excitation wavelength and solvent dependent fluorescence behavior, it was observed that fluorescence emission spectra of g-CNQDs is very sensitive to pH of the medium as shown in Figure 3.13 (a and b). Fluorescence intensity decreases with increasing pH of the solution from pH = 2 to pH = 13, but the change of fluorescence intensity is comparatively small in the pH range of 2 to 8, as compared to other pH regions. The pH sensitive fluorescence behaviors for carbon dots⁵⁵ and graphene quantum dots⁴ are reported in the literature. But, the change of fluorescence intensity of g-CNQDs on varying pH is exactly opposite to that observed for all other fluorescent carbon nanomaterials. This change of the fluorescence intensity with pH suggests that fluorescent species in g-CNQDs probably have acidic sites since the fluorescence is quenched in basic media.

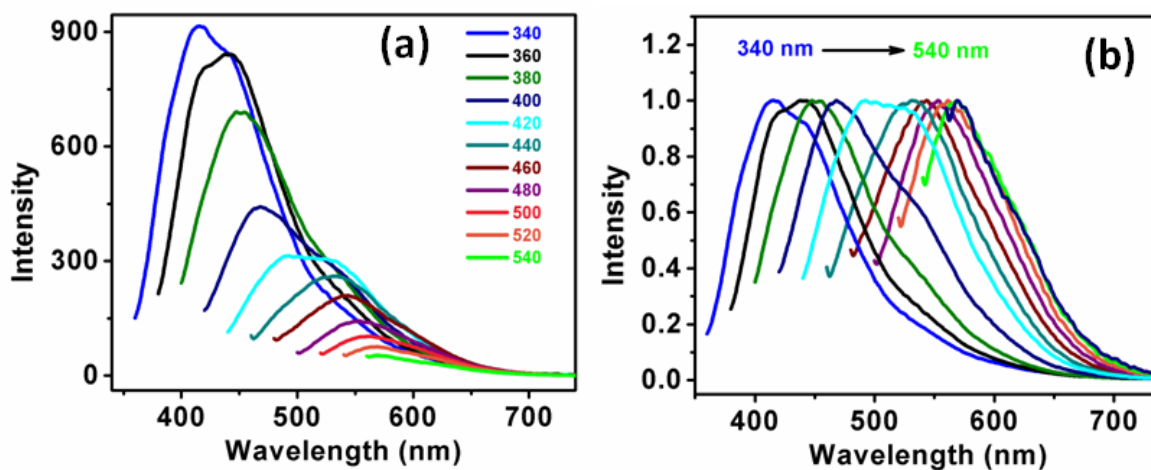


Figure 3.11. (a) Excitation wavelength dependent Fluorescence spectra of g-CNQDs in water solvent. (b) Normalized fluorescence spectra of g-CNQDs in water solvent at different excitation wavelengths.

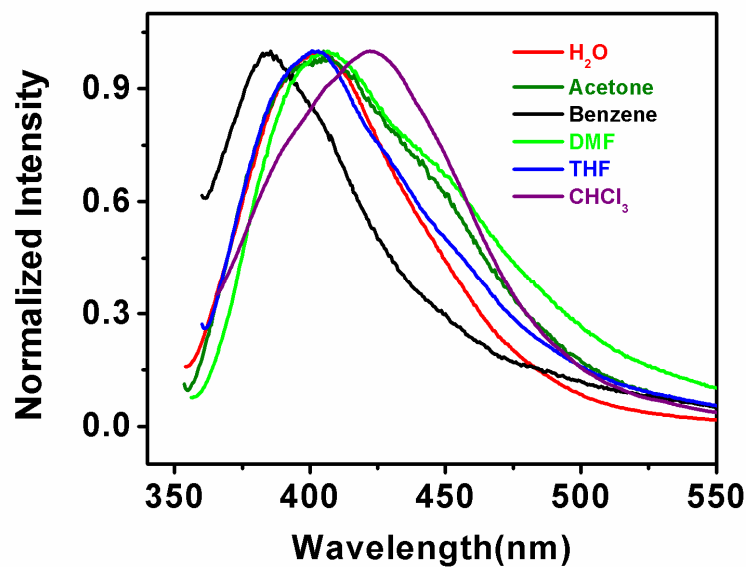


Figure 3.12. Solvent dependent fluorescence emission spectra of g-CNQDs.

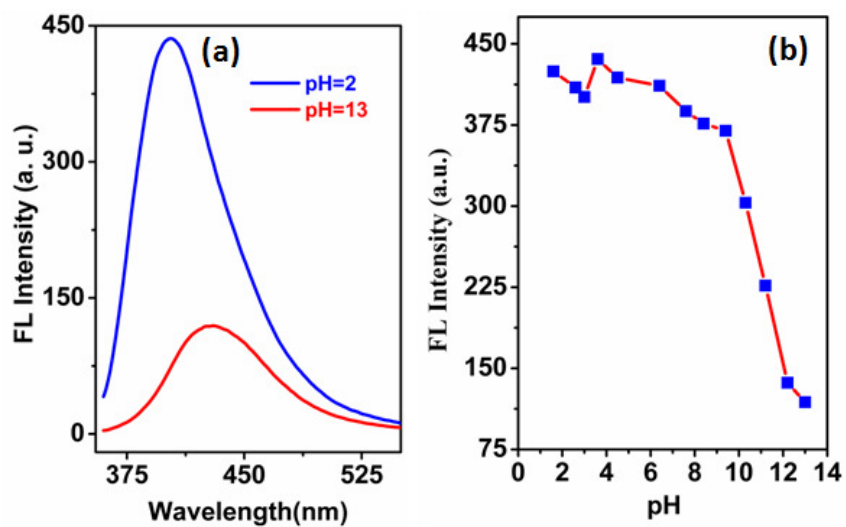


Figure 3.13. (a) Fluorescence spectra of g-CNQDs in water at pH 2 and 13 displaying the change of fluorescence intensity between pH 2 and 13 (b) pH dependent fluorescence intensity plot of g-CNQDs in water (Excitation wavelength =340 nm).

However, basic sites are generally present in carbon nanomaterials⁵⁷. Study of ionic strength effect of fluorescent quantum dots is important due to its different biological application. Figure 3.14 shows the ionic strength effect of g-CNQDs where potassium chloride (KCl) was used as the ionic salt. And pH of the solution was kept at 6. Moreover, this emission behavior was found to be independent of ionic strength of the medium as the fluorescence intensity was constant with varying concentration of KCl in the medium.

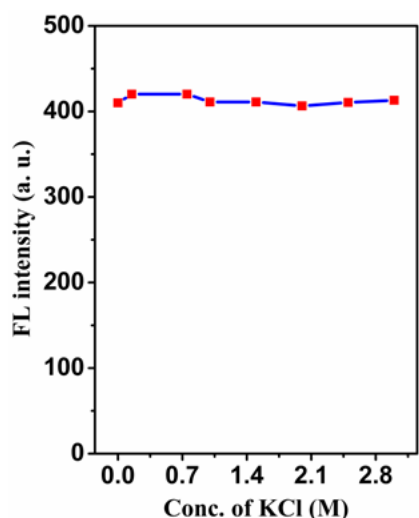


Figure 3.14. Ionic strength effect on fluorescent intensity of g-CNQDs in water.

3.4. Properties of g-CNQDs

3.4.1. Solubility of g-CNQDs

The g-CNQDs exhibit exceptional solubility in water and polar organic solvents such as DMF, DMSO, HCONH₂ etc. and the solutions are very much stable for several months without any precipitation. The g-CNQDs are less soluble in non polar solvents compare to polar solvents.

3.4.2. Fluorescence Quantum yield measurement of g-CNQDs

The fluorescent quantum yield of g-CNQDs was measured by exciting the molecule at 340 nm excitation wavelength. The absorbance of the solution of g-CNQDs in different solvents and reference (Quinine sulfate in 0.1M H₂SO₄) were kept below 0.10 at 340 nm. The fluorescent quantum yield of g-CNQDs is ~29% whereas the highest reported quantum yield of graphene dots is 11.4%⁴⁹. Moreover, the relative quantum yield of emission at 407 nm in toluene, ethanol and water is 1 : 15 : 90. This indicates the ¹(π , π^*) and ¹(n, π^*) are very close to each other such that a polar solvent lowers the energy level of ¹(π , π^*) below ¹(n, π^*), making them more fluorescent.

3.4.3. Average Fluorescence lifetime measurement of g-CNQDs

Figure 3.15 shows the fluorescence decay profile of g-CNQDs in different solvents proves that the g-CNQDs has strong solvent dependent emission lifetime. The emission decays were recorded for g-CNQDs at 400 nm emission wavelength and at excitation wavelength of 330 nm.

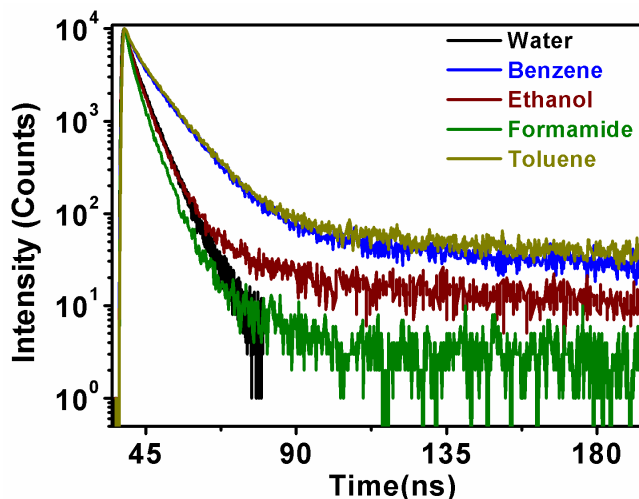


Figure 3.15. Fluorescence decay plots of g-CNQDs in different solvents (excitation wavelength = 330 nm, emission wavelength = 400 nm).

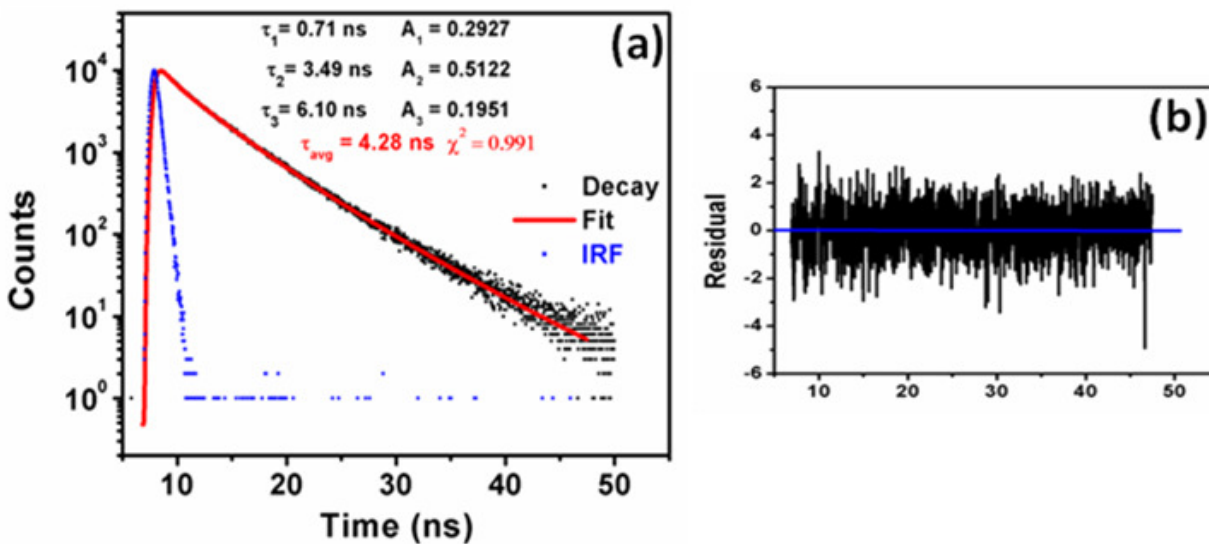


Figure 3.16. (a) Fluorescence decay curve and its exponential fitting curve of g-CNQDs in polar water solvent. IRF is also plotted in this graph. (b) Residual after fitting the fluorescence decay curve.

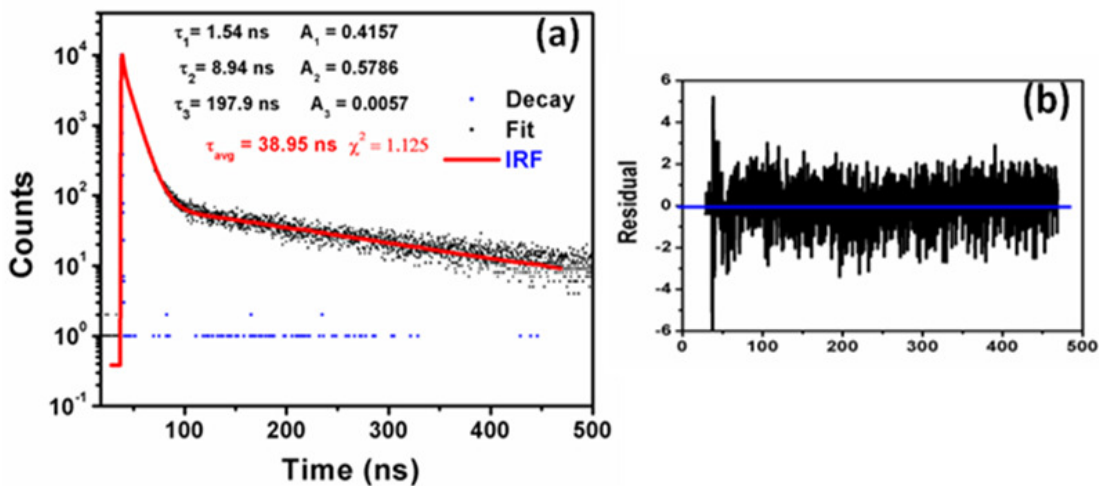


Figure 3.17. (a) Fluorescence decay curve and its exponential fitting curve of g-CNQDs in non polar toluene solvent. IRF is also plotted in this graph. (b) Residual after fitting the fluorescence decay curve.

The details of fluorescence decay profiles with tri-exponential fitting and the residual plots after fitting are shown in Figure 3.16 and Figure 3.17. Figure 3.16 represents the fluorescence decay analysis of g-CNQDs in water and the Figure 3.17 represents the fluorescence decay analysis of g-CNQDs in toluene. It was observed that the average lifetime in polar solvent formamide is shorter (3.25 ns), whereas it is longer (38.9 ns) in non polar solvent toluene. The fluorescence decay profiles of g-CNQDs in various solvents fitted with a tri-exponential fitting equation that indicates the presence of three emitting species with different lifetimes (Figure 3.16 and Figure 3.17). Following Figures 3.15, 3.16 and 3.17 and Table 3.1 prove the strong effects of the solvents on the fluorescence life time of g-CNQDs. This is due to the effect of polarity of solvent on energy states of the molecules. The strong solvent dependent behavior of g-CNQDs is distinctly different from that of other carbon based nanomaterials, whereas the behavior of hetero-aromatic compounds such as pyridine, quinolines, etc. is similar to that of g-CNQDs.

Table 3.1. Fluorescence decay time (τ) and its corresponding pre-exponential factor (A), average life time (τ_{avg}) of g-CNQDs in various solvents.

Solvent	$\tau_1(A_1)$	$\tau_2(A_2)$	$\tau_3(A_3)$	τ_{avg}	χ^2
Formamide	1.58 ns (0.666)	4.18 ns (0.3325)	20.23ns (0.0015)	3.27 ns	0.97
Water	0.71 ns (0.2927)	3.49 ns (0.5122)	6.10 ns (0.1951)	4.28 ns	0.99
Ethanol	2.67ns (0.7902)	6.03ns (0.2085)	83.93ns (0.0013)	6.43 ns	1.125
Benzene	1.52ns (0.4645)	8.94ns (0.5311)	184.5ns (0.0044)	30.84 ns	1.17
Toluene	1.55ns (0.4157)	8.94ns (0.5786)	197.9ns (0.0057)	38.95 ns	1.16

3.4.4. Structural prediction of g-CNQDs

Based on UV-Visible spectra, fluorescence spectra, FT-IR spectra, XPS analysis and ^{13}C NMR spectroscopic studies, we propose a triazine based graphitic model structure of g-CNQDs as shown in Figure 3.18. However, these studies do not completely rule out the other possible structure(s) of g-CNQDs.

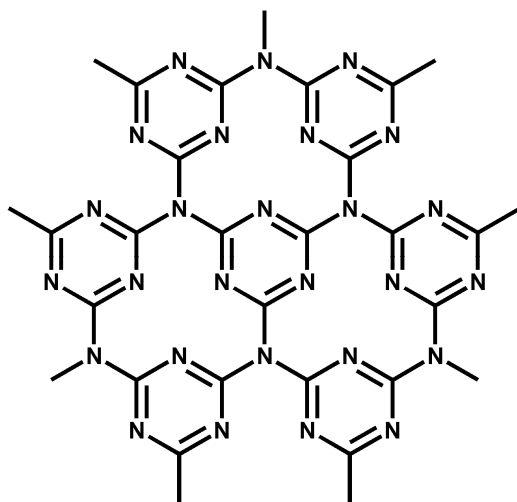


Figure 3.18. The plausible structure of g-CNQDs.

3.4.5. Room temperature ferromagnetic property of g-CNQDs

Synthesis of metal free magnetic material is a challenging work now a day. Metal free room temperature ferromagnetic material is very much important in the spintronic devices. Single layer graphene, a two dimensional sheet of graphite has attracted enormous amount of attention in the research field such as nanoelectronics, sensor, energy storage, optoelectronics due to its unique properties such as quantum hall effect, unique electronic structure, extremely high charge carrier mobility and high current density. In addition graphene has application to the metal free

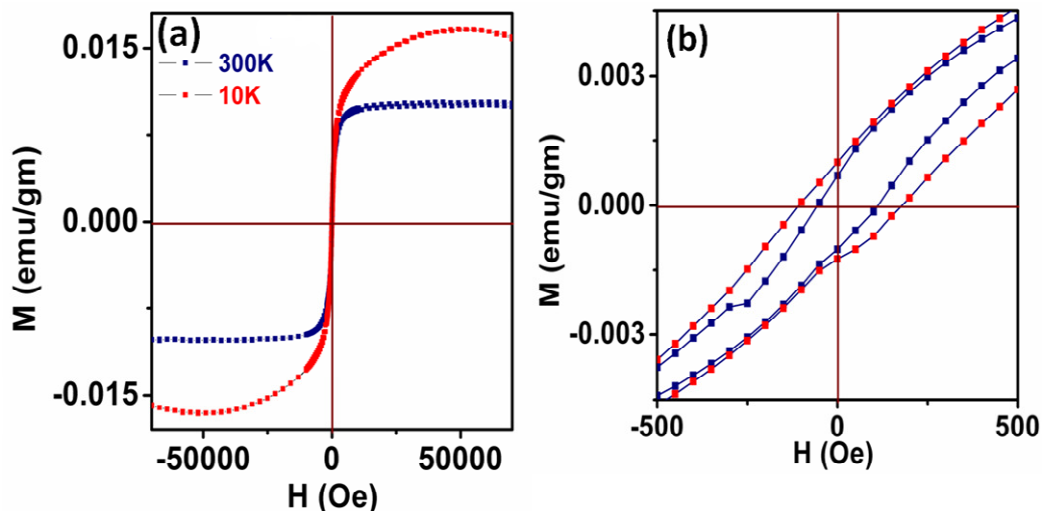


Figure 3.19. (a) Magnetic Hysteresis loops (M-H curve) of g-CNQDs at 300K and 10K. (b) Lower magnetic field region of magnetic Hysteresis loops (M-H curve) of g-CNQDs at 300K and 10K.

next generation spintronic devices⁵⁸. Graphitic carbon nitride quantum dot have similar structure and properties like graphene quantum dot. To the best of our knowledge there is no report of room temperature ferromagnetic property of g-CNQDs. The microwave synthesized g-CNQDs compound from formamide shows ferromagnetic property at room temperature. A superconducting quantum interference device (SQUID) was used to prove the ferromagnetic nature of the metal free g-CNQDs. The magnetic field and temperature dependent magnetization study was analyzed to prove the ferromagnetic property of g-CNQDs. Magnetic properties of the as synthesized compounds were studied by measuring the Hysteresis loop i.e. magnetization (M) vs. magnetic field (H) curve at room temperature (300K) and as well as low temperature (10K). Figure 3.19 (a) shows the hysteresis loop of the g-CNQDs composite at room temperature (300K) and at low temperature (10K) whereas the lower field region is represented in Figure

3.19 (b). At room temperature (300K) g-CNQDs has saturated magnetization value (M_s) of 0.01 emu/gm with coercive field (H_c) of 110.9 Oe and at low temperature (10K) it has saturated magnetization value of 0.0167 emu/gm with coercive field (H_c) of 174.5 Oe (Table 3.2). During measurement of Hysteresis loop when the magnetic field drops to zero, the ferromagnetic material still shows some degree of magnetization value which is called remnant magnetization (M_r). g-CNQD is having sufficient amount of remnant magnetization at both the temperatures at 10K and 300k which are shown in Table 3.2.

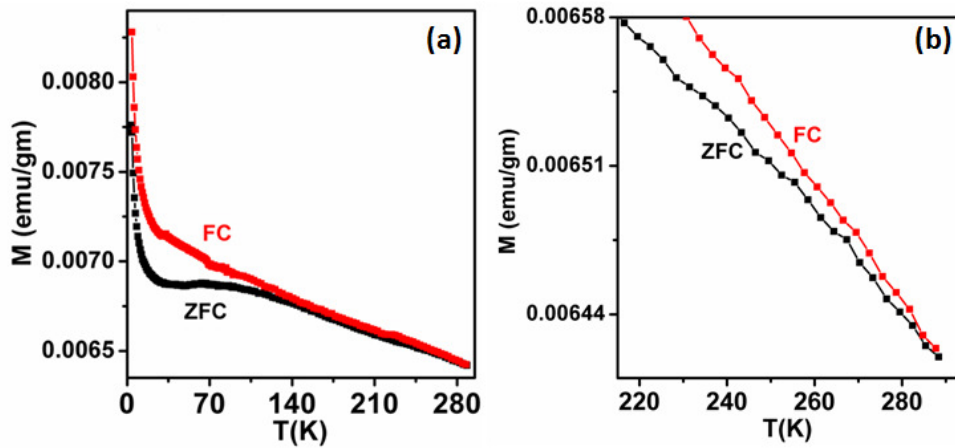


Figure 3.20. (a) Field cooled (FC) and Zero field cooled (ZFC) magnetization curves of g-CNQDs. Data measured at the external magnetic field of 1000 Oe. (b) The higher temperature region of FC and ZFC curves.

Table 3.2. Magnetic parameters of the g-CNQDs

M_s (emu/g)		M_r (emu/g)		Coercive field (Oe)	
10K	300K	10K	300K	10K	300K
0.0167	0.010	0.001	0.007	174.5	110.9

The values of saturated magnetization, remnant magnetization and coercive field of g-CNQD is comparable with the other dopant free diluted magnetic semiconductor materials⁵⁹. Diluted magnetic semiconductor materials have attracted in the scientific community due to its spintronic application. Therefore, g-CNQD composite materials can be used in the spintronic devices.

Table 3.3. Comparison of Magnetic parameters of the g-CNQDs with other compounds

Sample	M_s (emu/g)		Coercive field (Oe)		Ref.
	10K	300K	10K	300K	
g-C ₃ N ₄ nanosheet	0.0093	0.0076	96	45	59
CN-4	----	0.015	----	87	60
CNF-3.3%	----	0.011	----	145	61
FGO	----	-----	----	64	62
g-CNQDs	0.0167	0.010	174.5	110.9	this work

Sufficient amount of remnant magnetization value of g-CNQD open a new application window with these materials in magnetic memory devices. Figure 3.20 (a) displays the field cooled (FC)–zero field cooled (ZFC) magnetization curve of g-CNQDs in presence of external magnetic field of 1000 Oe whereas the Figure 3.20 (b) represents the Field cooled (FC) and Zero field cooled (ZFC) magnetization curves at the high temperature region. In the FC-ZFC magnetization curve of g-CNQD there is distinct splitting up to 288K which proves Curie temperature of g-CNQD is higher than the 288K. High Curie temperature of a magnetic material is one of the very much

important criteria to be using that magnetic material in the spintronic devices. Therefore, g-CNQD can be used in the spintronic devices. The absence of any peak in the FC-ZFC magnetization curve proves that there is no magnetic phase transition in g-CNQDs. In ZFC curve of g-CNQDs there is no blocking temperature which proves the absence of ferromagnetic cluster in the samples. The ZFC and FC curves of g-CNQDs also prove their ferromagnetic behaviour with absence of Curie temperature. So g-CNQD has intrinsic room temperature ferromagnetic property. A comparison study of different magnetic parameters such as saturated magnetization and the coercivity was compared with the other metal free nanosheets and represented in Table 3.3. The magnetic parameters of g-CNQDs are comparable with other metal free nanosheets.

3.4.6. Origin of ferromagnetic property of g-CNQDs

Among different carbon based materials graphene can be used as a magnetic material. Though, it is reported that graphene has no intrinsic magnetic property due to its conjugated π electron cloud, but different kind of defect during synthesis time or a particular structure of graphene can induces the magnetic property into the graphene material. Magnetism can be induced at the zig-zag edge of the one dimensional graphene nanoribbon. X. Li *et. al.* have demonstrated that zig-zag edged triangular graphene nanoflakes linked by 1,3,5-benzenetriyl units shows ferromagnetic property⁶³. It is well known that due to localized states or the edge effect is the cause of magnetization of metal free graphene material. The localized spin is present at the non bonding edge of metal free graphene is creating the spin magnetism⁶⁴. Carbon nitride is an alternative carbon material of graphite with nitrogen atom substitution. Among different phases of carbon nitride, g-C₃N₄ is most interesting material due its two dimensional layer structure like graphene. It is well known that pure g-C₃N₄ is nonmagnetic which is proved theoretically by first principle calculation⁵⁹. Due to lack of intrinsic spin ordering the metal free two dimensional materials are

not ferromagnetic. In 2013 Q. Wang and his coworkers have proved that non magnetic g-C₃N₄ can be ferromagnetic when pattern of this g-C₃N₄ became kagome lattice by using first-principles calculation based on density functional theory⁶⁵. The magnetic properties of kagome pattern g-C₃N₄ can be increased by applying external strain. The electrons in p orbital of carbon and nitrogen atoms in g-C₃N₄ compound can create magnetism property proved by first-principles study⁶⁶. Doping of hole into the material is one kind of defect which can create magnetic behavior into the material. Substitution of nitrogen by carbon atom to the pure g-C₃N₄ material can create hole which is responsible for the ferromagnetic property⁶⁶. Apart from hole defect carbon defect can also increase the ferromagnetic behavior of graphitic carbon nitride⁶⁷. Experimentally, D Gao *et. al.*⁵⁹ have proved that the saturated magnetization (M_s) value decreases with increase of the C/N ratio of metal free g-C₃N₄ nanosheet. Therefore, they have concluded that the intrinsic carbon defect is cause of ferromagnetic property of metal free g-C₃N₄ nanosheet. D. Gao *et. al.*⁶¹ have studied the origin of ferromagnetism property in fluorinated graphitic carbon nitride by ESR spectroscopy study and compared with graphitic carbon nitride compound where they have shown in ESR spectrum of graphitic carbon nitride only one peak is there but in the fluorinated graphitic carbon nitride compound there is two peaks, the extra peak present in the fluorinated graphitic carbon nitride compound is indicating the ferromagnetic property of it. They provided the theoretical evidence of ferromagnetic property of fluorinated graphitic carbon nitride by doing the spin resolved total density of states (TDOS) calculation. They have shown that there is significant spin split near the Fermi energy level in the TDOS calculation which is origin of ferromagnetism. In the spin up polarization band structure the fluorinated g-C₃N₄ have semiconductor nature and in the spin down polarization band structure the fluorinated g-C₃N₄ have metallic nature. Therefore, the fluorinated g-C₃N₄ is 100% spin

polarized half metal. During the thermal polycondensation of dicyanamide to synthesize the $g-C_3N_4$ the amino group exits at the edge of the bulk $g-C_3N_4$ moiety. The nitrogen (N) sites present into the $g-C_3N_4$ structure have high affinity towards the proton and it occurs during the exfoliation process under high power ultrasonication in aqueous solution. These hydrogen increases the hydrogen concentration into the $g-C_3N_4$ structure during the synthesis process. K. Xu *et. al.*⁶⁰ have shown that the hydrogen dangling bonds into the $g-C_3N_4$ nanosheet induces the ferromagnetism property. They have done total density of state (TDOS) calculation considering the hydrogen dangling bonds at the nitrogen site of $g-C_3N_4$ sheet. In the TDOS calculation there is significant asymmetry between spin up and spin down states near the Fermi level which is the origin of the ferromagnetic property of $g-C_3N_4$ sheet.

Table 3.4. Elemental content in g - CNQDs

Fe (ppm)	Co (ppm)	Ni (ppm)	Cr (ppm)	Mn (ppm)	Cu (ppm)
0.351	0.0122	0.0205	0.0124	0.0082	0.064

The magnetic moment of the ferromagnetic $g-C_3N_4$ sheet was contributed by the p orbital of carbon and nitrogen atoms of $g-C_3N_4$ sheet which was proved by doing spin resolved corresponding atomic projected density of states calculation (N-PDOS and C-PDOS). Among p orbital of carbon and nitrogen atoms the main contribution of magnetic moment comes from the p orbital of carbon atom of $g-C_3N_4$ sheet. Therefore it can be stated that hydrogenation can create magnetic behaviour to the non magnetic graphitic carbon nitride materials. Presence of magnetic metals such as iron, cobalt, nickel chromium, manganese and copper with concentration more

than 10 ppm can create the ferromagnetic property into the material⁶⁰. In order to prove magnetic metal impurities are not responsible for the ferromagnetic property of g-CNQDs, we have measured the concentration of different magnetic metals present by atomic absorption spectroscopy. The different magnetic metal concentrations present in g-CNQDs are tabulated in the Table 3.4. The concentrations of the magnetic metals are found to be below 10 ppm which is much lower than 10 ppm. Therefore it can be concluded that the observed ferromagnetism property of the g-CNQDs is not originating from any metal impurity present into the compound; this is the intrinsic property of the material. Incomplete condensation during synthesis of g-CNQDs from formamide incorporates hydrogen atoms at the terminal position of g-CNQD framework as primary or secondary amine. Presence of hydrogen at the terminal position of g-C₃N₄ due to incomplete condensation increases the amount of hydrogen which incorporates hydrogen dangling bond to show ferromagnetic property of g-CNQDs. From CHN analysis it has been shown that the N/C ratio was 1.1 which is lower than that of g-C₃N₄ (N/C = 1.33). The XPS studies also prove the decrease amount of nitrogen into the g-CNQDs compare to the identical g-C₃N₄ structure. So the amount nitrogen present into the g-CNQDs decreases by the substitution with the carbon atoms leading to generate hole defect into the g-CNQDs moiety which is responsible to show the ferromagnetic property of it. Therefore, the hydrogen dangling bond and the intrinsic hole defect into the g-CNQDs may be the cause of ferromagnetism property of the metal free g-CNQDs compound.

3.5. Application of g-CNQDs as a sensor for mercuric and iodide ions

As application, the g-CNQDs can be used as sensor of Hg²⁺ ion in water by observing the change of the fluorescence intensity of it. Figure 3.21 (a) represents the fluorescence quenching g-

CNQDs with addition of different amount of Hg^{2+} ion into the aqueous solution of g-CNQDs where excitation wavelength was kept at 340 nm.

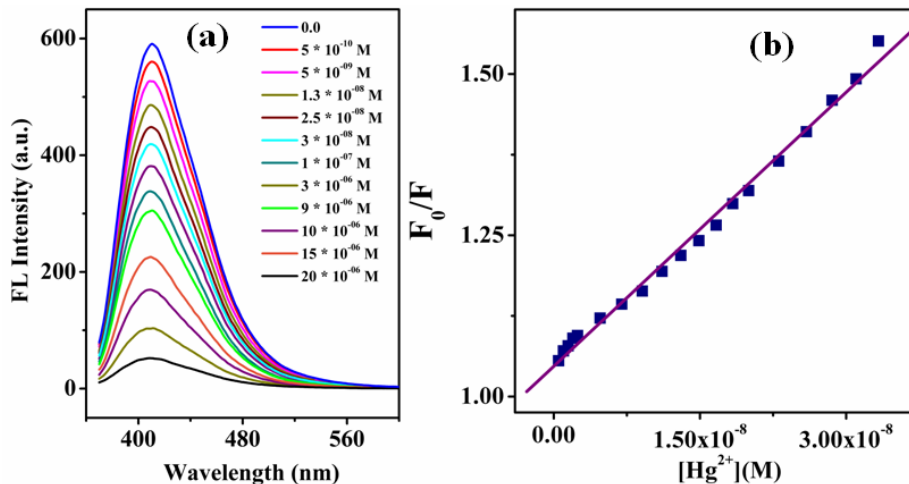


Figure 3.21. (a) The change of fluorescence emission intensity of g-CNQDs in water on addition of Hg^{2+} ions. Excitation wavelength was 340 nm. (b) Stern–Volmer plot for the fluorescence quenching of g-CNQDs with Hg^{2+} ions in water.

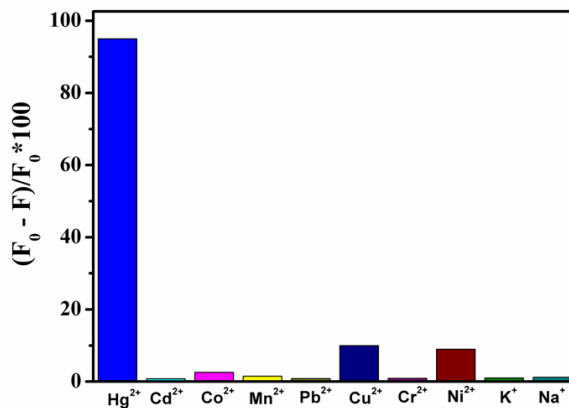


Figure 3.22. Fluorescence quenching of g-CNQDs in presence of Hg^{2+} ions and compared with other different metal ions.

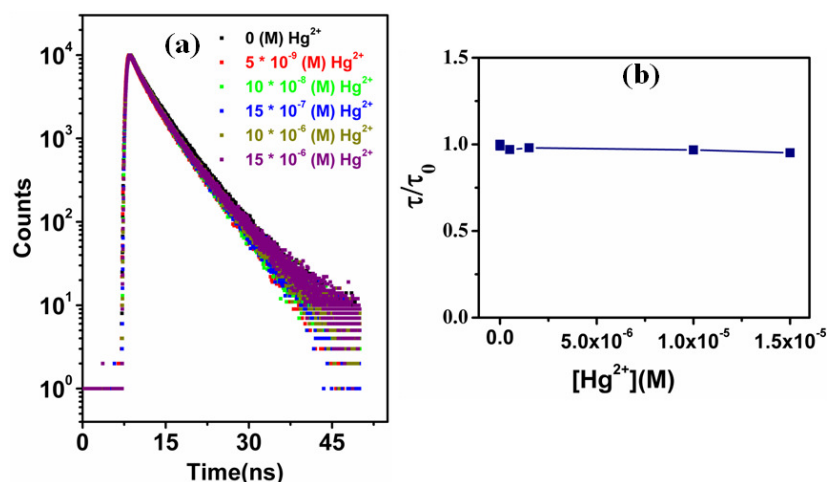


Figure 3.23. (a) Fluorescence decay profiles of g-CNQDs in presence of different concentration (5-30 μM) of Hg^{2+} ions in aqueous medium (Excitation wavelength = 330 nm and Emission wavelength = 400 nm) (b) Plot shows τ/τ_0 is invariant with added Hg^{2+} ions.

It was observed that the fluorescence intensity of g-CNQDs was gradually decreasing with addition of the Hg^{2+} ions. The fluorescence quenching of g-CNQDs by Hg^{2+} ions can be analyzed by Stern–Volmer analysis. Hg^{2+} ions quench the fluorescence emission of g-CNQDs in aqueous medium. The Stern-Volmer plot of F_0/F versus $[\text{Hg}^{2+}]$ is given in Figure 3.21 (b) and the Stern–Volmer quenching constant was calculated from the slope. The Stern–Volmer plot of fluorescence quenching by Hg^{2+} ions shows the linear dependence with concentration of Hg^{2+} ions in the low quencher concentration regime. The calculated Stern–Volmer quenching constant (K_{SV}) from the slope is $1.4 \times 10^7 \text{ M}^{-1}$. This value is a few orders of magnitude higher than that of the conventional quenching between simple organic dye–quencher pairs and thus it represents the case of “superquenching”,⁶⁸ of fluorescence by g-CNQD and Hg^{2+} pairs. A similar quenching behavior was reported for dye aggregates⁶⁸ and conjugated polymers⁶⁹. The observed detection limit of Hg^{2+} ions is $\sim 10^{-9} \text{ M}$ calculated from Figure 3.21(b) clearly suggests that g-

CNQDs are highly sensitive to Hg^{2+} ions. The fluorescence quenching of the synthesized g-CNQDs towards different metal ions in water was studied by observing the change in fluorescence intensity before and after the addition of the same amount of perchlorate salts of different metal ions such as Na^+ , K^+ , Zn^{2+} , Cd^{2+} , Hg^{2+} , Pb^{2+} , Co^{2+} , Ni^{2+} and Cu^{2+} . The quenching of fluorescence response of g-CNQDs with various metal ions clearly represents the selectivity of Hg^{2+} to bind with it (Figure 3.22). No significant spectral change of g-CNQDs was observed in the presence of alkali metals such as Na^+ , K^+ and other heavy metals and transition metals such as Zn^{2+} , Cd^{2+} , Pb^{2+} , Co^{2+} . However, in the case of Cu^{2+} and Ni^{2+} metal ions very small spectral changes were observed. There are two types of fluorescence quenching, one is static quenching and another is dynamic quenching. The nature of fluorescence quenching of g-CNQDs by Hg^{2+} ion was studied by time resolved average life time measurement of g-CNQDs after addition of different concentration of Hg^{2+} ion in water. Fluorescence decay curves of g-CNQDs in presence Hg^{2+} ions of different concentrations are given in Figure 3.23 (a). This plot shows the fluorescence life times of g-CNQDs are constant with added mercuric ions. It is proved that the static quenching takes place during complex formation between Hg^{2+} ions and CN_x sheets, as the dependence of fluorescence lifetime with varying concentration of Hg^{2+} in solution is found to be a constant (Figure 3.23 (b)). The highly efficient superquenching of g-CNQDs by Hg^{2+} ions is perhaps due to static quenching owing to the formation of a stable non-fluorescent complex between g-CNQD and Hg^{2+} , on the basis of the report existing in the literature⁶⁸⁻⁶⁹. Therefore, g-CNQDs are selective and sensitive for Hg^{2+} ion detection with fluorescence switching “OFF” phenomenon due to the formation of non fluorescent chelating complex of g-CNQD-(Hg^{2+})_x.

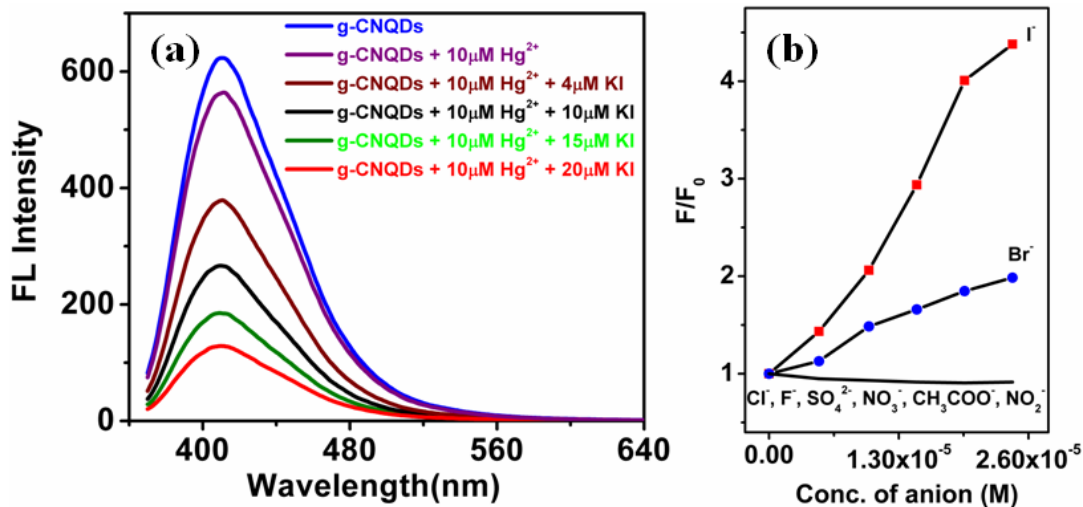


Figure 3.24. (a) The fluorescence enhancement of g-CNQD–(Hg^{2+})_x complex at different concentrations of iodide ions. (b) Comparison of fluorescence enhancement ratio of g-CNQD–(Hg^{2+})_x complex for different anions at various concentrations.

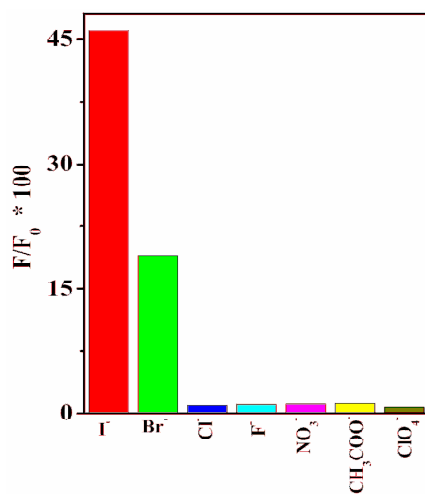


Figure 3.25. Fluorescence enhancement by iodide ions compared to other anions.

We have observed that this non-fluorescent “OFF” state can be switched “ON” by adding iodide ions, indicating that the chelating complex of Hg^{2+} is a promising candidate of fluorescent sensor for iodide (I^-) ions. Figure 3.24 (a) shows the fluorescence intensity enhancement of the g-CNQD-(Hg^{2+})_x complex in the presence of different concentrations of I^- ions where excitation wavelength was kept at 340nm. Comparison of fluorescent enhancement ratio for different anions at various concentrations has been shown in Figure 3.24 (b). The fluorescent enhancement ratio is more for I^- ions compare to other ions. The selectivity of g-CNQD-(Hg^{2+})_x towards different anions was studied by adding the same amount of anion solution to the non-fluorescent g-CNQD-(Hg^{2+})_x complex solution shown in Figure 3.25. It was observed that F^- , Cl^- , NO_3^- , NO_2^- , SO_4^{2-} and CH_3COO^- could not induce any significant spectral enhancement except bromide (Br^-) ions, which show some fluorescent enhancement. The selective fluorescence enhancement by iodide ions towards the complex can be explained by the soft I^- anions binding to the soft Hg^{2+} ions (Hard soft acid base principle), forming HgI_2 and thereby regenerating the free g-CNQDs. The above observation proves that g-CNQDs can play a dual role for selective and sensitive detection of Hg^{2+} ions as well as iodide ions in aqueous media via “ON-OFF-ON” fluorescence response.

The formation of the non-fluorescent g-CNQD-(Hg^{2+})_x complex and the regeneration of the g-CNQDs after addition of I^- ions was proved by ^1H NMR, ATR-FTIR, UV-Visible spectroscopic studies and XPS analysis. ^1H NMR experiments were performed in d_6 -DMSO solvent in the presence of 60% water. Figure 3.26 and 3.27 shows the water suppressed ^1H NMR of the free g-CNQDs, in the presence of Hg^{2+} ions and in the presence of both Hg^{2+} and iodide ions.

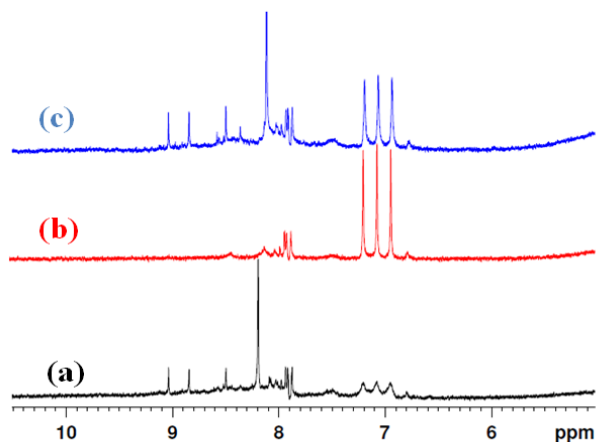


Figure 3.26. Higher ppm region of ^1H NMR spectra of (a) free g-CNQDs (4 mg/mL) (b) g-CNQDs with the presence of mercuric perchlorate salt (0.002 M) (c) g-CNQDs with the presence of mercuric perchlorate (0.002 M) and potassium iodide (0.006 M).

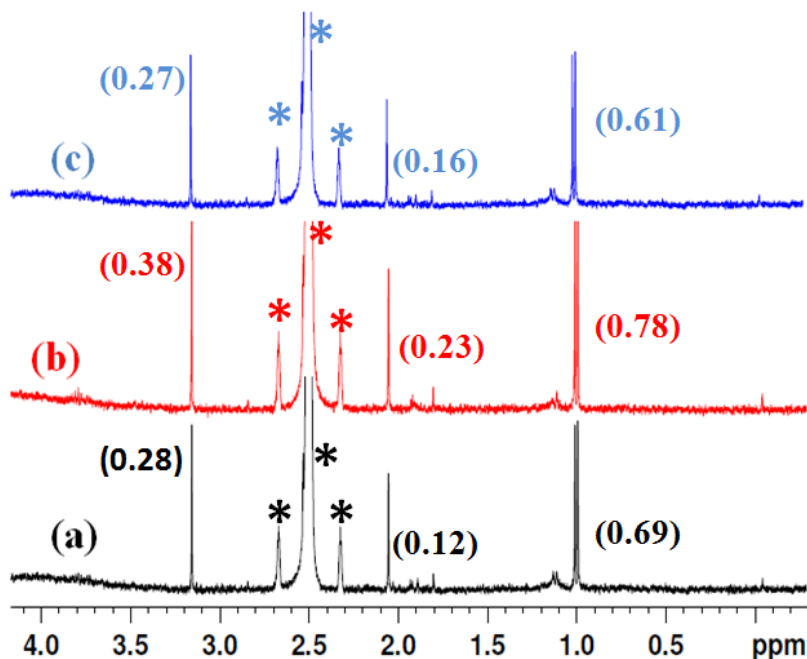


Figure 3.27. Lower ppm region of ^1H NMR spectra of (a) free g-CNQDs (4 mg/mL) (b) g-CNQDs with the presence of mercuric perchlorate salt (0.002 M), (c) g-CNQDs with the presence of mercuric perchlorate salt (0.002 M) and potassium iodide (0.006 M). The values within bracket represent the area under the peak.

The large number of aromatic protons observed in the aromatic region is probably due to different sizes of quantum dots having protons in different chemical environments into the moiety. These carbon nitride species contain a few non aromatic or aliphatic protons between 1.0 and 4.0 ppm in its ^1H NMR spectrum. The most remarkable feature observed on addition of Hg^{2+} ions is the upfield shifting of all the aromatic protons to the aliphatic region (1.0–4.0 ppm), indicating complete loss of aromaticity due to complex formation between the g-CNQDs and Hg^{2+} ions. After addition of Hg^{2+} ion the decrease in peak intensities of aromatic protons is apparent, however, an increase in peak intensities of aliphatic protons is not very prominent. But, the area under the peaks clearly demonstrates that the number of aliphatic protons is increased at the expense of aromatic protons after the addition of Hg^{2+} ions (Figure 3.27). All aromatic protons appeared again into the ^1H NMR spectra on further addition of iodide ions, indicating the dissociation of the complex leading to regeneration of g-CNQDs. Figure 3.28 represents the ATR-FTIR spectra of the free g-CNQDs, in the presence of Hg^{2+} ions and in the presence of Hg^{2+} ions followed by the addition of iodide ions. The ATR-FTIR has been used as a tool to analyze the ON-OFF-ON mechanism of g-CNQDs. The ATR-FTIR spectrum of g-CNQDs has two peaks, one is at 1230 cm^{-1} and the other one is at 1380 cm^{-1} which are due to the vibration stretching of aromatic C=N bond into the g-CNQDs moiety, which are disappeared after addition of Hg^{2+} ions. After addition of Hg^{2+} ion into the g-CNQDs moiety; a new peak is appeared at 1102 cm^{-1} which is due to the C–N stretching. On addition of iodide ions the aromatic double bond stretching bands are appeared again and the single bond stretching band disappeared. Therefore, it is proved that the addition of Hg^{2+} ions onto the g-CNQDs destroy the conjugation into the g-CNQDs and which is again generated after addition of I^- ions.

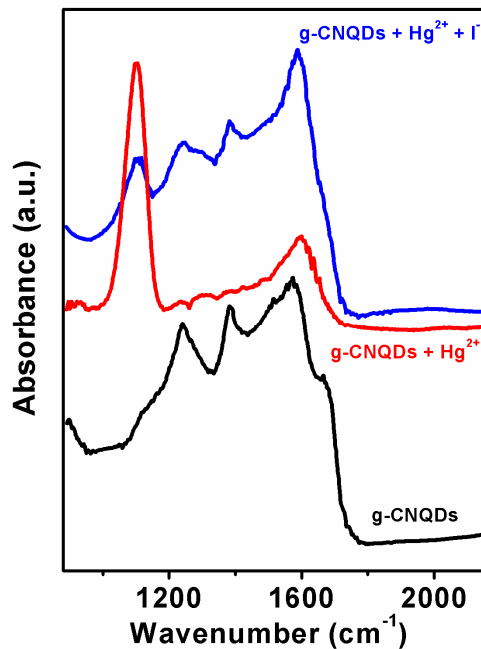


Figure 3.28. ATR-FTIR spectra of free g-CNQDs, g-CNQDs with the presence of Hg²⁺ ions and g-CNQDs with the presence of both Hg²⁺ and I⁻ ions.

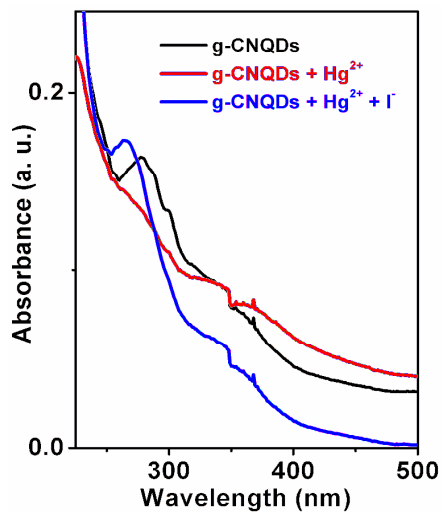


Figure 3.29. UV-visible spectra of free g-CNQDs, g-CNQDs with the presence of Hg²⁺ ions and g-CNQDs with the presence of both Hg²⁺ and I⁻ ions.

Figure 3.29 represents the UV-visible spectra of the free g-CNQDs, g-CNQDs in the presence of Hg^{2+} ions and g-CNQDs in the presence of Hg^{2+} ions followed by the addition of iodide ions. The transition at 260 nm of g-CNQDs is due to a $\pi \rightarrow \pi^*$ transition in the UV-visible spectra which disappeared completely on addition of Hg^{2+} ions, indicating the loss of conjugated aromatic π systems of g-CNQDs. As expected, on addition of iodide ions to this solution, the $\pi \rightarrow \pi^*$ transition appeared again in the UV-visible spectra which proves that the regeneration of the conjugation into the g-CNQDs. Thus, Hg^{2+} ions induced a chemical shift in the ^1H NMR spectra; the disappearance of aromatic C=N stretch in the ATR-FTIR spectra and the disappearance of the $\pi \rightarrow \pi^*$ transition in the UV-visible spectra suggest that Hg^{2+} ions bind with the g-CNQDs framework via covalent bonding and losing the structural integrity of the moiety. XPS spectroscopy has been widely used to monitor the change of electronic structure of g-CNQDs on addition of Hg^{2+} and iodide ions. It is known that the binding energy of $4f_{7/2}$ of metallic mercury⁷⁰ and mercuric chloride⁷¹ appeared at 99.9 and 101.4 eV respectively and their separation (ΔeV) is 4.1 ± 0.1 eV. Figure 3.30 (a) shows the Hg 4f spectrum of g-CNQD-(Hg^{2+})_x complex, which was deconvoluted into four components by Gaussian fitting. The two features at 106.0 eV and 110.0 eV can be assigned to Hg $4f_{7/2}$ and Hg $4f_{5/2}$, respectively of the Hg^{2+} bound g-CNQD complex and ΔeV is ~ 4 eV. The remaining two features at 100.01 eV and 103.5 eV are due to the presence of Hg^0 . The shift of ~ 5.0 eV towards the higher binding energy of Hg^{2+} in g-CNQD-(Hg^{2+})_x compared to free Hg^{2+} also indicated the formation of a covalent bond between an empty orbital of Hg^{2+} and the π electrons of the g-CNQDs moiety, leading to a change in the electronic distribution of the g-CNQDs framework. The iodide ions abstract the bound Hg^{2+} from the CN_x sheet to form HgI_2 and this is confirmed by the presence of two peaks at 101.0 eV and 105.0 eV in the Hg 4f XPS spectrum (Figure 3.30 (b)).

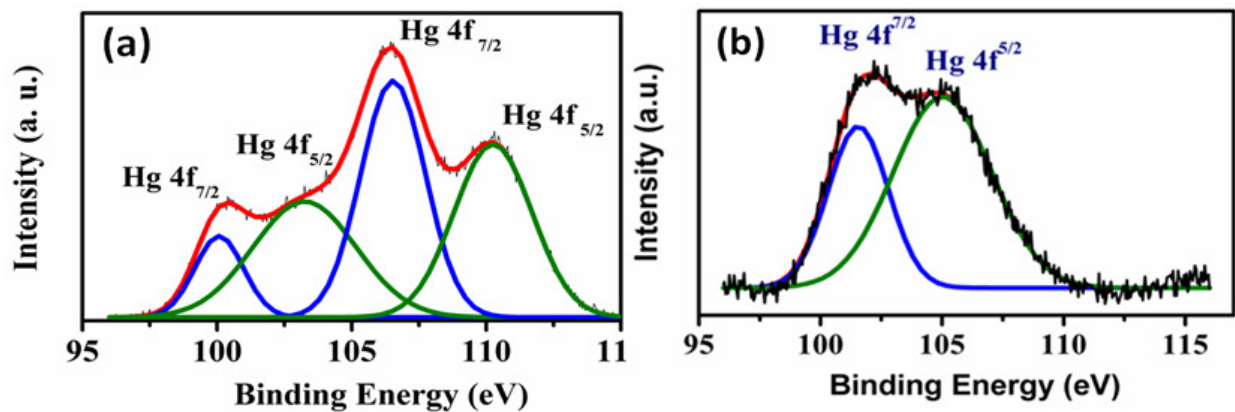


Figure 3.30. Hg 4f XPS spectra of g-CNQDs obtained after treatment with (a) Hg^{2+} and (b) both Hg^{2+} and I^- ions.

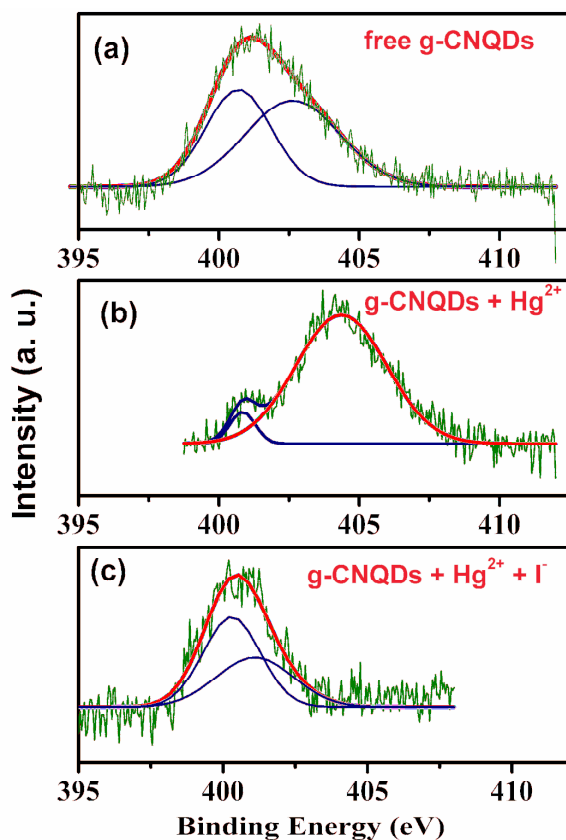


Figure 3.31. XPS spectra in the N1s region of (a) free g-CNQDs, (b) g-CNQDs after treatment with Hg^{2+} ion and (c) g-CNQDs after addition of both Hg^{2+} and I^- ions.

The N1s spectrum of free g-CNQDs exhibits a peak centered at 400.5 eV and the N1s peak is shifted to higher binding energy at 404.5 eV upon addition of Hg^{2+} ions which is shown in Figure 3.31. The shift of 4.0 eV to higher N1s binding energy of the $\text{g-CNQD}-(\text{Hg}^{2+})_x$ complex compared to free g-CNQDs suggests that the Hg^{2+} ions are bonded with nitrogen atoms of g-CNQDs. Upon addition of iodide ions to the Hg^{2+} bound complex, the N1s XPS peak appears at 400.7 eV shown in Figure 3.31 suggesting the regeneration of free g-CNQDs. However, no significant changes in the C1s XPS spectrum (Figure 3.32) were observed on addition of Hg^{2+} ions into the g-CNQDs indicating no interaction between Hg^{2+} ions and carbon atoms.

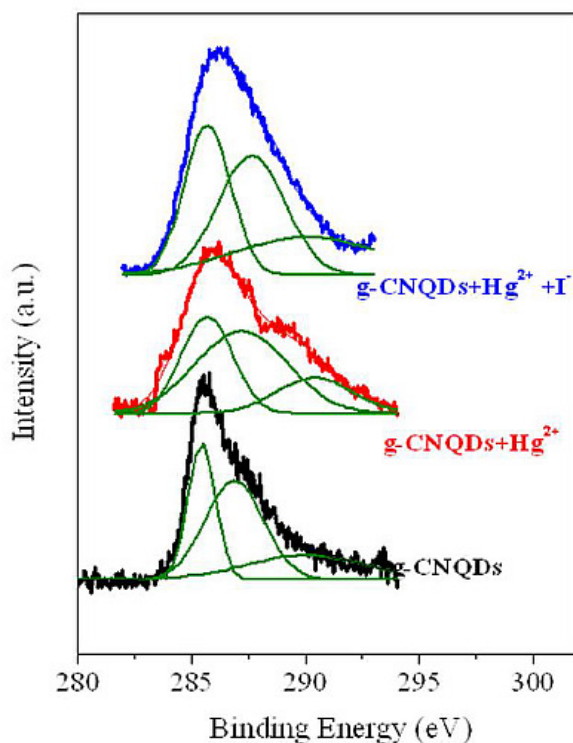


Figure 3.32. High resolution C1s XPS spectra of free g-CNQDs, g-CNQDs after treatment with Hg^{2+} and g-CNQDs after addition of Hg^{2+} and I^- ions.

The unique selectivity for Hg^{2+} ions towards quenching of fluorescence of g-CNQDs is possibly due to several reasons, such as greater affinity of Hg^{2+} ions towards nitrogen, larger radius of Hg^{2+} ion and its ability to form a complex with g-CNQD with a geometry that is energetically favorable; possibly the tetrahedral one where the Hg^{2+} ion binds to three nitrogen atoms and the fourth tetrahedral site is most likely occupied by a water molecule as shown in Figure 3.33. The tetrahedral geometry of $\text{g-CNQD}-(\text{Hg}^{2+})_x$ has been proposed on the basis of the trend that most complexes of Hg^{2+} generally adopt a tetrahedral geometry.

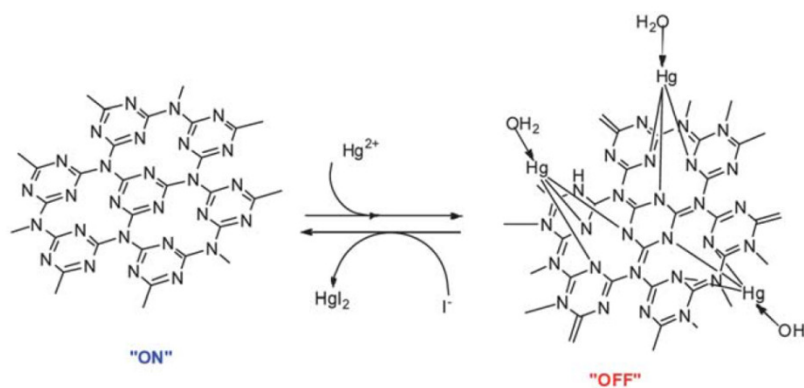


Figure 3.33. Plausible structure of $\text{g-CNQD}-(\text{Hg}^{2+})_x$ complex and regeneration of free g-CNQDs on addition of I^- ions.

3.6. Application of g-CNQDs in the adsorptive removal of metal ions from water

3.6.1. Adsorption isotherm study of metal ions on g-CNQDs

Langmuir adsorption isotherm model is based on the homogeneous adsorption. Langmuir adsorption assumes that there is no interaction among the adsorbent molecules. Langmuir adsorption isotherm is based on monolayer coverage of adsorbent on the adsorbate which means

that one adsorption site of the adsorbate can take one molecule of metal, further it cannot take another molecule. Langmuir adsorption isotherm model which is expressed by equation⁷²

$$\frac{C_e}{q_e} = \frac{1}{q_{\max}K_L} + \frac{C_e}{q_{\max}}$$

where q_e is the amount of metal adsorbed at equilibrium (mg/gm), K_L is the fitting parameter or Langmuir constant which is related to heat of adsorption, q_{\max} is the maximum adsorption capacity (mg/gm), C_e is the equilibrium concentration of metal ion in solution (mg/L). If we plot C_e/q_e vs. C_e then we will get a straight line where slope will be $1/q_{\max}$ and intercept will be $1/(q_{\max} \cdot K_L)$. Therefore, q_{\max} can be calculated from the slope and K_L can be calculated from the intercept of the straight line. Freundlich adsorption isotherm model is based on heterogeneous adsorption. Freundlich adsorption isotherm model is expressed as where k_f and n are the fitting parameter constants.

$$\ln q_e = \ln K_f + \frac{1}{n} \ln C_e$$

q_e (mg/gm) is the equilibrium concentration of the metal ion adsorption. K_f is the Freundlich adsorption constant (L/gm); $1/n$ is the measure of the adsorption intensity⁷³. The adsorption isotherm of each metal ion was studied at room temperature and at normal pH. Different initial concentration was taken to study the adsorption isotherm. All the experimental adsorption isotherms are fitted with Langmuir adsorption isotherm equation and Freundlich adsorption isotherm equation separately. Figure 3.34 (a) and (b) represent the adsorption isotherm plots of Cu^{2+} ion on g-CNQDs after fitting with Langmuir and Freundlich adsorption isotherm

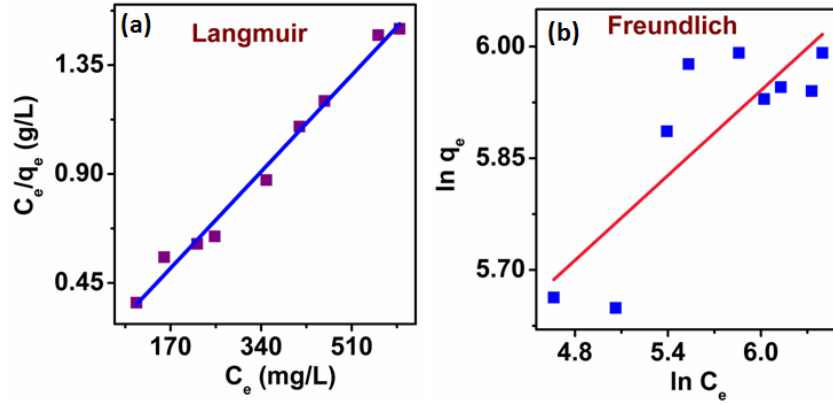


Figure 3.34. Adsorption isotherm plots of Cu^{2+} ion on g-CNQDs after fitting with (a) Langmuir fitting and with (b) Freundlich fitting.

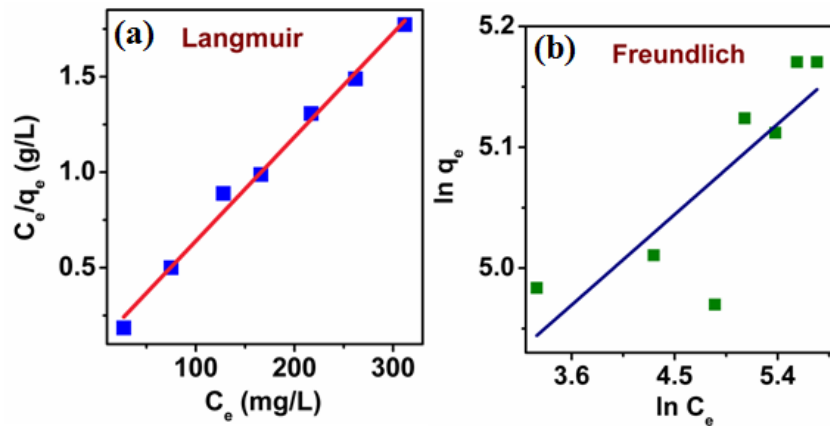


Figure 3.35. Adsorption isotherm plots of Cd^{2+} ion on g-CNQDs after fitting with (a) Langmuir fitting and with (b) Freundlich fitting.

respectively. Figure 3.35 (a) and (b) represents the adsorption isotherm plots of Cd^{2+} ion on g-CNQDs after fitting with Langmuir and Freundlich adsorption isotherm respectively. With respect to the value of correlation coefficient (R^2) Langmuir adsorption isotherm equation satisfies more closely with the experimental adsorption data for each metal ion (Cu^{2+} and Cd^{2+}

ions) adsorption on g-CNQDs. Therefore, all the metal ions adsorption on g-CNQDs are monolayer type of adsorption. After fitting with Langmuir adsorption isotherm equation the calculated parameters are listed in Table 3.5. The maximum adsorption capacities (q_{max}) of the Cu^{2+} and Pb^{2+} ions onto g-CNQDs composite calculated after fitting with Langmuir adsorption isotherm are 184.0 mg/gm and 425.5 mg/gm respectively. The presence of heteroatom nitrogen into the g-CNQDs moiety helps to adsorb the metal ions onto the surface of g-CNQDs composite. Therefore, g-CNQDs have potential to the application of the wastewater treatment.

Table 3.5. Relative parameters of adsorption isotherm of different metal ions after fitting with Langmuir and Freundlich adsorption isotherm model

Metal Ion	Langmuir constants			Freundlich constants		
	q_m (mg/gm)	b (L/mg)	R^2	K_f	n	R^2
Cu^{2+}	184.0	0.0568	0.990	106.7	12	0.593
Cd^{2+}	425.5	0.02098	0.986	121.6	5.3	0.654

3.6.2. Adsorption kinetic study of Cu^{2+} ions on g-CNQDs

The adsorption kinetics depends on the structural properties of the adsorbent for example porosity, specific area. In case of adsorbent of metal or metal oxide composite the adsorption kinetics depends on the particle size, coordination number of metal or metal oxide, radius of metal or metal oxide. Generally there are two models for kinetic study of adsorption method one is pseudo first order kinetic model and another one is pseudo second order kinetic model. The pseudo first order kinetic model represented as

$$\log (q_e - q_t) = \log q_e - \frac{K_1}{2.303t}$$

where K_1 is the first order rate constant (min^{-1}) and q_e and q_t are the metal ion concentration at equilibrium and at time t (mg/gm)⁷⁴. The pseudo second order kinetic model represents as

$$\frac{t}{q_t} = \frac{1}{K_2 q_e^2} + \frac{1}{q_e} t$$

where K_2 is the second order rate constant ($\text{g mg}^{-1} \text{min}^{-1}$)⁷⁵. Figure 3.36 represents the adsorption kinetics of Cu^{2+} ion onto g- CNQDs. The adsorption kinetic data is well fitted with the pseudo second order model. After fitting with pseudo second order model the value of the parameters and the correlation coefficients are listed in the Table 3.6.

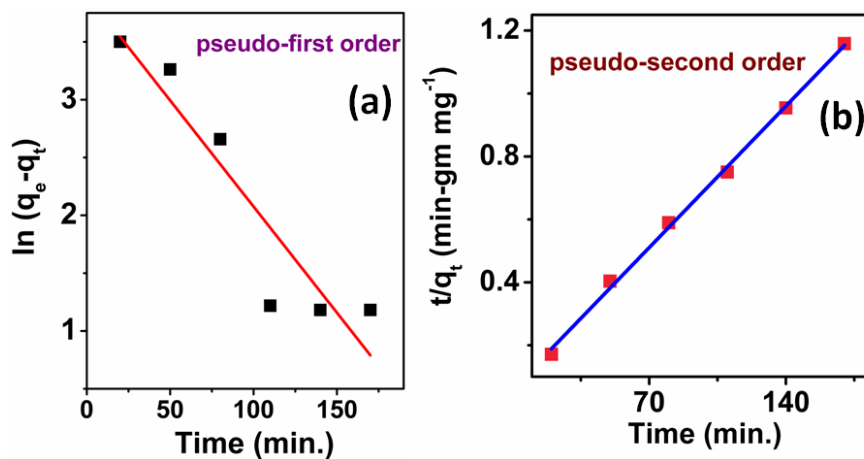


Figure 3.36. Adsorption kinetic plot of Cu^{2+} ion on g-CNQDs with (a) pseudo-first order and (b) pseudo-second order model fitting.

Table 3.6. The adsorption kinetic model parameters of Cu²⁺ ion after fitting with pseudo-second order kinetic models

Pseudo-second order			Pseudo-first order			
q _e (mg/g) (theor.)	K ₂ X 10 ⁻⁴ (g mg ⁻¹ min ⁻¹)	R ²	q _e (mg/gm) (exp.)	K ₁ (min ⁻¹)	q _e (mg/gm) (theor.)	R ²
155.5	6.84	0.997	150.0	0.01836	49.96	0.8449

3.7. Conclusion

We have successfully synthesized and characterized the highly blue fluorescent g-carbon nitride quantum dots (g-CNQDs). It has high fluorescent quantum yield of 29% which is greater than graphene dot. The g-CNQDs are highly soluble in water and most polar solvents and the solutions are very stable for long time. The fluorescence behavior of g-CNQDs is strongly dependent on excitation wavelength, pH of the solution and polarity of the solvent but it is independent of ionic strength of the medium. The g-CNQDs (synthesized from formamide by microwave method) is a new metal free room temperature ferromagnetic zero dimensional nanomaterial. The saturated magnetization value of the g-CNQDs at room temperature (300K) was high as 0.01 emu g⁻¹. Therefore, the g-CNQDs can be used as a building block for producing next generation electronic and spintronic devices. g-CNQDs can be used as mercury ion sensor selectively with high sensitivity by fluorescence quenching of g-CNQDs. The Stern–Volmer constant (K_{SV}) of the quenching is ~ 1 X 10⁷ M⁻¹, which is few orders of magnitude greater than that of simple organic dye and quencher pairs, confirms the “superquenching” behavior of it. We have shown by fluorescence, ¹H NMR, XPS and ATR-IR experiments that the selective affinity of g-CNQDs towards Hg²⁺ ions leads to the formation of a stable complex.

Furthermore, we have shown that the significant fluorescence enhancement of g-CNQD-(Hg²⁺)_x complex in presence of iodide ions. Therefore, application of g-CNQDs is as a highly selective and sensitive “ON-OFF-ON” fluorescence sensor for Hg²⁺ ions in aqueous media with the lower limit of its detection being ~10⁻⁹ M. Thus, these g-CNQDs may find their application as a fast and highly selective sensor for Hg²⁺ and I⁻ in biological as well as environmental samples. g-CNQDs also show good adsorption property of Cu²⁺ and Cd²⁺ ions in water with maximum adsorption capacity of 184 mg/gm and 425.5 mg/gm respectively.

Part B

Carbon Quantum Dots

3.1. Introduction

CQD, a new carbon based quantum dot has got a great interest due to its unique optical, electrical properties. The unique properties of CQD open up various applications in different field such as electrochemistry, bioimaging, drug delivery etc. The quantum confinement phenomenon and the edge effect of CQD are the responsible factor to show the unique properties of it. It can be used as a fluorescent probe in the bioimaging application due to its high biocompatibility under the physiological condition. Traditional fluorescent semiconductor quantum dot also has attention in the application field of biological imaging, biological sensing and in medicine due to its high fluorescence emission property with high quantum yield. But fluorescent semiconductor quantum dot has high toxicity which creates its limitation in the vivo and vitro studies in biology. Therefore there is need of alternative fluorescent quantum dot material which has low toxicity. Zero dimensional graphene quantum dots are the alternative carbon based material due to its high fluorescence intensity, high solubility in water, high resistance to photo bleaching, chemical inertness and low toxicity and superior biocompatibility which open up a great application in the biological imaging and sensing. The synthesis method of CQD can be well categorized into the top-down and bottom-up fabrication method. Among them top-down fabrication method is much easier to synthesis the CQD because the size of CQD can be controlled very easily by this method and we can get the uniform size distribution of CQDs. The size of the CQD is one of the important characteristic parameter because size can

change the band gap of the CQD which is responsible for its optical properties. CQD can be synthesized by chemical synthesis, a bottom up fabrication method where specific organic materials are used and specific experimental conditions are maintained⁹. Carbon quantum dots have also application in optoelectronics, catalysis and sensor due to its chemiluminescence and electrochemical luminescence properties. The synthesis method of CQDs is also simple. Several methods^{4, 57, 76-77} has been used to synthesis the carbon quantum dots for example carbon quantum dots can be synthesized from the pyrolysis of mixture citric acid and ethylene diamine tetra acetic acid salts, the hydrothermal synthesis from grass and graphene sheets etc. Highly sensitive and selective determination of hydrogen peroxide (H_2O_2) is important and fluorometric method is one of the important determination method of H_2O_2 sensing due to its high sensitivity with high reproducibility.

3.2. Synthesis method of CQDs

Formic acid ($HCOOH$) was used as a precursor for microwave assisted synthesis of carbon quantum dots (CQDs). In a typical synthesis procedure, 30 ml of formic acid was heated by a microwave synthesizer at $90^{\circ}C$ for 3 hours. Then, the resulting solution was vacuum evaporated several times in a rotary evaporator at $120^{\circ}C$ to produce CQDs.

3.3. Characterization of CQDs

3.3.1. Characterization of CQDs by AFM

The AFM measurements of CQDs were done to measure the size and thickness of CQDs. The AFM samples were prepared by drop casting method from the aqueous solution of CQDs on AFM mica disc. The AFM mica disk was cleaned by mild sonication with different solvents such

as water, isopropyl alcohol and acetone. The aqueous solution of CQDs was drop casted on the cleaned mica disk and then evaporates the solution in air. The stock solution of CQDs was diluted 200 times before being used for AFM sample preparation. Figure 3.37 (a and b) represent the AFM images of CQDs where carbon quantum dots are uniformly distributed all over the mica foil. The topographic height along the line AB in Figure 3.37 (a) and along the line CD in Figure 3.37 (b) is shown in Figure 3.37 (c and d) respectively. They are in the range between 0.3 and 2.0 nm and their average height is about 1.0 nm.

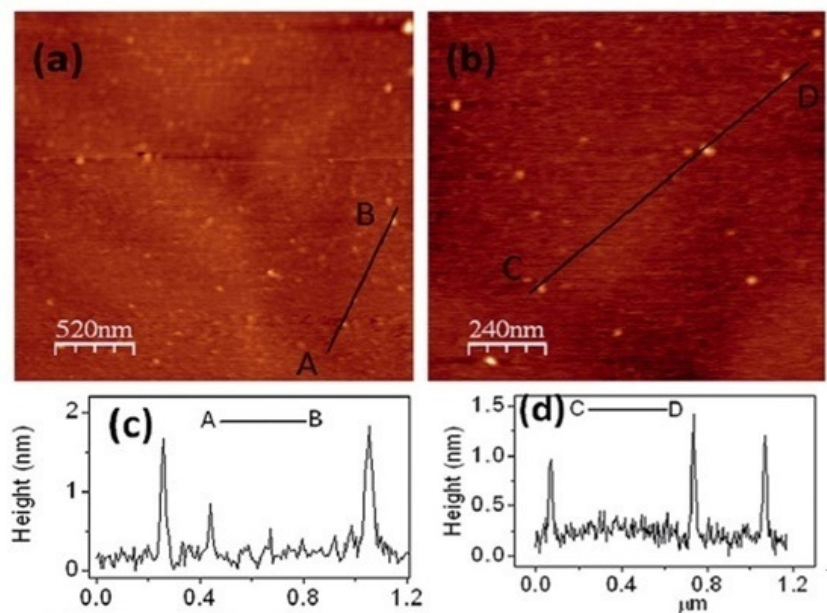


Figure 3.37. (a, b) AFM images of CQDs. (c, d) are the AFM line profile along the line AB and CD on the images of (a) and (b) respectively.

3.3.2. Characterization of CQDs by TEM

The TEM analysis was done to know the size of the CQDs synthesized from formica acid by microwave mediated method. The TEM samples were prepared by drop casting method from the

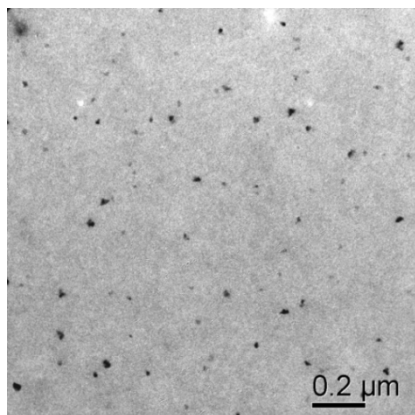


Figure 3.38. TEM image of CQDs.

aqueous solution of CQDs on TEM grid, and then evaporate the solution in air. A TEM image of CQDs is shown in Figure 3.38 where the CQDs are well distributed all over the grid with their size varies ranging from 2–18 nm. Graphite nanoparticles shown in Figure 3.39 (a) are produced when the stock solution was diluted 100 times with water before being used for TEM sample preparation. The graphite nanoparticles are also well distributed all over the TEM grid. The

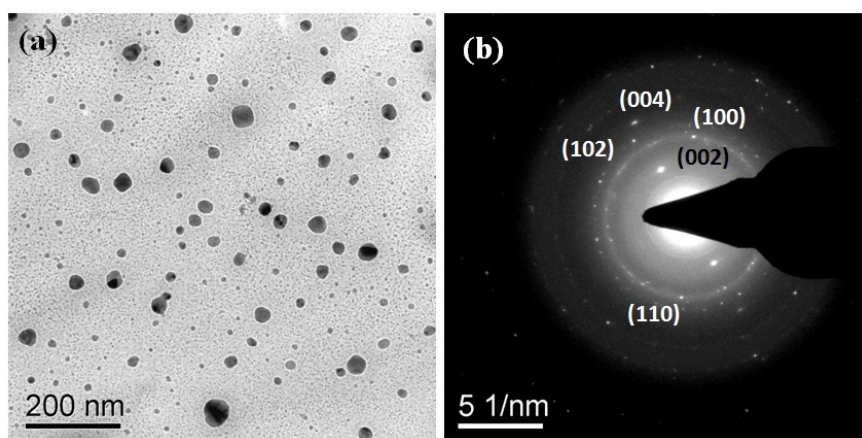


Figure 3.39. (a) TEM image and (b) SAED pattern of graphite nanoparticles.

SAED pattern of the graphite nanoparticles are shown in Figure 3.39 (b). The calculated interplanar distances are 3.2, 2.12, 1.80, 1.62, 1.23 Å calculated from SAED image correspond to the (002), (100), (102), (004) and (110) planes respectively of hexagonal graphite (PDF-00-041-1487). CQDs were aggregated and thereby graphite nanoparticles were formed.

3.3.3. Characterization of CQDs by UV-Visible Spectroscopy

Study of optical properties of CQDs is important on the view of biological and electrical applications. UV-visible spectroscopy is one of the important optical properties. Figure 3.40 displays the UV-visible spectrum of CQDs in aqueous solution. The absorption peak due to π to π^* transition for aromatic sp^2 domain appeared at ~ 230 nm^{4, 28, 57, 76-77}. In addition, an absorption peak centered at 276 nm was also observed in the UV-visible spectrum of CQDs.

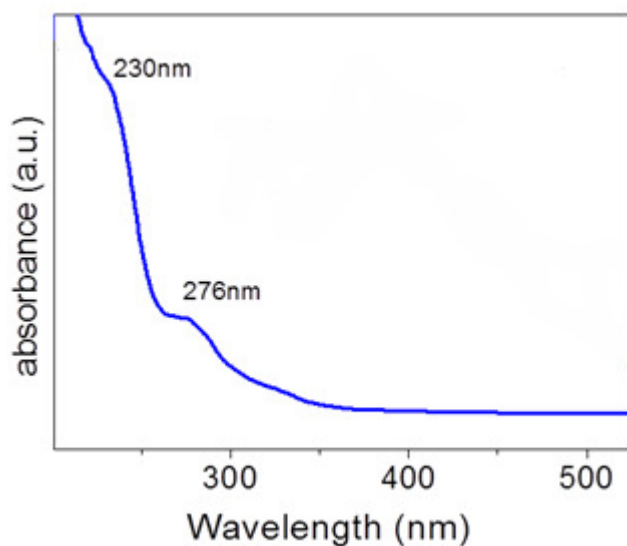


Figure 3.40. UV-visible spectrum of CQDs dissolved in water.

3.3.4. Characterization of CQDs by Fluorescence Spectroscopy

In the fluorescence emission spectrum the two emission peaks at 309 and 375 nm appeared when CQDs are excited at 276 nm shown in Figure 3.41. Several groups suggested^{4, 10, 28, 57, 76-77} that the presence of conjugated structure, zigzag sites in graphene and emission trap on the surface is responsible for the fluorescence emission of CQDs. The fluorescence excitation spectrum of CQDs for 375 nm emission is shown in Figure 3.42. The fluorescence excitation spectrum exhibits three peaks at 230, 276 and 309 nm. Therefore, if the CQDs are excited at 230, 276 and 309 nm, strong fluorescence emissions are observed. The peaks at 230 and 276 nm in fluorescence excitation spectrum correspond to the 230 and 276 nm absorption peaks respectively which is shown in Figure 3.40. The fluorescence excitation spectrum clearly suggests that the observed fluorescence emissions from CQDs may be directly correlated with the three new transitions at 230, 276 and 309 nm rather than commonly observed $\pi \rightarrow \pi^*$ transition. According to Radovic and Bockrath⁷⁸, the carbene-like, with triplet ground state in zigzag sites whereas carbyne like, with singlet ground state in armchair sites are most common in graphene. The electronic configuration for triplet ground state of carbene can be described as $\sigma^1 \pi^1$ and singlet carbene two non bonding electrons are paired in either σ or π orbital, leaving one orbital vacant. The carbene ground state spin multiplicity is related to energy difference (δE) between σ and π orbital; δE should be below 1.5 eV for carbene triplet ground state. In fluorescence excitation spectrum, the two electronic transitions at 230 nm (5.39 eV) and 276 nm (4.49 eV) can be described as a transition from the σ and π orbital (highest occupied molecular orbital, HOMO) to the lowest unoccupied molecular orbital (LUMO). The energy difference, δE was found to be 0.9 eV which is lower than the required value (<1.5 eV) for triplet state. This suggests that assignment of these two transitions is quite reasonable. The third transition at 310

nm in fluorescence excitation spectrum may possibly be related to surface states. The schematic description of the different energy which is responsible for emissions is shown in Scheme 3.1. Apart from this, the fluorescence emission of CQDs was found to be dependent on the excitation wavelengths. When CQDs are excited at the different wavelength ranging from 200 to 650 nm, both emission peaks are shifted from 310 to 820 nm and fluorescence intensity

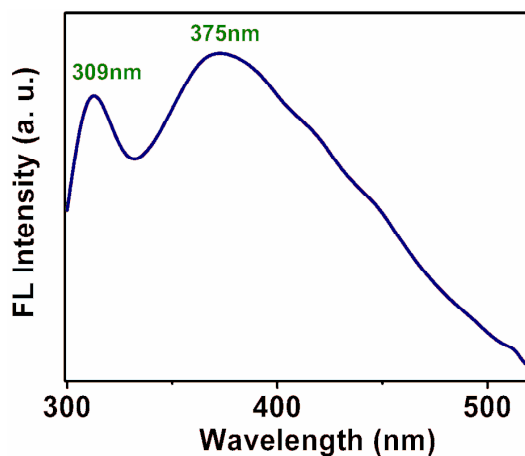


Figure 3.41. Fluorescence emission spectrum of CQDs dissolved in water where excitation wavelength is 276 nm.

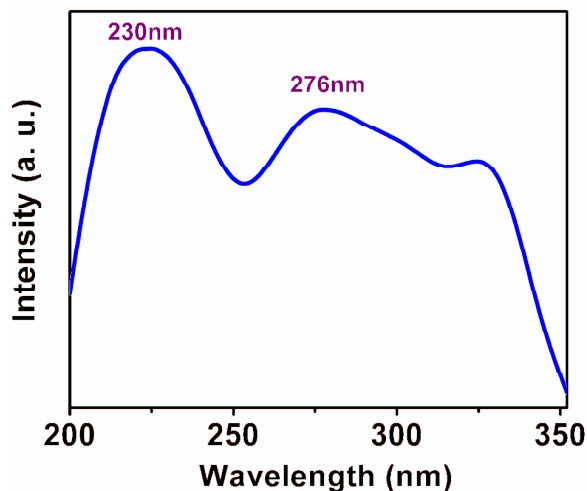
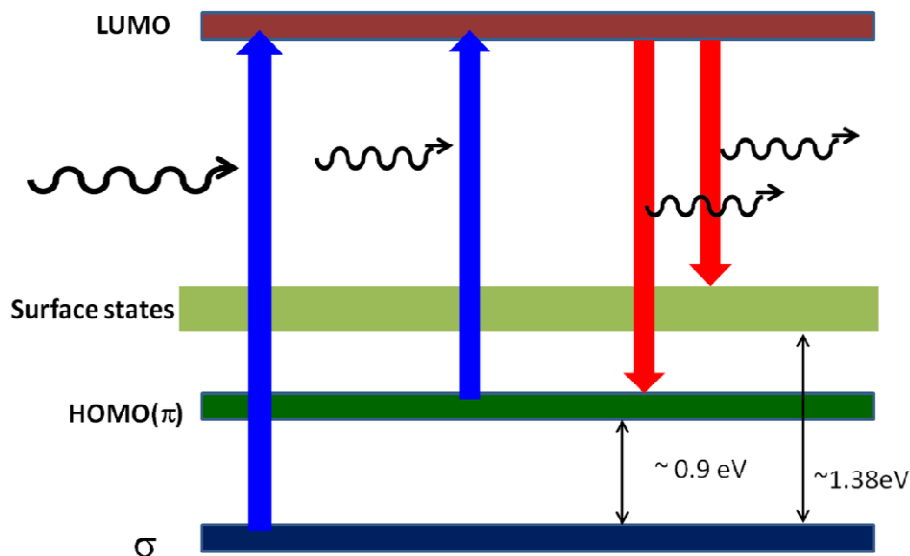


Figure 3.42. Fluorescence excitation spectrum of CQDs dissolved in water where emission wavelength was kept at 375 nm.



Scheme 3.1. Schematic diagram for electronic transitions of CQDs during fluorescence emission.

gradually decreases with increase in excitation wavelength from 310 to 650 nm (Figure 3.43 and 3.44). The excitation wavelength dependent emission of graphene quantum dots^{4, 28, 57, 76-77}, carbon nitride quantum dots⁷⁹, carbon dots⁸⁰ are reported in literature. This is the first report to our knowledge that these CQDs exhibit deep ultraviolet, visible as well as near infrared (NIR) fluorescence emission. However, there is a recent report of deep ultra violet emission¹⁰ of small sized graphene quantum dots. These CQDs owing to their NIR emission may find biological optical imaging and detection applications because of low tissue absorption and scattering effect in the NIR wavelength range (650–900 nm)⁸¹. In addition to excitation dependent emission property of CQDs its emission is strongly sensitive to the different solvents, as shown in Figure 3.45. It shows that the variation of emission peak positions of CQDs with variation of solvents. The emission peak positions for methanol is 315 nm, for water it is 311 and 375 nm, for

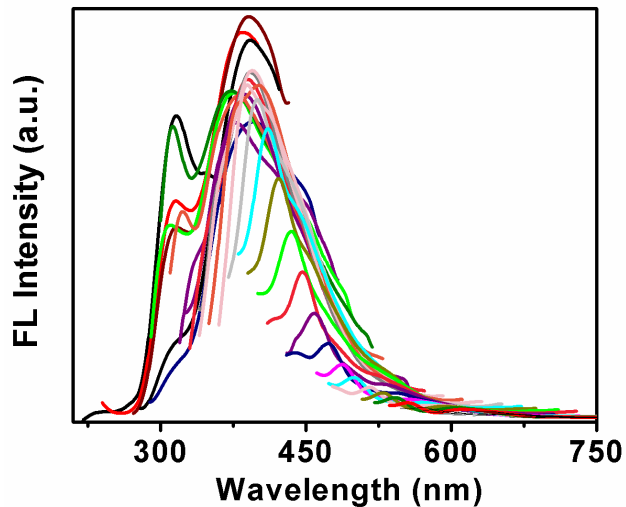


Figure 3.43. Fluorescence spectra of CQDs in water at different excitation wavelengths ranging from 200 to 650 nm.

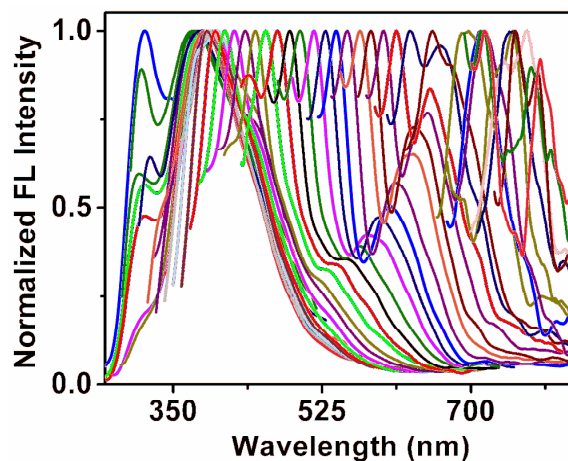


Figure 3.44. Normalized FL spectra of CQDs in water at different excitation wavelengths ranging from 200 to 650 nm.

cyclohexane it is 330 and 389 nm, for benzene it is 339 and 404 nm and for THF solvent it is 355 and 405 nm. The excitation dependent emission spectra of CQDs in other solvents are also observed. The excitation dependent emission spectra of CQDs in methanol, cyclohexane and

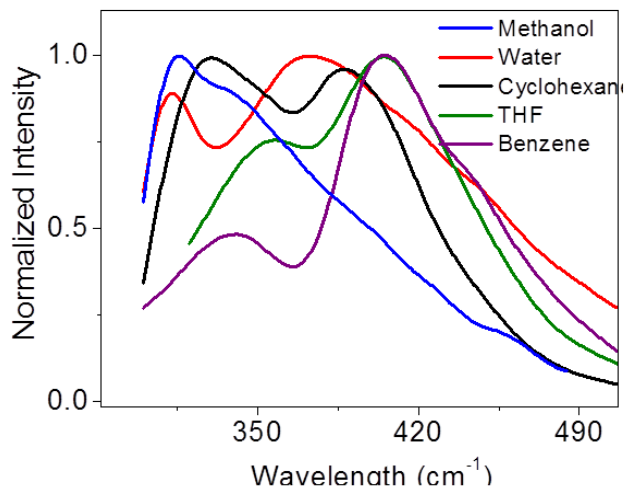


Figure 3.45. FL spectra of CQDs in different solvents where excitation wavelength is 320 nm.

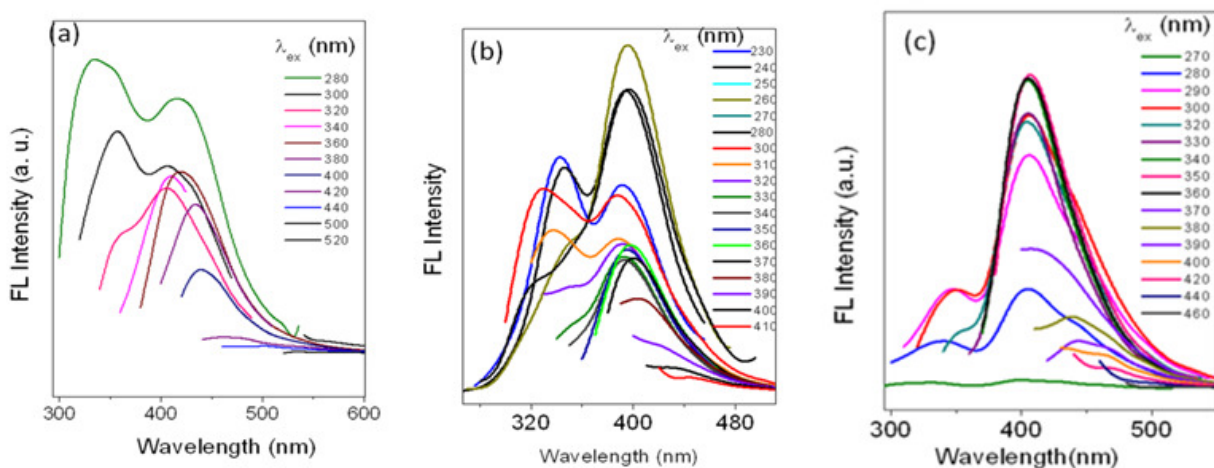


Figure 3.46. Fluorescence spectra of CQDs at different excitation wavelengths in (a) methanol, (b) cyclohexane and (c) benzene.

benzene are shown in Figure 3.46. It shows that CQDs in methanol solvent shows strong emission mainly in UV region while CQDs in cyclohexane and benzene solvent produce primarily blue emission. Fluorescence intensity of CQDs in aqueous medium is sensitive to the

pH of the medium. Figure 3.47 shows the fluorescence intensity is lowest in acidic pH and highest in basic medium. The possible explanation of quenching of fluorescence of CQDs in acidic medium is probably due to the protonation of zigzag sites of graphene in acidic medium to form a non-fluorescent complex.

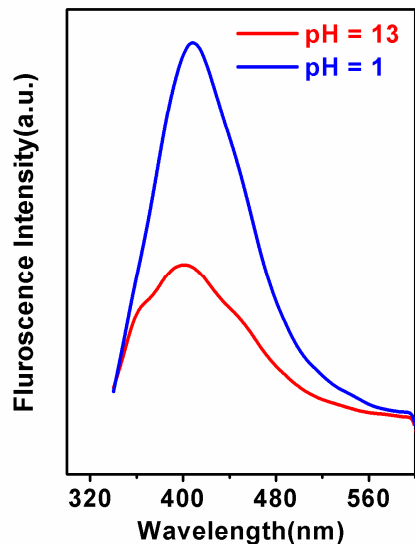


Figure 3.47. Fluorescence spectra of CQDs in water at different pHs where excitation wavelength was kept at 320 nm.

3.3.5. Characterization CQDs by FT-IR spectroscopy

Solid state FT-IR spectra of CQDs have done and shown in Figure 3.48 where KBr pallet has been used a reference. The intense band at $\sim 1600\text{ cm}^{-1}$ corresponds to aromatic C=C stretch whereas bands at 1088 cm^{-1} can be assigned to C–O stretch⁸²⁻⁸³. The O–H deformation peak appeared at 1380 cm^{-1} . The two peaks at 2925 cm^{-1} and 2854 cm^{-1} correspond to an asymmetric and symmetric stretch of CH_2 group whereas the broad band at 3420 cm^{-1} can be attributed to O–H stretch.

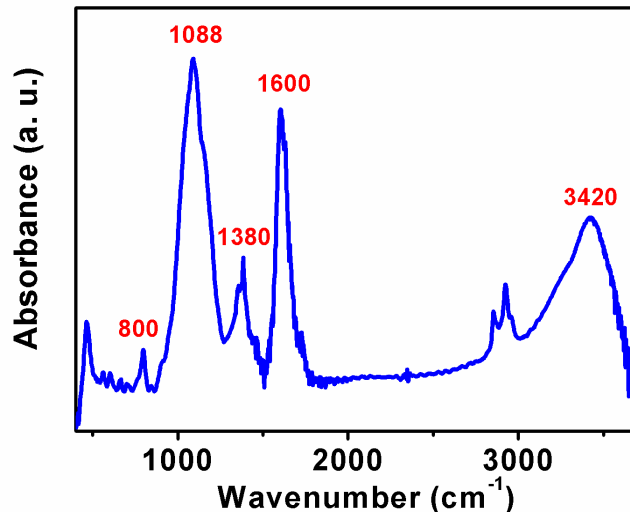


Figure 3.48. FT-IR spectrum of CQDs.

A peak at 800 cm^{-1} can be assigned to the C–H out of plane bending vibration and the low intense peaks between 580 cm^{-1} to 800 cm^{-1} can be attributed to the vibration of the C–H bonds in benzene rings⁸²⁻⁸³.

3.4. Properties of CQDs

3.4.1. Quantum yield measurement of CQDs

The fluorescence quantum yield (QY) of CQDs in water at the excitation wavelength of 280 nm was found to be 4.5% using quinine sulfate as a reference. The QY of CQDs is also sensitive to different solvents and follows the trend such as in methanol solvent it is 1.1%, in water it is 4.5%, in cyclohexane it is 12%, in THF it is 14%, in benzene it is 17%. The QYs of CQDs is close to the reported values of carbon dots and graphene quantum dots^{4, 10, 28, 57, 76-77}.

3.4.2. Average life time measurement of CQDs

The fluorescence decay profile of CQDs in different solvent is presented in Figure 3.49, which followed a tri-exponential behavior indicating the presence of three emitting species with three

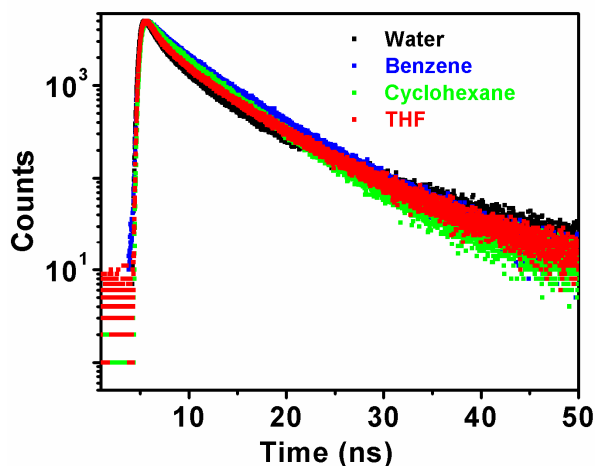


Figure 3.49. Fluorescence decay curves of CQDs in water, cyclohexane, THF and benzene solvents.

Table 3.7. Fluorescence decay time (τ) and its corresponding pre-exponential factor (A) of CQDs in different solvents

Solvent	$\tau_1(A_1)$	$\tau_2(A_2)$	$\tau_3(A_3)$	τ_{avg}	χ^2
Water	0.6612(0.5155)	3.435(0.3827)	11.25(0.1018)	6.293	1.016
THF	0.8046(0.5217)	4.1597(0.3478)	9.1295(0.1305)	5.6354	1.057
Benzene	0.6364(0.2594)	3.513(0.3705)	7.368(0.3701)	5.90	1.016
Cyclohexane	0.7204(0.3334)	4.6727(0.619)	10.74(0.0476)	5.263	1.081

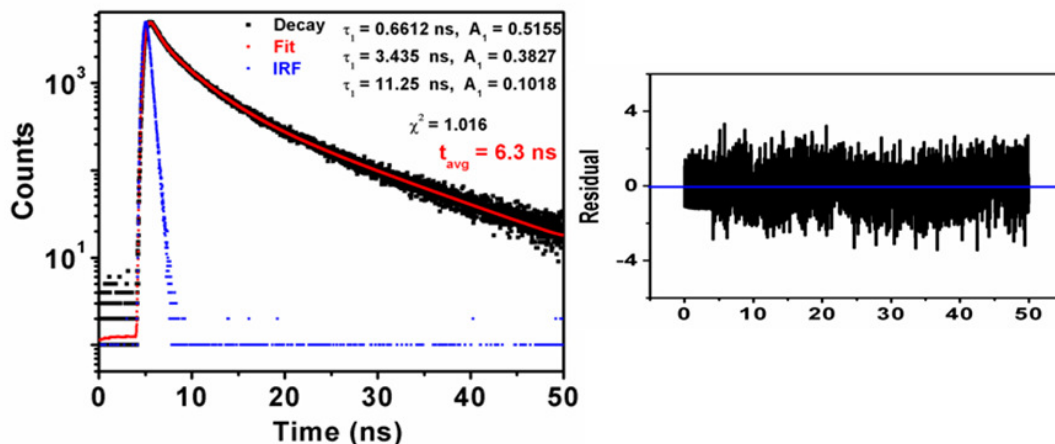


Figure 3.50. (a) Fluorescence decay profile of CQDs in water and its fitting curve and instrument response function (IRF) plot (excitation wavelength is 330 nm and emission wavelength is 400 nm) (b) Residual plot after fitting the fluorescence decay profile of CQDs in water.

different lifetimes. Fluorescence decay time (τ) and its corresponding pre-exponential factor (A) of CQDs in different solvents are listed in Table 3.7. Figure 3.50 represents the fluorescence decay profile of CQDs in water solvent with its fitting curve, the residual plot after fitting also shown in this figure. From Figure 3.50, 3.51 and Table 3.7 it can be concluded that the average lifetime (τ_{avg}) of CQDs is independent of solvents. The average lifetime (τ_{avg}) of CQDs is close to the reported values of carbon dots and graphene quantum dots^{4, 10, 28, 57, 76-77}. The average lifetime of CQDs in water is ~ 6.0 ns indicating that the synthesized CQDs are suitable for biological as well as optoelectronic applications.

3.5. Application of CQDs as H_2O_2 sensor by Fluorescence spectroscopy

Large amount of hydrogen peroxide (H_2O_2) is produced by human tumor cells. Similarly H_2O_2 is produced from different biological processes. Therefore it is important to determine the

concentration of H_2O_2 . Fluorescence spectroscopy technique has been used here for detection of H_2O_2 . The decrease of fluorescence emission intensity of CQDs with the addition hydrogen peroxide is shown in Figure 3.51 (a). With increasing the concentration of H_2O_2 the fluorescence emission intensity of CQDs gradually decreases. Figure 3.51 (b) is the calibration plot of the

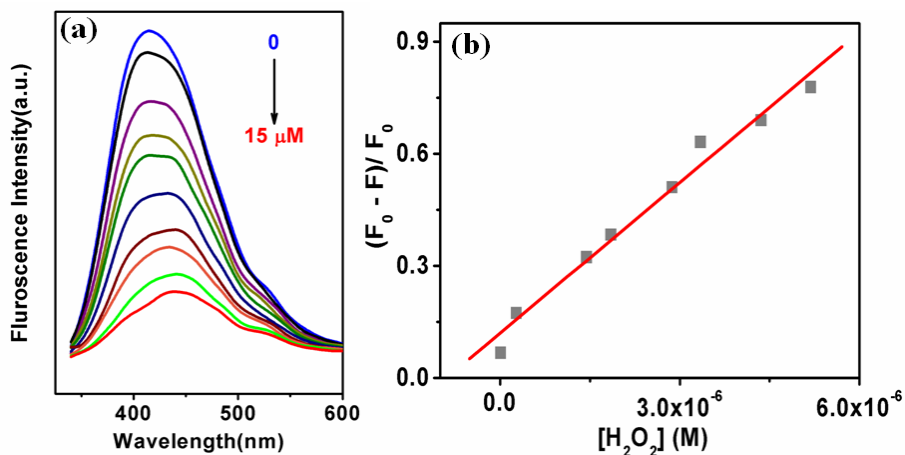


Figure 3.51. (a) The variation of fluorescence intensity of CQDs in water in presence of different concentration of H_2O_2 where excitation wavelength was kept at 320 nm. (b) Fluorescence quenching plot of CQDs by H_2O_2 in water.

fluorescence quenching of CQDs by the H_2O_2 which is linear over the range from 10 nM to 5 mM. The detection limit of H_2O_2 , calculated from the Figure 3.51 (b) was ~ 700 nM. Thus, CQDs can be used as fluorescence probe for selective and sensitive determination of H_2O_2 due to quenching of their fluorescence. The fluorescence response of CQDs in presence of hydrogen peroxide and different ions suggested that the emission of CQDs is only sensitive towards hydrogen peroxide (Figure 3.52). No significant spectral change of CQDs was observed in the presence of different ions such as Hg^{2+} , Pb^{2+} , Cu^{2+} , Zn^{2+} , Ni^{2+} , ClO^- and glucose.

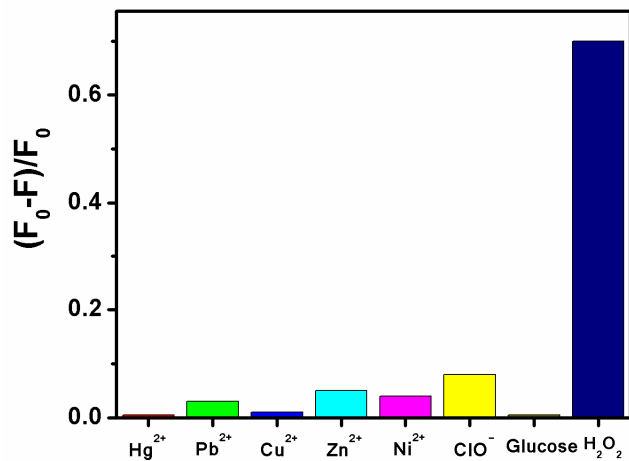


Figure 3.52. Comparison of fluorescence intensity quenching of CQDs by H₂O₂ and different metal ions and anions.

3.6. Conclusion

We have successfully synthesized fluorescent carbon quantum dots (CQDs) at low temperature from formic acid by microwave synthesizer. The fluorescence emission spectra of CQDs in water can be tuned by changing the excitation wavelength. These CQDs exhibit deep ultra violet, visible and near infrared fluorescence emission in its aqueous solution, therefore it can be used in biological optical imaging application. The CQDs can be used as a fluorescence sensor of H₂O₂ in water with detection limit of ~700 nM.

Chapter References

1. Geim, A. K.; Novoselov, K. S., *Nat Mater* **2007**, *6*, 183-191.
2. Geim, A. K., *Science* **2009**, *324*, 1530-1534.
3. Schnez, S.; Molitor, F.; Stampfer, C.; Güttinger, J.; Shorubalko, I.; Ihn, T.; Ensslin, K., *Appl. Phys. Lett.* **2009**, *94*, 012107.
4. Pan, D.; Zhang, J.; Li, Z.; Wu, M., *Adv. Mater.* **2010**, *22*, 734-738.

5. Liu, R.; Wu, D.; Feng, X.; Müllen, K., *J. Am. Chem. Soc.* **2011**, *133*, 15221-15223.
6. Li, Y.; Hu, Y.; Zhao, Y.; Shi, G.; Deng, L.; Hou, Y.; Qu, L., *Adv. Mater.* **2011**, *23*, 776-780.
7. Tian, R.; Zhong, S.; Wu, J.; Jiang, W.; Shen, Y.; Jiang, W.; Wang, T., *Opt. Mater.* **2016**, *60*, 204-208.
8. Lu, J.; Yeo, P. S. E.; Gan, C. K.; Wu, P.; Loh, K. P., *Nat Nano* **2011**, *6*, 247-252.
9. Yan, X.; Cui, X.; Li, L.-s., *J. Am. Chem. Soc.* **2010**, *132*, 5944-5945.
10. Tang, L.; Ji, R.; Cao, X.; Lin, J.; Jiang, H.; Li, X.; Teng, K. S.; Luk, C. M.; Zeng, S.; Hao, J.; Lau, S. P., *ACS Nano* **2012**, *6*, 5102-5110.
11. Shen, J.; Zhu, Y.; Yang, X.; Zong, J.; Zhang, J.; Li, C., *New J. Chem.* **2012**, *36*, 97-101.
12. Shen, J.; Zhu, Y.; Chen, C.; Yang, X.; Li, C., *Chem. Commun.* **2011**, *47*, 2580-2582.
13. Liu, W.-W.; Feng, Y.-Q.; Yan, X.-B.; Chen, J.-T.; Xue, Q.-J., *Adv. Func. Mater.* **2013**, *23*, 4111-4122.
14. Ruiyi, L.; Yuanyuan, J.; Xiaoyan, Z.; Zaijun, L.; Zhiguo, G.; Guangli, W.; Junkang, L., *Electrochimica Acta* **2015**, *178*, 303-311.
15. Gao, P.; Ding, K.; Wang, Y.; Ruan, K.; Diao, S.; Zhang, Q.; Sun, B.; Jie, J., *J. Phys. Chem. C* **2014**, *118*, 5164-5171.
16. Peng, J.; Gao, W.; Gupta, B. K.; Liu, Z.; Romero-Aburto, R.; Ge, L.; Song, L.; Alemany, L. B.; Zhan, X.; Gao, G.; Vithayathil, S. A.; Kaiparettu, B. A.; Marti, A. A.; Hayashi, T.; Zhu, J.-J.; Ajayan, P. M., *Nano Lett.* **2012**, *12*, 844-849.
17. Liu, A. Y.; Cohen, M. L., *Science* **1989**, *245*, 841-842.
18. Teter, D. M.; Hemley, R. J., *Science* **1996**, *271*, 53-55.
19. Liu, A. Y.; Wentzcovitch, R. M., *Phys. Rev. B* **1994**, *50*, 10362-10365.

20. Yu, K. M.; Cohen, M. L.; Haller, E. E.; Hansen, W. L.; Liu, A. Y.; Wu, I. C., *Phys. Rev. B* **1994**, *49*, 5034-5037.
21. Niu, C.; Lu, Y. Z.; Lieber, C. M., *Science* **1993**, *261*, 334-337.
22. Hoffman, A.; Gouzman, I.; Brener, R., *Appl. Phys. Lett.* **1994**, *64*, 845-847.
23. Riascos, H.; Neidhardt, J.; Radnóczy, G. Z.; Emmerlich, J.; Zambrano, G.; Hultman, L.; Prieto, P., *Thin Solid Films* **2006**, *497*, 1-6.
24. Wang, Y.; Wang, X.; Antonietti, M.; Zhang, Y., *ChemSusChem* **2010**, *3*, 435-439.
25. Yang, J.; Wu, X.; Li, X.; Liu, Y.; Gao, M.; Liu, X.; Kong, L.; Yang, S., *Applied Physics A* **2011**, *105*, 161-166.
26. Jie, L.; Chuanbao, C.; Hesun, Z., *Nanotechnology* **2007**, *18*, 115605.
27. Montigaud, H.; Tanguy, B.; Demazeau, G.; Alves, I.; Courjault, S., *J. Mater. Sci.* **2000**, *35*, 2547-2552.
28. Liu, S.; Tian, J.; Wang, L.; Luo, Y.; Zhai, J.; Sun, X., *J. Mater. Chem.* **2011**, *21*, 11726-11729.
29. Zimmerman, J. L.; Williams, R.; Khabashesku, V. N.; Margrave, J. L., *Nano Lett.* **2001**, *1*, 731-734.
30. Wood, J. M.; Kennedy, F. S.; Rosen, C. G., *Nature* **1968**, *220*, 173-174.
31. Wu, D.; Huang, W.; Duan, C.; Lin, Z.; Meng, Q., *Inorg. Chem.* **2007**, *46*, 1538-1540.
32. Ros-Lis, J. V.; Marcos, M. D.; Martínez-Mañez, R.; Rurack, K.; Soto, J., *Angew. Chem. Int. Ed.* **2005**, *44*, 4405-4407.
33. Yang, J.; Wu, X.; Li, X.; Liu, Y.; Gao, M.; Liu, X.; Kong, L.; Yang, S., *Appl. Phys. A* **2011**, *105*, 161-166.
34. Huang, C.-C.; Chang, H.-T., *Anal. Chem.* **2006**, *78*, 8332-8338.

35. Dai, G.; Levy, O.; Carrasco, N., *Nature* **1996**, *379*, 458-460.
36. Yokota, K.; Fukushi, K.; Takeda, S.; Wakida, S.-I., *J. Chromatogr. A* **2004**, *1035*, 145-150.
37. Lee, D. Y.; Singh, N.; Kim, M. J.; Jang, D. O., *Org. Lett.* **2011**, *13*, 3024-3027.
38. Larous, S.; Meniai, A. H.; Lehocine, M. B., *Desalination* **2005**, *185*, 483-490.
39. Aydın, H.; Bulut, Y.; Yerlikaya, Ç., *J. Environ. Manage.* **2008**, *87*, 37-45.
40. Goel, J.; Kadirvelu, K.; Rajagopal, C.; Garg, V. K., *Ind. Eng. Chem. Res.* **2006**, *45*, 6531-6537.
41. Darwish, I. A.; Blake, D. A., *Anal. Chem.* **2001**, *73*, 1889-1895.
42. El Mouzdahir, Y.; Elmchaouri, A.; Mahboub, R.; ElAnssari, A.; Gil, A.; Korili, S. A.; Vicente, M. A., *Appl. Clay Sci.* **2007**, *35*, 47-58.
43. Pan, B.; Pan, B.; Zhang, W.; Lv, L.; Zhang, Q.; Zheng, S., *Chem. Eng. J.* **2009**, *151*, 19-29.
44. Chen, C.; Yang, X.; Wei, J.; Tan, X.; Wang, X., *J. Colloid Interface Sci.* **2013**, *393*, 249-256.
45. Ekmekyapar, F.; Aslan, A.; Bayhan, Y. K.; Cakici, A., *J. Hazard. Mater.* **2006**, *137*, 293-298.
46. Thomas, A.; Fischer, A.; Goettmann, F.; Antonietti, M.; Muller, J.-O.; Schlogl, R.; Carlsson, J. M., *J. Mater. Chem.* **2008**, *18*, 4893-4908.
47. Matsumoto, S.; Xie, E. Q.; Izumi, F., *Diamond Relat. Mater.* **1999**, *8*, 1175-1182.
48. Khabashesku, V. N.; Zimmerman, J. L.; Margrave, J. L., *Chem. Mater.* **2000**, *12*, 3264-3270.

49. Zhu, S.; Zhang, J.; Qiao, C.; Tang, S.; Li, Y.; Yuan, W.; Li, B.; Tian, L.; Liu, F.; Hu, R.; Gao, H.; Wei, H.; Zhang, H.; Sun, H.; Yang, B., *Chem. Commun.* **2011**, *47*, 6858-6860.
50. Zhao, Y.; Liu, Z.; Chu, W.; Song, L.; Zhang, Z.; Yu, D.; Tian, Y.; Xie, S.; Sun, L., *Adv. Mater.* **2008**, *20*, 1777-1781.
51. Xingbin, Y.; Tao, X.; Gang, C.; Shengrong, Y.; Huiwen, L.; Qunji, X., *J. Phys. D: Appl. Phys.* **2004**, *37*, 907.
52. Thomé, T.; Colaux, J. L.; Louette, P.; Terwagne, G., *J. Electron. Spectrosc. Relat. Phenom.* **2006**, *151*, 19-23.
53. Arrigo, R.; Havecker, M.; Schlogl, R.; Su, D. S., *Chem. Commun.* **2008**, 4891-4893.
54. Shao, Y.; Zhang, S.; Engelhard, M. H.; Li, G.; Shao, G.; Wang, Y.; Liu, J.; Aksay, I. A.; Lin, Y., *J. Mater. Chem.* **2010**, *20*, 7491-7496.
55. Yu, D. L.; Xiao, F. R.; Wang, T. S.; Tian, Y. J.; He, J. L.; Li, D. C.; Wang, W. K., *J. Mater. Sci. Lett.* **2000**, *19*, 553-556.
56. Zhang, Z.; Leinenweber, K.; Bauer, M.; Garvie, L. A. J.; McMillan, P. F.; Wolf, G. H., *J. Am. Chem. Soc.* **2001**, *123*, 7788-7796.
57. Pan, D.; Zhang, J.; Li, Z.; Wu, C.; Yan, X.; Wu, M., *Chem. Commun.* **2010**, *46*, 3681-3683.
58. Candini, A.; Klyatskaya, S.; Ruben, M.; Wernsdorfer, W.; Affronte, M., *Nano Lett.* **2011**, *11*, 2634-2639.
59. Gao, D.; Xu, Q.; Zhang, J.; Yang, Z.; Si, M.; Yan, Z.; Xue, D., *Nanoscale* **2014**, *6*, 2577-2581.
60. Xu, K.; Li, X.; Chen, P.; Zhou, D.; Wu, C.; Guo, Y.; Zhang, L.; Zhao, J.; Wu, X.; Xie, Y., *Chem. Sci.* **2015**, *6*, 283-287.

61. Gao, D.; Liu, Y.; Song, M.; Shi, S.; Si, M.; Xue, D., *J. Mater. Chem. C* **2015**, *3*, 12230-12235.
62. Avinash, M. B.; Subrahmanyam, K. S.; Sundarayya, Y.; Govindaraju, T., *Nanoscale* **2010**, *2*, 1762-1766.
63. Liu, S.; Tian, J.; Wang, L.; Luo, Y.; Sun, X., *RSC Adv.* **2012**, *2*, 411-413.
64. Enoki, T.; Takai, K., *Solid State Commun.* **2009**, *149*, 1144-1150.
65. Li, X.; Zhou, J.; Wang, Q.; Kawazoe, Y.; Jena, P., *J. Phys. Chem. Lett.* **2013**, *4*, 259-263.
66. Qiu, H.; Wang, Z.; Sheng, X., *Physica B* **2013**, *421*, 46-49.
67. Du, A.; Sanvito, S.; Smith, S. C., *Phys. Rev. Lett.* **2012**, *108*, 197207.
68. Lu, L.; Helgeson, R.; Jones, R. M.; McBranch, D.; Whitten, D., *J. Am. Chem. Soc.* **2002**, *124*, 483-488.
69. Fan, C.; Wang, S.; Hong, J. W.; Bazan, G. C.; Plaxco, K. W.; Heeger, A. J., *Proc. Natl. Acad. Sci.* **2003**, *100*, 6297-6301.
70. Lee, S. J.; Seo, Y.-C.; Jurng, J.; Lee, T. G., *Atmos. Environ.* **2004**, *38*, 4887-4893.
71. Hutson, N. D.; Attwood, B. C.; Scheckel, K. G., *Environ. Sci. Technol.* **2007**, *41*, 1747-1752.
72. Langmuir, I., *J. Am. Chem. Soc.* **1918**, *40*, 1361-1403.
73. Ali, S. A.; Kazi, I. W.; Ullah, N., *Ind. Eng. Chem. Res.* **2015**, *54*, 9689-9698.
74. Wang, Y.; Ye, G.; Chen, H.; Hu, X.; Niu, Z.; Ma, S., *J. Mater. Chem. A* **2015**, *3*, 15292-15298.
75. Vuković, G. D.; Marinković, A. D.; Čolić, M.; Ristić, M. Đ.; Aleksić, R.; Perić-Grujić, A. A.; Uskoković, P. S., *Chem. Eng. J.* **2010**, *157*, 238-248.

76. Krysmann, M. J.; Kellarakis, A.; Dallas, P.; Giannelis, E. P., *J. Am. Chem. Soc.* **2012**, *134*, 747-750.
77. Liu, S.; Tian, J.; Wang, L.; Zhang, Y.; Qin, X.; Luo, Y.; Asiri, A. M.; Al-Youbi, A. O.; Sun, X., *Adv. Mater.* **2012**, *24*, 2037-2041.
78. Radovic, L. R.; Bockrath, B., *J. Am. Chem. Soc.* **2005**, *127*, 5917-5927.
79. Barman, S.; Sadhukhan, M., *J. Mater. Chem.* **2012**, *22*, 21832-21837.
80. Lai, C.-W.; Hsiao, Y.-H.; Peng, Y.-K.; Chou, P.-T., *J. Mater. Chem.* **2012**, *22*, 14403-14409.
81. Klostranec, J. M.; Chan, W. C. W., *Adv. Mater.* **2006**, *18*, 1953-1964.
82. Tsai, C.-W.; Tu, M.-H.; Chen, C.-J.; Hung, T.-F.; Liu, R.-S.; Liu, W.-R.; Lo, M.-Y.; Peng, Y.-M.; Zhang, L.; Zhang, J.; Shy, D.-S.; Xing, X.-K., *RSC Adv.* **2011**, *1*, 1349-1357.
83. Kumar, N. A.; Choi, H.-J.; Shin, Y. R.; Chang, D. W.; Dai, L.; Baek, J.-B., *ACS Nano* **2012**, *6*, 1715-1723.

Chapter 4

Bottom up Fabrication of two-dimensional Carbon nitride, Graphene sheets and their applications

4.1. Introduction

Now days the two-dimensional (2D) carbon materials have attracted a great attention in both fundamental and applied scientific research for their potential applications¹⁻⁴ in electronics, sensing, catalysis and energy storage. Beside carbon materials the other 2D materials, such as boron nitride (BN), molybdenum disulfide (MoS₂), tungsten sulfide (WS₂), etc., have received great interest to synthesize them for their potential applications in materials science. 2D nanomaterials have two dimensions with size of nanometer range. 2D nanomaterials with single or few layers have different characteristic properties from its low dimension and its bulk material. To get single or few layers 2D materials is a challenging task. The successful isolation of 2D nanosheets of WS₂, MoS₂ and BN was reported recently⁵⁻⁷. Although several methods¹⁻⁴ are available for the production of single or few layered 2D materials, the bottom-up fabrication of layered materials from their fundamental building blocks (such as atoms, molecules, quantum dots, etc.) is very rare⁸. The bottom up fabrication method is one of the most important method to synthesis the 2D carbon materials. Thermal decomposition, thermal cutting, combustion and microwave heating are used in the bottom up fabrication method. Andrew Geim *et al.*¹ first discovered the single plane layer of honeycomb network of sp² hybridized carbon atoms i.e. graphene which is also a 2D carbon material. After this discovery it has attracted enormous amount of interest from the scientific community due to its unique optical, thermal and electrical

properties⁹⁻¹⁴. The interesting properties of graphene reported in the literature are ballistic electron transport property, integer and fractional quantum hall effect, extremely high carrier mobility and high ability to sustain very high current densities. Thus, it is considered as a next-generation material for nanoelectronics, spintronics, sensors, energy storage. However, the synthesis of large-area graphene on different substrate is hindering its applications. Several methods^{1, 9-19} such as mechanical exfoliation of graphite, chemical exfoliation, synthesis from solid carbon sources, chemical vapor deposition (CVD) of hydrocarbons on metal substrates, sublimation of silicon from silicon carbide wafers etc. are available to synthesize a single or few layers of graphene. Although mechanical exfoliation of graphite provides excellent quality of graphene but by this method it is not possible to synthesis of large scale production of graphene. The main difficulty in producing high quality of graphene from graphite is especially due to the high van der Waals energy adhering graphene layers to one another. The most popular solution based approach is the chemical exfoliation from graphite which involves chemical oxidation of graphite into graphite oxide, followed by exfoliation of graphite oxide in water to form graphene oxide by ultrasonication¹⁵. Chemical oxidation induces defects^{15, 20} into the sheets due to presence of oxygenated functional groups such as carboxyl, hydroxyl, epoxy etc. Although reduction of graphene oxide by different reducing agent leads to increasing the π -conjugation of graphene²⁰, the restoration of complete π -conjugation is not possible to achieve and hence it has low conductivity. Although chemical vapor deposition (CVD) produces high quality graphene on metal surfaces, there is a need for reliable method(s) for the production of high yield, high quality and large surface area graphene on silicon substrate. Carbon nitride is also a two dimensional carbon based superhard material predicted by Liu and Cohen²¹ in 1989 has got more attention in the scientific community due to its unique optical and electrical properties. It has

high biocompatibility, chemical inertness and extreme hardness. Therefore, synthesis of flat 2D carbon nitride sheet is very much important. Among different synthesis method of 2D carbon nitride the bottom up fabrication method is the easier method.

However, there is no report in the literature on the synthesis of 2D flat carbon nitride and its application in electrochemical determination of metal ions. Highly sensitive detection of heavy metal ions is important since they play an active role in different biological and environmental processes. Mercury is one of the most toxic heavy metal that exists in the environment. The oxidized form of mercury (Hg^{2+}) is the main source of contamination. Thus, there is a need to develop a simple method to detect mercuric ions at a very low concentration in water. The available techniques²²⁻²⁵ to detect the mercury level in the environment are cold vapor atomic absorption, atomic fluorimetry, high performance liquid chromatography, inductively coupled plasma atomic emission spectroscopy, and plasma mass spectroscopy. But, all these techniques are time consuming for data acquisition and they do not give reliable results if the concentration of mercury is below a certain level. On the other hand, the electrochemical techniques for determination of metal ions are one of the best methods because of their low cost, high sensitivity and portability. Highly sensitive and selective determination of hydrogen peroxide (H_2O_2) is also important²⁶ since it is the product of several biological enzyme catalyzed reactions and also plays an active role in food, pharmaceutical, clinical, industrial, and environmental analyses. Several analytical methods²⁷⁻³³ such as titration, chromatographic, fluorometric, colorimetric, chemiluminescent and electrochemical methods are available for determination of H_2O_2 . Among these methods electrochemical methods for determination of H_2O_2 are the best methods because of their low costs, environment friendly, high sensitivity and portability.

4.2. Bottom up fabrication method to synthesis of 2D Carbon Nitride sheet

The blue fluorescent graphitic carbon nitride quantum dots (g-CNQDs) were synthesized by a microwave assisted method which was presented in the chapter 3 of this thesis. These g-CNQDs are used as precursor for the formation of 2D graphitic carbon nitride sheets and 3D graphitic carbon nitride by bottom-up fabrication method. The g-CNQDs were dispersed in water by sonication method. These dispersed g-CNQDs are drop casted on different substrate such as glass, silicon wafer, mica disk, quartz etc. and dried in air or at 45⁰C to form 2D graphitic carbon nitride sheets. With varying the concentration of g-CNQDs or maintaining the number of drops we can form different thickness of 2D graphitic carbon nitride sheets. This method is called bottom up fabrication method.

4.3. Characterization of 2D Carbon nitride sheet

4.3.1. Characterization by TEM

Formation of 2D carbon nitride sheets from its quantum dot (g-CNQDs) by bottom up fabrication method was proved by doing transmission electron microscopy (TEM) imaging. Different concentration of aqueous g-CNQDs solution was used for TEM imaging. TEM samples were prepared by drop casting a drop of aqueous g-CNQDs solution on a TEM grid and then allowed to evaporate in air at 45⁰C. Figure 4.1 (a - c) display the TEM images of 2D carbon nitride sheets prepared from 1 mg L⁻¹, 0.01 mg L⁻¹ and 2 x 10⁻⁵ mg L⁻¹ solutions of g-CNQDs respectively. Figure 4.1 (a) shows that several carbon nitride sheets are stacked when a concentrated solution (1 mg L⁻¹) of g-CNQDs was used. We have seen that from Figure 4.1 (a) to Figure 4.1 (c), the size as well as the thickness of carbon nitride sheets decreases with decreasing

concentration of g-CNQDs in solution which was used for synthesis. Thus, TEM measurements suggest that the g-CNQDs are self assembled on the TEM grid by drying at 45⁰C and then condensation of self-assembled g-CNQDs occurs at the same temperature to form graphitic carbon nitride sheets. Figure 4.1 (d) shows the typical SAED image obtained from Figure 4.1(a) indicating the amorphous nature of carbon nitride sheets and the calculated lattice d-spacing from the diffraction ring is 0.33 nm which is consistent with the lattice spacing of reported graphitic carbon nitrides³⁴.

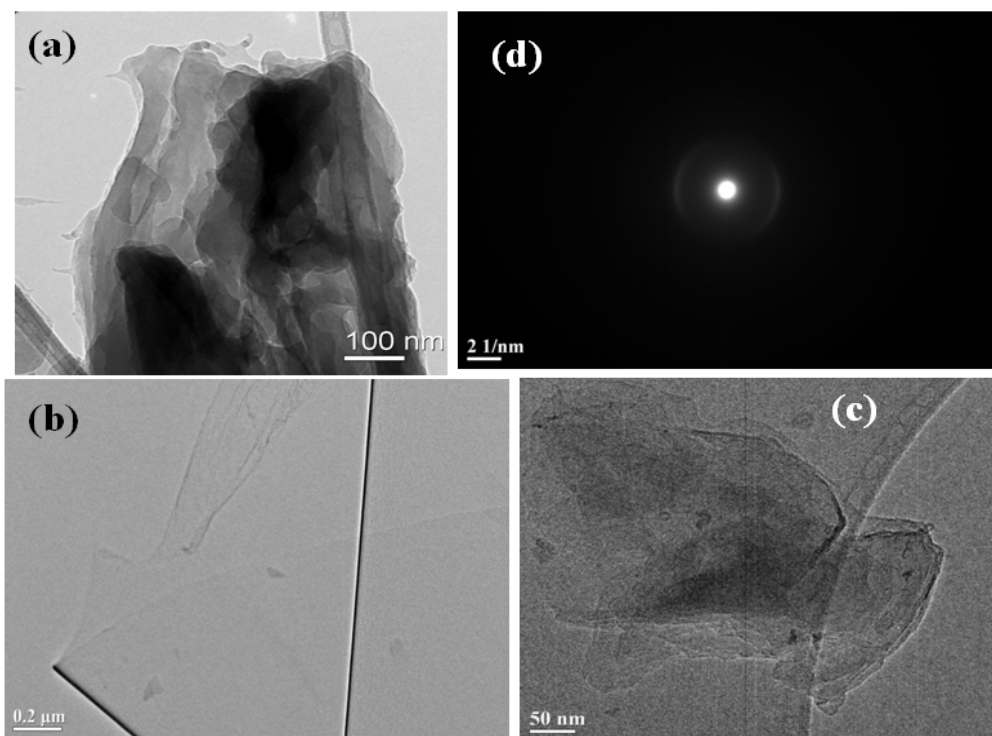


Figure 4.1. TEM images of carbon nitride sheets formed by evaporation induced condensation of g-CNQDs. The concentrations of g-CNQDs in aqueous solutions were (a) 1 mg L⁻¹, (b) 0.01 mg L⁻¹ and (c) 2 X 10⁻⁵ mg L⁻¹. (d) SAED pattern of carbon nitride sheets taken from the sheets in figure 4.1 (a).

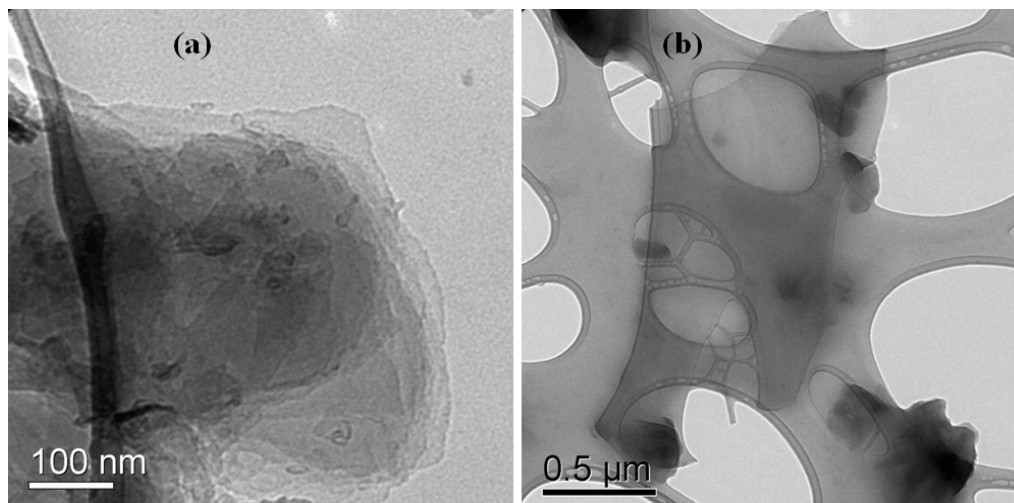


Figure 4.2. (a, b) TEM images of carbon nitride sheets produced from a diluted, centrifuged aqueous solution of g-CNQDs.

2D carbon nitride has layer structure which is stacked together due to van der Waals interaction between the layers. Figure 4.2 (a and b) give the TEM images of carbon nitride sheets that are produced from the centrifuged aqueous solution of g-CNQDs. The aqueous solution of g-CNQDs was centrifuged at 15000 rpm for 1 hour and then diluted to 10^5 times before being used for TEM sample preparation. Figure 4.2 (a) shows the layer by layer stacked assembly of several carbon nitride sheets. A close observation of TEM images (Figure 4.2 (a and b) reveals that the transparent layer and several stacked layers of 2D carbon nitride are clearly shown, representing a flat morphology of it.

4.3.2. Characterization by p-XRD

The g-CNQDs were drop casted on a glass slide and heated at 45°C to get 2D carbon nitride sheets by self assembly growth to 2D sheets from its quantum dots.

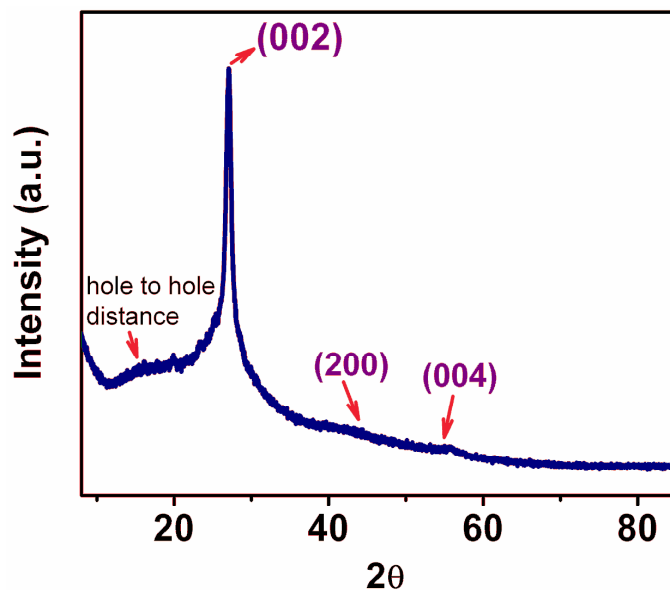


Figure 4.3. Powder X-ray diffraction pattern of the carbon nitride sheets.

The powder X-ray diffraction pattern of this carbon nitride sheet (Figure 4.3) exhibits a sharp and intense peak at 27.26° (2θ) with a d-spacing of 3.27\AA , which is assigned to the (002) reflection of graphitic carbon nitride. Additionally, there are another two peaks at 2θ values of 44.1° and 54.9° which are assigned to (200) and (004) reflection of crystalline graphitic carbon nitride material respectively³⁵. Apart from this one broad peak is there in the p-XRD pattern of 2D carbon nitride sheets at 2θ value of $\sim 13.1^\circ$ corresponds to a distance of 0.67nm can be related to in-plane structural repeated units of carbon nitride (hole-to-hole distance of pores of carbon nitride)³⁶.

4.3.3. Characterization by AFM

Formation of 2D carbon nitride sheets from its quantum dot by bottom up fabrication method was proved by doing atomic force microscopy (AFM) imaging. It can also examine the structural

characteristics of the sheet morphologies and thickness of the carbon nitride sheets. The AFM samples were prepared by depositing the sonicated aqueous solution of g-CNQDs of different concentrations on mica surfaces and dried at 45⁰C in air. It was observed that the size and thickness of carbon nitride sheets can be controlled by using different concentrations of the g-CNQD aqueous dispersed solutions. Figure 4.4 (a) shows the representative AFM image of the sample prepared from 10⁻⁵ mg L⁻¹ g-CNQDs solution.

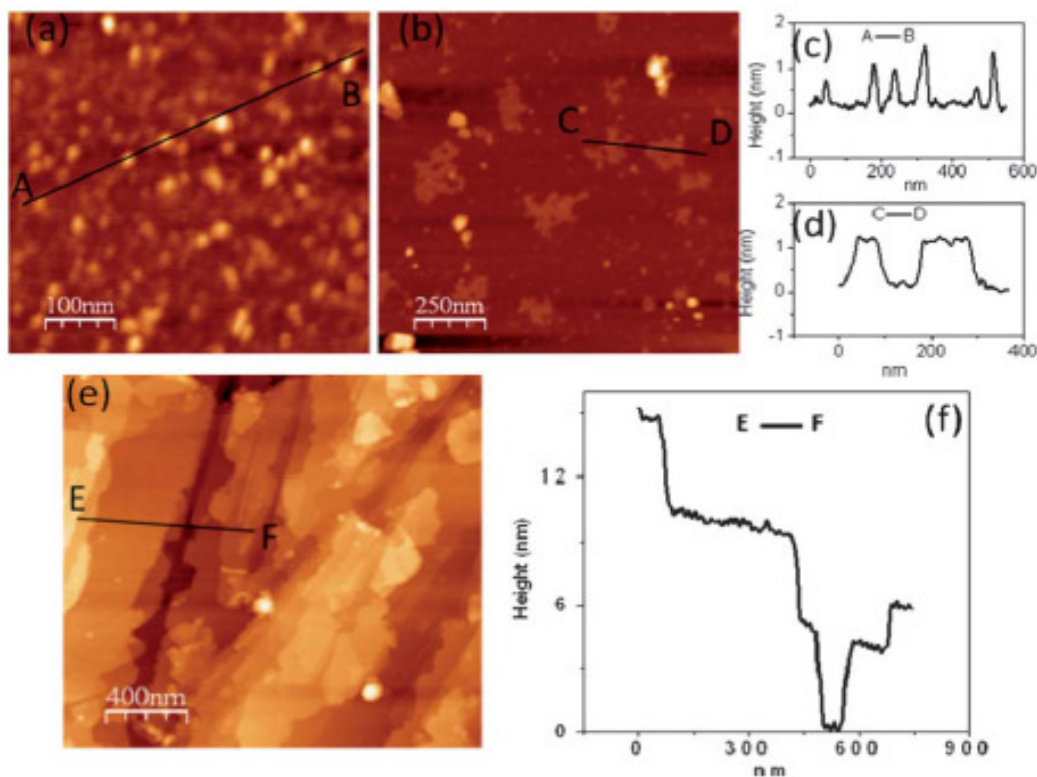


Figure 4.4. AFM images of (a) g-CNQDs, (b) carbon nitride nanosheets and (e) micron sized carbon nitride sheets formed from different concentrations (10⁻⁵, 10⁻⁴ and 0.1 mg L⁻¹ respectively) of g-CNQDs solutions, (c, d and f) The line profiles along the line AB, CD and EF in image of (a), (b) and (e) respectively.

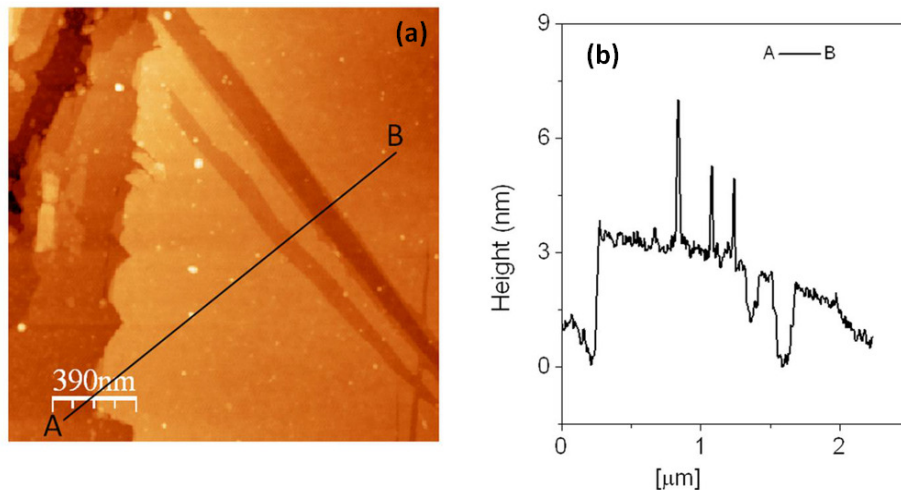


Figure 4.5. (a) AFM image of carbon nitride sheets produced by drying a higher concentration (1 mg L^{-1}) of g-CNQDs solution. (b) The line profile along the line AB in image (a) indicating the presence of g-CNQDs on the surface on carbon nitride sheets.

The line profile in the AFM image of Figure 4.4 (a) along AB shown in Figure 4.4 (c) reveals the presence of carbon nitride quantum dots with thickness of 0.5 nm to 2.5 nm and their lateral dimension are from 5 nm to 20 nm. The AFM image 4.4 (b) represents the carbon nitride sheets which were prepared by depositing the 10^{-4} mg L^{-1} aqueous dispersed solution of g-CNQDs concentrations on mica surfaces and dried at 45°C in air. This AFM image and its line profile (Figure 4.4 (d)) analysis reveals the formation of 2–4 layer thick carbon nitride sheets with their size ranging from 50 to 100 nm. Figure 4.4 (e) displays the AFM image of the sample prepared from the 10^{-1} mg L^{-1} dispersed solution of g-CNQDs and the line profile on it shown in Figure 4.4 (f). The AFM image and the line profile along the line EF in Figure 4.4 (e) indicate that micron sized sheets are remarkably flat with a thickness that varies from 2 nm to 5 nm. This suggests that each carbon nitride sheet consists of multiple of carbon nitride layers. This AFM image also confirms stacking of several sheets when a higher concentration of g-CNQDs was

used for sample preparation. The AFM images and line profiles reflect a remarkable flatness of the sheets. The root mean square values of surface roughness are found to be in the range 0.2–0.5 nm. The carbon nitride quantum dots are randomly grown on the surface of carbon nitride sheets as shown in Figure 4.5 (a) when the concentration of evaporated g-CNQDs dispersed solution was 1 mg L⁻¹. The line profile along the line AB in Figure 4.5 (a) is shown in Figure 4.5 (b) proves the formation of carbon nitride quantum dots on the surface of carbon nitride sheets. From AFM studies this can be concluded that the thickness of carbon nitride sheets varies from 1 nm to 5 nm whereas their lateral size varies ranging from few nanometers to several micrometers depending on the amount of g-CNQDs used for sample preparation.

4.3.4. Characterization by DLS

The dynamic light scattering (DLS) measurements were used for measuring the size of carbon nitride quantum dots in aqueous solution. The average size of g-CNQDs in aqueous solution increases with increasing concentration of g-CNQDs (Table 4.1). This suggests that g-CNQDs in solutions are probably held together by weak attractive forces. On evaporation of these aqueous solutions, the g-CNQDs are self-assembled on a solid surface to form 2D carbon nitride sheets by condensation of g-CNQDs at 45⁰C.

Table 4.1. Average diameter of g-CNQDs of different concentrations of g-CNQDs in its aqueous solution measured by dynamic light scattering measurement

Sl. No.	Concentration of g-CNQDs	Average Diameter
1	1 mg/L	432 nm
2	0.001 mg/L	188.9 nm
3	10 ⁻⁵ mg/L	104.5 nm
4	10 ⁻⁷ mg/L	28.5 nm

4.3.5. Characterization by SEM

Figure 4.6 represents the scanning electron microscopy (SEM) images of 2D carbon nitride grown on silicon substrate by evaporating a higher concentration of g-CNQDs solution at 45⁰C. The SEM image clearly shows the rectangular plates which were grown randomly on a silicon substrate (Figure 4.6 (a)). In addition with these nanoplates, fully 3D carbon nitride with their size of about 0.5–5 mm (Figure 4.6 (b) and (c)) are also formed.

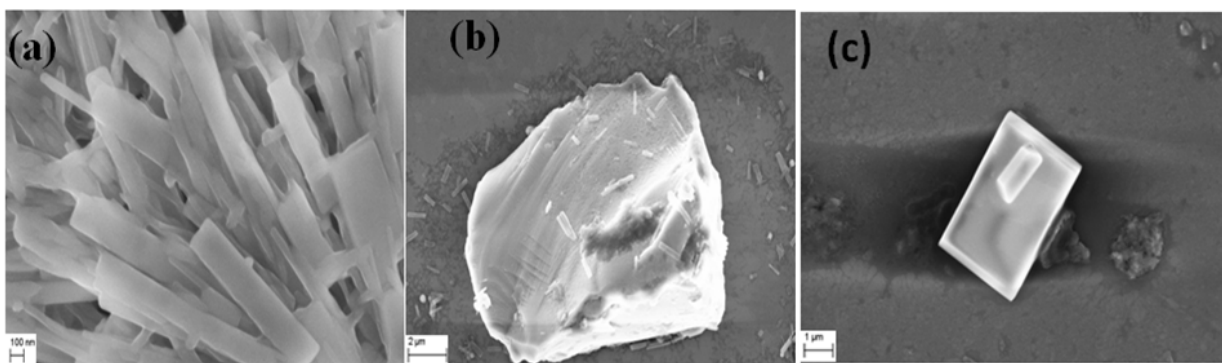


Figure 4.6. SEM images of carbon nitride sheets prepared by evaporation of 30 mL solution of g-CNQDs (1mg/L) in air at 45⁰C.

4.3.6. Characterization by FT-IR Spectroscopy

The information about chemical bonding in 2D carbon nitride sheets was obtained from FT-IR spectroscopy. Figure 4.7 shows the FT-IR spectrum of 2D carbon nitride sheets. The intense bands at 1216, 1314 and 1405 cm⁻¹ can be assigned to aromatic C=N stretching whereas the band at 1614 cm⁻¹ corresponds to C=N stretching. The peak at 801 cm⁻¹ is attributed to the breathing mode of s-triazine rings³⁷ and a broad band in 3100–3400 cm⁻¹ corresponds to the stretching mode of –NH_x groups.

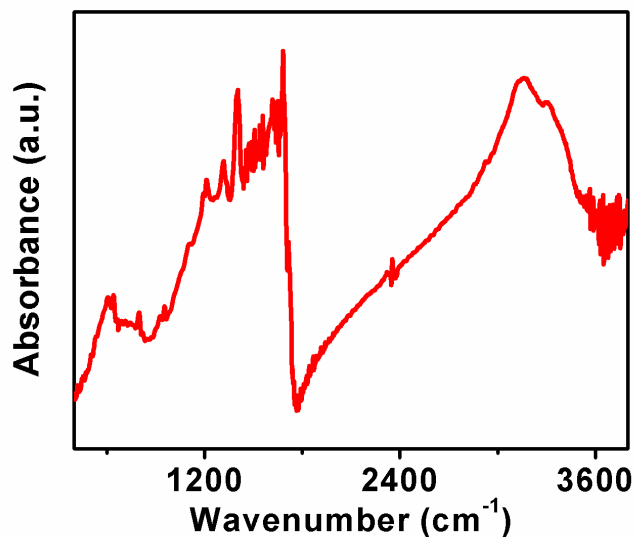


Figure 4.7. FT-IR spectrum of 2D carbon nitride sheets.

4.3.6. Characterization by FT-Raman Spectroscopy

The g-CNQDs were drop casted on glass slide and heated at 45⁰C to get 2D carbon nitride sheets by self assembly method i.e. bottom up fabrication method. This glass slide was used to take FT-Raman spectrum of 2D carbon nitride sheets.

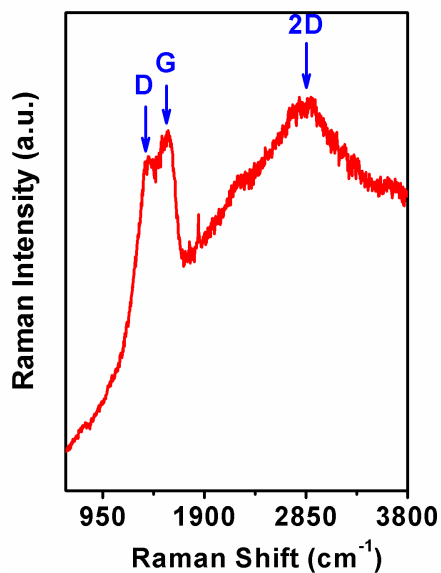


Figure 4.8. FT-Raman spectrum of 2D carbon nitride sheets.

The FT-Raman spectrum of 2D carbon nitride sheets is given in Figure 4.8. The two peaks at $\sim 1567\text{ cm}^{-1}$ and 1373 cm^{-1} can be attributed to G and D bands respectively of amorphous C_3N_4 ³⁸. According to Lee *et al.*³⁹ the position of the G band for carbon materials is shifted to a higher wave number ($>1580\text{ cm}^{-1}$) with increasing crystalline nature and to a lower wave number ($<1575\text{ cm}^{-1}$) for amorphous carbon materials. This suggests the amorphous nature of carbon nitride sheets. In addition a broad peak at $\sim 2785\text{ cm}^{-1}$ is probably due to 2D bands of carbon nitride sheets.

4.4. Electrochemical application of 2D a carbon nitride sheets

4.4.1. Preparation of 2D carbon nitride modified GC electrode

First, glassy carbon (GC) electrode was polished with 1.0, 0.1 and 0.05 μm alumina slurry on Buehler microcloth polishing cloth. After rinsing with deionizer water, the electrode was sonicated in deionizer water for about 5 minutes. 0.25 mg of g-CNQDs was dispersed in water with ultrasonicated to form well dispersed graphite carbon nitride quantum dot solution of concentration 0.01mg/L. This solution is then centrifuged at 15000 rpm for ~ 1 hour. Finally, 30 ml of this solution was drop cast on the active surface of cleaned GC electrode and allowed to evaporate the solvent under flowing of N_2 . Hence, GC electrode is coated with the film of carbon nitride.

4.4.2. Determination of mercuric ions by 2D carbon nitride modified GC electrode

2D Carbon nitride modified GC electrode was used to determine the Hg^{2+} ions in aqueous solution by the anodic stripping voltammetric determination. Figure 4.9 shows the cyclic

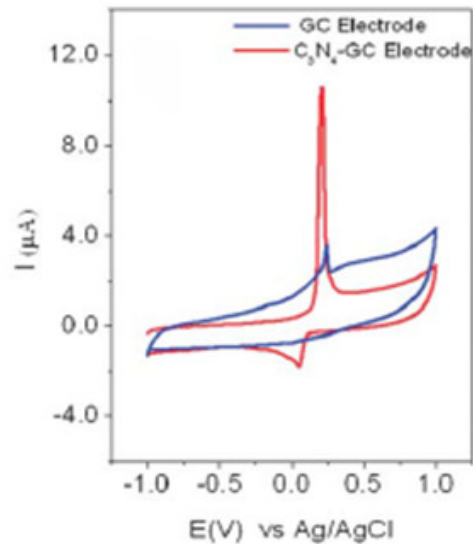


Figure 4.9. CVs of 1.0×10^{-6} M Hg^{2+} at the bare GC electrode and the carbon nitride modified GC electrode. Electrolyte: 0.02 M HCl, accumulation time: 15 min, accumulation potential: -1 V.

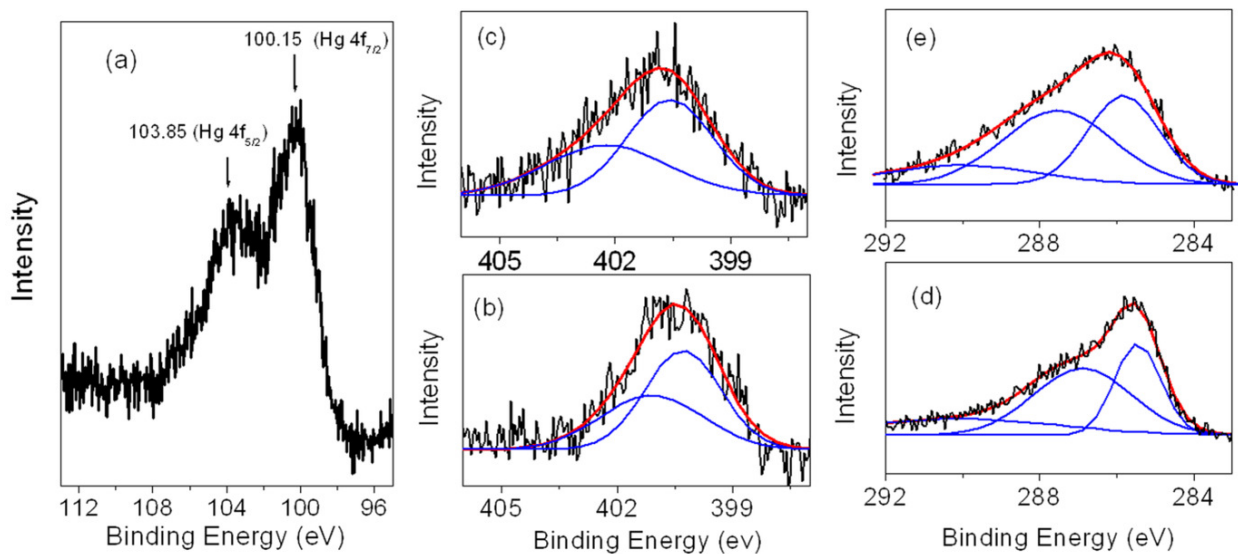


Figure 4.10. (a) Hg 4f XPS spectrum of carbon nitride obtained after electrochemical accumulation of Hg^{2+} ions at carbon nitride modified GC electrode. High resolution XPS spectra in the N1s region of (b) free carbon nitride sheet and (c) carbon nitride after electrochemical accumulation of Hg^{2+} ions. High resolution XPS spectra in the C1s region of (d) free carbon nitride sheet and (e) carbon nitride after accumulation of Hg^{2+} ions.

voltammograms (CVs) of 1×10^{-6} M Hg^{2+} concentration at the bare GC electrode and the carbon nitride modified GC electrode after accumulation of Hg^{2+} at a potential of -1 V for 15 minutes. Here 0.02 M HCl has been used as an electrolyte. In the bare GC electrode, there is a small oxidative peak appearing at 0.2 V, implying that some absorption of Hg^{2+} ions could have occurred at the bare GC electrode surface. However, a well-defined symmetrical anodic stripping peak at 0.2 V was obtained under similar experimental conditions when the GC electrode is modified with carbon nitride forming 2D carbon nitride modified GC electrode. Therefore, there is a significant enhancement in the anodic stripping peak current when the carbon nitride modified GC electrode is used. This suggests that the carbon nitride modified GC electrode is highly sensitive towards Hg^{2+} ions. In order to understand the electrochemical reaction mechanism, XPS measurement of the carbon nitride sample was collected from the carbon nitride modified electrode, after accumulation of Hg^{2+} at a potential of -1 V for 15 minutes on the carbon nitride modified GC electrode. The sample preparation of XPS is as follows. The electrochemical accumulation of Hg^{2+} ion was done at carbon nitride modified GC electrode on 1.0×10^{-6} M Hg^{2+} solution at -1V for 15 min. After accumulation of Hg^{2+} ion the carbon nitride modified GC electrode was sonicated in distilled water for ~ 20 minutes to remove the carbon nitride from the GC electrode and to be dispersed in the water. Then this carbon nitride dispersed solution was drop casted on silicon substrate and then allowed to dry in air. Figure 4.10 (a) shows the Hg 4f XPS spectrum of carbon nitride after electrochemical accumulation of Hg^{2+} ions. The two peaks at 100.05 eV and 103.56 eV can be assigned to Hg 4f_{7/2} and Hg 4f_{5/2} of Hg^0 respectively. This indicates that Hg^0 was absorbed by electrochemical reduction of Hg^{2+} at the accumulation step under negative potential of -1V. These Hg^0 are oxidized at 0.2 V to give a well defined stripping anodic peak in cyclic voltammograms. Figure 4.10 (b and c) represents

the N1s high resolution XPS spectra of free carbon nitride sheet and carbon nitride after electrochemical accumulation of Hg^{2+} ions respectively whereas Figure 4.10 (d and e) represents the C1s high resolution XPS spectra of free carbon nitride sheet and carbon nitride after electrochemical accumulation of Hg^{2+} ions respectively. There is no significant change of N1s and C1s XPS spectra of carbon nitride before and after accumulation of Hg^{2+} ions. Based on the above electrochemical observations and XPS studies the possible mechanism can be illustrated as follows:

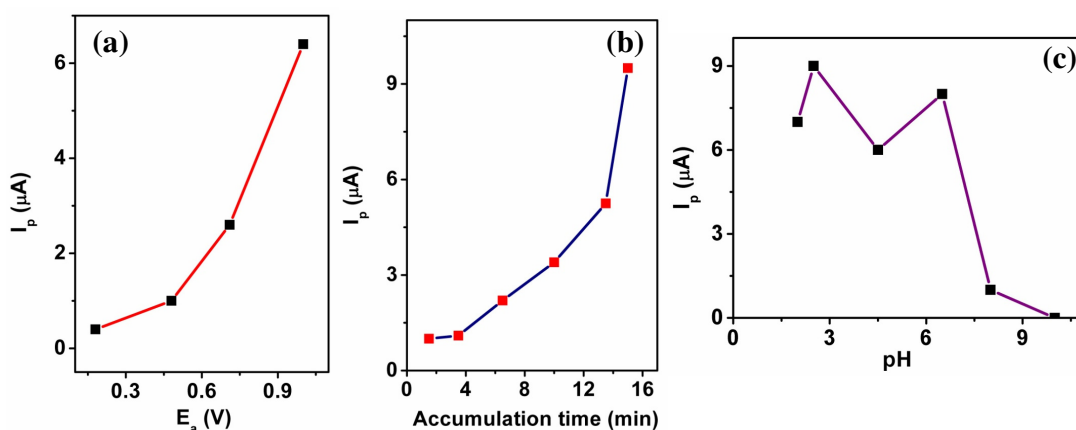


Figure 4.11. (a) Effect of accumulation potential E_a (V) on anodic stripping cyclic voltammetric response for 1×10^{-6} M of Hg^{2+} at carbon nitride modified GC electrode, electrolyte: 0.02 M HCl, accumulation time: 15 minutes. (b) Effects of accumulation time on anodic stripping cyclic voltammetric response for 1×10^{-6} M of Hg^{2+} at carbon nitride modified GC electrode, electrolyte: 0.02 M HCl and accumulation potential = -1 V. (c) Effect of pH of the solutions on anodic stripping cyclic voltammetric response for 1×10^{-6} M of Hg^{2+} at carbon nitride modified GC electrode, accumulation potential = -1 V and accumulation time = 15 minutes.

- (i) Accumulation on carbon nitride modified GC surface and reduction step: $\text{GC}/\text{C}_3\text{N}_4$ (surface) + Hg^{2+} (solution) + $2e^- / \text{GC}/\text{C}_3\text{N}_4\text{-Hg}^0$ (surface)
- (ii) Oxidation step: $\text{GC}/\text{C}_3\text{N}_4\text{-Hg}^0$ (surface) / $\text{GC}/\text{C}_3\text{N}_4$ (surface) + Hg^{2+} (solution) + $2e^-$.

In this study the accumulation time and accumulation potential are generally the important parameters for enhancing the sensitivity of a sensor (Hg^{2+} ion). It was observed that the stripping peak current is increased with increasing potential and accumulation time shown in Figure 4.11a and 4.11b respectively. The higher anodic peak current at more negative potential and longer accumulation time is due to the efficient reduction of Hg^{2+} to Hg^0 at carbon nitride modified GC electrode surface. In addition, the effect of pH on the carbon nitride modified GC electrode for detection of Hg^{2+} ions was also investigated.

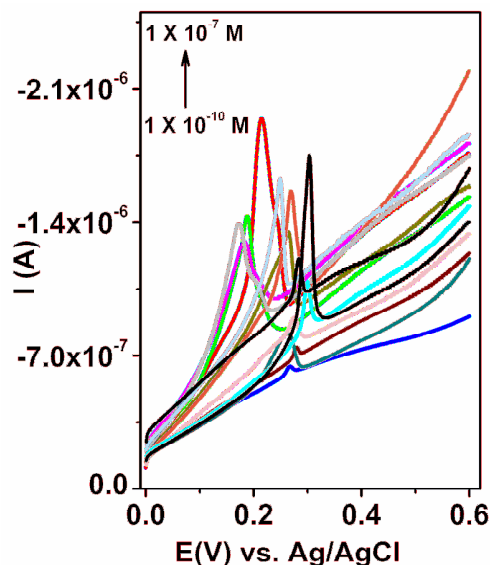


Figure 4.12. The anodic stripping cyclic voltammograms of different concentration of Hg^{2+} ions at carbon nitride modified GC electrode under optimum conditions.

It was observed that at high pH the sensitivity of the carbon nitride modified GC electrode is very poor and is better in the lower pH (1 to 6) range (Figure 4.11c). The enhancement of anodic stripping current with lowering the pH of the solution is probably due to formation of stable complex between Hg^{2+} ions and carbon nitride surface at lower pH. The conditions used for volumetric determination of Hg^{2+} ions involve two steps, first is accumulation and reduction of Hg^{2+} to Hg^0 at -1 V for 15 minutes by stirring aqueous solution containing 0.02 M HCl and last one is doing CV from 0 V to 0.6V in the same solution. Figure 4.12 shows the anodic stripping cyclic voltammograms of the carbon nitride modified GC electrode towards Hg^{2+} ions at various concentrations. For each stripping voltammetric measurement fresh new GC electrode was used. However, similar results were obtained when carbon nitride modified GC electrode was reused by holding at +1V for 15 minutes. The anodic stripping current peak increases with increasing concentration of Hg^{2+} ions (Figure 4.12). To know the unknown concentration of Hg^{2+} ion and to find out the detection limit of Hg^{2+} ion we have done calibration plot from Figure 4.12.

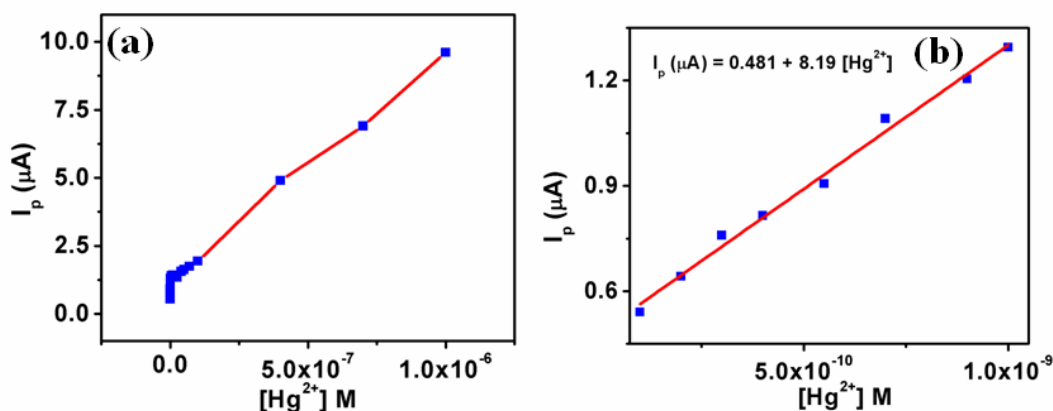


Figure 4.13. The calibration plot of voltammetric stripping current vs. the different concentration of Hg^{2+} ions: (a) full range of Hg^{2+} concentration and (b) lower Hg^{2+} concentration region.

In the calibration curve, there are two concentrations regions, 1×10^{-9} M to 1×10^{-10} M and 1×10^{-6} M to 1×10^{-9} M which is shown in Figure 4.13 where a linear relationship between the peak current and the concentration of Hg^{2+} ions was observed. The lower detection limit calculated from the lower concentration region is found to be 9.1×10^{-11} M ($S/N = 3$, $R^2 = 0.9967$) which is much lower than that recently reported⁴⁰⁻⁴² for Hg^{2+} detection using pyrrole/graphene oxide (1.5×10^{-8} M), DNA-functionalized gold nanoparticles (1×10^{-8} M), and an oligonucleotide probe (4.2×10^{-8} M) etc. Figure 4.14 shows the interferences of different metal ions such as Cu^{2+} , Pb^{2+} , Cd^{2+} , Fe^{3+} , Zn^{2+} , etc. in the determination of Hg^{2+} ions by anodic stripping voltammogram measurement by using the carbon nitride modified GC electrode after accumulation of metal ions at a accumulation potential of -1 V for accumulation time of 15 minutes. In this study also 0.02M HCl has been used as electrolyte solution.

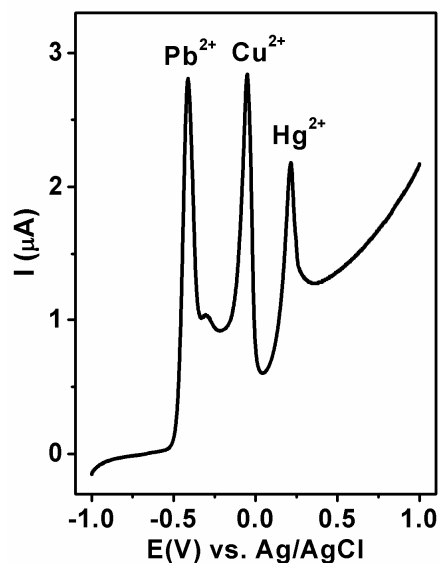


Figure 4.14. The anodic stripping voltammograms of 1×10^{-6} M Hg^{2+} ions in presence of 1×10^{-6} M each of Pb^{2+} , Cu^{2+} , Cd^{2+} , Fe^{3+} , Zn^{2+} ions at carbon nitride modified GC electrode at an accumulation potential of -1 V for accumulation time of 15 minutes and in presence of 0.02M HCl solution.

It can be seen that sharp anodic stripping peaks due to Pb^{2+} and Cu^{2+} also appeared at -0.45 V and 0.05 V respectively with the peak of Hg^{2+} ion whereas Zn^{2+} , Cd^{2+} , and Fe^{3+} have no significant effect. The simultaneous detection of Cu^{2+} , Pb^{2+} and Hg^{2+} was then investigated. The anodic stripping voltammograms of simultaneous detection of Cu^{2+} , Pb^{2+} and Hg^{2+} were shown in Figure 4.15 (a) by using the carbon nitride modified GC electrode after accumulation of metal ions (Cu^{2+} , Pb^{2+} and Hg^{2+}) at a accumulation potential of -1 V for accumulation time of 15 minutes and 0.02M HCl has been used as electrolyte solution in this study. The anodic peak currents gradually decreased linearly with decreasing concentration of metal ions (Figure 4.15 (a)). The lower detection limits of Cu^{2+} and Pb^{2+} calculated from the calibration curves (Figure 4.15 (b)) are found to be $\sim 7 \times 10^{-8}$ M. However, it was observed that the sensitivity of Pb^{2+} and Cu^{2+} ions showed a significant decrease when they were analyzed

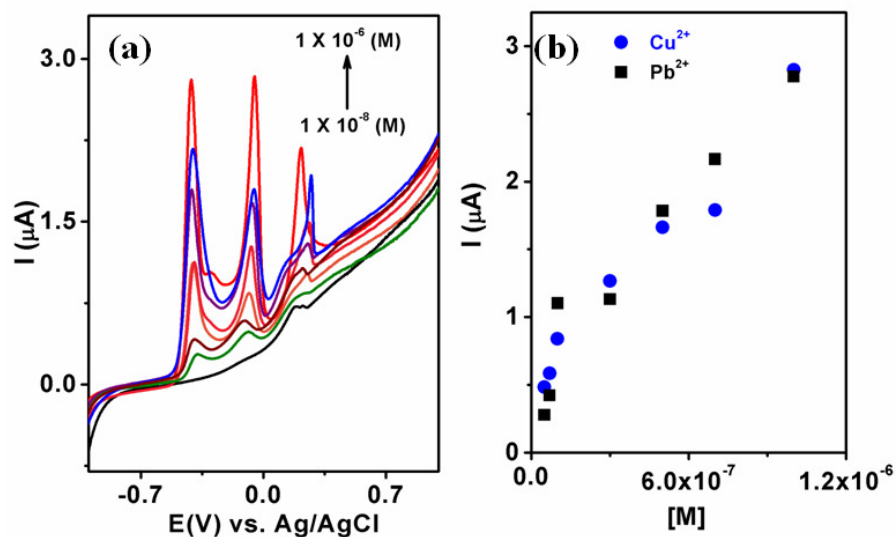


Figure 4.15. (a) Anodic stripping voltammograms for the different concentrations of Pb^{2+} , Cu^{2+} and Hg^{2+} ions at carbon nitride modified GC electrode at an accumulation potential of -1 V for accumulation time of 15 minutes and in presence of 0.02M HCl solution. (b) The calibration curve of Pb^{2+} and Cu^{2+} ions.

individually. The enhanced electrochemical response of Pb^{2+} and Cu^{2+} ions in the presence of Hg^{2+} ions is probably due to the formation of amalgam with the reduced mercury on the carbon nitride sheet surface.

4.4.3. Dopamine sensing by carbon nitride modified GC electrode

Another aspect of this work is the determination of dopamine concentration by using differential pulse voltammetry (DPV) technique in an electrochemical set up. Using DPV technique anodic peak current has been generated by the electrooxidation of dopamine. Detection of dopamine has been done in PBS (Phosphate Buffered Saline) solution by using carbon nitride modified GC electrode. In the bare GC electrode there is no peak in the DPV scan implying that there is no sensing property of bare GC electrode. DPV curves at different concentration of dopamine at the carbon nitride modified GC electrode have been shown in Figure 4.16. Figure 4.17 (a) represents that with increasing concentration of dopamine the DPV current gradually increasing. In the calibration curve there are two regions; one is lower dopamine concentration region from 7×10^{-7} M to 5×10^{-5} M and another one is higher dopamine concentration region from 6×10^{-5} M to 1.2×10^{-4} M.

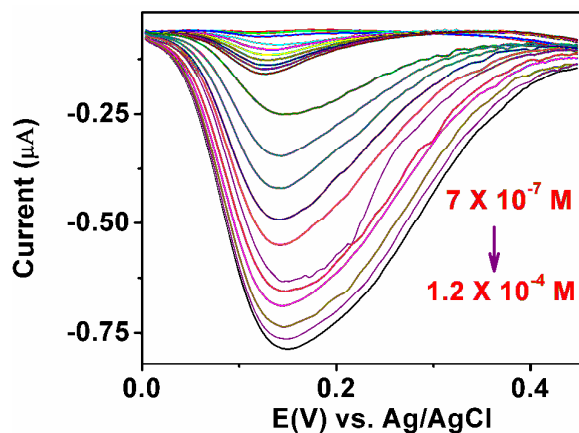


Figure 4.16. DPV plot of different concentration of Dopamine at the carbon nitride modified GC electrode.

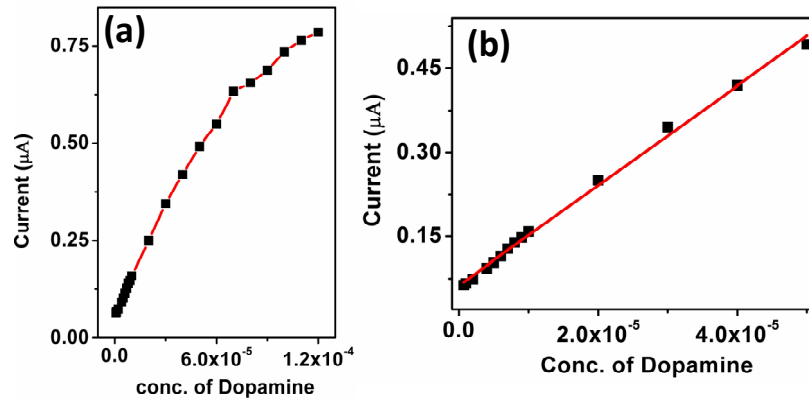


Figure 4.17. (a) Calibration plot of DPV current vs. concentration of dopamine. (b) Calibration plot in a lower dopamine concentration region.

The slope of first region i.e. lower dopamine concentration region is higher than that of higher dopamine concentration region due to kinetic effect⁴³. The lower detection limit of dopamine concentration has been calculated from lower region of $7 \times 10^{-7} \text{ M}$ to $5 \times 10^{-5} \text{ M}$ which is shown in Figure 4.20 (b). The lower detection limit of dopamine concentration calculated from Figure 4.20 (b) is $2.8 \mu\text{M}$.

4.5. Synthesis of 2D Graphene sheets

2D graphene sheets were prepared from CQDs which was prepared by microwave mediated method from formic acid. CQDs are dispersed in solvent then it was drop casted on solid substrate for example mica foil, quartz, glassy carbon surface etc. Then it was dried at 45°C to form 2D graphene sheets after evaporation of solvent.

4.6. Characterization of 2D graphene sheets

4.6.1. Characterization by AFM

Figure 4.18 (a, c) represents the AFM images of graphene formed from CQDs by bottom up fabrication method. Figure 4.18 (a) shows that the graphene layers are stacked one by one and forming layer structure of graphene. Figure 4.18 (c) represents the AFM image of graphitic film on mica foil indicating few-micron sized continuous graphene film. Figure 4.18 (a) and line profile along AB (Figure 4.18 (b)) suggest that several sheets are self assembled on mica disc and their thickness varies from 3 to 10 nm. Thus, each sheet consists of 10–30 graphene layers.

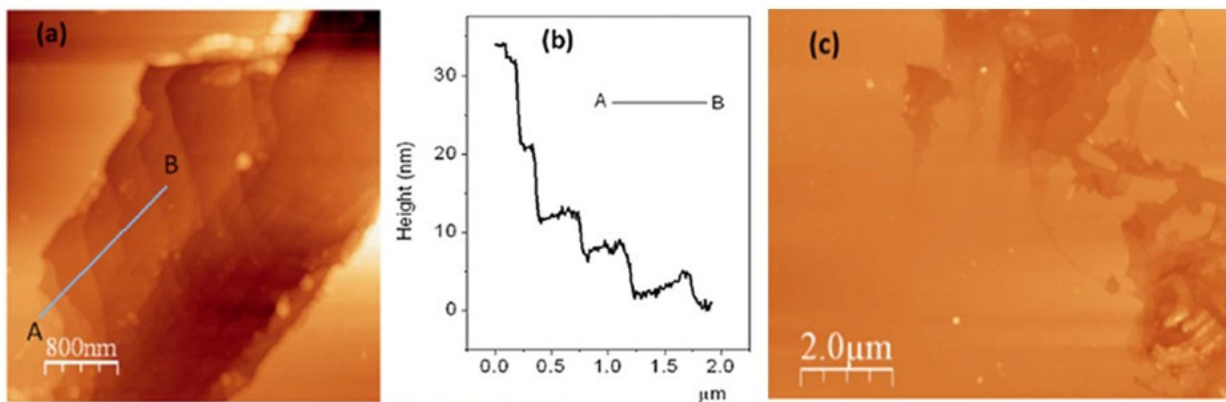


Figure 4.18. (a) AFM image of graphene film showing the several sheets. (b) Line profile along the AB on (a) AFM image. (c) AFM image of micron sized graphene film on mica foil.

4.6.2. Characterization by TEM

The 2D graphene thin sheets are formed due to evaporation induced self assembly of CQDs and their growth on a solid substrate. The TEM images of graphene sheets are shown in the Figure 4.19 (a, c and d). The size of sheets varies from few hundreds of nanometer to few microns. A closer look of TEM images reveals the transparent and several stacked layers of 2D graphene

sheets indicating flat morphology of these sheets. Figure 4.19b presents a representative selected area electron diffraction (SAED) pattern from graphene sheets taken from Figure 4.19 (a). The crystal planes corresponding to d-spacing of 2.139, 1.233, 1.059 Å, calculated from the ring of SAED image, were indexed as (100), (110), (201) respectively. This is in agreement with the reported results for single or bi-layer of graphene⁴⁴. The high resolution TEM (HRTEM) images of graphene sheets are shown in Figure 4.20 (b and c).

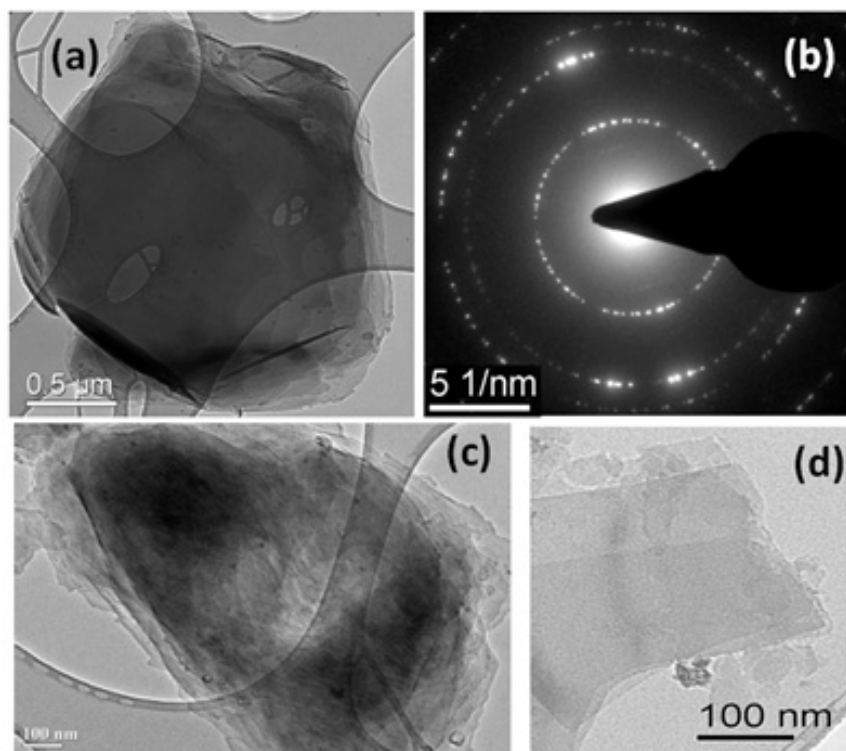


Figure 4.19. (a, c and d) TEM images of 2D graphene sheets formed from evaporation induced 2D self assembly and growth of CQDs. (b) SAED pattern taken from the sheets on TEM image of (a).

The crystalline lattice of graphene is clearly seen in the HRTEM images. The sheets are multi layered graphene sheets consisting of 20–40 graphene layers as shown in Figure 4.20 (c). The inter planner distance was measured from lattice fringes to be 0.35 nm which is consistent with the spacing of the (002) planes of hexagonal graphite. The folded graphene sheet can also be seen in Figure 4.20 (a). The energy dispersive X-ray spectroscopic (EDX) measurement was carried out to analyze the chemical composition of graphene sheets. Figure 4.20 (d) shows EDX spectrum of graphene sheets indicating the presence of mostly carbon with small amount of oxygen and copper. Thus, TEM measurements proved that evaporation induced self assembly of CQDs and growth in two dimensions lead to the formation of 2D multi layered graphene sheets.

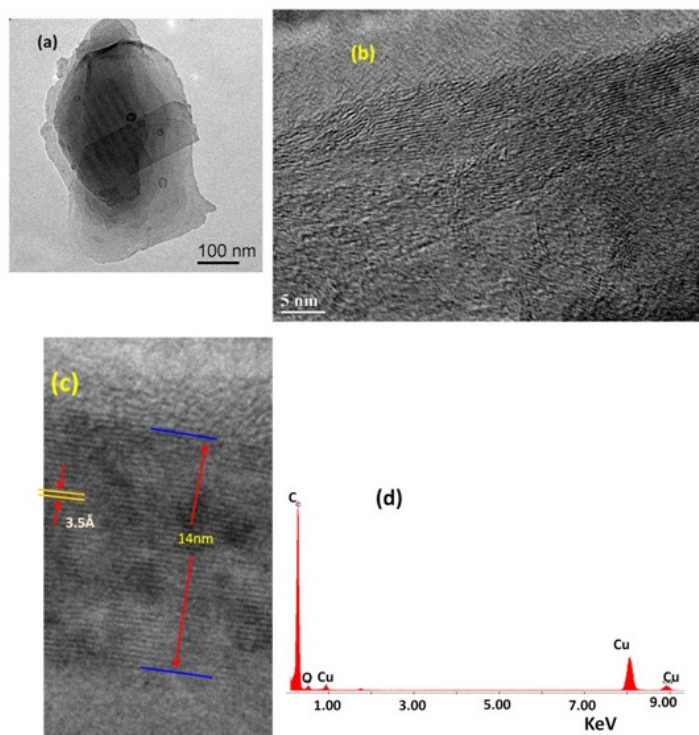


Figure 4.20. (a) TEM image of 2D folded graphene sheets. (b, c) HRTEM images of 2D graphene sheets. (d) EDX spectrum of graphene sheets taken on TEM image of (a).

4.6.3. Characterization by p-XRD

The powder X-ray diffraction (p-XRD) pattern of graphene/graphite on quartz substrate is shown in Figure 4.21. p-XRD sample was prepared by evaporating aqueous solution of CQDs on quartz substrate. A sharp intense peak at 2θ value of 26.8° with interlayer spacing of 3.3\AA is indexed as (002) reflection of graphitic sheets. In addition, two peaks are also appeared at lower 2θ values at 20.05° ($d = 4.98\text{\AA}$) and 9.2° ($d = 9.7\text{\AA}$). The oxidation^{15, 45} of graphite causes the shift of (002) reflection peak to lower values and the increase in d-spacing is due to the intercalation of water molecules and the formation of different oxygen functionalities in graphite oxide.

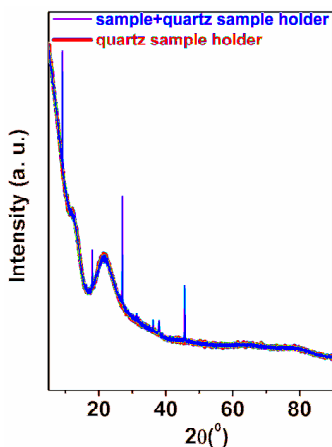


Figure 4.21. p-XRD pattern of graphite/graphene.

The interlayer spacing of 9.7\AA is close to reported d-value for graphene oxide⁴⁶. Therefore, increased d spacing values (9.7 and 4.98\AA) can be attributed to the intercalation of water/the presence oxygen functionalities in graphene sheets.

4.6.4. Characterization by FESEM

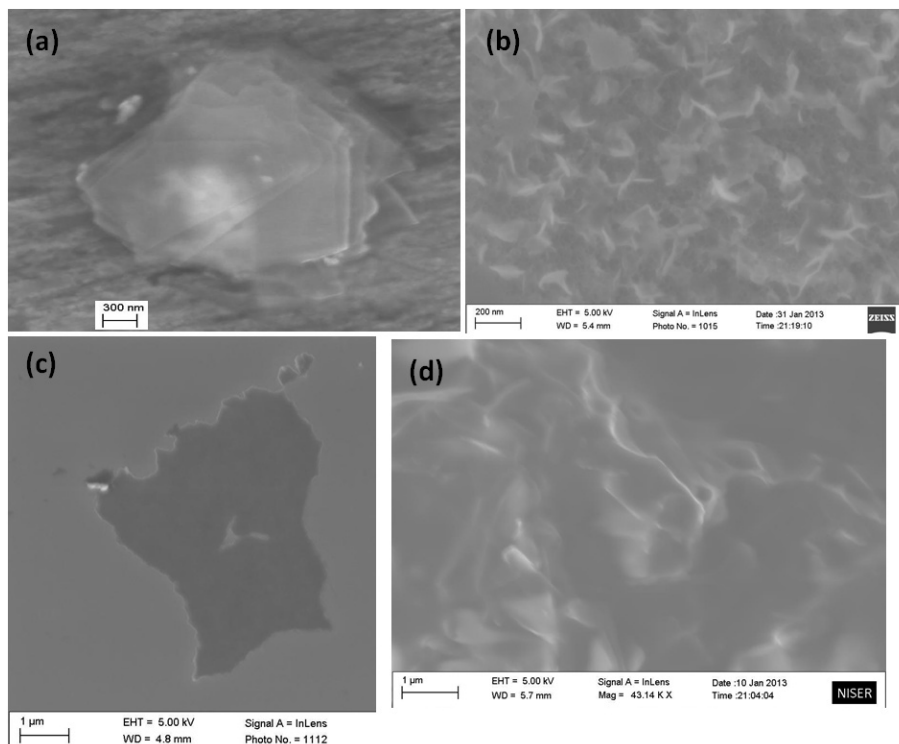


Figure 4.22. FESEM images of graphene on copper foil showing (a) stacked assembly of thin graphene sheets and (b) graphene flakes. FESEM images of graphene on silicon substrate showing (c) flat graphene sheet (d) aggregated and wrinkled sheets of graphene.

The field emission electron microscopy (FESEM) images of graphene sheets are presented in the Figure 4.22 (a - d). Different morphologies of graphene were observed during FESEM imaging. The thin, flat and layer structure graphene sheets were formed on copper foil shown in Figure 4.22 (a) which is in accordance with the TEM observations. Figure 4.22 (b) represents the FESEM images of graphene formed on copper foil where the graphene flakes are vertically oriented with respect to copper substrate. Flat graphene sheets were also formed on silicon substrate shown in Figure 4.22 (c). Figure 4.22 (d) is the FESEM image of graphene film on

silicon substrate showing the wrinkle and protrusion morphologies of graphene. We have not noticed any charging during SEM imaging indicating that sheets are electrically conductive.

4.6.5. Characterization by DLS

After vacuum evaporation the CQDs were dissolved in 20 ml of water and used as a stock solution. The dynamic light scattering measurements were performed for determining the size of CQDs in solution. It was found that hydrodynamic diameter (average size) of CQDs in aqueous solution was 6, 80, 300, 330 nm at 2, 4, 20, 60 minutes respectively after solution preparation (Figure 4.23).

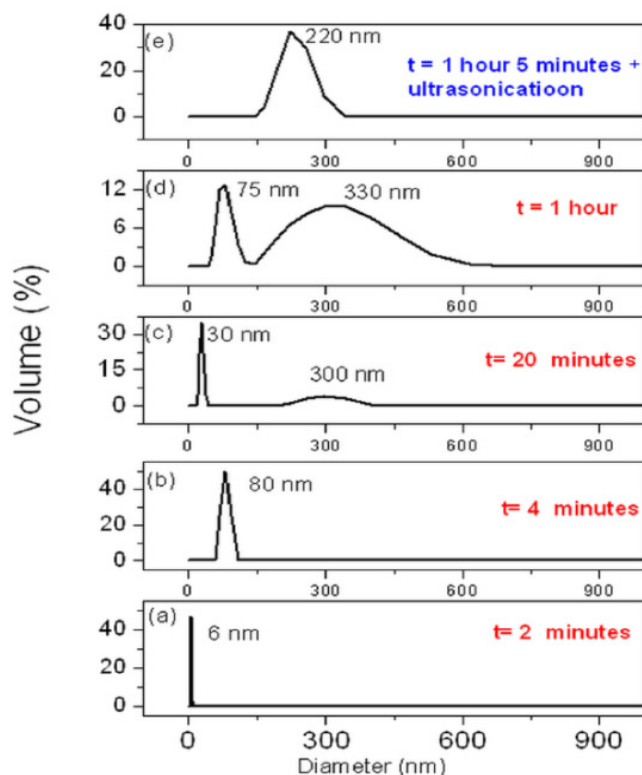


Figure 4.23. Change of Hydrodynamic diameter of CQDs in water with time and after ultrasonication. The whole product was dissolved in 20ml water and DLS measurements were performed at different time.

The average size of CQDs in aqueous solution increases with time and is also changed with dilution and ultrasonication. This suggests that CQDs in solutions are self assembling in solution and held together by weak attractive forces.

4.6.6. Characterization by XPS

X-ray photo electron spectroscopy (XPS) was used to examine the chemical environment around carbon in graphene sheets. Figure 4.24 shows the XPS survey scan of graphene sheets indicating the presence of carbon and oxygen with no other impurities. The C1s XPS spectra of graphene sheets were deconvoluted to three different Gaussian components shown in Figure 4.25. The binding energy of 284.5 eV is attributed to sp^2 hybridized carbon in aromatic rings ($C=C$)⁴⁷. The peaks at 285.9 eV and 287.56 eV can be assigned to carbon bonded to hydroxyl ($C-OH$) and carbonyl ($C=O$) group⁴⁷ respectively.

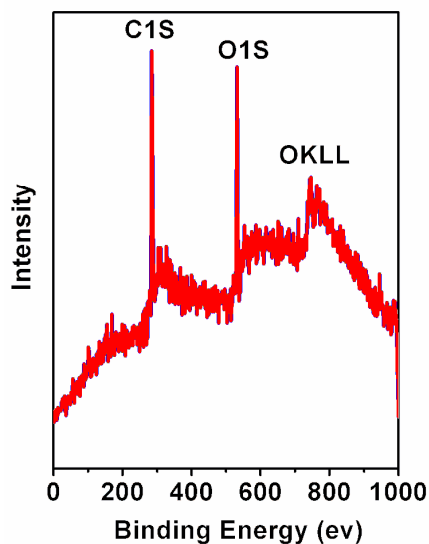


Figure 4.24. XPS survey scan of graphene sheets on silicon substrate.

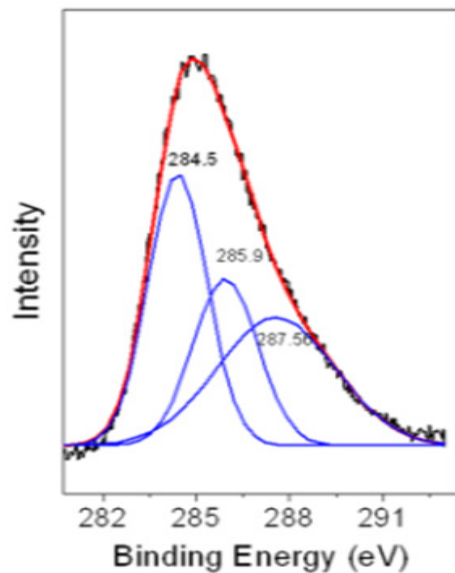


Figure 4.25. C1s XPS spectrum of graphene sheets on silicon substrate.

4.7. Properties and application of 2D graphene sheets

4.7.1. Preparation procedure of thin graphene sheets modified glassy carbon electrode from CQDs

Glassy carbon (GC) electrode was polished first with 1.0, 0.1 and 0.05 μm alumina slurry on Buehler microcloth polishing cloth respectively. After rinsing with distilled water, the electrode was sonicated in distilled water for about 10 min. 30.0 mL of this aqueous stock solution of CQDs was drop cast on the cleaned GC electrode and allowed to evaporate the solvent at $\sim 45^{\circ}\text{C}$. Hence, GC electrode is coated with a film of graphene sheets called as graphene sheets modified glassy carbon electrode.

4.7.2. Fast electron transfer kinetics of thin graphene sheets

Graphene sheets modified glassy carbon electrode showed fast electron transfer kinetics which was proved by using aqueous solution containing $\text{Fe}(\text{CN})_6^{3-/4-}$ graphene modified

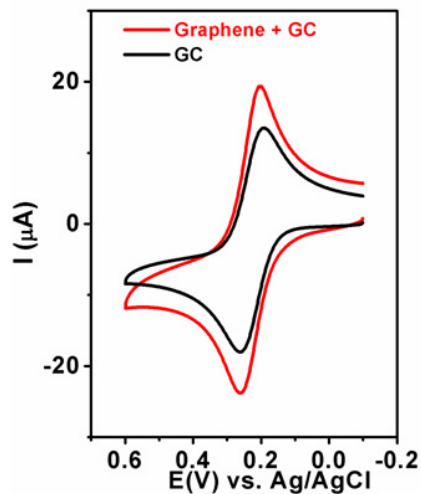


Figure 4.26. Cyclic voltammogram of $\text{Fe}(\text{CN})_6^{3-/4-}$ at bare GC electrode and graphene sheets modified GC electrode where electrolyte was 1 M KCl.

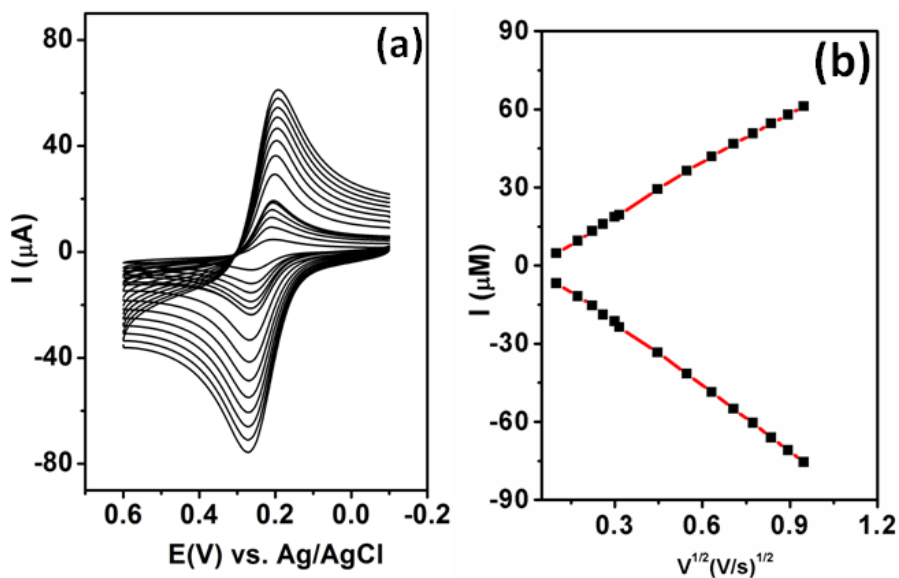


Figure 4.27. (a) CVs of $\text{Fe}(\text{CN})_6^{3-/4-}$ at GS/GC electrode at various scan rate ranging from 10 mV to 900 mV. (b) Cathodic and anodic peak current vs. square root of scan speed.

electrode/solution interface. It is well known that the electrochemical reaction of $\text{Fe}(\text{CN})_6^{3-/4-}$ is sensitive to surface⁴⁸, but less significant effect on oxygen functionalities in carbon based electrode⁴⁹. Figure 4.26 shows a comparison of cyclic voltammetric (CV) responses in 1.0 M KCl solution containing potassium ferrocyanide at bare glassy carbon (GC) electrode and graphene sheets modified glassy carbon (GS/GC) electrode. The CV at bare GC electrode showed a redox peak with a peak potential difference (ΔE_p) of 68 mV indicating a quasi-reversible redox reaction. However, the CV obtained using GS/GC electrode exhibited a redox peak with ΔE_p of ~60 mV under similar experimental condition. In addition, enhancement of 1.4 times peak currents are also observed when GC electrode is modified with graphene sheets. The ΔE_p is ~60 mV with enhancement of peak currents suggesting fast electron-transfer kinetics of graphene sheets for $\text{Fe}(\text{CN})_6^{3-/4-}$ redox couple. The CVs obtained with various scan rate ranging from 10 mV to 900 mV at GS/GC electrode using 1.0 M KCl solution containing 1 mM $\text{Fe}(\text{CN})_6^{3-/4-}$ are shown in Figure 4.27 (a). As shown in Figure 4.27 (b), both the anodic and cathodic peak currents increases linearly with the square root of the scan speeds suggesting that reaction is predominantly diffusion controlled process. Similar experiments were carried out using several GS/GC electrodes and it was observed that ΔE_p values were always in the range 60–64 mV. This slight variation of ΔE_p value is probably due to the different quality of graphene sheets that are formed on GC electrode surface in each case. The fast electron transfer in graphene and better electrochemical behavior were reported⁵⁰⁻⁵¹ due to the presence sharp edge plane in graphene. The sharp edges of graphene sheets already we have seen in TEM, SEM, AFM images. Thus, we can conclude that fast electron transfer kinetics of these graphene sheets can be attributed to the presence sharp edges of graphene sheets.

4.7.3. Application of 2D graphene sheets

Graphene modified GC electrode was used as a sensor of hydrogen peroxide by electrochemical method. The electrocatalytic property of graphene modified GC electrode towards the electrochemical reduction and oxidation of H_2O_2 was studied using cyclic voltammetry. Figure 4.28 (a) shows cyclic voltamograms at GS/GC electrode in absence and presence of 4 mM H_2O_2 in 0.1 M PBS buffer solution. A small background current was observed in the blank of 0.1 M PBS solution at GS/GC electrode where as a drastic increase of electrocatalytic current was observed in 0.1 M PBS solution containing 4 mM H_2O_2 . Figure 4.28 (b) represents the comparison of the voltametric response of 4 mM H_2O_2 in 0.1 M PBS solution at bare GC electrode and GS/GC electrode. This suggests the superior electrocatalytic activity at GS/GC electrode toward H_2O_2 .

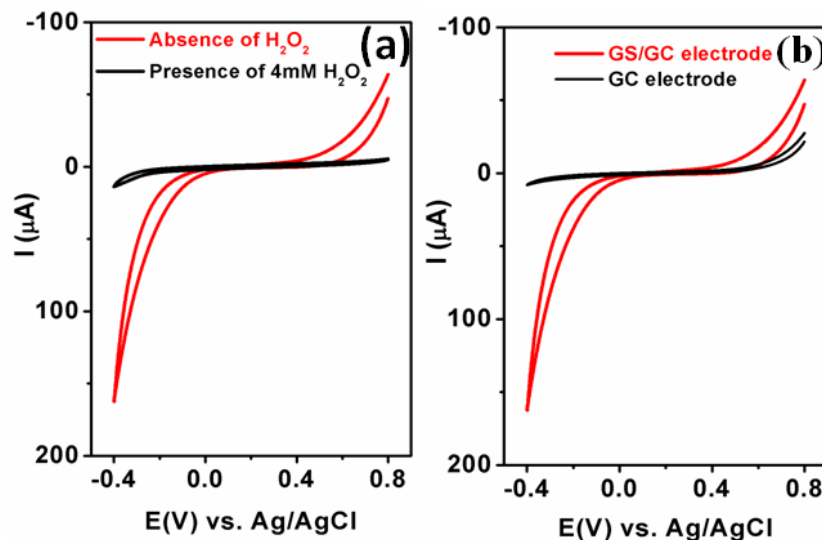


Figure 4.28. (a) CVs of GS/GC electrode in absence and presence of 4 mM H_2O_2 in 0.1M PBS (pH = 7) solution. (b) CVs of 4 mM H_2O_2 in 0.1M PBS at bare GC and GS/GC electrode.

Figure 4.29 shows a typical amperometric current-time response at GS/GC electrode for successive addition of H_2O_2 into stirring 0.1 M PBS buffer solution at an applied potential of -0.4 V. The reproducibility of the current response for ten different electrodes was examined in 0.1 M solution containing 4 mM H_2O_2 by measuring cyclic voltammetric scans. The relative standard deviation (RSD) was 8% indicating that graphene modified electrode had good reproducibility. To find out the detection limit of current vs. concentration of H_2O_2 at graphene sheets modified GC electrode the calibration plot has been done shown in Figure 4.30, there are two regions of H_2O_2 concentration ranging from 100 nM to 10 mM and from 10 mM to 1 mM, where a linear relation of current with concentration of H_2O_2 was observed. Figure 4.30 (a) represents the full concentration region of H_2O_2 . From the slope of calibration plot as shown in Figure 4.30 (b), the lower detection limit at GS/GC electrode to H_2O_2 was measured to be 300 nM at signal-to-noise ratio of 3 ($R^2 = 0.999$). This experimental detection limit of GS/GC electrode for H_2O_2 detection is comparable to the reported graphene based electrochemical H_2O_2 sensor⁵².

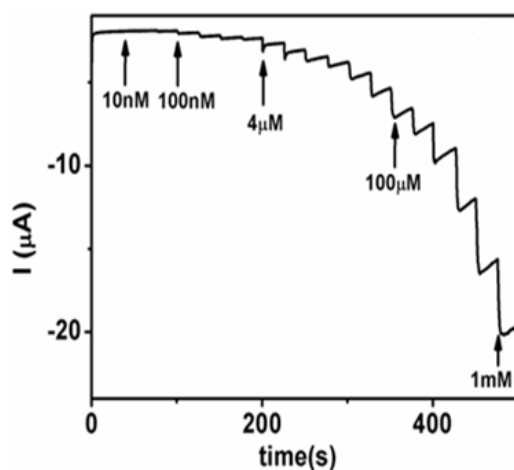


Figure 4.29. Amperometric response of GS/GC electrode during successive addition of H_2O_2 into 0.1 M PBS solution with stirring at an applied potential of -0.4 V.

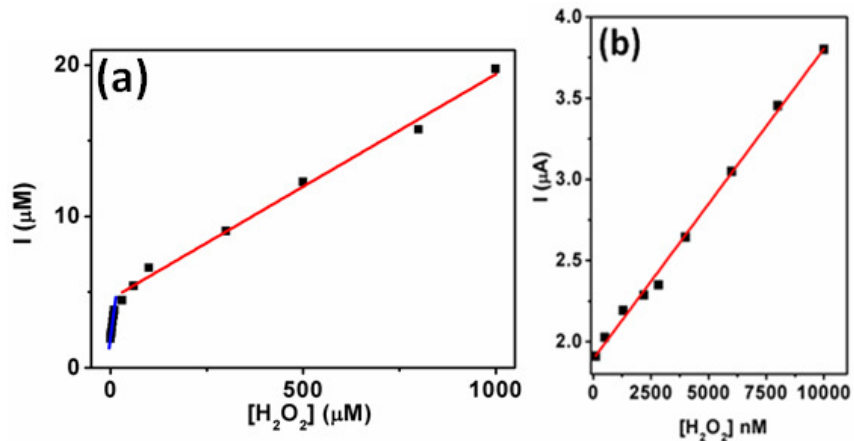


Figure 4.30. Calibration plot of current vs. concentration of H_2O_2 at graphene sheets modified GC electrode (a) Full concentration region and (b) Lower concentration region.

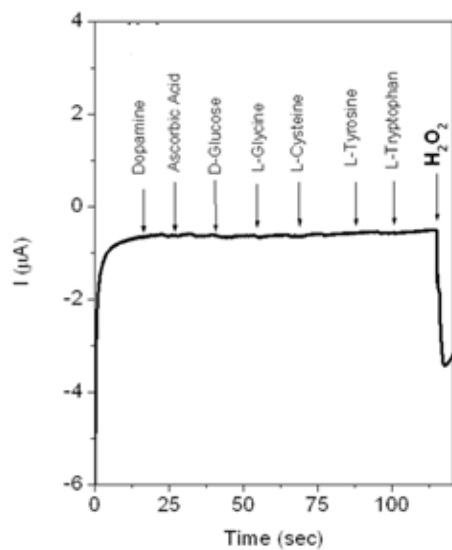


Figure 4.31. Amperometric responses of graphene sheets modified GC electrode at a potential of -0.4V on subsequent addition of dopamine (DA), ascorbic acid (AA), D-Glucose, L-Glycine, L-Cysteine, L-Tyrosine, L-Tryptophan and H_2O_2 (each concentration was $10\mu\text{M}$).

However, the detection limit of ~50 nM for metal nanoparticle or biomolecule functionalized graphene biosensors^{47, 53-56} was reported recently. The enhanced electrocatalytic behavior of graphene sheets is probably due to their fast electron transfer of graphene sheets owing to the presence of sharp edge planes in the graphene sheets. The interference of other biomolecules such as dopamine (DA), ascorbic acid (AA), D-glucose, L-glycine, L-cysteine, L-tyrosine, L-tryptophan on biosensor response were examined. As shown in Figure 4.31, the addition of 10 mM of H₂O₂ causes a significant increase of the amperometric response at the applied potential of ~0.4 V, but addition of similar concentration of AA, DA, D-glucose, L-glycine, L-cysteine, L-tyrosine, L-tryptophan did not cause interference the amperometric response of H₂O₂.

4.9. Conclusion

In summary, we have successfully demonstrated the bottom-up fabrication method for the formation of flat 2D carbon nitride sheets from g-CNQDs and 2D graphene sheets from CQDs. Based on DLS, TEM, AFM and FESEM studies a proposed growth mechanism of 2D flat carbon nitride sheets and 2D graphene sheets from g-CNQDs and CQDs respectively is shown schematically in Scheme 4.1. The schematic diagram represents the evaporation induced self assembly of g-CNQDs/CQDs and followed by condensation on solid substrate to form flat 2D carbon nitride/graphene sheet. The morphologies of carbon nitride, such as 0D, 2D and 3D, are produced by drying different concentrations of g-CNQD solution. As application the 2D carbon nitride modified GC electrode can be used as a sensor of Hg²⁺ ion in aqueous solution by electrochemical method. It can be used as the simultaneous electrochemical detection of Pb²⁺, Cu²⁺ and Hg²⁺ in aqueous solution. Additionally, dopamine can be detected by 2D carbon nitride modified GC electrode by DPV method. We have also shown the graphene



Scheme 4.1. Schematic diagram for the formation of 2D carbon nitride sheets from g-CNQDs and 2D graphene sheets from CQDs.

sheets modified glassy carbon electrode exhibits fast electron transfer kinetics for $\text{Fe}(\text{CN})_6^{3-/4-}$ redox couple indicating the possibility of a graphene based electrode for electrochemical applications. We have also demonstrated that graphene sheets modified glassy carbon electrode can be used for highly sensitive and selective non enzymatic determination of H_2O_2 . We believe that 2D carbon nitride sheets and graphene sheets may find applications in sensors or electrocatalysis in nanoelectronics or optoelectronic devices.

Chapter References

1. Novoselov, K. S.; Geim, A. K.; Morozov, S. V.; Jiang, D.; Zhang, Y.; Dubonos, S. V.; Grigorieva, I. V.; Firsov, A. A., *Science* **2004**, *306*, 666-669.
2. Lin, Y.-M.; Dimitrakopoulos, C.; Jenkins, K. A.; Farmer, D. B.; Chiu, H.-Y.; Grill, A.; Avouris, P., *Science* **2010**, *327*, 662-662.

3. Rangappa, D.; Murukanahally, K. D.; Tomai, T.; Unemoto, A.; Honma, I., *Nano Lett.* **2012**, *12*, 1146-1151.
4. Gong, K.; Du, F.; Xia, Z.; Durstock, M.; Dai, L., *Science* **2009**, *323*, 760-764.
5. Coleman, J. N.; Lotya, M.; O'Neill, A.; Bergin, S. D.; King, P. J.; Khan, U.; Young, K.; Gaucher, A.; De, S.; Smith, R. J.; Shvets, I. V.; Arora, S. K.; Stanton, G.; Kim, H.-Y.; Lee, K.; Kim, G. T.; Duesberg, G. S.; Hallam, T.; Boland, J. J.; Wang, J. J.; Donegan, J. F.; Grunlan, J. C.; Moriarty, G.; Shmeliov, A.; Nicholls, R. J.; Perkins, J. M.; Grievson, E. M.; Theuwissen, K.; McComb, D. W.; Nellist, P. D.; Nicolosi, V., *Science* **2011**, *331*, 568-571.
6. Komsa, H.-P.; Kotakoski, J.; Kurasch, S.; Lehtinen, O.; Kaiser, U.; Krasheninnikov, A. V., *Phys. Rev. Lett.* **2012**, *109*, 035503.
7. Song, L.; Ci, L.; Lu, H.; Sorokin, P. B.; Jin, C.; Ni, J.; Kvashnin, A. G.; Kvashnin, D. G.; Lou, J.; Yakobson, B. I.; Ajayan, P. M., *Nano Lett.* **2010**, *10*, 3209-3215.
8. Cai, J.; Ruffieux, P.; Jaafar, R.; Bieri, M.; Braun, T.; Blankenburg, S.; Muoth, M.; Seitsonen, A. P.; Saleh, M.; Feng, X.; Mullen, K.; Fasel, R., *Nature* **2010**, *466*, 470-473.
9. Geim, A. K.; Novoselov, K. S., *Nat Mater* **2007**, *6*, 183-191.
10. Geim, A. K., *Science* **2009**, *324*, 1530-1534.
11. Seol, J. H.; Jo, I.; Moore, A. L.; Lindsay, L.; Aitken, Z. H.; Pettes, M. T.; Li, X.; Yao, Z.; Huang, R.; Broido, D.; Mingo, N.; Ruoff, R. S.; Shi, L., *Science* **2010**, *328*, 213-216.
12. Zhang, Y.; Tan, Y.-W.; Stormer, H. L.; Kim, P., *Nature* **2005**, *438*, 201-204.
13. Rao, C. N. R.; Sood, A. K.; Subrahmanyam, K. S.; Govindaraj, A., *Angew. Chem. Int. Ed.* **2009**, *48*, 7752-7777.

14. Bolotin, K. I.; Ghahari, F.; Shulman, M. D.; Stormer, H. L.; Kim, P., *Nature* **2009**, *462*, 196-199.
15. Park, S.; Ruoff, R. S., *Nat Nano* **2009**, *4*, 217-224.
16. Hernandez, Y.; Nicolosi, V.; Lotya, M.; Blighe, F. M.; Sun, Z.; De, S.; McGovern, I. T.; Holland, B.; Byrne, M.; Gun'Ko, Y. K.; Boland, J. J.; Niraj, P.; Duesberg, G.; Krishnamurthy, S.; Goodhue, R.; Hutchison, J.; Scardaci, V.; Ferrari, A. C.; Coleman, J. N., *Nat Nano* **2008**, *3*, 563-568.
17. Sun, Z.; Yan, Z.; Yao, J.; Beitler, E.; Zhu, Y.; Tour, J. M., *Nature* **2010**, *468*, 549-552.
18. Wang, M.; Fu, L.; Gan, L.; Zhang, C.; Rummeli, M.; Bachmatiuk, A.; Huang, K.; Fang, Y.; Liu, Z., *Sci. Rep.* **2013**, *3*, 1238.
19. Berger, C.; Song, Z.; Li, X.; Wu, X.; Brown, N.; Naud, C.; Mayou, D.; Li, T.; Hass, J.; Marchenkov, A. N.; Conrad, E. H.; First, P. N.; de Heer, W. A., *Science* **2006**, *312*, 1191-1196.
20. Stankovich, S.; Dikin, D. A.; Piner, R. D.; Kohlhaas, K. A.; Kleinhammes, A.; Jia, Y.; Wu, Y.; Nguyen, S. T.; Ruoff, R. S., *Carbon* **2007**, *45*, 1558-1565.
21. Liu, A. Y.; Cohen, M. L., *Science* **1989**, *245*, 841-842.
22. Hight, S. C.; Cheng, J., *Food Chem.* **2005**, *91*, 557-570.
23. Guimarães, J. R. D.; Roulet, M.; Lucotte, M.; Mergler, D., *Sci. Total Environ.* **2000**, *261*, 91-98.
24. Sallsten, G.; Nolkrantz, K., *Analyst* **1998**, *123*, 665-668.
25. Evans, O.; McKee, G. D., *Analyst* **1988**, *113*, 243-246.
26. Schreier, T. M.; Rach, J. J.; Howe, G. E., *Aquaculture* **1996**, *140*, 323-331.
27. Klassen, N. V.; Marchington, D.; McGowan, H. C. E., *Anal. Chem.* **1994**, *66*, 2921-2925.

28. Chang, M. C. Y.; Pralle, A.; Isacoff, E. Y.; Chang, C. J., *J. Am. Chem. Soc.* **2004**, *126*, 15392-15393.
29. Shi, G.; Lu, J.; Xu, F.; Zhou, H.; Jin, L.; Jin, J., *Anal. Chim. Acta* **2000**, *413*, 131-136.
30. King, D. W.; Cooper, W. J.; Rusak, S. A.; Peake, B. M.; Kiddle, J. J.; O'Sullivan, D. W.; Melamed, M. L.; Morgan, C. R.; Theberge, S. M., *Anal. Chem.* **2007**, *79*, 4169-4176.
31. Chen, W.; Cai, S.; Ren, Q.-Q.; Wen, W.; Zhao, Y.-D., *Analyst* **2012**, *137*, 49-58.
32. Chang, Q.; Zhu, L.; Jiang, G.; Tang, H., *Anal. Bioanal. Chem.* **2009**, *395*, 2377-2385.
33. Liu, S.; Tian, J.; Wang, L.; Luo, Y.; Sun, X., *RSC Adv.* **2012**, *2*, 411-413.
34. Thomas, A.; Fischer, A.; Goettmann, F.; Antonietti, M.; Muller, J.-O.; Schlogl, R.; Carlsson, J. M., *J. Mater. Chem.* **2008**, *18*, 4893-4908.
35. Matsumoto, S.; Xie, E. Q.; Izumi, F., *Diamond Relat. Mater.* **1999**, *8*, 1175-1182.
36. Goettmann, F.; Fischer, A.; Antonietti, M.; Thomas, A., *Angew. Chem. Int. Ed.* **2006**, *45*, 4467-4471.
37. Zhao, Y.; Liu, Z.; Chu, W.; Song, L.; Zhang, Z.; Yu, D.; Tian, Y.; Xie, S.; Sun, L., *Adv. Mater.* **2008**, *20*, 1777-1781.
38. Ferrari, A. C.; Rodil, S. E.; Robertson, J., *Phys. Rev. B* **2003**, *67*, 155306.
39. Lee, E. H.; Hembree, D. M.; Rao, G. R.; Mansur, L. K., *Phys. Rev. B* **1993**, *48*, 15540-15551.
40. Zhao, Z.-Q.; Chen, X.; Yang, Q.; Liu, J.-H.; Huang, X.-J., *Chem. Commun.* **2012**, *48*, 2180-2182.
41. Lee, J.-S.; Han, M. S.; Mirkin, C. A., *Angew. Chem. Int. Ed.* **2007**, *46*, 4093-4096.
42. Liu, X.; Tang, Y.; Wang, L.; Zhang, J.; Song, S.; Fan, C.; Wang, S., *Adv. Mater.* **2007**, *19*, 1471-1474.

43. Chandra, U.; Kumara Swamy, B. E.; Gilbert, O.; Sherigara, B. S., *Electrochim. Acta* **2010**, *55*, 7166-7174.
44. Meyer, J. C.; Geim, A. K.; Katsnelson, M. I.; Novoselov, K. S.; Booth, T. J.; Roth, S., *Nature* **2007**, *446*, 60-63.
45. Kuila, T.; Bose, S.; Khanra, P.; Mishra, A. K.; Kim, N. H.; Lee, J. H., *Carbon* **2012**, *50*, 914-921.
46. Marcano, D. C.; Kosynkin, D. V.; Berlin, J. M.; Sinitskii, A.; Sun, Z.; Slesarev, A.; Alemany, L. B.; Lu, W.; Tour, J. M., *ACS Nano* **2010**, *4*, 4806-4814.
47. Chen, D.; Feng, H.; Li, J., *Chem. Rev.* **2012**, *112*, 6027-6053.
48. Chen, P.; McCreery, R. L., *Anal. Chem.* **1996**, *68*, 3958-3965.
49. Shang, N. G.; Papakonstantinou, P.; McMullan, M.; Chu, M.; Stamboulis, A.; Potenza, A.; Dhesi, S. S.; Marchetto, H., *Adv. Funct. Mater.* **2008**, *18*, 3506-3514.
50. Zhou, K.; Zhu, Y.; Yang, X.; Luo, J.; Li, C.; Luan, S., *Electrochim. Acta* **2010**, *55*, 3055-3060.
51. Fang, Y.; Zhang, D.; Qin, X.; Miao, Z.; Takahashi, S.; Anzai, J.-i.; Chen, Q., *Electrochim. Acta* **2012**, *70*, 266-271.
52. Shao, Y.; Wang, J.; Wu, H.; Liu, J.; Aksay, I. A.; Lin, Y., *Electroanalysis* **2010**, *22*, 1027-1036.
53. Cao, X.; Zeng, Z.; Shi, W.; Yep, P.; Yan, Q.; Zhang, H., *Small* **2013**, *9*, 1703-1707.
54. Lin, S.; Shen, C.; Lu, D.; Wang, C.; Gao, H.-J., *Carbon* **2013**, *53*, 112-119.
55. Chen, D.; Feng, H.; Li, J., *Chemical Reviews* **2012**, *112*, 6027-6053.
56. Yu, B.; Feng, J.; Liu, S.; Zhang, T., *RSC Adv.* **2013**, *3*, 14303-14307.

CHAPTER 5

Iron oxide nanoparticles embedded on Carbon nitride matrix: Synthesis, magnetic property and Photocatalytic degradation of Organic dye

5.1. Introduction

In the last decades the study of magnetic nanomaterials including synthesis of new magnetic materials and understanding its spin dynamics and spin transport property is one of the goals to the scientific community. The magnetic nanoparticles has application into the ultrahigh density media to storage the information, in spin transistor with high gain, in magnetic recording media and as a nanobiomagnetic sensor¹. The nanomagnetic materials can be used as nearly 100% spin polarized material to create a circuit. It can also be used in magnetic random access memory (MRAM) chip, a spintronic device which is better than semiconductor charge based RAM and also in magnetic logic, a new spintronic device used in computer technology¹. There are different types of magnetic nanoparticle for example ferromagnetic, paramagnetic, superparamagnetic and antiferromagnetic materials. Superparamagnetic material does not magnetise in presence of magnetic field. Superparamagnetic nanoparticle has got interest due to its different biomedical applications. It can be used as contrast agent for magnetic resonance imaging (MRI) or tumor therapy or cardiovascular disease². It also used in drug delivery in medical science. Iron oxide nanoparticle is one of the best candidates for the use as a superparamagnetic material which is called superparamagnetic iron oxide nanoparticle (SPION). Each SPION acts like single domain and the corresponding magnetic moment of each particle is oriented in same direction. This

nature of SPION can be proved by measuring the field dependent magnetization. The SPION particles have no hysteresis cycles i.e. null value of remnant magnetization and coercive field proves its superparamagnetic nature³. As the SPIONs behave like single domain therefore the nanoparticles do not interact each other, helps to protect from the aggregation of the nanoparticles. This property helps the SPIONs to be applicable in the vivo and vitro studies of biomedical application. SPIONs has got more interested in the field of medical science especially in the drug delivery application due to its good biocompatible property⁴. SPIONs can be used as contrast agent for magnetic resonance imaging of bone marrow, bowel, liver etc⁵. Addition with this it has various applications in the field of catalysis reaction⁶ and environmental pollutant remedy⁷. Among different iron oxide compounds hematite (α -Fe₂O₃), maghemite (γ -Fe₂O₃) and magnetite (Fe₃O₄) got more interest in the different application fields. Iron oxide magnetic nanoparticles can be synthesized by hydrothermal method⁸, chemical precipitation method⁹, thermal decomposition method¹⁰, one pot microemulsion method¹¹, sonochemical synthesis method¹², laser pyrolysis method¹³ and electrochemical synthesis method¹⁴. High saturated magnetization value of magnetic nanomaterials makes it more applicable in different application field. The saturated magnetization value of SPION can be controlled by changing the size and shape of the nanomaterials. For this purpose a large number of coating materials has been used for example alkoxysilane³, mesoporous silica¹⁵. It is known that iron oxide nanoparticle will behave as superparamagnetic at room temperature when the particle size of the iron oxide nanoparticles are less than 15 nm. The experimental difficulties to synthesis the superparamagnetic iron oxide nanoparticle is its aggregation phenomenon. To prevent the aggregation property different coating materials such as gold, silver, cobalt oxide has been used.

Beside this different 2D carbon based material can also be used as a support material to prevent the aggregation property of iron oxide nanoparticles.

Dyes are widely used in different industries for example textile, leather, painting, photography, printing etc. During the use of dye in different industries they are coming out as waste water which is creating environmental pollution. Dyes have high chemical and biological stability. Therefore removal of these dyes is very much important. There are different removal technologies to remove dyes from waste water. We can divide the technological methods in three different categories- biological method¹⁶, physical methods (membrane filtration¹⁷, nanofiltration, electrodialysis, adsorption¹⁸ etc.) and chemical methods (e.g. coagulation-flocculation¹⁹, electrochemical oxidation²⁰ etc.). Each technological method has some disadvantages. For example, membrane filtration method, one of the physical technological methods has the disadvantage of limited life time, high cost of membrane and periodic replacement of membrane. The major disadvantage of chemical method is disposal problem due to sludge accumulation during the chemical process. The disadvantage associated with biological method is slow kinetic process. Therefore, in recent studies proves that photo degradation is an efficient method to remove the dyes from waste water. During photodegradation study with photocatalyst recombination between electron and hole decreases the overall quantum efficiency of the photocatalyst²¹. Therefore it is challenging to synthesis a photocatalyst which can prevent to recombination process between electron and hole. Two dimensional (2D) graphene, due to its unique physical and chemical properties²²⁻²³ such as high specific surface area, excellent electrical conductivity, high charge carrier mobility, high mechanical strength, became a promising candidate as a support for different nanoparticles forming a composite material²⁴. The metal (Au, Pt) or semiconductor (TiO₂, ZnO) nanoparticles decorated graphene have been used

as an effective nanocomposite material for photovoltaic²⁵, fuel cell and biosensor²⁶⁻²⁷ applications. Now a day, 2D g-C₃N₄ is used as a complement material of 2D graphene material due to its similar structure like graphene. Among different allotrope of carbon nitride, g-C₃N₄ is considered the most stable allotrope in ambient condition. Graphitic carbon nitride (g-C₃N₄), a metal-free 2D material with layered structure possesses moderate band gap, high chemical stability and suitable valence and conduction band potentials which leads to a potential application in the photocatalysis, organic reactions and fuel cell. However, it has been found that g-C₃N₄ has some demerits in the field of photocatalytic study. It has narrow visible light response range which limits its broad range of visible light. Fast charge recombination rate between electron and hole and slow rate of charge transport of g-C₃N₄ decreases the efficiency of photocatalysis²⁸. To overcome these drawbacks of g-C₃N₄, mesoporous carbon nitride composite²⁸ or metal doped carbon nitride²⁹⁻³¹ has been used in photo degradation study. The synthetic procedure of mesoporous compound needs high temperature and need to use hazardous materials which is not environmental friendly. Sometimes it is difficult to remove the template during synthesis of mesoporous composite. Among metal doped carbon nitride compound iron is more suitable due to its low cost, high stability and strong connectivity through interface between carbon nitride and metal ions. In g-C₃N₄ moiety there are repeated triazine units containing six nitrogen lone pairs which has strong potential to bind with metal ions. Thus, 2D sheet of carbon nitride can be considered as feasible alternative for stabilizing metal nanoparticles for their unusual catalytic properties. There is different metal oxide doped graphitic carbon nitride composite which are used in the photocatalytic dye degradation study with higher efficiency than pure carbon nitride³²⁻³⁴. Different noble metal doped graphitic carbon nitride^{29, 35} is used as photocatalyst but due to its high cost low cost metal doped such as iron doped

graphitic carbon nitride³⁶⁻³⁷ has been focused to be use as photocatalyst. To utilize the solar energy it is highly demandable to synthesis the catalyst which can do degradation of different dyes under sunlight.

5.2. Synthesis method of Fe₃O₄-CN_x composite

6.0 mg of graphitic carbon nitride was dispersed in 3 ml of water by sonication for 10 min. In another vial 0.03 g of iron (III) chloride was taken in 5 ml of water. 3.0 mg of sodium borohydride was added to the iron (III) chloride solution. Next, this solution is mixed with the dispersed g-CNQDs sonicated for 15 min. Finally, the mixture was ultra sounded with 28 kHz frequency for 2 hours at 400 watt. After ultrasound the solid product was separated by centrifugation washing this solid product with water and vacuum dried, was taken for further characterization and others experimental procedure. The Fe₃O₄-CN_x composite with different amount of iron loading were prepared by ultrasonic treatment of graphitic carbon nitride and taking different amount of iron chloride (FeCl₃) solid. The maximum loading of iron in the composite we could achieve is 80 wt%. The catalytic activity of Fe₃O₄-CN_x composite is better when iron loading into Fe₃O₄-CN_x composite is 40–50 wt%. Therefore the characterization and all the measurements were done with 40 wt% iron loaded Fe₃O₄-CN_x composite.

5.3. Characterization

The characterization of the synthesized Fe₃O₄-CN_x composite was done by using p-XRD, TEM, SEM, XPS and FT-IR-spectroscopy measurements. There are different crystallographic phases of iron oxide compounds. The p-XRD was done to determine the crystallographic phases of iron oxide present into the composite. The p-XRD pattern of the Fe₃O₄-CN_x composite also gives the

information about the crystallographic phases of carbon nitride support into the composite. Figure 5.1 (a) shows the p-XRD diffraction pattern of the composite. In the Figure 5.1 (a) five distinguished peaks are observed at different 2θ values of 27.3° , 35.5° and 44.7° , 56.2° and 62.8° . The p-XRD diffraction pattern demonstrates that the diffraction peaks at 2θ value of 35.5° , 44.7° , 56.2° and 62.8° correspond to the (321), (400), (511) and (440) reflection planes of cubic phase of magnetite Fe_3O_4 compound (JCPDS No. 65-3107) respectively³⁸. This confirms the formation of Fe_3O_4 nanoparticles into the $\text{Fe}_3\text{O}_4\text{-CN}_x$ composite by ultrasonic treatment. In addition, p-XRD pattern of the composite shows the peak at 2θ value of 27.3° corresponding to the (002) plane of graphitic carbon nitride with interlayer d-spacing of 3.27 \AA .

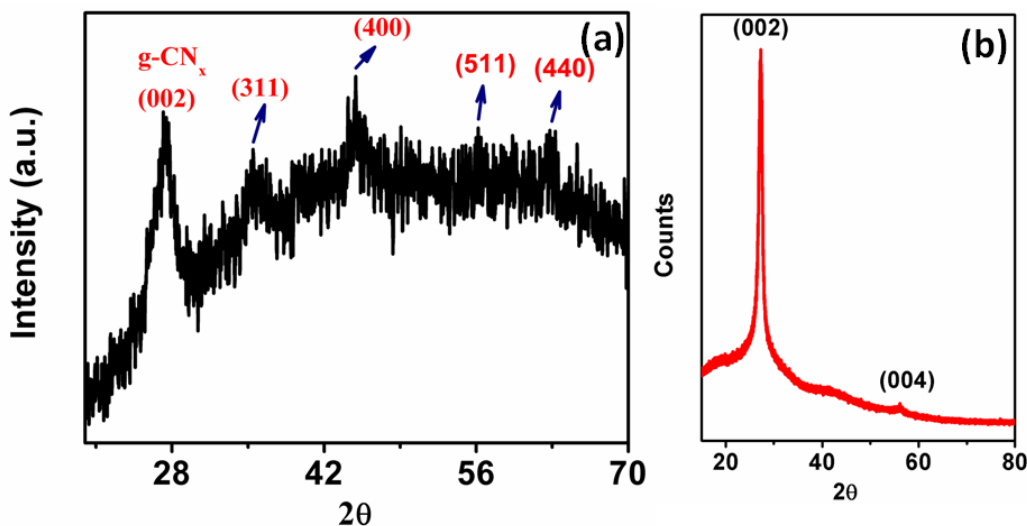


Figure 5.1. (a) p-XRD diffraction pattern of $\text{Fe}_3\text{O}_4\text{-CN}_x$ composite. (b) p-XRD diffraction pattern of graphitic carbon nitride.

The p-XRD diffraction pattern of the graphitic carbon nitride is also given in Figure 5.1 (b). The presence of peak at 2θ value of 27.3° in the $\text{Fe}_3\text{O}_4\text{-CN}_x$ composite suggests that graphitic nature

of carbon nitride remains into the composite even after loading of iron oxide but the intensity of the (002) peak in the p-XRD pattern of the composite is significantly decreases and the width, broadness of the peak increases significantly. This implies that there is strong interaction between Fe_3O_4 nanoparticles and g-CN_x material³⁶. The morphology of the $\text{Fe}_3\text{O}_4\text{-CN}_x$ composite was investigated by doing transmission electron microscopy (TEM) and field emission scanning electron microscopy (FESEM). TEM sample was prepared on TEM grid after evaporation of the well dispersed aqueous solution of the composite. Figure 5.2 (a) shows the TEM image of $\text{Fe}_3\text{O}_4\text{-CN}_x$ composite. TEM image shows $\text{g-C}_3\text{N}_4$ sheets are observed with sharp edge and the small Fe_3O_4 nanoparticles are well distributed on the g-CN_x sheets.

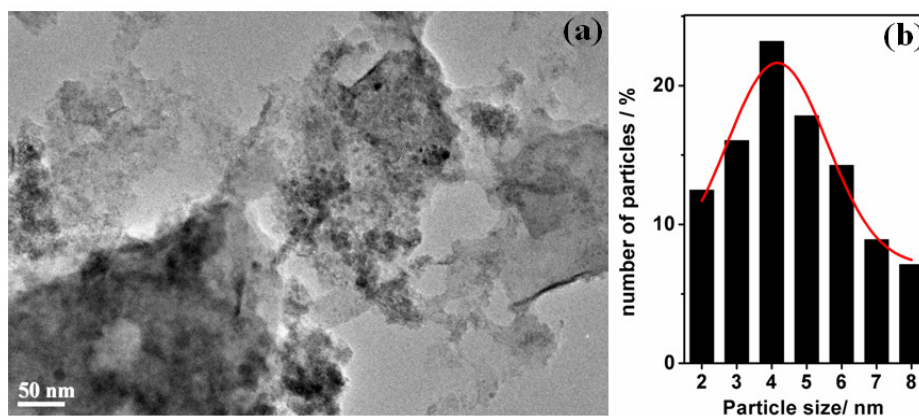


Figure 5.2. (a) TEM image of $\text{Fe}_3\text{O}_4\text{-CN}_x$ composite showing highly dispersed Fe nanoparticles on CN_x sheet. (b) Size distribution of Fe nanoparticle.

Figure 5.2 (b) shows the size distribution of Fe_3O_4 nanoparticles present on the size graphitic carbon nitride sheets calculated from the image in Figure 5.2 (a). It shows that sizes of iron oxide nanoparticles are from 2nm – 8nm with average size of ~5nm after fitting by Gaussian function.

The selected electron diffraction (SAED) pattern was done to study the crystal structure of the composite. Figure 5.3 (a) shows the SAED pattern of the composite taken from the TEM image presented in the Figure 5.2 (a). The interlayer spacing (d) calculated from the SAED pattern are 0.2928 nm, 0.2528 nm and 0.1480 nm corresponding to the (220), (311) and (440) planes magnetite cubic Fe_3O_4 magnetite nanoparticles respectively. Figure 5.3 (b) displays the high resolution transmission electron microscopy (HRTEM) image of $\text{Fe}_3\text{O}_4\text{-CN}_x$ composite. Lattice fringes have been observed in the HRTEM image proves the crystalline nature of $\text{Fe}_3\text{O}_4\text{-CN}_x$ composite. Lattice spacing of 0.252 nm and 0.148 correspond to the (311) and (440) plane of magnetite cubic Fe_3O_4 magnetite nanoparticles and 0.33 nm represents the (002) plane of graphitic carbon nitride sheet in the $\text{Fe}_3\text{O}_4\text{-CN}_x$ composite.

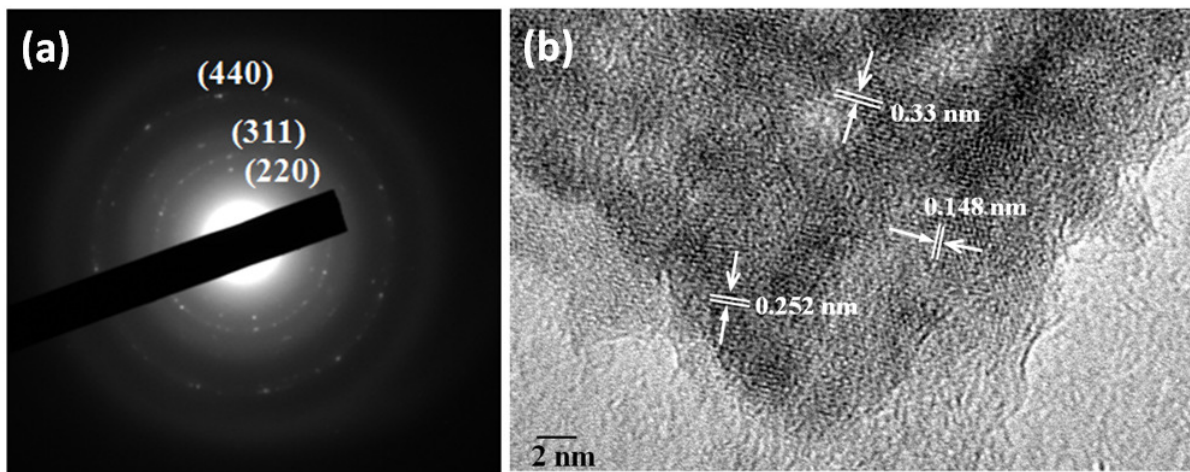


Figure 5.3. (a) HRTEM image of $\text{Fe}_3\text{O}_4\text{-CN}_x$ composite and (b) SAED pattern of $\text{Fe}_3\text{O}_4\text{-CN}_x$ composite taken from TEM image presented in Figure 5.4 (a).

Therefore, the crystal phases in $\text{Fe}_3\text{O}_4\text{-CN}_x$ composite from HRTEM image is exactly matching with the p-XRD pattern of it. From the p-XRD, SAED and HRTEM we can conclude that Fe_3O_4

nanoparticles are formed on the CN_x sheets both are crystalline in nature. Figure 5.4 represents the FESEM image of $\text{Fe}_3\text{O}_4\text{-CN}_x$ taken after evaporation of the composite material from its aqueous suspension on silicon wafer.

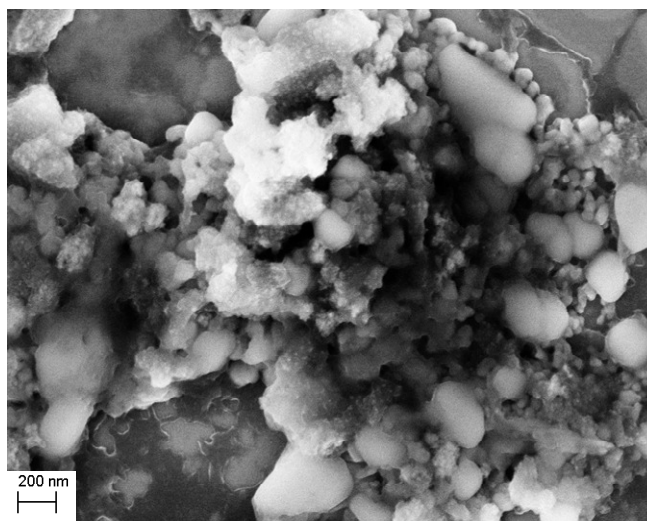


Figure 5.4. FESEM image of $\text{Fe}_3\text{O}_4\text{-CN}_x$ composite.

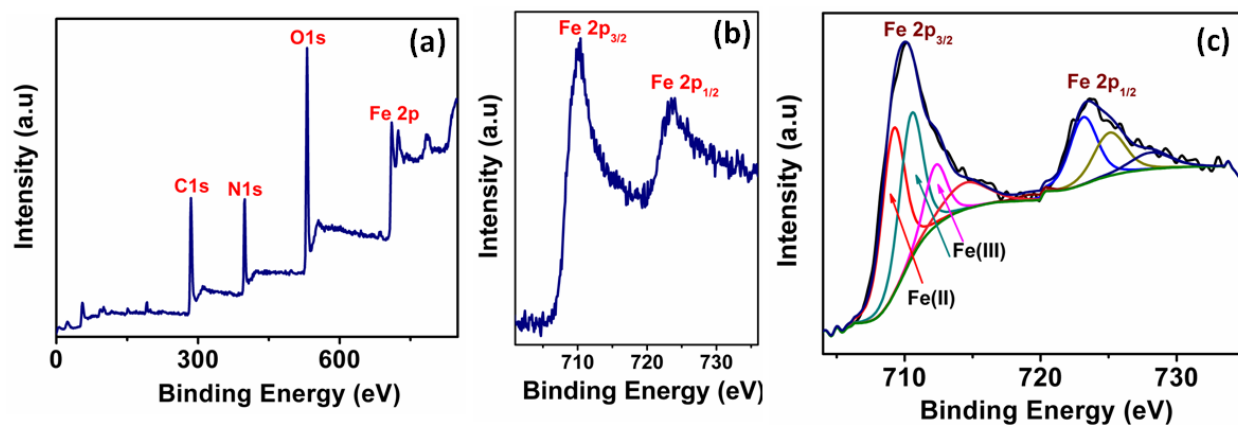


Figure 5.5. (a) XPS survey spectrum of $\text{Fe}_3\text{O}_4\text{-CN}_x$ composite. (b) High resolution Fe 2p XPS spectrum of $\text{Fe}_3\text{O}_4\text{-CN}_x$ composite (c) High resolution deconvoluted Fe 2p XPS spectrum of $\text{Fe}_3\text{O}_4\text{-CN}_x$ composite after fitting with Gaussian function.

From the FESEM image it is observed that very small Fe_3O_4 nanoparticles are formed and distributed all over on the surface of graphitic carbon nitride sheets which is consistent with the TEM image. X-ray photoelectron spectroscopy (XPS) measurement was carried out to know the chemical composition of the composite and the chemical environment of iron, carbon and nitrogen into the $\text{Fe}_3\text{O}_4\text{-CN}_x$ composite. Figure 5.5 (a) shows the survey scan of the XPS spectrum clearly indicates the presence of iron, carbon, nitrogen and oxygen atoms into the $\text{Fe}_3\text{O}_4\text{-CN}_x$ composite. In the survey scan there is no satellite peak at 718.0 eV which is a characteristic peak of Fe^{3+} in $\gamma\text{-Fe}_2\text{O}_3$ compound⁶. Therefore into the $\text{Fe}_3\text{O}_4\text{-CN}_x$ composite there is absence of $\gamma\text{-Fe}_2\text{O}_3$ phase. It is well known that the binding energy of Fe^{3+} oxidation state is appeared in the range of (710.3 – 711.8 eV)³⁷ for Fe $2p_{3/2}$ whereas the binding energy of Fe^{2+} oxidation state is appeared at 709.4 eV for Fe $2p_{3/2}$ ³⁹. The high resolution Fe 2p XPS spectrum of the synthesized composite has shown in Figure 5.5 (b).

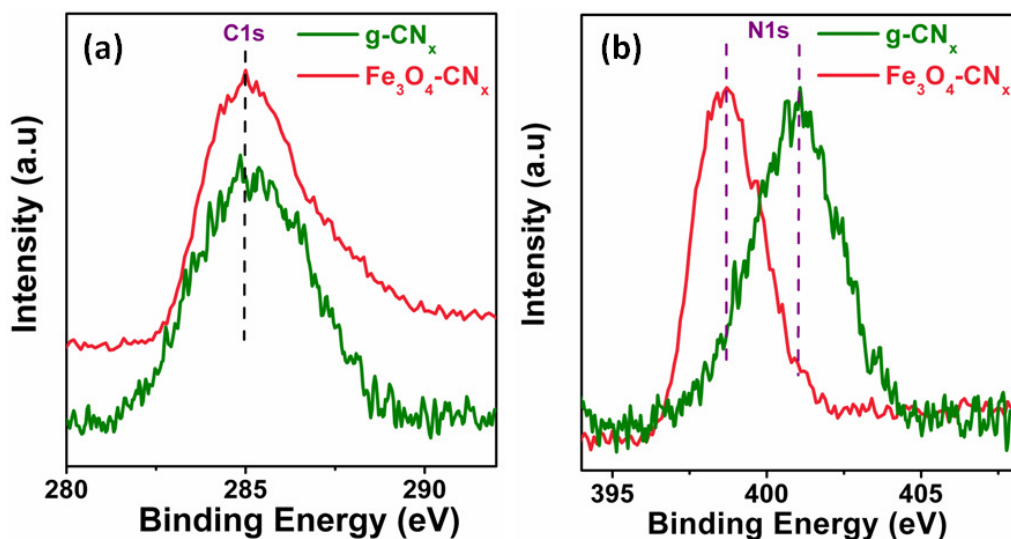


Figure 5.6. (a) XPS spectra of N1s region of $g\text{-C}_3\text{N}_4$ and $\text{Fe}_3\text{O}_4\text{-CN}_x$ composite. (b) XPS spectra of C1s region of $g\text{-C}_3\text{N}_4$ and $\text{Fe}_3\text{O}_4\text{-CN}_x$ composite.

The two distinct peaks at binding energy of 710.1 eV and 723.7 eV have been observed in the Figure 5.5 (b) and represents the Fe 2p_{3/2} and Fe 2p_{1/2} respectively. Both the peaks of Fe 2p are deconvoluted with using Gaussian function and shown in Figure 5.5 (c). In the high resolution deconvoluted Fe 2p XPS spectrum of the composite four peaks are appeared at binding energies of 709.3 eV, 710.6, 712.4 and 714.7 eV. The peaks at binding energies of 709.3 eV and 710.6 eV demonstrate the Fe 2p_{3/2} of Fe²⁺ oxidation state whereas the peak at binding energy of 712.4 eV demonstrates the Fe 2p_{3/2} of Fe³⁺ oxidation state. This proves that both Fe²⁺ and Fe³⁺ present into the Fe₃O₄-CN_x composite. A comparison study of the C1s XPS spectra of graphitic carbon nitride compound and Fe₃O₄-CN_x composite is shown in Figure 5.6 (a) whereas a comparison of their N1s XPS spectra is shown in Figure 5.6 (b). Figure 5.6 (a) demonstrates that there is no change of nature and position of C1s XPS spectra in Fe₃O₄-CN_x composite compare to graphitic carbon nitride.

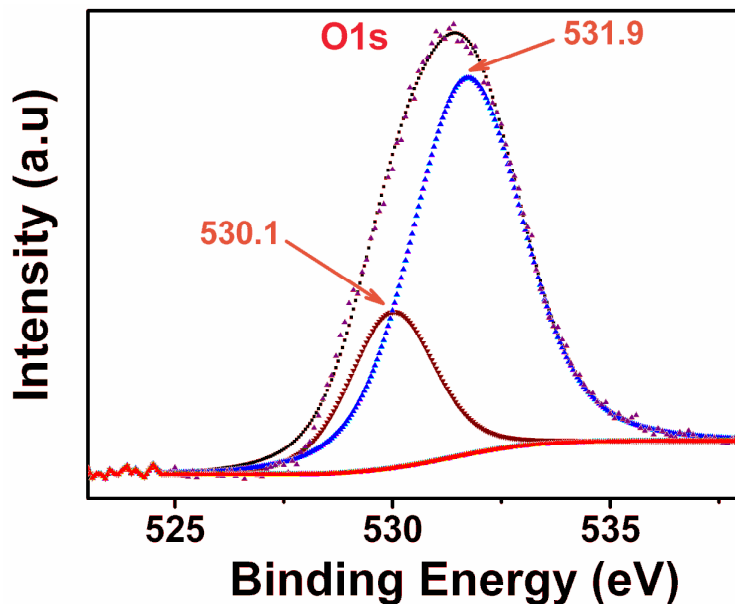


Figure 5.7. O1s XPS spectrum of Fe₃O₄-CN_x composite.

Figure 5.6 (b) represents that the N1s peak of $\text{Fe}_3\text{O}_4\text{-CN}_x$ composite becomes sharp and is shifted toward lower binding energy in comparison to that of graphitic carbon nitride compound. It proves that there is strong interaction between the Fe_3O_4 nanoparticles and the g- CN_x sheets. It is well known that the O1s peak at binding energy of 530.1 eV corresponds to the Fe-O bond of Fe_3O_4 compound⁴⁰. The high resolution O1s XPS spectrum of $\text{Fe}_3\text{O}_4\text{-CN}_x$ composite has shown in Figure 5.7. The O1s XPS spectrum of $\text{Fe}_3\text{O}_4\text{-CN}_x$ composite was deconvoluted into two peaks after fitting with the Gaussian function. There are two Gaussian peaks positioned at 530.1 eV and 531.9 eV of binding energies. The presence of peak at binding energy of 530.1 eV proves the formation of Fe_3O_4 nanoparticles in the composite. In the Figure 5.7 there is another peak at the binding energy of 531.9 eV corresponds to the C-O bond in CO_x present in graphitic carbon nitride (g- CN_x) compound. It is reported that the O1s peak of chemisorbed water appears at the binding energy of 534.7 eV⁴¹. The O1s XPS spectrum of $\text{Fe}_3\text{O}_4\text{-CN}_x$ composite falls at the binding energy region of 534.7 eV proves the presence of chemisorbed water into the composite.

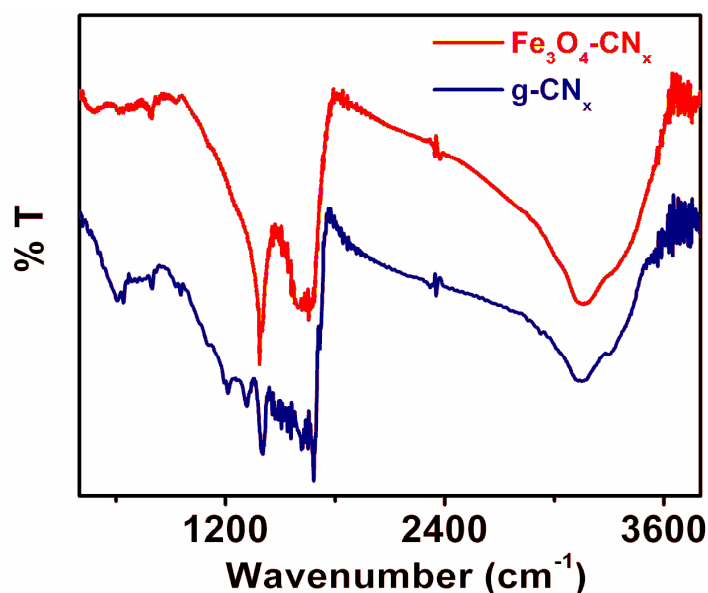


Figure 5.8. FT-IR spectra of graphitic carbon nitride and $\text{Fe}_3\text{O}_4\text{-CN}_x$ composite.

Figure 5.8 shows the Fourier-Transformed Infrared (FT- IR) spectra of $g\text{-C}_3\text{N}_4$ and $\text{Fe}_3\text{O}_4\text{-CN}_x$. The intense and sharp peaks observed at 1213, 1317 and 1408 cm^{-1} are due to stretching of aromatic C=N into the $g\text{-C}_3\text{N}_4$ moiety where 1213 cm^{-1} is for stretching of secondary amine and 1408 cm^{-1} is for stretching of tertiary amine which is observed in Figure 5.8. In the FT-IR spectra of $\text{Fe}_3\text{O}_4\text{-CN}_x$ the peaks at 1213 and 1317 cm^{-1} are completely disappeared after iron oxide doping into the $g\text{-C}_3\text{N}_4$ moiety. Additionally, in the FT-IR spectra of $g\text{-C}_3\text{N}_4$ the bands at 1559 and 1616 cm^{-1} are observed which correspond to the C=N stretching of $g\text{-C}_3\text{N}_4$ moiety. In the FT-IR spectra of $\text{Fe}_3\text{O}_4\text{-CN}_x$ those bands are also disappeared and instead of it a broad band centered at 1660 cm^{-1} has been observed. Therefore, FT-IR spectra reveal that there is strong interaction between iron oxide nanoparticles and the $g\text{-C}_3\text{N}_4$ moiety. Moreover, there is no change of -NH_x stretching frequency in the FT-IR spectra of $g\text{-C}_3\text{N}_4$ and $\text{Fe}_3\text{O}_4\text{-CN}_x$ composite which is observed at 3100 – 3400 cm^{-1} with broad in nature. The band at 800 cm^{-1} is the characteristic peak of s-triazine breathing mode of $g\text{-C}_3\text{N}_4$ moiety which remains intact after iron oxide doping.

5.4. Magnetic properties of $\text{Fe}_3\text{O}_4\text{-CN}_x$ composite

Magnetic properties of the iron oxide nanoparticles generally depend on the size of the nanoparticles and their crystalline phases. K Woo *et. al.*⁴² have synthesized different size of iron oxide magnetic nanoparticles and studied their magnetic properties by SQUID magnetometer. Magnetic properties of Fe_3O_4 nanoparticles depend on functionalization of it. J. Carvell *et. al.*⁴³ have synthesized different size of iron nanoparticles on silicon surface by high pressure sputtering technique. They have studied the magnetic properties of those nanoparticles by doing

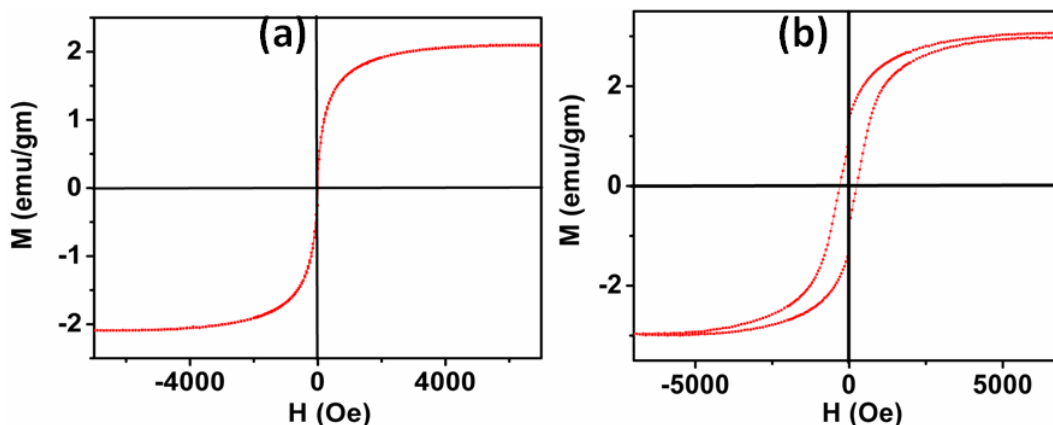


Figure 5.9. M vs. H curves of $\text{Fe}_3\text{O}_4\text{-CN}_x$ at (a) 300K (a) and (b) 2K.

measurement of field dependent magnetization and temperature dependent magnetization separately. They have observed that both the superparamagnetic and ferromagnetic particles are present into the synthesized iron nanoparticles. R. A. Bini *et. al.* have shown that the saturated magnetization value depends on different alkoxyisilane functionalized Fe_3O_4 nanoparticles³. We have studied the magnetic properties of the $\text{Fe}_3\text{O}_4\text{-CN}_x$ composite by field dependent and temperature dependent magnetization studies separately. Firstly, the magnetic properties of the synthesized $\text{Fe}_3\text{O}_4\text{-CN}_x$ composite have done by measuring the magnetic moment with varying magnetic field i.e. field dependent magnetization (M-H) measurement at 300K and 2K separately which is shown in Figure 5.9 (a ,b) respectively. At 300K the magnetic properties of $\text{Fe}_3\text{O}_4\text{-CN}_x$ shows that there is no Hysteresis loop at room temperature which proves its superparamagnetic behavior at 300K. At low temperature (2K) a clear Hysteresis loop has been observed in the field dependent magnetization magnetic curve of $\text{Fe}_3\text{O}_4\text{-CN}_x$ composite. At 300K the values of saturated magnetization and coercivity field are 2.08 emu gm^{-1} and 18.6 Oe respectively whereas at 2K saturated magnetization value and coercivity are 3 emu gm^{-1} and 250 Oe respectively. In

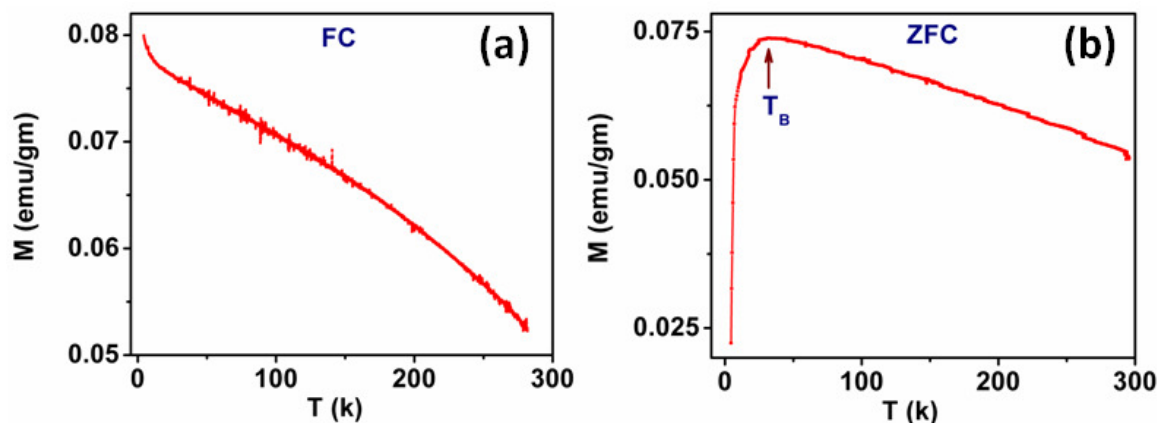


Figure 5.10. Temperature dependent magnetization plot with (a) FC and (b) ZFC processes.

order to confirm the superparamagnetic behavior of $\text{Fe}_3\text{O}_4\text{-CN}_x$ composite we have done FC and ZFC studies of this composite. Figure 5.10 represents the field cool/zero field cool (FC/ZFC) magnetization curve of the $\text{Fe}_3\text{O}_4\text{-CN}_x$ composite. Figure 5.10 (a) represents the temperature dependent field cooled magnetization curve of $\text{Fe}_3\text{O}_4\text{-CN}_x$ composite. From this curve it is clear that with increases the temperature the magnetization gradually decreases. Figure 5.10 (b) represents the temperature dependent zero field cooled magnetization curve of $\text{Fe}_3\text{O}_4\text{-CN}_x$ composite. It is shown that in the temperature dependent zero field cooled magnetization curve the magnetization value of the composite sharply increases with increase the temperature but after reach at certain temperature (42K), called blocking temperature (T_B) the magnetization value started to gradually decrease with increase the temperature. This proves that the $\text{Fe}_3\text{O}_4\text{-CN}_x$ composite shows super paramagnetic behavior with a blocking temperature of 42K. Figure 5.11 (a) demonstrates the field dependent magnetization curves at below the blocking temperature and above the blocking temperature. Below the blocking temperature there is no hysteresis loop whereas above the blocking temperature there is hysteresis loop. Therefore, the coercivity value

depends on the temperature. It is well known that coercivity value of magnetic materials depend on the temperature. Temperature dependence coercivity plot of the $\text{Fe}_3\text{O}_4\text{-CN}_x$ is shown in Figure 5.11 (b). From the Figure 5.11 (b) it has been observed that at high temperature there is negligible change of coercivity value of the composite material and also the composite material has low coercivity value at high temperature. The significant increase of coercivity value starts below 50K which is the good agreement with the blocking temperature obtained from temperature dependent magnetization plot (ZFC curve). It is well established that the coercivity of randomly oriented non interacting particle follow the following equation⁴⁴

$$H_c(T) = H_{C0} [1 - (T/T_B)^{1/2}]$$

where $H_c(T)$ is coercivity field at temperature TK and H_{C0} is the coercivity field at zero Kelvin temperature, T_B is the blocking temperature.

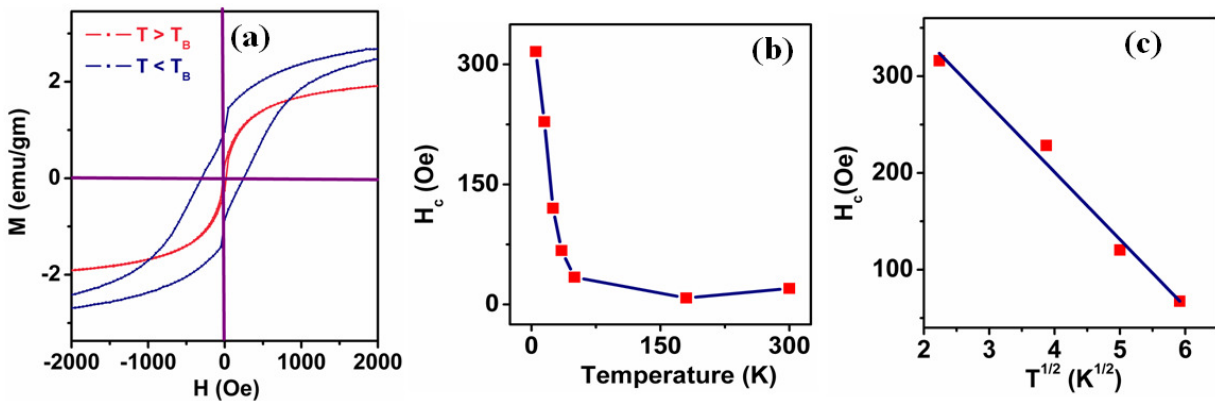


Figure 5.11. (a) M vs. H curves of $\text{Fe}_3\text{O}_4\text{-CN}_x$ composite below and above T_B . (b) Temperature dependence coercivity plot of $\text{Fe}_3\text{O}_4\text{-CN}_x$ composite. (c) Plot of H_c vs. $T^{1/2}$ showing the linear relationship.

Table 5.1. Magnetic characterization of various samples calculated from magnetic measurements

Sample	Particle size	H_{C0}	T_B	Ref.
Fe ₃ O ₄ -CN _x	5nm	482.7Oe	42K	this work
FeNPs/Si	3.8nm	---	113K	43
NiNPs/SiO ₂	3nm	780 Oe	20K	44
CoNPs/C	0.5-5nm	450Oe	160K	45
Spherical Iron oxide	~9.9nm	---	142K	46

Therefore, if we plot $H_c(T)$ vs. $T^{1/2}$ then from the slope we can get the blocking temperature (T_B) and from the intercept we can get the coercivity field at zero Kelvin temperature. Figure 5.11 (c) shows the plot of $H_c(T)$ vs. $T^{1/2}$ which follows the straight line with positive intercept. The T_B and H_{C0} were calculated from the slope and the intercept from Figure 5.11 (c) are 48 K and 482.7 Oe respectively. The blocking temperature (T_B) of 48K calculated from Figure 5.11 (c) has consistency with the obtained blocking temperature from ZFC curve (42K). K. Woo *et. al.*⁴² have synthesized 5 nm, 11 nm γ -Fe₂O₃ and 19 nm Fe₃O₄ nanoparticles. At the zero field cooling (ZFC) curve of 5 nm γ -Fe₂O₃ nanoparticles, the magnetization decreases rapidly with increase of temperature and shows 30K blocking temperature suggests that they are superparamagnetic nanoparticles without interaction among the particles. At the ZFC curve of 11 nm γ -Fe₂O₃ nanoparticles the magnetization decreases slowly with increase of temperature and shows 215K blocking temperature suggests that they are superparamagnetic nanoparticles with some interaction among the particles. The 19 nm Fe₃O₄ nanoparticles shows ferromagnetic in nature at

room temperature as in the ZFC curve the magnetization increases continuously with increase of temperature. In the ZFC curve of the synthesized $\text{Fe}_3\text{O}_4\text{-CN}_x$ composite shows blocking temperature of 42K and below this temperature the magnetization value decreases sharply with decrease the temperature proves that the Fe_3O_4 nanoparticles acts like non interacting dilute system. Blocking temperature and the coercivity field depend on the particle size of the magnetic nanoparticles. The particle size, coercivity field value (at zero Kelvin temperature) and blocking temperature of various compounds have been tabulated in the Table 5.1 and compared with the $\text{Fe}_3\text{O}_4\text{-CN}_x$ composite.

5.5. Application: Photocatalytic degradation of organic dye

5.5.1. Method of Photocatalytic activity study

Photocatalytic activity of $\text{Fe}_3\text{O}_4\text{-CN}_x$ catalyst has tested by using RhB dye under visible light and natural sunlight separately at room temperature and at neutral pH. Visible light photocatalytic studies have been done by using 130W Xenon lamp with a cutoff filter 3 ($\lambda > 400 \text{ nm}$). The distance between light source and analyzed sample was kept 20cm for each time of experiment. Photocatalytic experiment under natural sunlight was done in the month of April 2016 at NISER, Bhubaneswar, India between 12 am to 3 pm under clear sky. The photocatalytic studies were done with 5.0 mg of $\text{Fe}_3\text{O}_4\text{-CN}_x$ catalyst and 5.0 ml of 10ppm of RhB dye solution. At each time the catalyst was separated from the solution by centrifuge at a speed of 8000 rpm for 5 minutes. The degradation efficiency of photocatalytic degradation was evaluated by using following equation⁴⁷

$$\text{Degradation (\%)} = (C_0 - C)/C_0 \times 100 \%$$

where C_0 is the initial concentration of RhB dye and C is the concentration of RhB dye at time t .

5.5.2. Photocatalytic degradation of RhB on Fe₃O₄-CN_x composite

The pollution due to various dyes is one of the main environmental problems. It is thus important to remove the organic dye from aqueous media. The photocatalytic degradation of organic dye using a suitable photocatalyst is one of efficient method to remove organic dye from water. RhB is one of the most hazardous dye and widely used in several industries. We have chosen the RhB dye to study the photocatalytic activity of Fe₃O₄-CN_x composite. Here, the photocatalytic activity of the Fe₃O₄-CN_x catalyst was evaluated by degradation of RhB dye on irradiation of the visible light and natural sunlight separately in presence of hydrogen peroxide (H₂O₂). Before photodegradation study of RhB, adsorption of RhB dye was done by the Fe₃O₄-CN_x composite. In the typical adsorption process of RhB on Fe₃O₄-CN_x catalyst the photocatalyst was added into the water solution of 10 ppm RhB dye with continuous stirring and kept in dark for 6 hours to reach at adsorption equilibrium. After adsorption of RhB on the Fe₃O₄-CN_x photocatalyst, the composite material was removed from the solution by centrifugation. To monitor the adsorption process UV-visible adsorption method has been used for this study. UV-visible absorption spectra of RhB was done before and after adsorption by Fe₃O₄-CN_x composite separately which is shown in Figure 5.12. There is slight decrease of absorbance of RhB dye after adsorption process suggests that Fe₃O₄-CN_x composite has little adsorption property of the RhB dye. Since there is slight adsorption behavior of the RhB dye on Fe₃O₄-CN_x composite, therefore each photocatalytic degradation studies of RhB dye was done after this adsorption process. The

absorption maximum at 543 nm of UV- visible spectrum of RhB dye in its water solution was monitored for RhB degradation study by the photocatalyst.

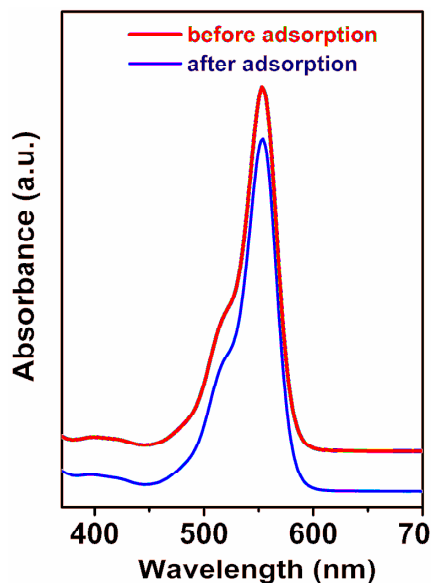


Figure 5.12. Adsorption study of RhB on Fe₃O₄-CN_x catalyst by UV-visible spectroscopy.

10 ppm initial concentration of RhB dye was taken during the photocatalytic studies. This is considered as initial concentration (C_0) for photocatalysis degradation of RhB dye. Photocatalytic degradation of RhB dye was done by using 130 watt visible light irradiation ($\lambda > 420$ nm). Figure 5.13 (a) shows the change of UV-visible absorption spectrum of RhB in presence of Fe₃O₄-CN_x photocatalyst and H₂O₂ under visible light irradiation. There is significant decrease of absorbance of RhB with visible light irradiation time in presence of Fe₃O₄-CN_x catalyst and H₂O₂. Here, H₂O₂ acts as an activating agent. Therefore, the catalyst has photocatalytic activity towards degradation of RhB under visible light irradiation in presence of H₂O₂. In order to understand the role of H₂O₂ we have performed photodegradation of RhB by

$\text{Fe}_3\text{O}_4\text{-CN}_x$ composite in presence of different concentration of H_2O_2 . Figure 5.13 (b) represents the H_2O_2 effect on the photocatalytic degradation study of RhB in presence of photocatalyst. This

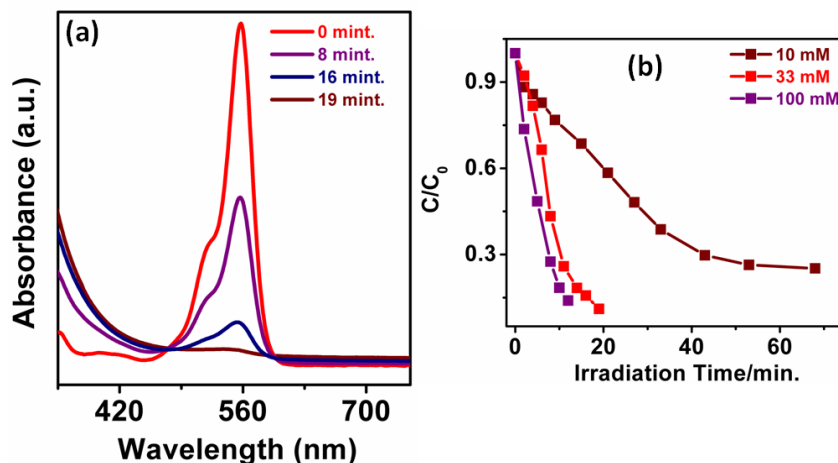


Figure 5.13. (a) Change of UV-Visible absorption spectra of aqueous solution of RhB in presence of $\text{Fe}_3\text{O}_4\text{-CN}_x$ composite and H_2O_2 under irradiation of visible light (concentration of $\text{H}_2\text{O}_2 = 33\text{mM}$). (b) Photocatalytic degradation of RhB dye in aqueous solution by $\text{Fe}_3\text{O}_4\text{-CN}_x$ composite under irradiation of visible light with different concentration of H_2O_2 .

Figure demonstrates that in absence of H_2O_2 the photocatalyst has negligible activity towards degradation of RhB dye under illumination of visible light. Three different concentrations of H_2O_2 were taken for the degradation study of RhB separately. At 10 mM concentration of H_2O_2 the photocatalyst was taking more than 70 minutes for complete degradation of RhB under illumination of visible light whereas at 33 mM and 100 mM concentration of H_2O_2 it is taking less than 20 minutes. Therefore, H_2O_2 has active role to promote the photocatalytic degradation process which is explained latter in details. The remaining all photocataytic studies were done by taking 33 mM H_2O_2 concentrations.

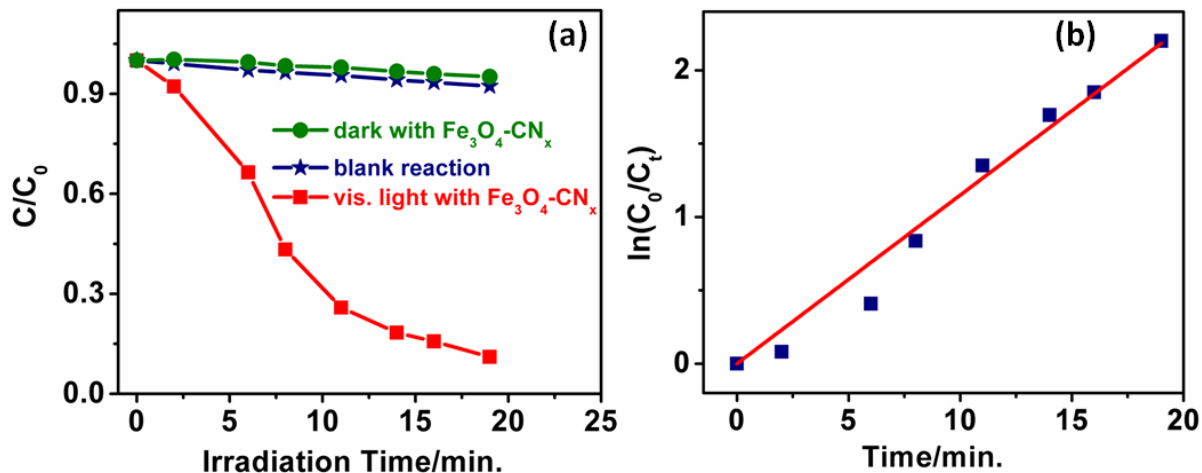


Figure 5.14. (a) The photocatalytic activity of Fe₃O₄-CN_x composite for RhB dye degradation under visible light irradiation. (b) The degradation kinetic of RhB on Fe₃O₄-CN_x catalyst under visible light irradiation.



Figure 5.15. Photograph showing the color of RhB solution on its photodegradation under visible light illumination by Fe₃O₄-CN_x catalyst.

Figure 5.14 (a) shows the plot of C/C_0 vs. the visible light irradiation time of RhB dye degradation in presence of 33mM H₂O₂ concentration and it is compared with two control

experiments. The control experiments were done in absence of light and in absence of Fe₃O₄-CN_x photocatalyst separately. There is significant change of C/C₀ value with the visible light irradiation time in presence of photocatalyst and H₂O₂ compare to the control experiments. It confirms that Fe₃O₄-CN_x catalyst has enhanced RhB dye removal efficiency under visible light irradiation in presence of H₂O₂. The photocatalyst has degradation efficiency of 90% in only 19 minutes under visible light irradiation proves that RhB shows excellent photo degradation efficiency with Fe₃O₄-CN_x under visible light irradiation. The rate of the photo oxidative degradation of RhB dye was measured by the Langmuir–Hinshelwood model, the equation is as follows

$$r = -dC/dt = kKC/(1 + KC)$$

where r is reaction rate, K is the absorption coefficient, k is reaction rate constant, and C is the reactant concentration. If the reactant concentration is low these equation reduced to

$$\ln(C_0/C) = kt$$

where k is the pseudo-first order rate constant, C₀ and C are the initial concentration and concentration after time t respectively⁴⁸. If we plot ln(C₀/C) vs. t then from the slope of this curve will get the pseudo-first order rate constant (k) value. Figure 5.14 (b) shows the degradation rate of the RhB in presence of photocatalyst. The plot of ln(C₀/C) vs. time (t) for RhB dye degradation using Fe₃O₄-CN_x photocatalyst is shown in Figure 5.14 (b) showing a straight line going through the origin with a positive slope. The rate constant for degradation of

RhB under visible light irradiation is found to be 0.115 min^{-1} . The degradation rate constant of RhB dye with the $\text{Fe}_3\text{O}_4\text{-CN}_x$ composite is compared with other reported photocatalysts and shown in Table 5.2. Although very small amount of catalyst (5.0 mg) was used for the degradation of high concentration of RhB dye (10 ppm) the rate constant value of the degradation process much higher than the other reported photocatalysts. This confirms that $\text{Fe}_3\text{O}_4\text{-CN}_x$ has high rate of photo degradation efficiency under irradiation of visible light. The Figure of before and after photodegradation of RhB under visible light irradiation have shown in Figure 5.15. The photocatalytic performance of RhB under natural sunlight is also studied and shown in Figure 5.16. Figure 5.16 (a) represents the photocatalytic degradation of RhB in presence of H_2O_2 under illumination of natural sunlight and compared with the control experiment. The control experiment was done in absence of photocatalyst under irradiation of natural sunlight.

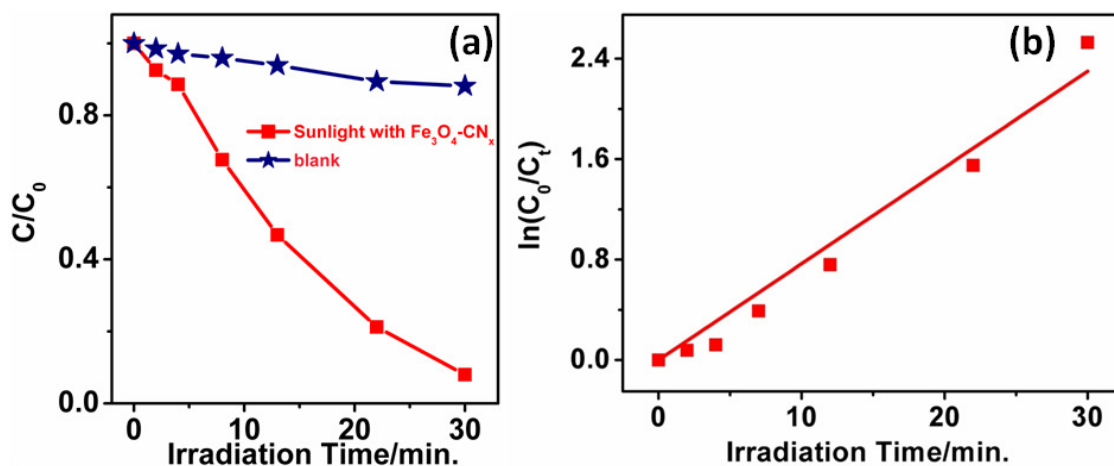


Figure 5.16. (a) The photocatalytic activity of $\text{Fe}_3\text{O}_4\text{-CN}_x$ composite for RhB dye degradation under sunlight irradiation (b) The degradation kinetics of RhB under Natural light irradiation. Conc. of $\text{H}_2\text{O}_2 = 33\text{mM}$.

Table 5.2. Comparison of rate constant for photocatalytic degradation of RhB dye by different photoactalysts under visible light irradiation

Photocatalyst	Catalyst amount	RhB conc.	Rate Constant (min ⁻¹)	Ref.
8-CN/NN	10mg	10ppm	0.0315	33
RGO-CuNO ₃	6.3mg	2.5ppm	0.0150	49
pg-C ₃ N ₄ /Ag/Fe ₂ O ₃ -2	25mg	5ppm	0.0895	50
CN-M-A	40mg	10ppm	0.0666	51
20wt%Ag@AgCl/Bi ₂ WO ₃	250mg	----	0.0005	47
CMTi-2	40mg	50ppm	0.0624	28
ZnO/Ag ₃ PO ₄	10mg	10ppm	0.0421	52
A-Fe ₂ O ₃ nanocube	50mg	----	0.8760	53
Fe ₃ O ₄ -CN _x	5mg	10ppm	0.115	this work

Therefore, the Figure 5.16 (a) represents that the Fe₃O₄-CN_x catalyst has higher photocatalytic activity under the irradiation of natural sunlight. The kinetic study of RhB dye degradation under irradiation of natural sunlight was also done and shown in Figure 5.16 (b). The rate of the photodegradation of RhB dye under natural sunlight irradiation was also measured by the Langmuir–Hinshelwood model which is discussed previously. The kinetic study RhB dye degradation follows the pseudo-first order kinetic model. The rate constant (k) for degradation of RhB is found to be 0.077 min⁻¹ under irradiation of natural sunlight. Therefore, Fe₃O₄-CN_x

catalyst has also high photocatalytic degradation efficiency with high rate of RhB under visible as well as natural sunlight irradiation.

5.5.3. Photocatalytic stability

In the photocatalytic study one of the most important properties of the catalyst is the photo stability and reusability of the catalyst for the practical application. To perform the photocatalytic stability and efficiency of the $\text{Fe}_3\text{O}_4\text{-CN}_x$ composite circulating run of the photocatalytic

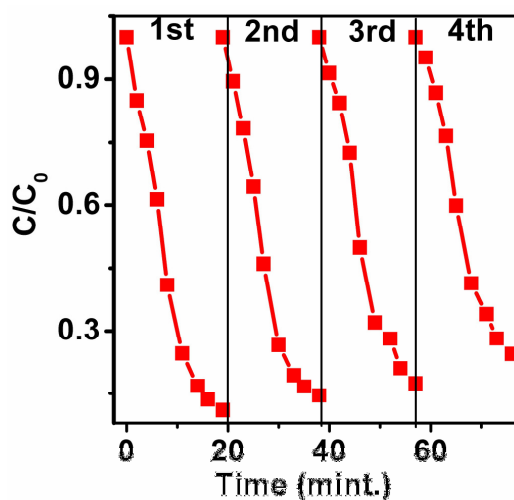


Figure 5.17. Degradation efficiency of $\text{Fe}_3\text{O}_4\text{-CN}_x$ composite with increasing number of catalytic cycles during degradation of RhB under visible light irradiation.

degradation process was done. The photocatalyst can be successfully recycled by centrifugation followed by washed with water and dried under vacuum. Four successive photocatalytic experiments were done to study the stability and reusability of the $\text{Fe}_3\text{O}_4\text{-CN}_x$ catalyst. Figure 5.17 shows the photocatalytic degradation efficiency of the catalyst with number of the cycles

under irradiation of visible light. The RhB degradation efficiency of $\text{Fe}_3\text{O}_4\text{-CN}_x$ catalyst is 90% after 1st cycle to 76% after 4th cycle. The catalyst has high photo stability up to four cycles with high degradation ability. Therefore, this photocatalyst has high power to prevent the corrosion effect during RhB dye degradation under visible light irradiation.

5.5.4. Proposed Photocatalytic mechanism

The $\text{Fe}_3\text{O}_4\text{-CN}_x$ composite have excellent photocatalytic activity towards degradation of RhB under illumination of visible light as well as natural sunlight. Therefore this composite material has high potential to be use as an efficient photocatalyst for dye removal. It is well known that the active species such as hydroxyl radicals (HO^\bullet), superoxide radicals ($\cdot\text{O}_2$), holes (h^+) are produced during photocatalytic reaction in presence of light during the photocatalytic dye degradation process. Therefore, it is very much essential to know that which active species are involved in the photocatalytic degradation reaction to understand the mechanism of the photocatalytic degradation study.

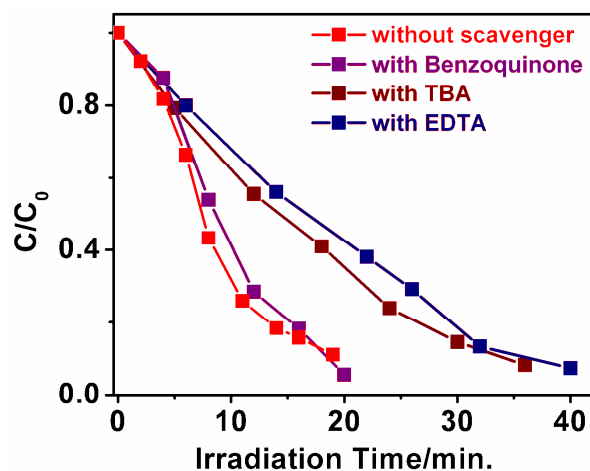


Figure 5.18. Scavenger effect on the rate of RhB dye degradation under irradiation of visible light, conc. of $\text{H}_2\text{O}_2 = 33\text{mM}$.

To know the role of different active species different scavengers are used during the photocatalytic degradation study which can deactivate the activity of the specific active species. Ethylenediamine tetraacetic (EDTA), tert-butyl alcohol (TBA) and benzoquinone are used as the scavengers in the photocatalytic degradation process. EDTA, TBA and benzoquinone are the scavenger of hole, hydroxyl radical and superoxide radical respectively. To study the photocatalytic mechanism of RhB degradation by $\text{Fe}_3\text{O}_4\text{-CN}_x$ composite TBA, benzoquinone and EDTA are introduced into the degradation system to entrap hydroxyl radical, superoxide radical and holes respectively. Figure 5.18 shows the effect of these scavengers on the degradation rate of RhB by Iron oxide - CN_x catalyst under illumination of visible light. Addition of EDTA and TBA separately inhibited the degradation of RhB under illumination of visible light which prove that hole and hydroxyl radical has significant role in photocatalytic degradation of RhB. The introduction of benzoquinone scavenger to the solution during photocatalytic degradation of RhB in presence of $\text{Fe}_3\text{O}_4\text{-CN}_x$ catalyst have no influences on the degradation rate, proves that superoxide radical has no role in the photocatalytic degradation rate of RhB. Therefore, effect of different scavenger on the degradation study proves that degradation rate of RhB by the $\text{Fe}_3\text{O}_4\text{-CN}_x$ composite depends on hole and as well on hydroxyl radical. As both Fe^{2+} and Fe^{3+} ions are present into the $\text{Fe}_3\text{O}_4\text{-CN}_x$ composite and the hydroxyl radical is involved in the photodegradation process of RhB; therefore we can illustrate this fact as Fenton/Fenton like process. It is well known that combination of Fe^{2+} and H_2O_2 and combination of Fe^{3+} and H_2O_2 are called Fenton reagent ($\text{Fe}^{2+}/\text{H}_2\text{O}_2$) and Fenton like reagent ($\text{Fe}^{3+}/\text{H}_2\text{O}_2$) respectively⁵⁴. Fenton and Fenton like reagent can generate hydroxyl radical efficiently and can degrade the dyes or organic pollutants. The following equations (equation number 1, 2 and 3) explain the mechanism for the formation of hydroxyl radical from the Fe^{2+} and Fe^{3+} ions⁵⁴. The presence of Fe^{2+} and

Fe^{3+} into the $\text{Fe}_3\text{O}_4\text{-CN}_x$ composite helps to generate the hydroxyl radical in presence of H_2O_2 and represents the Fenton and Fenton like process.

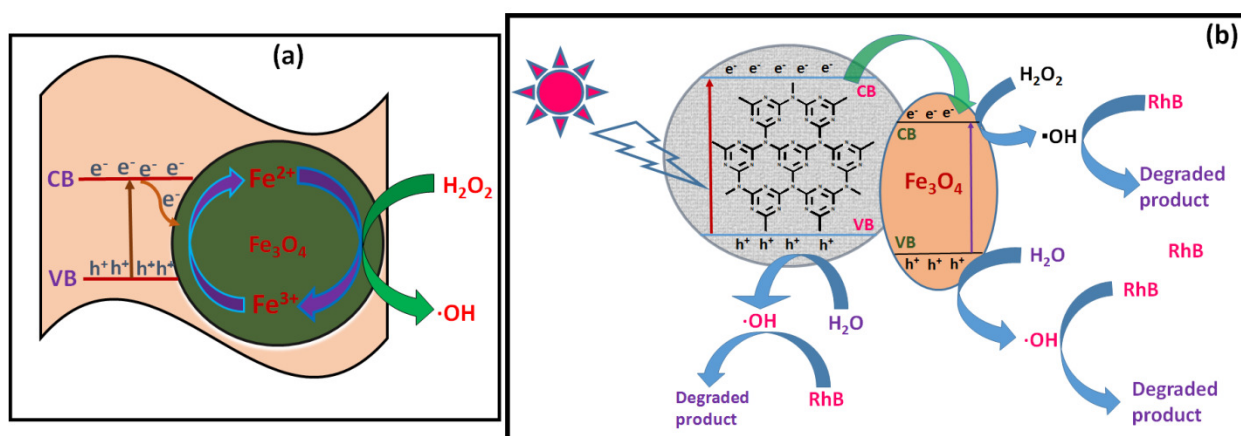


Figure 5.19. (a) Plausible mechanism of Fenton and Fenton like processes during photocatalytic degradation of RhB by $\text{Fe}_3\text{O}_4\text{-CN}_x$ composite. (b) The proposed photocatalytic mechanism of RhB degradation by $\text{Fe}_3\text{O}_4\text{-CN}_x$ composite under visible light irradiation.

On the basis of role of Fe^{2+} and Fe^{3+} ions into the $\text{Fe}_3\text{O}_4\text{-CN}_x$ composite a schematic diagram is shown in the Figure 5.19 (a). Under the visible light irradiation the photoinduced electrons are excited from valence band to conduction band of g-CN_x , forming the holes at the valence band of g-CN_x . The photoinduced electron present in the conduction band of g-CN_x can transfer to the

valence band of Fe₃O₄. This is very fast process due to formation of hetero-junction between Fe₃O₄ and the g-CN_x sheet. As this process is fast there is very little chance of recombination between electron and hole into the g-CN_x sheet which increases the efficiency of the photocatalyst. Therefore, the doped Fe₃O₄ nanoparticles facilitate the separation of photogenerated electron-hole pairs by forming hetero-junction to promote the interfacial electron transfer process. The photo-induced electron present in the conduction band of Fe₃O₄ can be trapped by hydrogen Peroxide to form hydroxyl radical. This hydroxyl radical is active agent to degrade the RhB dye. During the photocatalytic degradation of RhB by Fe₃O₄-CN_x composite hydrogen peroxide has been used as an activating agent. It has been observed that with increasing concentration of hydrogen peroxide the photocatalytic degradation rate increases; therefore, hydrogen peroxide has a great role to the photocatalytic degradation of RhB. The H₂O₂ also decreases the recombination process rate of electron and hole by accepting the photogenerated electron present in the conduction band of Fe₃O₄ and generates the hydroxyl radical by the following equation⁵⁵ (equation number 4)



Simultaneously, the photogenerated holes present in the valence band of g-CN_x and Fe₃O₄ can be trapped by water forming hydroxyl radical which also degrades the RhB dye. This hydroxyl radical destroys the RhB and different degraded products like carbon dioxide or small molecules are formed. All these electron transfer behavior to degrade the RhB dye is shown by drawing a schematic diagram shown in the Figure 5.19 (b).

5.6. Conclusion

We have prepared iron oxide nanoparticles decorated in carbon nitride sheet by ultrasound method. From TEM and FESEM analysis it is clear that iron oxide nanoparticle are uniformly distributed on the 2D carbon nitride sheet with average size of 5 nm. This composite material shows superparamagnetic behavior above its blocking temperature. Below the blocking temperature Fe_3O_4 nanoparticles are randomly oriented and behaves like a non interacting magnetic particles which follows the temperature dependent coercivity field equation $H_c(T) = H_{C0} [1 - (T/T_B)^{1/2}]$. The experimentally calculated coercivity field at zero temperature (H_{C0}) is 482.7 Oe. Due to this superparamagnetic behavior this composite can be used in different biomedical application as well as in different spintronic devices. It has shown that the $\text{Fe}_3\text{O}_4\text{-CN}_x$ composite has enhanced photocatalytic degradation property of RhB compare to the $\text{g-C}_3\text{N}_4$ due to efficient charge transfer property between iron metal and $\text{g-C}_3\text{N}_4$ moiety. It is an effective photocatalyst to remove the RhB dye in neutral condition from water. The photodegradation of RhB by the photocatalyst well fits to the pseudo first order kinetic model. The rate constant for degradation of RhB under visible light irradiation is 0.115 min^{-1} . The high photocatalytic activity of the composite towards degradation of RhB is due to good contact through surface between carbon nitride and iron particles which induces high photo induced charge separation. Therefore it can be used as an efficient heterogeneous photocatalyst for waste water treatment.

Chapter References

1. Bader, S. D., *Rev. Mod. Phys.* **2006**, 78, 1-15.
2. Neuberger, T.; Schöpf, B.; Hofmann, H.; Hofmann, M.; von Rechenberg, B., *J. Magn. Mater.* **2005**, 293, 483-496.

3. Bini, R. A.; Marques, R. F. C.; Santos, F. J.; Chaker, J. A.; Jafelicci Jr, M., *J. Magn. Magn. Mater.* **2012**, *324*, 534-539.
4. Mahmoudi, M.; Sant, S.; Wang, B.; Laurent, S.; Sen, T., *Adv. Drug Deliv. Rev.* **2011**, *63*, 24-46.
5. Wang, Y.-X. J.; Hussain, S. M.; Krestin, G. P., *Eur. Radiol.* **2001**, *11*, 2319-2331.
6. Verma, S.; Nasir Baig, R. B.; Han, C.; Nadagouda, M. N.; Varma, R. S., *Chem. Commun.* **2015**, *51*, 15554-15557.
7. Zhong, L. S.; Hu, J. S.; Liang, H. P.; Cao, A. M.; Song, W. G.; Wan, L. J., *Adv. Mater.* **2006**, *18*, 2426-2431.
8. Li, G.-y.; Jiang, Y.-r.; Huang, K.-l.; Ding, P.; Chen, J., *J. Alloys Compd.* **2008**, *466*, 451-456.
9. Yang, X.; Zhang, X.; Ma, Y.; Huang, Y.; Wang, Y.; Chen, Y., *J. Mater. Chem.* **2009**, *19*, 2710-2714.
10. Sun, S.; Zeng, H., *J. Am. Chem. Soc.* **2002**, *124*, 8204-8205.
11. Vidal-Vidal, J.; Rivas, J.; López-Quintela, M. A., *Colloids Surf., A* **2006**, *288*, 44-51.
12. Vijayakumar, R.; Kolytyn, Y.; Felner, I.; Gedanken, A., *Mater. Sci. Eng., A* **2000**, *286*, 101-105.
13. Bomatí-Miguel, O.; Mazeina, L.; Navrotsky, A.; Veintemillas-Verdaguer, S., *Chem. Mater.* **2008**, *20*, 591-598.
14. Pascal, C.; Pascal, J. L.; Favier, F.; Elidrissi Moubtassim, M. L.; Payen, C., *Chem. Mater.* **1999**, *11*, 141-147.
15. Gandhi, S.; Venkatesh, S.; Sharma, U.; Jagannathan, N. R.; Sethuraman, S.; Krishnan, U. M., *J. Mater. Chem.* **2011**, *21*, 15698-15707.

16. Ahmad, R.; Mondal, P. K.; Usmani, S. Q., *Bioresour. Technol.* **2010**, *101*, 3787-3790.
17. Xu, Y.; Lebrun, R. E.; Gallo, P.-J.; Blond, P., *Sep. Sci. Technol.* **1999**, *34*, 2501-2519.
18. Ghorai, S.; Sarkar, A.; Raoufi, M.; Panda, A. B.; Schönherr, H.; Pal, S., *ACS Appl. Mater. Interfaces* **2014**, *6*, 4766-4777.
19. Won, S. W.; Choi, S. B.; Chung, B. W.; Park, D.; Park, J. M.; Yun, Y. S., *Ind. Eng. Chem. Res.* **2004**, *43*, 7865-7869.
20. Lin, S. H.; Peng, C. F., *Water Res.* **1996**, *30*, 587-592.
21. Zhuang, J.; Dai, W.; Tian, Q.; Li, Z.; Xie, L.; Wang, J.; Liu, P.; Shi, X.; Wang, D., *Langmuir* **2010**, *26*, 9686-9694.
22. Novoselov, K. S.; Geim, A. K.; Morozov, S. V.; Jiang, D.; Katsnelson, M. I.; Grigorieva, I. V.; Dubonos, S. V.; Firsov, A. A., *Nature* **2005**, *438*, 197-200.
23. Zhang, Y.; Tan, Y.-W.; Stormer, H. L.; Kim, P., *Nature* **2005**, *438*, 201-204.
24. Xu, C.; Wang, X.; Zhu, J., *J. Phys. Chem. C* **2008**, *112*, 19841-19845.
25. Khurana, G.; Sahoo, S.; Barik, S. K.; Katiyar, R. S., *J. Alloys Compd.* **2013**, *578*, 257-260.
26. Shan, C.; Yang, H.; Han, D.; Zhang, Q.; Ivaska, A.; Niu, L., *Biosens. Bioelectron.* **2010**, *25*, 1070-1074.
27. Kavitha, T.; Gopalan, A. I.; Lee, K.-P.; Park, S.-Y., *Carbon* **2012**, *50*, 2994-3000.
28. Wang, H.; Yuan, X.; Wu, Y.; Zeng, G.; Chen, X.; Leng, L.; Li, H., *Appl. Catal. B: Environ.* **2015**, *174-175*, 445-454.
29. Cheng, N.; Tian, J.; Liu, Q.; Ge, C.; Qusti, A. H.; Asiri, A. M.; Al-Youbi, A. O.; Sun, X., *ACS Appl. Mater. Interfaces* **2013**, *5*, 6815-6819.
30. Ge, L.; Han, C.; Liu, J.; Li, Y., *Appl. Catal. A: General* **2011**, *409-410*, 215-222.

31. Chang, C.; Fu, Y.; Hu, M.; Wang, C.; Shan, G.; Zhu, L., *Appl. Catal. B: Environ.* **2013**, *142–143*, 553-560.
32. Wang, M.; Fu, L.; Gan, L.; Zhang, C.; Rummeli, M.; Bachmatiuk, A.; Huang, K.; Fang, Y.; Liu, Z., *Sci. Rep.* **2013**, *3*, 1238.
33. Chengjie, S.; Mingshan, F.; Bo, H.; Tianjun, C.; Liping, W.; Weidong, S., *CrystEngComm* **2015**, *17*, 4575-4583.
34. Yan, S. C.; Lv, S. B.; Li, Z. S.; Zou, Z. G., *Dalton Trans.* **2010**, *39*, 1488-1491.
35. Ge, L.; Han, C.; Liu, J.; Li, Y., *Applied Catalysis A: General* **2011**, *409–410*, 215-222.
36. Wang, X.; Chen, X.; Thomas, A.; Fu, X.; Antonietti, M., *Adv. Mater.* **2009**, *21*, 1609-1612.
37. Tonda, S.; Kumar, S.; Kandula, S.; Shanker, V., *J. Mater. Chem. A* **2014**, *2*, 6772-6780.
38. Han, R.; Li, W.; Pan, W.; Zhu, M.; Zhou, D.; Li, F.-s., *Sci. Rep.* **2014**, *4*, 7493.
39. Choudhury, T.; Saied, S. O.; Sullivan, J. L.; Abbot, A. M., *J. Phys. D: Appl. Phys.* **1989**, *22*, 1185.
40. Gu, F.; Liang, M.; Han, D.; Wang, Z., *RSC Adv.* **2015**, *5*, 39964-39972.
41. Ganguly, A.; Sharma, S.; Papakonstantinou, P.; Hamilton, J., *J. Phys. Chem. C* **2011**, *115*, 17009-17019.
42. Woo, K.; Hong, J.; Choi, S.; Lee, H.-W.; Ahn, J.-P.; Kim, C. S.; Lee, S. W., *Chem. Mater.* **2004**, *16*, 2814-2818.
43. Carvell, J.; Ayieta, E.; Gavrin, A.; Cheng, R.; Shah, V. R.; Sokol, P., *J. Appl. Phys.* **2010**, *107*, 103913.
44. Fonseca, F. C.; Goya, G. F.; Jardim, R. F.; Muccillo, R.; Carreño, N. L. V.; Longo, E.; Leite, E. R., *Phys. Rev. B* **2002**, *66*, 104406.

45. McHenry, M. E.; Majetich, S. A.; Artman, J. O.; DeGraef, M.; Staley, S. W., *Phys. Rev. B* **1994**, *49*, 11358-11363.
46. Chalasani, R.; Vasudevan, S., *J. Phys. Chem. C* **2011**, *115*, 18088-18093.
47. Liang, Y.; Lin, S.; Liu, L.; Hu, J.; Cui, W., *Appl. Catal. B: Environ.* **2015**, *164*, 192-203.
48. Bhowmik, T.; Kundu, M. K.; Barman, S., *RSC Adv.* **2015**, *5*, 38760-38773.
49. Xiong, Z.; Zhang, L. L.; Zhao, X. S., *Chem. Eur. J.* **2011**, *17*, 2428-2434.
50. Xue, J.; Ma, S.; Zhou, Y.; Zhang, Z.; Liu, X., *RSC Adv.* **2015**, *5*, 58738-58745.
51. Hu, S. W.; Yang, L. W.; Tian, Y.; Wei, X. L.; Ding, J. W.; Zhong, J. X.; Chu, P. K., *Appl. Catal. B: Environ* **2015**, *163*, 611-622.
52. Wang, J.; Xia, Y.; Dong, Y.; Chen, R.; Xiang, L.; Komarneni, S., *Appl. Catal. B: Environ.* **2016**, *192*, 8-16.
53. Bharathi, S.; Nataraj, D.; Senthil, K.; Masuda, Y., *J. Nanopart. Res.* **2012**, *15*, 1346.
54. Ai, Z.; Lu, L.; Li, J.; Zhang, L.; Qiu, J.; Wu, M., *J. Phys. Chem. C* **2007**, *111*, 4087-4093.
55. Cui, Y.; Ding, Z.; Liu, P.; Antonietti, M.; Fu, X.; Wang, X., *Phys. Chem. Chem. Phys.* **2012**, *14*, 1455-1462.

Chapter 6

Highly dispersed Platinum nanoparticles on Graphitic Carbon Nitride: A Highly efficient Electrocatalyst for Oxidation of Small Organic Molecules

6.1. Introduction

The depletion of the fossil fuels and environmental problems are continuously rising due to use of fossil fuels for increasing energy demand. There is a need of green alternate and sustainable energy source. The fuel cells which are considered as alternative green energy sources, transforms the chemical energy of fuel to electrical energy due to electrochemical oxidations of fuel molecule. The main advantages of fuel cell are that it has high efficiency to produce the energy, low cost and low pollutant emission¹. The research on electrochemical oxidation of small organic molecules such as methanol (CH₃OH), formic acid (HCOOH) and formaldehyde (HCHO) is important for the development of direct fuel cell due to their efficient energy converting power. The methanol is the most promising alcohol among all alcohols for fuel cell applications, since it has high solubility in aqueous electrolytes, easily handled, low cost, easily transportable and good storage property². Methanol can be produced from natural sources and it contains huge amount of energy (6000 W h kg⁻¹) can be used as future power needs². The Direct Methanol Fuel Cell (DMFC) is also better than hydrogen gas fed fuel cell. The hydrogen storage and transportation problems are the main issues in hydrogen

gas fed fuel cell³. In DMFCs, methanol is used as fuel, without converting methanol to hydrogen. The high energy conversion efficiency, low operating temperature, low pollutant emissions are also the advantages of DMFCs over hydrogen fuel cell. Thus, electrocatalytic oxidation of methanol with better efficiency is important for its application in DMFCs. The main obstacles for commercialization of DMFCs are the carbon monoxide (CO) poisoning, high methanol cross over from anode to cathode through the proton exchange membrane and slow kinetics of methanol electro oxidation due to its higher theoretical energy density⁴. The high methanol cross over problem can be overcome by improving the membrane or by developing a new membrane and the methanol oxidation kinetics can be improved by developing a new anode catalyst. Formic acid can be used as an alternative to the methanol fuel since formic acid is a strong electrolyte and is also electron and proton transporter. The Direct Formic Acid Fuel Cells (DFAFCs) has many advantages such as higher power density, low fuel crossover, higher energy efficiency and higher electromotive force (theoretical open circuit potential 1.48V vs. saturated hydrogen electrode)⁵. The main drawback in DMFC is the methanol crossover which is not the limitation for DFAFC⁶. The low fuel crossover in DFAFC is due to dissociation of formic acid to formate ions (HCOO^-) and their repulsive interaction⁷. The efficient formic acid oxidation is thus important for polymer electrolyte fuel cell applications. The main problem of Pt, usually used formic acid oxidation catalyst in DFAFCs, is the CO poisoning, since the electro oxidation of formic acid on Pt proceeds mostly through hydration (indirect) pathway forming large amount of poisonous CO species. The Platinum is known to be the best catalyst for the oxidation of methanol, formic acid and formaldehyde in fuel cells. The slow kinetics and CO poisoning are the

main issues of Pt catalyst. In addition, the cost of platinum is also one of main obstacles for the commercialization of fuel cells. The utilization of the Pt metals with proper way is thus important for their application in fuel cells. The PtNPs of few nanometers, narrow size distribution, stability and their high dispersion can provide proper utilization of the noble metals by increasing the electro catalytic activity. Several groups demonstrated that the rate of electrooxidation depends on size and shape of PtNPs⁸⁻⁹. Another important issue is the long term durability of carbon supported Pt-catalysts used for methanol, formic acid oxidation at anode. The normally used carbon support can easily electrochemically oxidized to carbon dioxide under fuel cell operating condition and this lead to structural degradation of support and PtNPs are also electrically detached from the support. The long term durability of fuel cell is reduced drastically due to migration, aggregation, oswald ripening¹⁰ of PtNPs. Usually, there are two common strategies available to improve catalytic activity and durability of Pt-catalysts: (1) by forming alloy of Pt with other metals and (2) by developing new support materials. H. Liu *et. al.* demonstrated the design and preparation of Ag-Pt bimetallic catalyst which have good electro catalytic activity towards methanol oxidation by decreasing the affinity of CO chemisorptions¹¹. The bimetallic catalyst also exhibited increased electrooxidation of formic acid by suppressing the formation of adsorbed CO. The electrocatalytic activity towards oxidation of methanol and formic acid is dependent on composition of bimetallic catalysts^{12-13,14,15}. The shape of bimetallic nanocatalyst can also play important role in enhancing the electro catalytic activity of formic acid oxidation¹⁶⁻¹⁷. The main drawback is in the synthesis of bimetallic catalyst, since it is important to maintain specific ratio of two metals and shape in order to achieve effective catalytic activities. Recently, focus has

been given to develop new support materials for the dispersion of metal nanoparticles, since they play an important role in improving the catalytic activity of the dispersed nanoparticles. The support material can modify the electronic property as well as structure of metal nanoparticles dispersed on the surface of support. Good support materials can prevent metal leaching, agglomeration and dissolution of the nanoparticles during fuel cell operation. In this context, a two dimensional support, graphene due to its unique physical and chemical properties¹⁸ such as high surface area, high electrical conductivity, high thermal stability has proven to be a very good supporting material for dispersion of nanoparticles for their high electrocatalytic activity^{19,20}. However, the low polarity and high hydrophobicity of the graphene carbon materials are the limitation for its electrocatalytic activity. The aggregation of graphene in aqueous solution and difficulties in uniform loading of metal nanoparticles on graphene surface prevent its further improvement in the electrocatalytic activities²¹. In acidic media, corrosion of the carbon support lead to agglomeration of nanoparticles leading to decrease the performance of the supported catalysts. In order to increase the stability and dispersion of the nanoparticles on the graphene surface, functionalization of graphene sheets is needed. Functionalization of graphene improves their solubility as well as their ability to disperse of nanoparticles on its surface. The attachment of graphene with polymer or surfactant molecules and oxidation of graphene to form graphene oxide, decrease the aggregation of graphene and high dispersion of metal nanoparticles improves for their electrocatalytic activities^{22,23}. Besides, doping of graphene with heteroatom such as boron, nitrogen etc can be applied to modify the properties of graphene. It is well known that nitrogen doped graphene can be used as support for the metal catalysts and enhanced electrocatalytic activity as well as

durability was observed resulting from strong catalyst-support interactions^{24-25,12}. Another two dimensional material, g-C₃N₄ which has similar graphene like structure, is also a promising support material due to the presence of abundant Lewis acid/ base sites for anchoring nanoparticles²⁶. The g-C₃N₄ supported metal/semiconductor nanoparticles composite have confirmed to be effective composites for the application in photocatalysis²⁷, organocatalysis²⁸, biosensors²⁹, electrochemical applications³⁰ etc. In recent years considerable efforts has been given to synthesize monometallic Pt catalysts supported on two dimensional (2D) nitrogen doped graphene²⁵ and three dimensional (3D) graphene porous composites³¹⁻³³ for electrochemical oxidation of methanol. Although the 3D architectures showed better performance for methanol oxidation, but, tolerance to carbonaceous species of Pt catalysts is still needed to improve^{24,34}. In addition, there are only few reports available in literature for monometallic Pt catalysts on electrochemical oxidation of formic acid and formaldehyde³⁵⁻³⁶. The oxidation of formic acid on monometallic^{37,36} Pt mainly proceeds through indirect (less preferred) pathways forming carbon monoxide, although several bimetallic catalysts^{14, 17, 38, 39} reported for direct pathway oxidation of formic acid. Thus, there is a need of new Pt-electrocatalyst for oxidation of methanol and formic acid for direct fuel cell applications.

6.2. Synthesis method of Pt/CN_x composite

g-CNQDs has been synthesized from formamide (HCONH₂) by microwave mediated method which is discussed in the third chapter of this thesis. The platinum nanoparticles (PtNPs) supported on carbon nitride was prepared by reduction of platinum salt solution in presence g-CNQDs using sodium borohydride (NaBH₄) as a reducing agent and by ultrasound treatment

method. The 11.5 mg of g-C₃N₄ was dispersed to 8.0 ml of water by sonication for 15 minutes. Then 0.08 (M) H₂PtCl₆, 6H₂O and 0.07284 gm NaBH₄ were added to the dispersed g-C₃N₄ solution. Sodium borohydride addition was performed slowly during stirring condition of the solution. This solution was subjected to ultra sounded for 140 minutes at 30⁰C temperature. During ultrasound treatment power of the instrument was kept at 400W with frequency 28,000 Hz. After ultrasound treatment the resultant solution was centrifuged at 16,000 rpm for 45 minutes. The solid product was then separated from the solution and it was dried under high vacuum for 12 hrs.

6.3. Characterization of Pt/CN_x composite

6.3.1. Characterization of Pt/CN_x by p-XRD method

The powder X-ray diffraction (p-XRD) patterns of Pt/CN_x composite and g-C₃N₄ are displayed in Figure 6.1. In both the p-XRD patterns, the peak at 2θ value of 27.2⁰ arise from graphitic (002) plane of g-C₃N₄. The p-XRD pattern of Pt/CN_x consists of five additional diffraction peaks positioned at 2θ values of 40.02⁰, 46.4⁰, 67.8⁰, 81.5⁰ and 86.1⁰

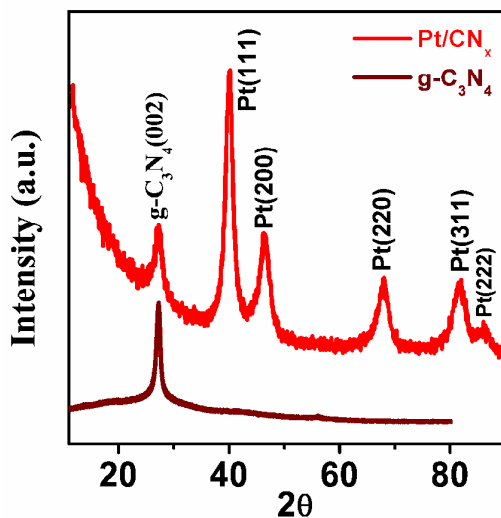


Figure 6.1. p-XRD of g-C₃N₄ and Pt/CN_x composite.

correspond to the (111), (200), (220), (311) and (222) planes respectively of the face centered cubic (fcc) lattice of platinum metal (JCPDS 04-0802). This suggests that the formation of PtNPs on CN_x. The size of the PtNPs was calculated from broadening of Bragg diffraction peak in the p-XRD pattern of Pt/CN_x composite by using the following Debye-Scherrer equation:

$$B = K \lambda / L \cos\theta$$

where K is shape factor with a value close to unity (the typical value of K is 0.9), θ is the Bragg angle, λ is the wavelength of the X-ray source, B is the line broadening at the half maxima in radians and L is the mean size of the particles. The highest intense diffraction peak, (111) plane of platinum was chosen to calculate the average size of PtNPs. The calculated average size of the PtNPs was 5 nm.

6.3.2. Characterization of Pt/CN_x by TEM analysis

The morphology of Pt/CN_x composite was studied by transmission electron microscope (TEM). The TEM samples were prepared by evaporating 10.0 μ L aqueous solution of the Pt/CN_x composite on TEM grid. Figure 6.2 (a) displays the TEM image of Pt/CN_x composites. It shows PtNPs are highly dispersed on 2D carbon nitride sheets. The particle size of PtNPs was calculated and their size distribution is shown in Figure 6.2 (b). The size of particles varies from 1 nm to 10 nm with average size of 5 nm. This is in good agreement with size calculated from the broadening of X-diffraction peak. The selected area electron diffraction (SAED) pattern is shown in Figure 6.2 (c) which suggests polycrystalline nature of this composite. The interlayer spacings calculated from SAED

image are 2.33, 2.02, 1.43, 1.27 and 0.92 Å which correspond to (111), (200), (220) and (311) and (222) planes of face centered cubic (fcc) platinum lattice respectively. Figure 6.2 (d) shows the energy dispersive spectroscopy (EDS) of Pt/CN_x catalyst obtained at the time of TEM measurement indicating the presence of platinum, nitrogen, carbon and small amount of oxygen in the Pt/CN_x composite. The high resolution transmission electron microscope (HRTEM) image is shown in Figure 6.3. In Figure 6.3 the lattice fringes with 2.24Å d spacing corresponds to the (111) plane of PtNPs whereas lattice spacing of 3.26 Å can be attribute to the (002) graphitic plane of carbon nitride.

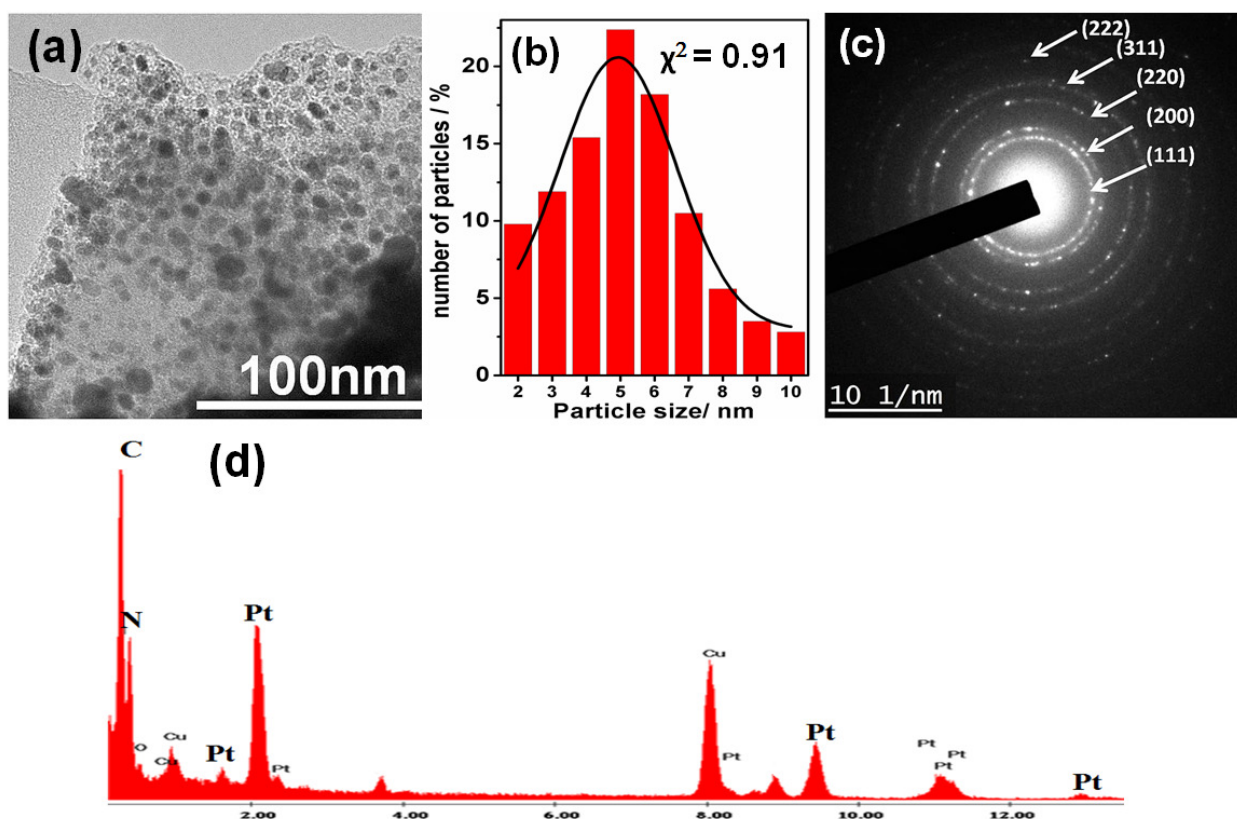


Figure 6.2. (a) TEM image of Pt/CN_x composite (b) PtNPs size distribution in Pt/CN_x composite (c) SAED pattern of Pt/CN_x composite showing (111), (200), (220) and (311) and (222) planes of PtNPs. (d) EDS spectrum of Pt/CN_x composite taken on the TEM image of Figure 6.2(a).

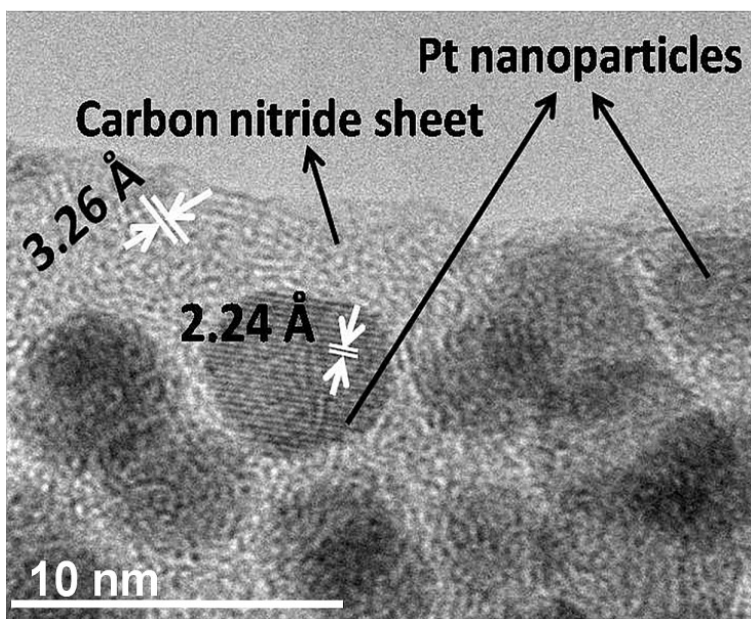


Figure 6.3. HRTEM image of Pt/CN_x composite.

6.3.3. Characterization of Pt/CN_x composite by FESEM analysis

FESEM sample was prepared by evaporation of 30.0 μl aqueous solution of Pt/CN_x composite on silicon wafer. Figure 6.4 show the FESEM images of the Pt/CN_x composite

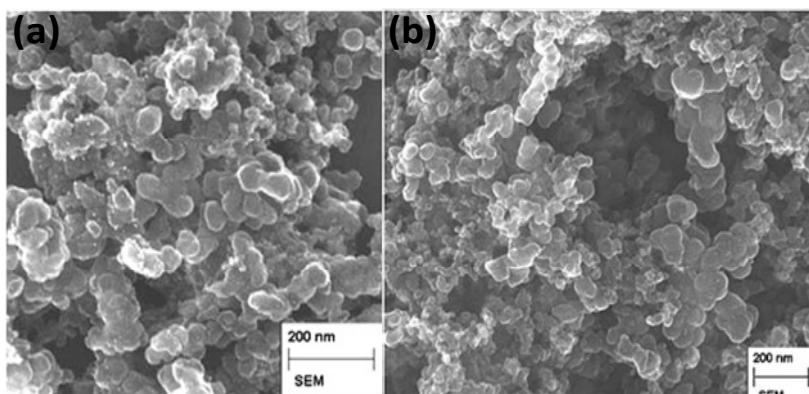


Figure 6.4. (a, b) FESEM images of Pt/CN_x composite showing porous morphology.

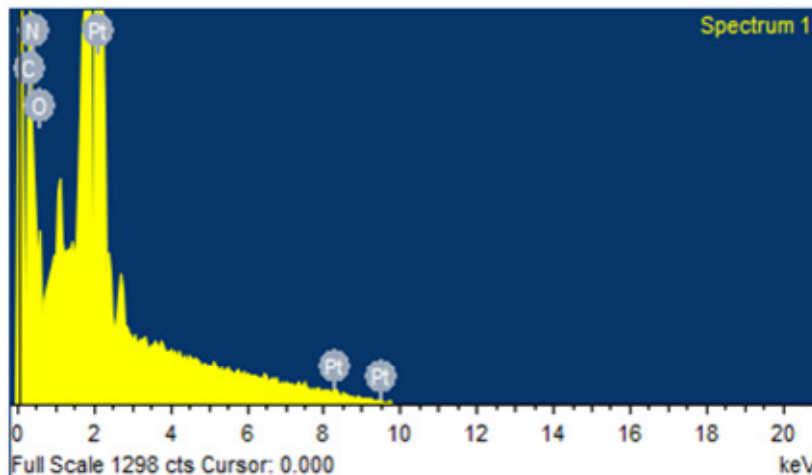


Figure 6.5. EDS spectrum of Pt/CN_x composite taken on the FESEM image showing the presence of C, N, O and Pt.

The small CN_x sheets containing small PtNPs are interconnected to porous morphology structure. Although all the PtNPs are not visible in the FESEM images, EDS measurements confirm the presence of PtNPs (Figure 6.5). Therefore, the p-XRD, TEM, SAED, HRTEM, FESEM and EDS prove the formation of PtNPs on CN_x sheets.

6.3.4. Characterization of Pt/CN_x by XPS analysis

X-ray photoelectron spectroscopy (XPS) measurement was performed to examine electronic property of Pt and CN_x support into the Pt/CN_x composite. The survey scan (Figure 6.6 (a)) of Pt/CN_x composite shows the presence of platinum, carbon, nitrogen and oxygen. It is known that the binding energies of platinum metal with oxidation state zero [Pt(0)] are 71.4 eV and 74.7 eV, corresponding to Pt 4f_{7/2} and Pt 4f_{5/2} respectively²⁵.

Figure 6.6 (b) represents the high resolution 4f Pt XPS spectrum of Pt/CN_x composite. The binding energies of Pt 4f_{7/2} and Pt 4f_{5/2} are observed at 71.9 eV and 75.2 eV respectively, suggesting a positive shifting of platinum binding energies of Pt/CN_x composite in comparison to metallic Pt(0).

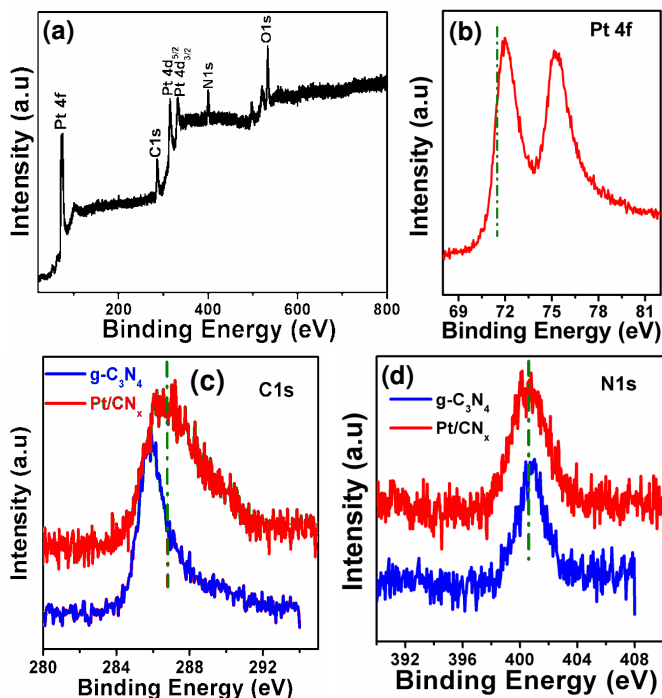


Figure 6.6. (a) XPS survey scan of Pt/CN_x composite. (b) XPS spectra of Pt 4f region of Pt/CN_x composite. (c) XPS spectra of C1s region of g-C₃N₄ and Pt/CN_x. (d) XPS spectra of N1s region of g-C₃N₄ and Pt/CN_x.

As shown in Figure 6.6 (c), the C1s XPS spectra of Pt/CN_x composite was compared with the C1s spectra of free CN_x support. It shows C1s peak becomes broad and binding energy is shifted towards 0.8 eV higher values as compared to free CN_x. In addition, the

comparison of N1s XPS spectra of Pt/CN_x and g-CNQDs is also shown in Figure 6.6 (d). The shape as well as position of N1s XPS spectra in Pt/CN_x remains same. The significant change of binding energies of C1s and Pt4f of Pt/CN_x in compared to that of g-C₃N₄, suggest strong interaction between a PtNPs and CN_x support.

6.3.6. Characterization of Pt/CN_x composite by FT-IR spectroscopy

FT-IR spectroscopy measurements were performed to examine electronic property of Pt and CN_x support. The Fourier transform infrared (FT-IR) spectra of g-C₃N₄ and Pt/CN_x were displayed in Figure 6.7. In FT-IR spectrum of g-C₃N₄, two peaks at 1245 cm⁻¹ and 1400 cm⁻¹ correspond to the aromatic C=N stretching and the peak at 1630 cm⁻¹ can be attributed to the C=N stretching. The FT-IR spectrum of Pt-CN_x composite is significantly different from that of free CN_x. The two peaks at 1245 cm⁻¹ and 1400 cm⁻¹ of

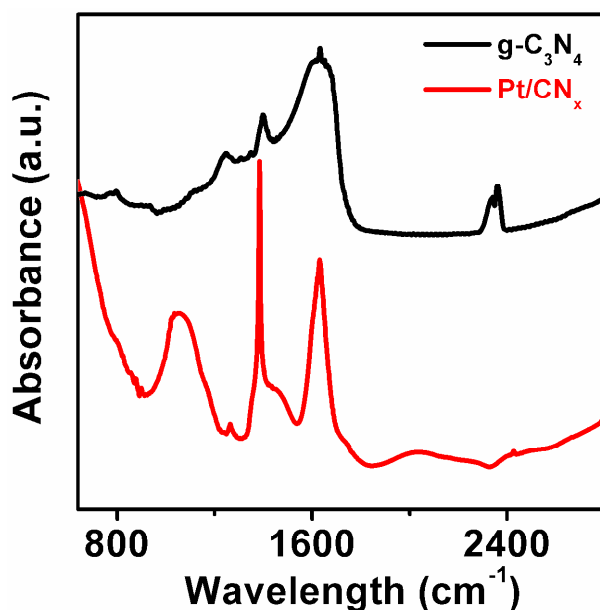


Figure 6.7. FT-IR spectra of g-C₃N₄ and Pt/CN_x composite.

free CN_x are completely disappeared in Pt/CN_x and a new broad peak at 1050 cm^{-1} and another new sharp intense peak at 1385 cm^{-1} are appeared. They can be assigned as the stretching of C-N bond and C=N bond respectively. The significant changes in FT-IR spectrum of Pt/CN_x suggest the change of electronic structure of CN_x support and a strong interaction between carbon nitride and PtNPs.

6.3.7. Characterization of Pt/CN_x composite by TGA, ICP-OES and CHN analysis

The thermo gravimetric analysis (TGA) curves of Pt/CN_x and CN_x were given in Figure 6.8 and amount of platinum present in the Pt/CN_x composite was calculated. It shows 74 wt% Pt present in the Pt/CN_x composite. In the Energy dispersive spectroscopy (EDS) taken during FESEM measurement, the Pt loading in Pt/CN_x composite was found to be 75%. The exact amount of Pt loading was determined by inductively coupled plasma optical emission spectrometry (ICP-OES) analysis.

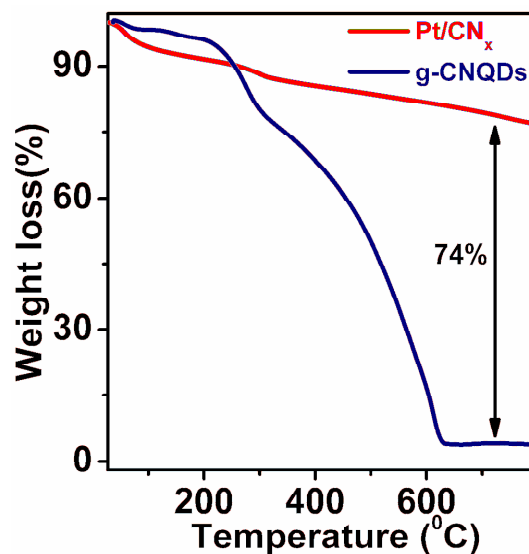


Figure 6.8. TGA plots of Pt/CN_x composite and $\text{g-C}_3\text{N}_4$ in N_2 atmosphere.

The exact Pt loading in Pt/CN_x composite is 73 wt% which is in good agreement with TGA and EDS measurements. We have also prepared Pt/CN_x compound with lower loading, but best electrochemical behaviour was observed for this 73 wt% Pt in Pt/CN_x, composite. The CHN analysis was done to find amount of carbon, nitrogen present in this composite. The ratio of carbon and nitrogen in Pt/CN_x composite was 1(C) : 0.6 (N) whereas this ratio for free g-C₃N₄ was 1 : 1.1.

6.3.8. ECSA calculation of Pt/CN_x composite

The electrochemical activity of Pt/CN_x catalyst was studied in N₂ saturated H₂SO₄ solution by doing cyclic voltammetric (CV) measurement with Pt/CN_x catalyst modified glassy carbon (GC) electrode. Fig. S6 (ESI) shows the CV curves of Pt/C and Pt/CN_x in N₂ saturated 1(M) H₂SO₄ solution at a scan rate 50 mV/sec. Both the CV curves have characteristic peaks for hydrogen adsorption and desorption.

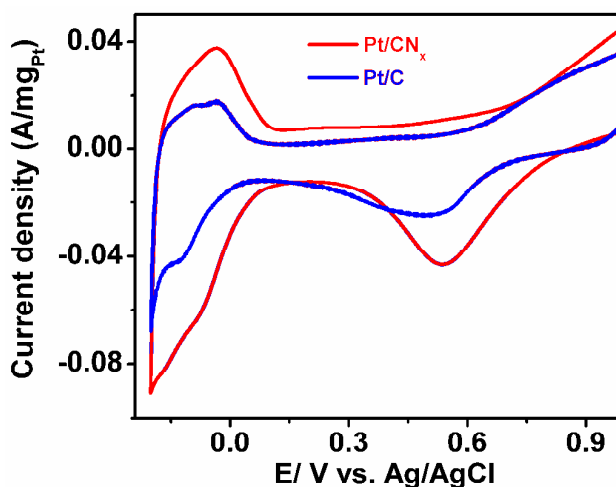


Figure 6.9. Cyclic Voltammograms of Pt/CN_x and Pt/C in 1(M) H₂SO₄ at the scan rate of 50 mV/sec in N₂ atmosphere.

After double layer correction hydrogen desorption peak of CV has been used to calculate the electrochemically active surface area (ECSA) by following equation:

$$\text{ECSA} = S / (m \times v \times c)$$

where S (mA-Volt) is double layer corrected surface area under hydrogen desorption curve, v is the scan rate (Volt/sec), c is the required charge to oxidize a monolayer of hydrogen on the platinum surface (mC cm^{-2}), the value of c is 0.21 mC cm^{-2} , m is the Pt loading on the electrode surface (mg)⁴⁰. The ECSA value of Pt/CN_x catalyst was found to be $68 \text{ m}^2 \text{ g}_{\text{Pt}}^{-1}$ is 1.8 times higher than that of the commercial Pt/C catalyst ($36.5 \text{ m}^2 \text{ g}_{\text{Pt}}^{-1}$). The high ECSA value of Pt/CN_x composite is probably due to high dispersion of PtNPs on the CN_x sheets and porous morphology of the composite. The higher ECSA value of Pt/CN_x composite proves the presence of more number of electrochemically active site into the Pt/CN_x composite which helps to improve the electrooxidation properties of methanol, formic acid and formaldehyde in acidic medium.

6.4. Application

6.4.1. Electrochemical oxidation of Methanol on porous Pt/CN_x catalyst

The electrochemical oxidation of methanol was performed in aqueous 1(M) H₂SO₄ solution containing 1(M) CH₃OH solution using CV. Figure 6.10 (a) shows CV curves for methanol oxidation on Pt/CN_x and Pt/C modified GC electrodes at the scan rate of 50 mV/sec in acidic medium. Both the curves consist of two well define oxidation peaks - one in the forward scan

and another peak in backward scan. The peak in the forward scan is characteristic to the oxidation of methanol whereas the peak during reverse scan represents the efficiency of the removal of carbonaceous species which is generated during forward scan of methanol oxidation. The forward peak current density ($310 \text{ mA/mg}_{\text{Pt}}$) of Pt/CN_x is 2.7 times higher than that on the Pt/C catalyst ($114 \text{ mA/mg}_{\text{Pt}}$). The onset potential of methanol oxidation is an important parameter in electro-catalytic study. Lower the onset potential higher is the power to break the C-H bonds of methanol and higher the removal efficiency of the carbonaceous species⁴¹. The onset

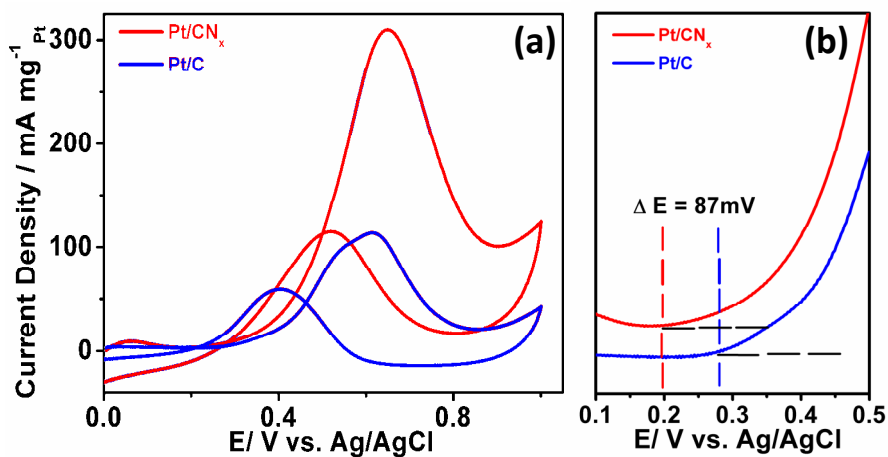


Figure 6.10. (a) Cyclic Voltammograms of methanol oxidation of Pt/CN_x and Pt/C catalysts in $1(\text{M}) \text{CH}_3\text{OH} + 1(\text{M}) \text{H}_2\text{SO}_4$ solution at scan rate of 50 mV/sec . (b) The comparison of the onset potentials of Pt/CN_x and Pt/C catalysts for methanol oxidation.

potentials for methanol oxidation on the Pt/CN_x and Pt/C are 0.193 and 0.28 V respectively. The onset potential of Pt/CN_x is shifted to the negative voltage of 87 mV in compare to the Pt/C catalyst (Figure 6.10 (b)). The high mass activity and low onset

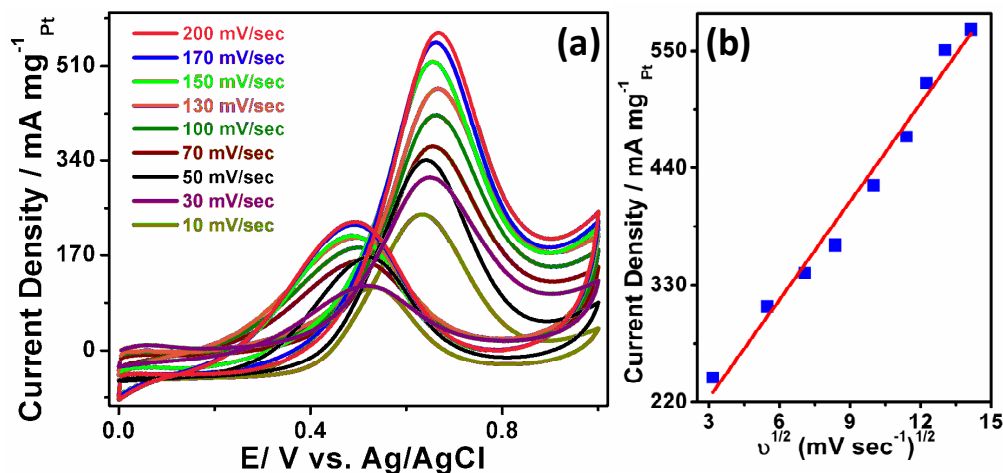


Figure 6.11. (a) CVs of Pt/CN_x of 1 (M) CH₃OH + 1 (M) H₂SO₄ solution at different scan rates ranging from 10 mV/sec to 200 mV/sec. (b) Plot of forward peak current densities vs. square root of scan rates.

potential suggest the superior electrocatalytic activity of Pt/CN_x towards methanol oxidation in compare to commercial Pt/C. The tolerance to the accumulation of carboneous species is another important parameter which determines the quality of the catalyst during electro catalytic oxidation. The ratio of forward current density to the backward current density (I_f/I_b) represents the poison tolerance of the catalyst to the carbonaceous species, formed due to methanol oxidation in the forward scan and the efficiency of the catalyst during methanol oxidation¹². The poisonous CO and different carbonaceous species which are formed in the forward scan due to oxidation of methanol are adsorbed on the platinum surface of the catalyst. These poisoning species are oxidized during backward scan and then catalyst becomes reactivated for next forward scan. The

Table 6.1. Summary of methanol oxidation on Pt/CN_x and commercial Pt/C electrocatalyst

Electro catalyst	onset potential/V	I _f	I _b	I _f /I _b
Pt/CN _x	0.193	310	115.8	2.68
Pt/C	0.280	114	60.0	1.90

low value of I_f/I_b ratio represents poor removal efficiency of the catalysts due to the blocking active site of the catalysts by carbonaceous materials. The I_f/I_b ratio of Pt/CN_x was found to be 2.68 which is 1.41 times higher than that of commercial Pt/C catalyst (I_f/I_b = 1.9). This suggests that methanol can be more easily oxidized on Pt/CN_x surface in the forward scan to generate smaller amount of carbonaceous species. The comparison study of electrocatalytic performances toward methanol oxidation of Pt/CN_x and Pt/C is given in Table 6.1. This proves that the Pt/CN_x catalyst has much better methanol oxidizing power to form carbon dioxide during the forward scan and less capability to accumulate the carbonaceous species on the catalyst surface, in comparison to the Pt/C. The transport characteristic of methanol on Pt/CN_x catalyst was studied by varying CV scan rate. Figure 6.11 (a) shows the CVs of methanol oxidation on Pt/CN_x electrode in 1(M) H₂SO₄ solution with different scan rates starting from 10 mV/sec to 200 mV/sec. With increasing the scan rates the oxidation peak current in the forward scans is increasing. As shown in Figure 6.11 (b), the methanol oxidation forward current density increases linearly with increasing square root of scan rate, which implies that methanol

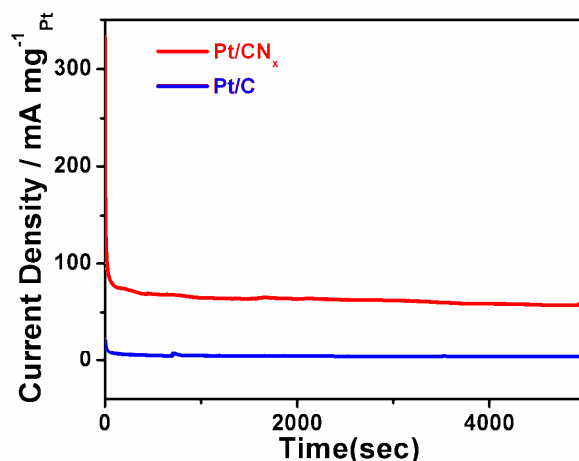


Figure 6.12. Chronoamperometry curves of Pt/CN_x and Pt/C catalysts of methanol oxidation in 1(M) CH₃OH + 1(M) H₂SO₄ solution at constant potential of 0.7V.

oxidation at Pt/CN_x catalyst is mainly diffusion controlled process³⁶. The durability is an important performance parameter for electrocatalytic studies. The long term electrocatalytic durability of the catalyst was examined by using chronoamperometric measurements. Figure 6.12 represents chronoamperometric curves for methanol oxidation at a constant potential of 0.7V on Pt/C and Pt/CN_x in N₂ saturated 1(M) H₂SO₄ solution containing 1(M) methanol. A rapid decrease of current density at initial stage of the scan, due to the formation of different adsorbed intermediate species such as CO, CHO etc. was observed and then decay of current density became very slow. The current density on Pt/CN_x was always higher in compare to the Pt/C over the entire scan time. After 5000 sec of amperometric scan, current density on Pt/CN_x (57.3 mA/mg_{Pt}) is 17 times higher than commercial Pt/C (3.3 mA/mg_{Pt}). In addition, the long term cycling stability of this catalyst was also studied as shown in Figure 6.13. This shows, although mass activity of

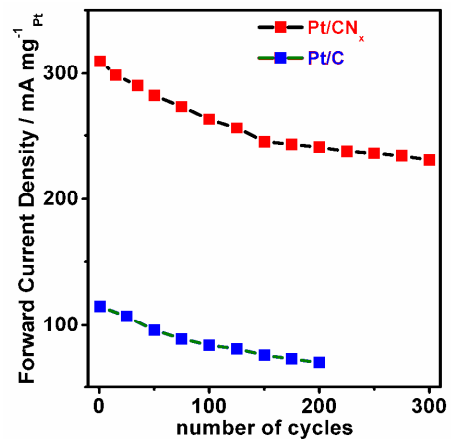


Figure 6.13. Change of forward current density of Pt/CN_x and Pt/C catalysts with the number cycle for methanol oxidation in 1(M) methanol + 1(M) H₂SO₄ solution.

Table 6.2. Summary of electrochemical performance of methanol oxidation on various electrocatalysts

Electro catalyst	onset potential/V ^a	I _f /I _b	Ref.
Pt-3D-G	0.17	0.87	34
Pt-4%ASG	0.40	2.56	42
Pt-TiO ₂ -C	0.30	0.95	43
Pt-rGO-AMs	---	0.95	44
PtNP/R-3DNG	---	2.6	32
Pt-MnO ₂ -ERGO	0.36	1.98	45
Pt-GNP-RTIL-2	---	0.728	46
Pt/CN _x	0.196	2.68	this work

^a The onset potential values are *vs.* Ag/AgCl reference electrode.

Pt/CN_x decreases gradually with number of cycles, after 300 cycle's current density of Pt/CN_x is still much higher than that of Pt/C. This suggests the outstanding long term stability of this Pt/CN_x catalyst. The comparison of electro catalytic performances toward methanol oxidation of Pt/CN_x with other reported catalysts is tabulated in Table 6.2. This confirms that superior catalytic activity of Pt/CN_x towards electrooxidation of methanol.

6.4.2. Electrochemical oxidation of Formic acid on porous Pt/CN_x catalyst

The electrooxidation of formic acid oxidation at electrode surface are known to occur in two different paths, one is dehydrogenation process which is the direct path involves oxidation of formic acid to carbon dioxide ($\text{HCOOH} \rightarrow \text{CO}_2 + 2\text{H}^+ + 2\text{e}^-$) and the other path is the indirect path which (dehydration path) occurs via intermediate step, oxidation of adsorbed CO species ($\text{HCOOH} \rightarrow \text{CO}_{\text{ads}} + \text{H}_2 \rightarrow \text{CO}_2 + 2\text{H}^+ + 2\text{e}^-$)⁴⁷. The energy barrier of C-H bond activation is more than that of C-O bond activation⁴⁸. In the formic acid oxidation through indirect path is easier than the direct path. But, to improve overall cell efficiency and avoid catalyst poisoning in DFAFC the dehydrogenation path is more attractive. Figure 6.14 represents the comparison of CVs for 1(M) formic acid oxidation at Pt/C and Pt/CN_x electrodes in 1(M) H₂SO₄ solution. Both the CVs have two separate peaks in the forward scan suggesting dual pathway mechanism of formic acid oxidation on these two electrodes. In the forward scan, Pt/CN_x catalyst showed two peaks, one was at 0.29V and another was at 0.73V. The first peak (P₁) at 0.29V can be attributed

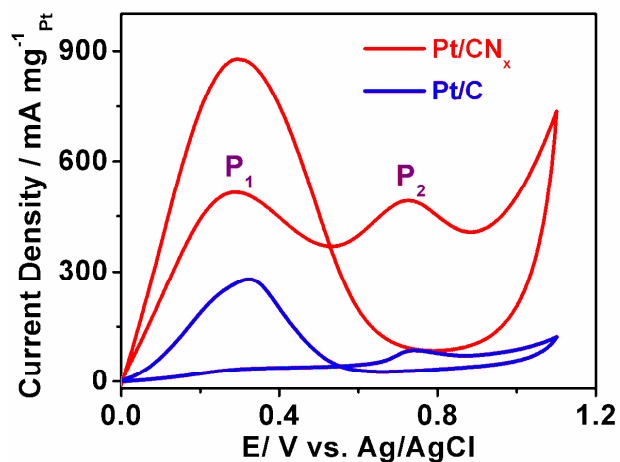


Figure 6.14. CV curves of Pt/CN_x and Pt/C catalyst in N₂ saturated 1(M) H₂SO₄ solution containing 1(M) HCOOH at the scan rate of 50 mV/sec.

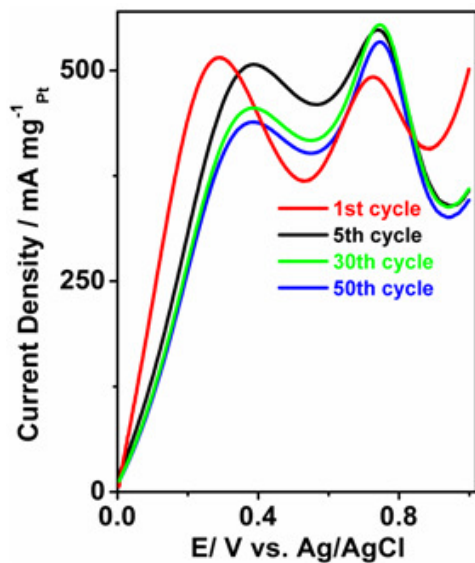


Figure 6.15. CVs of 1st cycle, 5th cycle, 30th and 50th cycle of Pt/CN_x catalyst of formic acid oxidation in 1(M) H₂SO₄ solution at the scan rate of 50 mV/sec.

to dehydrogenation reaction (direct) and the second peak (P₂) at 0.73V corresponds to the dehydration reaction to form poisoning CO species. The intensity of current density indicates the

probability of corresponding process⁴⁹. The intensities of these two peak for Pt/CN_x (515 mA/mg_{Pt} of P₁ and 493 mA/mg_{Pt} of P₂) is 15.1 and 5.7 times higher than those of Pt/C (34 mA/mg_{Pt} of P₁ and 86 mA/mg_{Pt} of P₂) suggesting mass activity is much higher at Pt/CN_x than that of commercial Pt/C. The ratio of current densities of these two peaks (P₁/P₂) for Pt/CN_x catalyst is 1.04 which is much higher than that of Pt/C (P₁/P₂= 0.40). The low ratio on Pt/C suggests that electro-oxidation of formic acid at Pt/C electrode surface mainly occurs through hydration pathway forming poisonous intermediate whereas large value ratio of these two peak of 1.04 on Pt/CN_x indicates that direct oxidation of formic acid to carbon dioxide occurs and lesser amount of carbonaceous intermediates are formed. Most importantly, at 0.3V (vs. NHE), a typical working voltage in DFAFC¹⁷, the mass activity of Pt/CN_x composite for formic acid oxidation is 25 time higher than that of commercial Pt/C catalyst. Moreover, the onset potential of formic acid oxidation on Pt/CN_x catalyst is about zero volts whereas the onset potential on Pt/C catalyst is at 0.15V as shown in the Figure 6.14. The lower the onset potential of Pt/CN_x electro-catalyst makes it more efficient than commercial Pt/C catalyst in formic acid oxidation.

Table 6.3. Comparison of different electrochemical performance during formic acid oxidation of Pt/CN_x with Pt/C catalyst

Electrocatalyst	onset potential/V	I _{P1}	I _{P2}	I _b	I _P /I _b
Pt/CN _x	0.0	515	493.0	878.8	1.15
Pt/C	0.15	34	86.0	280.6	0.43

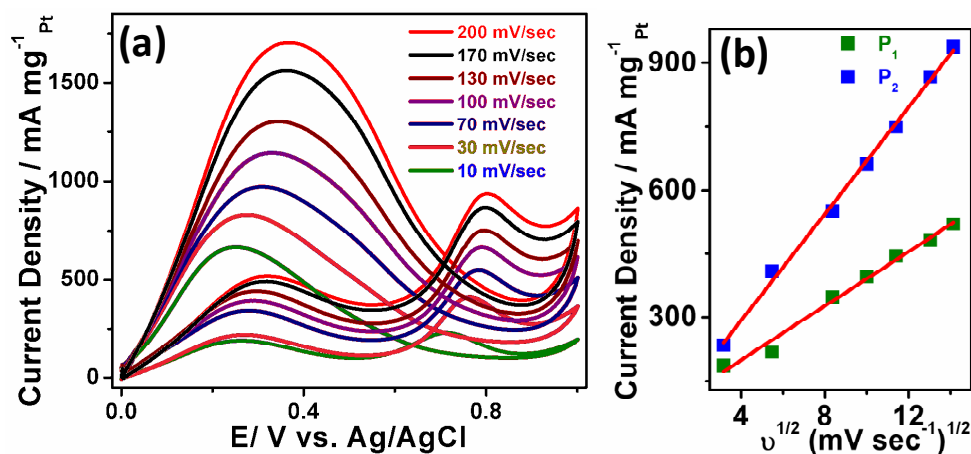


Figure 6.16. (a) CVs of Pt/CN_x in 1(M) HCOOH + 1(M) H₂SO₄ solution at different scan rates ranging from 30 mV/sec to 200 mV/sec. (b) Plot of forward current densities of first (P₁) and second peak (P₂) vs. square root of scan rates of Pt/CN_x catalyst for HCOOH oxidation.

Comparison of different electrochemical performance during formic acid oxidation ($\text{HCOOH} \rightarrow \text{CO}_{\text{ads}} + \text{H}_2\text{O} \rightarrow \text{CO}_2 + 2\text{H}^+ + 2\text{e}^-$)⁴⁷. The energy barrier of C-H bond activation is more than that of C-O bond activation⁴⁸. In the formic acid oxidation through indirect pathway is easier than the direct path. But, to improve overall cell efficiency and avoid catalyst poisoning in DFAFC the dehydrogenation path is more attractive. The ratio of current density of the peaks ($I_{\text{P}_1} + I_{\text{P}_2}$) in the forward scan and the peak (I_{b}) at backward scan during formic acid oxidation can also reveal the tolerance power of the electro-catalyst. The ratio of $I_{\text{f}}/I_{\text{b}}$ of Pt/CN_x is 1.15, which is 2.7 times higher than that of Pt/C also suggesting the higher tolerance of Pt/CN_x/GC electrode towards the incompletely oxidized carbonaceous species during formic acid oxidation. The slight decrease of the intensity of the first peak was observed on few initial cycling, and then it became very

slow (Figure 6.15). The electrooxidation at various scan rates was done to examine the transport mechanism of formic acid on Pt/CN_x. Figure 6.16 (a) shows the CVs on Pt/CN_x/GC electrode of formic acid oxidation in 1(M) H₂SO₄ solution with different scan rates starting from 10 mV/sec to 200 mV/sec. It shows, with increasing scan rate the current density of the first peak and as well as the second peak increases gradually. The current density of first peak and second peak follows the straight line separately with the square root of scan rate (Figure 6.16 (b)) suggesting the formic acid electro oxidation

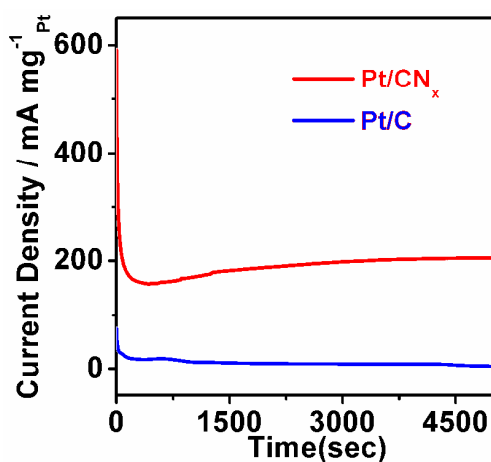


Figure 6.17. Chronoamperometry curves of Pt/CN_x and Pt/C catalysts in N₂ saturated 1(M) H₂SO₄ solution containing 1(M) HCOOH at a constant voltage of 0.3V.

processes on Pt/CN_x/GC electrode is a diffusion controlled process. The catalytic long term stability and durability during formic acid electro oxidation was done by chronoamperometry method in N₂ saturated solution of 1(M) HCOOH + 1(M) H₂SO₄ mixture at 0.3V vs. Ag/AgCl reference electrode. The comparison of chronoamperometry

curves of Pt/CN_x and commercial Pt/C catalyst was shown in Figure 6.17. The current densities on both the electrode decreases with time, but the current density of Pt/CN_x catalyst was higher than that of Pt/C over the entire scan time range. At 5000 sec the current density on Pt/CN_x is 204.7 mA/mg_{Pt} which is 45 times higher than that of Pt/C catalyst (4.5 mA/mg_{Pt}). This proves that Pt/CN_x catalyst has much higher tolerance to CO poisoning and superior stability towards formic acid oxidation than that of commercial Pt/C catalyst. In addition long term cycling stability of this catalyst was done as shown in Figure 6.18. It shows, after 500 cycles the current density of Pt/CN_x catalyst is much higher than that of Pt/C, suggesting significantly enhanced cycling stability for formic acid oxidation of Pt/CN_x in compare to commercial Pt/C. The comparison of the electrocatalytic performance towards formic oxidation of Pt/CN_x with other reported catalyst (Table 6.4) proves its superior catalytic activity for formic acid oxidation.

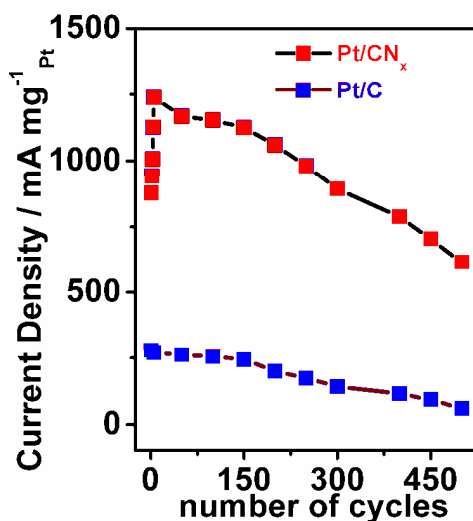


Figure 6.18. Change of backward current density with the number of cycle of Pt/CN_x and Pt/C catalyst during 1(M) formic acid oxidation in 1(M) H₂SO₄ medium.

Table 6.4. Summary of electrochemical performance for formic acid oxidation on reported electrocatalysts

Electro catalyst	onset potential/V (SCE ^b)	I _f /I _b	Ref.
Pt-Au/Graphene	-0.104	0.23	50
Pt ₅₀ Pd ₅₀ /Ti _{0.4} V	-0.1	0.26	51
PtAu/C(core-shell)	-----	0.34	14
PtAg/C	0	0.48	52
Pt-CeO ₂ /RGO/CCE	-0.2	1.14	53
Pt-Pd/SWCNT	0.01	0.94	36
Pt/CN _x	-0.045	1.15	this work

^b SCE represents saturated calomel electrode.

6.4.3. Formaldehyde electrooxidation on porous Pt/CN_x catalyst

The electrocatalytic activity towards formaldehyde oxidation was also studied by CV. The comparison of CVs for formaldehyde electro-oxidation on Pt/CN_x and Pt/C electrodes in 1(M) H₂SO₄ medium containing 1M formaldehyde at a scan speed of 50 mV/sec is presented in Figure 6.19. This shows significantly higher formaldehyde electrooxidation activity of Pt/CN_x than that of Pt/C. In case of Pt/C, low current density and slow increase of current at lower potential during forward scan suggests the formation of poisonous intermediate, CO_{ads} species on platinum leading to electrode poisoning. A quick increase of current at higher potential during forward scan is observed and a peak is appeared at 0.7 V is due to the oxidation of CO_{ads} to CO₂ on Pt surface. In the backward scan, a peak is observed due to the reduction of platinum oxide. This backward scan helps

to reactivate the catalyst for further adsorption and then oxidation of formaldehyde molecule. The comparison of the electrocatalytic performance of Pt/CN_x with Pt/C is shown in Table 6.5. The formaldehyde oxidation current density of Pt/CN_x at 0.72V is 301 mA/mg_{Pt} which is 3.2 times lower than that of commercial Pt/C (94 mA/mg_{Pt}). In addition, onset potential for this oxidation on Pt/CN_x is 0.15V, lower than Pt/C. These prove that the Pt/CN_x has higher electrocatalytic activity towards electro-oxidation of formaldehyde than that of commercial Pt/C. This is probably due to following reason. When PtNPs dispersed on CN_x sheets, oxidation of formaldehyde proceed through dual pathways mechanisms – direct pathway without forming poisonous intermediate and

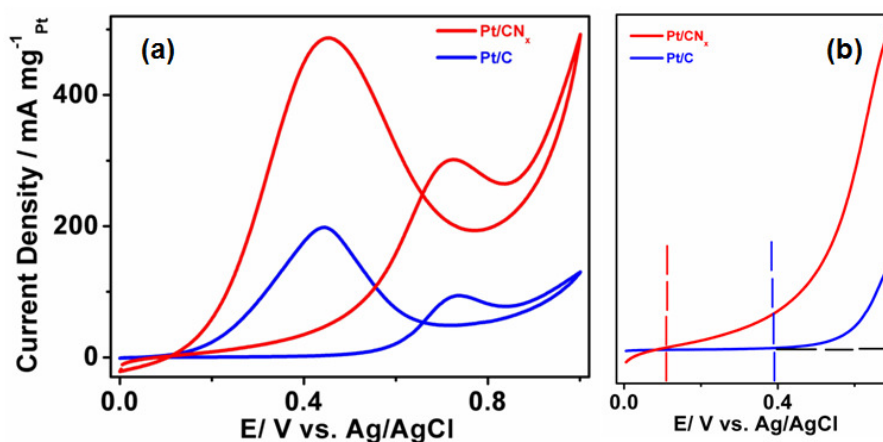


Figure 6.19. (a) CVs of Pt/CN_x and Pt/C catalysts of formaldehyde oxidation in N₂ saturated 1(M) H₂SO₄ solution containing 1(M) HCHO at scan rate is 50 mV/sec (b) Comparison of onset potential of Pt/CN_x and Pt/C catalysts for formaldehyde oxidation.

indirect hydrogenation pathway; but Pt/C favours dehydrogenation pathway. This electro-oxidation of formaldehyde on Pt/CN_x is similar to the electrochemical behaviour of

formic acid on Pt/CN_x electrode surface. The effect of scan rate on the electrooxidation of formaldehyde on Pt/CN_x electrode was studied and shown in Figure 6.20a. It shows that formaldehyde oxidation current increases with the scan rate. As shown in Figure 6.20b, the

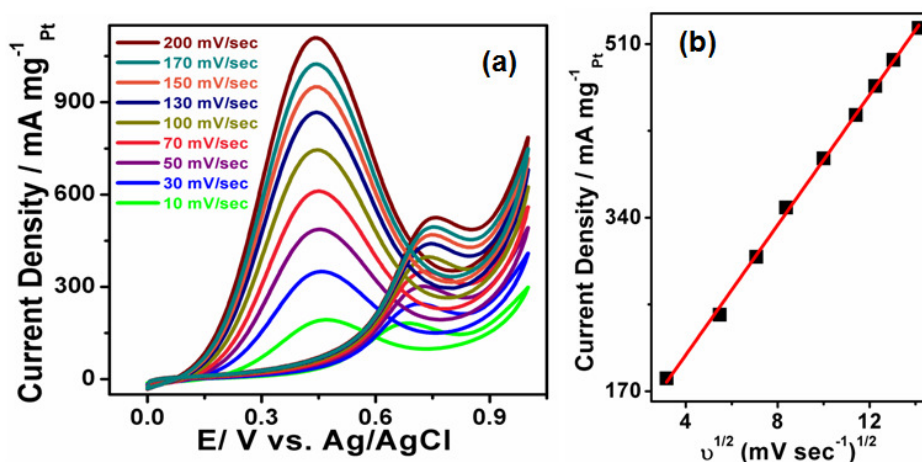


Figure 6.20. (a) CVs of Pt/CN_x catalyst in 1(M) H₂SO₄ + 1(M) HCHO solution at different scan rates starting from 30 mV/sec to 200 mV/sec. (b) Forward current densities vs. square root of scan rates of Pt/CN_x catalyst during HCHO oxidation in 1(M) HCHO + 1(M) H₂SO₄ solution.

oxidation current density is linearly proportional to square root of scan rate suggesting that formaldehyde oxidation on Pt/CN_x electrode is diffusion-controlled process. The oxidation peak in the forward scan is also found to be shifted towards to the higher voltage with increase of scan rate. This proves the formaldehyde oxidation on Pt/CN_x is an irreversible process. The long term stability of Pt/CN_x and Pt/C at 0.8V in 1(M) H₂SO₄ solution containing 1(M) formaldehyde was investigated using chronoamperometry and is shown in Figure 6.21. The current density on Pt/CN_x was always much higher than that of Pt/C over the whole period of chronoamperometric scan. This demonstrates the Pt/CN_x

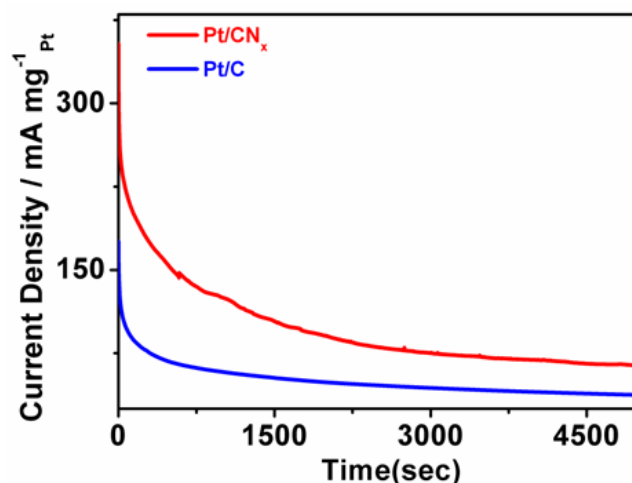


Figure 6.21. Cronoamperometry curves of Pt/CN_x and Pt/C catalysts in N₂ saturated 1(M) formaldehyde + 1(M) H₂SO₄ solution at constant voltage of 0.8V.

Table 6.5. Comparison of electrochemical performance parameters for formaldehyde oxidation

Electrocatalyst	onset potential/V	I _f	I _b	I _f /I _b
Pt/CN _x	0.15	301.0	486.0	0.62
Pt/C	0.35	94.0	198.0	0.47

electrode has much better long term electrocatalytic stability than Pt/C electrode during formaldehyde oxidation.

6.5. Effect of support (CN_x) in Pt/CN_x catalyst for electrooxidation of methanol, formic acid and formaldehyde

From the comparison of electro catalytic performances of Pt/CN_x with reported electro catalysts as given in Table 6.2-6.5 for the electrochemical oxidation of methanol, formic acid; it is obvious that Pt/CN_x exhibited better or comparable electrocatalytic performance than other reported catalysts. The superior catalytic activity and long term durability of Pt/CN_x towards electrooxidation of methanol, formic acid and formaldehyde can be attributed to the several factors:

(1) The high electrochemical surface area resulting from uniform distribution of PtNPs on CN_x sheets and porous morphology could be one of the reasons for enhanced electro-catalytic activities. TEM image of Pt/CN_x confirm uniform distribution of PtNPs with average diameter of 5 nm on the surface of CN_x. The porous morphology of this composite was confirmed by FESEM. This porous morphology not only increases the ECSA, but also increases efficient mass transport through porous network. The reactant can easily reach to active sites such as defect, edge, etc. and product can easily come out from the active through the pores. (2) The strong catalyst-support interaction at Pt/CN_x could also be playing an important role for the superior catalytic enhancements. The metal-support interaction modifies the electronic structure of Pt and carbon nitrides, which leads to fast electron transfer for catalytic reactions. The XPS and FT-IR studies confirm PtNPs are directly bonded to the CN_x sheets. The different of FT-IR spectrum of Pt/CN_x and CN_x suggest the change of electronic structure of CN_x sheets is due to presence of PtNPs on CN_x sheets. The shift of C1s peak and Pt 4f peaks in the XPS spectra of Pt/CN_x composites suggest change of electronic structure of Pt. From the previous theoretical⁵⁴ and experimental⁵⁵ studies it is known that the shift of d-band electron center for Pt due to formation multimetallic compounds with other metals

facilitates the electro-oxidation of methanol and formic acids. The XPS studies demonstrated that, when the PtNPs are dispersed on CN_x support, electronic modification of Pt occurs. Thus, adsorption strength of carbonaceous material on modified Pt surface is altered due to change of d-center character of Pt that enhances oxidation of the carbonaceous intermediate. As a result, enhanced electro-catalytic oxidation of methanol, formic acid on Pt/CN_x catalyst was observed. In addition, this catalyst-support interaction also may enhance superior long term durability of this Pt/CN_x , since this interaction may prevent the oxidation of the support as well as helps nanoparticles to remain bonded with support. (3) The presence of pyridinic and graphitic N-atom into carbon materials enhances the electro-catalytic activities of the catalysts. It is reported nitrogen doping in carbon support introduces atomic charge density and asymmetry in spin density into carbon networks that facilitates charge transfer from carbon support to the adsorbing molecules⁵⁶. J. Y. Kim and his co-workers suggested that presence of the N-species improved the electro-catalytic activity of cobalt doped $\text{g-C}_3\text{N}_4$ and also showed that among the different type N-functional groups, graphitic and pyridinic N are known to play more significant role in the improvement of electro-catalytic affects by superior the charge transfer⁵⁷. The presences of large amount of pyridinic and graphitic N-atoms in Pt/CN_x may be helping to enhance the catalytic activities. The lower nitrogen concentration in CN_x support of Pt/CN_x , as compared to $\text{g-C}_3\text{N}_4$, also helped^{30,58}. Based on this work and reported literature it may be concluded that superior electro-catalytic activity of Pt/CN_x 3D porous composite towards methanol, formic acid and formaldehyde oxidation is probably due to synergetic effect between PtNPs and porous CN_x supports.

6.6. Conclusion

In conclusion, we describe the fabrication of porous graphitic carbon nitride (g-CN_x) architecture supported highly dispersed PtNPs by ultrasound mediated sodium borohydride reduction method. XPS and FT-IR studies confirm the strong metal-support interactions exist in the composite. The Pt/CN_x composite has large electrochemical surface area due to the high dispersion of PtNPs on CN_x sheets and its porous morphology. Porous Pt/CN_x composite exhibits a much higher mass activity, better poison tolerance of CO and long-term durability than that of commercial Pt/C catalyst for electrooxidation of methanol, formic acid and formaldehyde. At 0.3V (vs. NHE), a typical working voltage in DFAFC, the mass activity of Pt/CN_x catalyst for formic acid oxidation is 25 times higher than that of commercial Pt/C catalyst. The porous morphology of this composite allow easy diffusion of reactant molecules such as CH₃OH, HCOOH, HCHO etc. through pores to reach active sites of the catalysts. The superior catalytic performances of Pt/CN_x catalyst is mainly attributed to synergistic interaction between CN_x support and PtNPs (electronic effect). The superior catalytic activity towards electro-oxidation of methanol, formic acids and exceptional long term stability of porous composite demonstrates that g-CN_x is a promising catalyst support for Pt electrocatalysts. We hope that this synthesis strategy may offer significant opportunity for designing new metallic electrocatalyst for their applications in direct fuel cell and other energy conversion devices.

Chapter References

1. Kordesch, K. V.; Simader, G. R., *Chem. Rev.* **1995**, *95*, 191-207.
2. Lamy, C.; Lima, A.; LeRhun, V.; Delime, F.; Coutanceau, C.; Léger, J.-M., *J. Power Sources* **2002**, *105*, 283-296.
3. Liu, H.; Song, C.; Zhang, L.; Zhang, J.; Wang, H.; Wilkinson, D. P., *J. Power Sources* **2006**, *155*, 95-110.
4. Paik, Y.; Kim, S.-S.; Han, O. H., *Angew. Chem. Int. Ed.* **2008**, *47*, 94-96.
5. Yu, X.; Pickup, P. G., *J. Power Sources* **2008**, *182*, 124-132.
6. Rice, C.; Ha, S.; Masel, R. I.; Waszczuk, P.; Wieckowski, A.; Barnard, T., *J. Power Sources* **2002**, *111*, 83-89.
7. Wang, X.; Hu, J.-M.; Hsing, I. M., *J. Electroanal. Chem.* **2004**, *562*, 73-80.
8. Park, S.; Xie, Y.; Weaver, M. J., *Langmuir* **2002**, *18*, 5792-5798.
9. Li, Y.; Jiang, Y.; Chen, M.; Liao, H.; Huang, R.; Zhou, Z.; Tian, N.; Chen, S.; Sun, S., *Chem. Commun.* **2012**, *48*, 9531-9533.
10. Shao-Horn, Y.; Sheng, W. C.; Chen, S.; Ferreira, P. J.; Holby, E. F.; Morgan, D., *Top. Catal.* **2007**, *46*, 285-305.
11. Liu, H.; Ye, F.; Yao, Q.; Cao, H.; Xie, J.; Lee, J. Y.; Yang, J., *Sci. Rep.* **2014**, *4*, 3969.
12. Yang, G.; Li, Y.; Rana, R. K.; Zhu, J.-J., *J. Mater. Chem. A* **2013**, *1*, 1754-1762.
13. Xu, Y.; Yuan, Y.; Ma, A.; Wu, X.; Liu, Y.; Zhang, B., *ChemPhysChem* **2012**, *13*, 2601-2609.
14. Kristian, N.; Yan, Y.; Wang, X., *Chem. Commun.* **2008**, 353-355.
15. Yuan, J.; He, B.; Hong, L.; Lu, J.; Miao, J.; Niu, L., *J. Mater. Chem.* **2012**, *22*, 19658-19665.
16. Nosheen, F.; Zhang, Z.-c.; Zhuang, J.; Wang, X., *Nanoscale* **2013**, *5*, 3660-3663.

17. Gong, M.; Li, F.; Yao, Z.; Zhang, S.; Dong, J.; Chen, Y.; Tang, Y., *Nanoscale* **2015**, *7*, 4894-4899.
18. Geim, A. K., *Science* **2009**, *324*, 1530-1534.
19. Guo, S.; Dong, S.; Wang, E., *ACS Nano* **2010**, *4*, 547-555.
20. Shang, N.; Papakonstantinou, P.; Wang, P.; Silva, S. R. P., *J. Phys. Chem. C* **2010**, *114*, 15837-15841.
21. Xu, C.; Wang, X.; Zhu, J., *J. Phys. Chem. C* **2008**, *112*, 19841-19845.
22. Wang, H.; Xia, B.; Yan, Y.; Li, N.; Wang, J.-Y.; Wang, X., *J. Phys. Chem. B* **2013**, *117*, 5606-5613.
23. Chen, X.; Wu, G.; Chen, J.; Chen, X.; Xie, Z.; Wang, X., *J. Am. Chem. Soc.* **2011**, *133*, 3693-3695.
24. Huang, H.; Ye, G.; Yang, S.; Fei, H.; Tiwary, C. S.; Gong, Y.; Vajtai, R.; Tour, J. M.; Wang, X.; Ajayan, P. M., *J. Mater. Chem. A* **2015**, *3*, 19696-19701.
25. Xiong, B.; Zhou, Y.; Zhao, Y.; Wang, J.; Chen, X.; O'Hayre, R.; Shao, Z., *Carbon* **2013**, *52*, 181-192.
26. Li, C.-Z.; Wang, Z.-B.; Sui, X.-L.; Zhang, L.-M.; Gu, D.-M., *Carbon* **2015**, *93*, 105-115.
27. Bhowmik, T.; Kundu, M. K.; Barman, S., *RSC Adv.* **2015**, *5*, 38760-38773.
28. Polshettiwar, V.; Varma, R. S., *Green Chem.* **2010**, *12*, 743-754.
29. Kundu, M. K.; Sadhukhan, M.; Barman, S., *J. Mater. Chem. B* **2015**, *3*, 1289-1300.
30. Kundu, M. K.; Bhowmik, T.; Barman, S., *J. Mater. Chem. A* **2015**, *3*, 23120-23135.
31. Qiu, H.; Dong, X.; Sana, B.; Peng, T.; Paramelle, D.; Chen, P.; Lim, S., *ACS Appl. Mater. Interfaces* **2013**, *5*, 782-7.

32. Qin, Y.; Chao, L.; Yuan, J.; Liu, Y.; Chu, F.; Kong, Y.; Tao, Y.; Liu, M., *Chem. Commun.* **2016**, 52, 382-5.
33. Huang, H.; Yang, S.; Vajtai, R.; Wang, X.; Ajayan, P. M., *Adv. Mater.* **2014**, 26, 5160-5165.
34. Li, Y.; Zhang, L.; Hu, Z.; Yu, J. C., *Nanoscale* **2015**, 7, 10896-10902.
35. Habibi, B.; Delnavaz, N., *Int J Hydrogen Energy* **2010**, 35, 8831-8840.
36. Selvaraj, V.; Grace, A. N.; Alagar, M., *J Colloid Interface Sci* **2009**, 333, 254-62.
37. Habibi, B.; Delnavaz, N., *Int. J. Hydrogen Energy* **2010**, 35, 8831-8840.
38. Chen, W.; Kim, J.; Sun, S.; Chen, S., *Langmuir* **2007**, 23, 11303-11310.
39. Xu, H.; Ding, L.-X.; Feng, J.-X.; Li, G.-R., *Chem. Sci.* **2015**, 6, 6991-6998.
40. Shen, Y.; Xiao, K.; Xi, J.; Qiu, X., *J. Power Sources* **2015**, 278, 235-244.
41. Wang, S.; Jiang, S. P.; White, T. J.; Guo, J.; Wang, X., *J. Phys. Chem. C* **2009**, 113, 18935-18945.
42. Thi Vu, T. H.; Thi Tran, T. T.; Thi Le, H. N.; Tran, L. T.; Thi Nguyen, P. H.; Essayem, N., *J. Power Sources* **2015**, 276, 340-346.
43. Qin, Y.-H.; Li, Y.; Lv, R.-L.; Wang, T.-L.; Wang, W.-G.; Wang, C.-W., *J. Power Sources* **2015**, 278, 639-644.
44. Lin, S.; Shen, C.; Lu, D.; Wang, C.; Gao, H.-J., *Carbon* **2013**, 53, 112-119.
45. Vilian, A. T. E.; Rajkumar, M.; Chen, S.-M.; Hu, C.-C.; Boopathi, K. M.; Chu, C.-W., *RSC Adv.* **2014**, 4, 41387-41397.
46. Do, I.; Drzal, L. T., *ACS Appl. Mater. Interfaces* **2014**, 6, 12126-12136.
47. Zhang, S.; Shao, Y.; Yin, G.; Lin, Y., *J. Power Sources* **2010**, 195, 1103-1106.
48. Neurock, M.; Janik, M.; Wieckowski, A., *Faraday Discuss.* **2009**, 140, 363-378.

49. Yan, H.; Li, H.; Tao, X.; Li, K.; Yang, H.; Li, A.; Xiao, S.; Cheng, R., *ACS Appl. Mater. Interface* **2014**, *6*, 9871-9880.
50. Venkateswara Rao, C.; Cabrera, C. R.; Ishikawa, Y., *J. Phys. Chem. C* **2011**, *115*, 21963-21970.
51. Yi, Q.; Huang, W.; Liu, X.; Xu, G.; Zhou, Z.; Chen, A., *J. Electroanal. Chem.* **2008**, *619-620*, 197-205.
52. Xu, J. B.; Zhao, T. S.; Liang, Z. X., *J. Phys. Chem. C* **2008**, *112*, 17362-17367.
53. Habibi, B.; Delnavaz, N., *RSC Adv.* **2015**, *5*, 73639-73650.
54. Demirci, U. B., *J. Power Sources* **2007**, *173*, 11-18.
55. Peng, Z.; You, H.; Yang, H., *Adv. Funct. Mater.* **2010**, *20*, 3734-3741.
56. Zhou, Y.; Neyerlin, K.; Olson, T. S.; Pylypenko, S.; Bult, J.; Dinh, H. N.; Gennett, T.; Shao, Z.; O'Hayre, R., *Energy Environ. Sci.* **2010**, *3*, 1437-1446.
57. Lee, J. H.; Park, M. J.; Yoo, S. J.; Jang, J. H.; Kim, H.-J.; Nam, S. W.; Yoon, C. W.; Kim, J. Y., *Nanoscale* **2015**, *7*, 10334-10339.
58. Negro, E.; Vezzù, K.; Bertasi, F.; Schiavuta, P.; Toniolo, L.; Polizzi, S.; Di Noto, V., *ChemElectroChem* **2014**, *1*, 1359-1369.

Chapter 7

Zinc doped Porous Carbon nitride Microspheres: Synthesis, Magnetic properties and Removal of Toxic Metal ions from water

7.1. Introduction

The contamination of water by toxic metals and dyes is a worldwide problem due to their non-biodegradability property. The metal ions and dyes are damaging the environment and the ecosystem. Numerous metals for example Lead (Pb), Copper (Cu), Chromium (Cr), Mercury (Hg), Cadmium (Cd), Arsenic (As) have toxic effects towards in environment and in human body. The most toxic forms of these metals are their stable oxidation states for example Cd^{2+} , Pb^{2+} , Hg^{2+} etc. At this stable oxidation state they bind with active bio-molecules of the body and form stable complex which is very much difficult to remove from the body. Cadmium is a highly toxic heavy metal which is staying at the surface and the subsurface of water and contaminated the water. It is well known that the cause of Itai-Itai disease in Japan is the toxic effect of cadmium. Toxicity of cadmium is the cause of different chronic disorder such as renal damage, hypertension, skeleton malformation in fetus, testicular atrophy, hypertension, emphysema in human beings². Cadmium can also damage the kidney, liver, gastrointestinal tract, lungs in human body³. Excess cadmium breaks the protein in urine and destroys the protein metabolism system. Generally copper needs in the body to form red blood cells in human body with the help of iron. Copper also keep the blood vessels active in the body. Toxicity of copper called copperiedus means excess of copper in the human body. The excess copper in the human body damage the nervous system and destroy the liver of the body⁴. Excess copper is coming in human body mainly from

drinking water and food. Sometimes the excess copper of the human body deposited in the cornea of the eye. The permissible limit of copper is 2.5 ppm⁵. Lead is one of the toxic heavy metal which affects the kidney, reproductive system, central nervous system, blood circulation system of human body. It can suppress the production of hemoglobin in human body⁶. The world health organization announces the maximum permissible limit of lead in drinking water is 0.01 ppm. Dyes are used in different industries such as pharmaceutical, textile, cosmetics, leather, plastics etc. Mainly textile industry discharge highly colored effluents containing different dyes. Moreover synthetic azo dyes are very much dangerous to the environment as well as to the living organism. The source of the toxicity of the azo dyes is the presence aromatic amine structure which is very much difficult to break and it gives high thermal, chemical and optical stability⁷. Congo red is one of the anionic azo dye contains two azo group. Benzidine is human carcinogenic and congo red contains benzidine moiety. Therefore, Congo red is a human carcinogenic dye⁸. Congo red biodegradation is very much difficult due to its complex aromatic structure. Now a day's removal of metal ions (Cu(II) , Pb(II) and Cd(II)) and Congo red dye from water solution is a hot topic in environmental science and technology. Industrial wastewater is contaminated by both toxic metal ions and dyes. As toxic metal ions and dyes have different properties therefore removal of them from wastewater by a single compound is a challenging work⁹. It is crucial to develop a single adsorbent which can adsorb simultaneously the toxic metal ions and dyes. Various technologies are there to remove the metal ions from water for example ion exchange method¹⁰, adsorption method¹¹, membrane filtration method¹², chemical precipitation method¹³ etc. The efficiency of metal removal is less for membrane method. Toxic sludge is generated by chemical method. In the ion exchange method the ion exchange resins are costly. Among them adsorption method was considered as a most promising method to remove

the metal ions from waste water due to its efficient low cost method and good removal efficiency. Similarly there are different technologies to remove dye from water such as membrane filtration, chemical precipitation, photochemical degradation, adsorption etc. Among them adsorption method is very much popular to remove the dye due to its low cost with high efficiency^{14,15}.

Recently porous materials such as zeolite, mesoporous silica nanomaterials have attracted great attention in the research field such as catalysis, gas adsorption, separation technology, drug delivery, biomedical application due to its high surface area¹⁶⁻¹⁷. Apart from this porous carbon based material has also got great attention in water purification, capacitor, and fuel cell application¹⁸⁻¹⁹. Hierarchical nanostructure and nanocomposite material have high surface area and large number of pores which make it a promising material as an adsorbent for waste water treatment. Due to hydrophobic nature graphene is not suitable to remove the metal ions and dye from water. So instead of graphene researchers are using graphene oxide^{20,21} or functionalized graphene oxide²² which are sufficient hydrophilic for adsorption study from water solution. In case of graphene oxide oxygen is functional group which helps to make it hydrophilicity. For the same reason carbon nanotube is not suitable for adsorption of metal ion from water solution but its oxidized form is quite suitable. But generally in oxidized carbon nanotube percentage of oxygen is 5% whereas in graphene oxide percentage of oxygen is 30%²³. In that sense the graphene oxide is more suitable than oxidized carbon nanotube for metal and dye removal from water solution. To improve the adsorption capacity graphene oxide can be modified by metal oxide²⁴ or by chelating polymer by chemical functionalization method²². Because of fine grain size of metal oxide in the metal oxide graphene composite during adsorption of metal ions the grains are aggregated which decreases the adsorption capacity. The functionalization to the

graphene in the metal oxide graphene composite can decrease the leaching method which decreases the efficiency of metal adsorption. After adsorption to improve the separation method magnetic composite nanomaterials are used where the adsorbent was separated by external magnetic field²⁵. Different adsorbent materials such as biomass²⁶, zeolite minerals²⁷, agricultural waste²⁸ are used to remove the heavy metals because of its low cost, biocompatibility, high natural abundance. Different porous materials for example porous silica, porous carbon aerogel², and porous metal organic framework²⁹ are used as adsorbents for metal ion removal due its high surface area. Activated carbon, zeolite and natural fiber are common adsorbent which have low adsorption capacity as well as separation difficulty. For example, Machida *et al.* prepared activated carbon supported zinc oxide and used this composite for the effective adsorption of Pb(II)³⁰. It has limitations to the removal efficiency and effectiveness. Magnetic materials have been extensively used for dye removal but its limitation is that magnetic material has low affinity towards organic dye³¹. Complicated synthetic method is another limitation to the use of magnetic materials towards dye removal. Low cost adsorbent with high adsorption capacity are more interesting material to remove the dye. There are lots of adsorbents which have good adsorption capacity to remove the dye from water but with this the adsorbent is contaminating the water. Special effort should give to improve the adsorbent which can improve the decontamination of water during dye removal. Therefore, overall we can concluded that a well performed adsorbent should be low cost, eco friendly, non toxic, high adsorption capacity, low weight and should have easy separation procedure from clean water. Hollow sphere materials have attracted to the metal and dye removal in the research field from waste water due its low density, high specific surface area and large number of void space³². Zinc doped carbon nitride composite has high adsorption capacity of metal ions and Congo red dye in water.

7.2. Synthesis method

7.2.1. Synthesis method of graphitic carbon nitride

Graphitic carbon nitride ($g\text{-C}_3\text{N}_4$) was synthesized from formamide by using microwave method. In a typical synthesis method of $g\text{-C}_3\text{N}_4$, 10.0 ml formamide was heated in autoclave at 180°C temperature for 6 hours. After heating, the brownish black colored solution was evaporated in a rotary evaporator at 180°C to get black colored solid product. This black colored product was washed with deionized water and dried in vacuum to get dry solid black colored $g\text{-C}_3\text{N}_4$.

7.2.2. Synthesis method of Zn-CN_x microspheres

In a typical synthesis procedure of Zn doped $g\text{-CN}_x$ microsphere, 10.0 ml formamide was heated with zinc dust in autoclave at 180°C temperature for 6 hours. The resulted black colored solution was evaporated in a rotary evaporator at 180°C to get black colored solid product. This black colored product was washed with de-ionized water and dried in vacuum to get dry solid black colored Zn doped $g\text{-CN}_x$ microspheres. We prepared different amount of zinc doped carbon nitride composite by taking different amount of zinc during the synthesis method. The best porous morphology with highest adsorption properties is observed for the composite where 0.1 gm zinc dust has been used to synthesis the composite with the 10.0 ml formamide solution. Therefore, 0.1 gm Zn doped $g\text{-CN}_x$ microsphere has been used to study all the adsorption measurements.

7.3. Characterization of Zn-CN_x composite

7.3.1. Morphological characterization of Zn-CN_x composite

To know the morphology of Zn-CN_x composite we have done FESEM and TEM analysis of it. Figure 7.1 (a, b and c) are the FESEM images of Zn-CN_x composite. Due to zinc doping into the g-C₃N₄ moiety the layer structure of g-C₃N₄ changes to the 3D porous microsphere. In order to find the distribution of Zn in the microspheres, we have done SEM element mapping. Figure 7.2 (a) shows the FESEM image of Zn-CN_x composite and its corresponding EDS mapping is shown in Figure 7.2. (b-d).

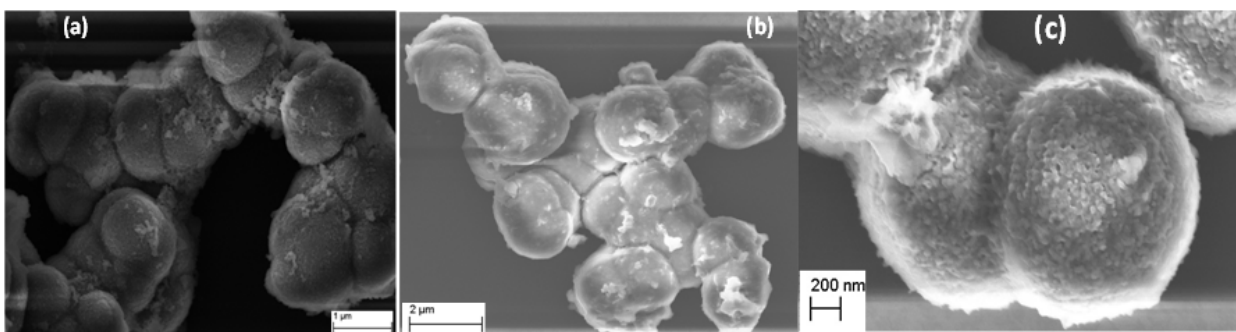


Figure 7.1. (a, b and c) FESEM images of Zn-CN_x composite confirming its 3D porous microsphere morphology.

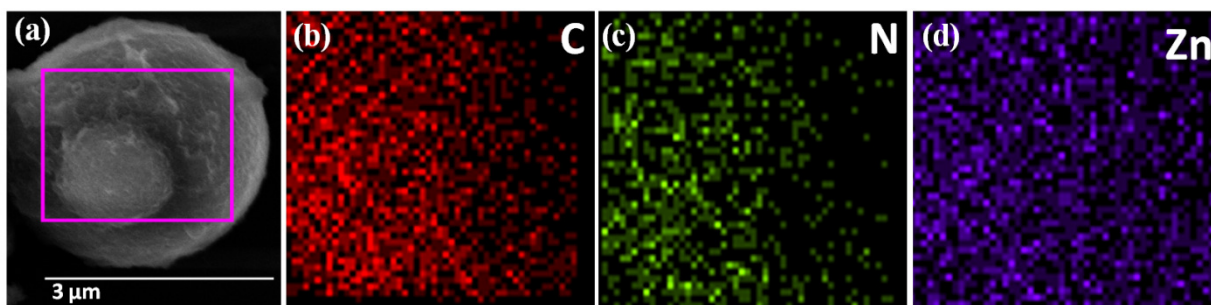


Figure 7.2. (a) FESEM image of Zn doped g-CN_x microsphere and its mapping images showing the homogeneous distribution of (b) carbon (c) nitrogen (d) zinc on Zn doped g-CN_x microsphere.

The EDS mapping demonstrates that the carbon, nitrogen and zinc elements are uniformly distributed throughout the surface of the porous microspheres of the composite. Figure 7.3 (a, b) and Figure 7.3 (c) represent the TEM and HRTEM images of Zn-CN_x composites respectively. Both the images show that the Zn-CN_x composite is porous in nature and forming 3D hollow sphere which is also confirmed from FESEM images. Figure 7.3 (d) shows the energy dispersive spectroscopy (EDS) spectra of Zn-CN_x composite obtained at the time of TEM measurement indicating the presence of zinc, nitrogen, carbon and small amount of oxygen in the Zn-CN_x composite.

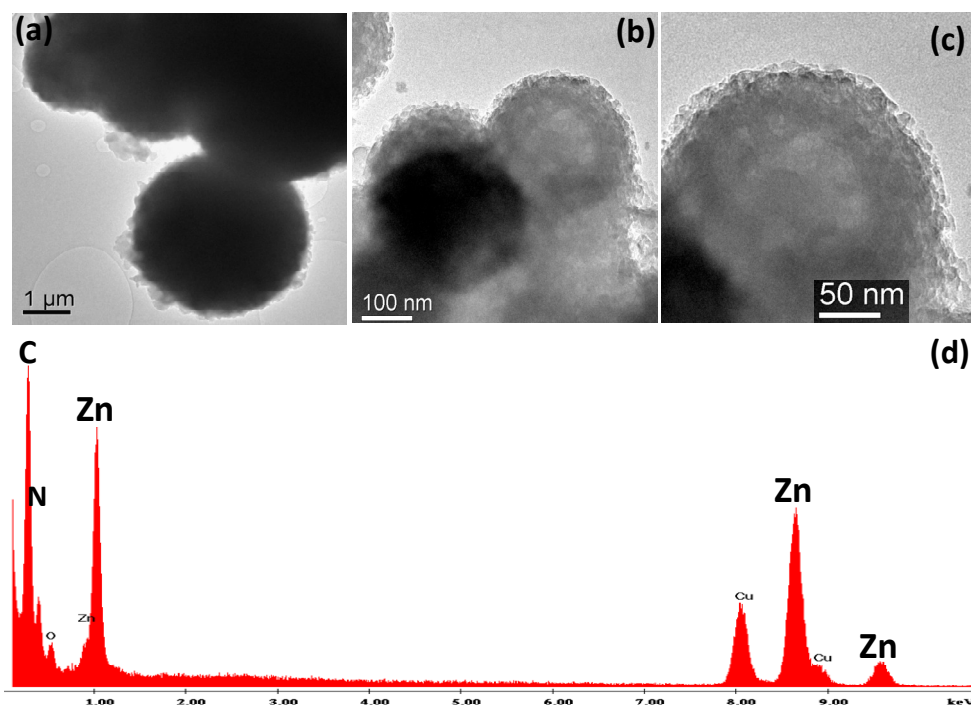


Figure 7.3. (a, b) TEM images of Zn-CN_x composite. (c) HRTEM image of Zn-CN_x composite. (d) EDS spectrum of Zn-CN_x composite taken on the TEM image showing the presence of Zn, C, N and O.

7.3.2. Structural Characterization of Zn-CN_x composite

The powder X-ray diffraction patterns of g-C₃N₄ and Zn-CN_x composite are shown in the Figure 7.4 and it is compared with the p-XRD pattern of g-C₃N₄. The p-XRD of g-C₃N₄ is showing the strongest peak at 2θ value of 27.4° corresponds to the (002) plane of g-C₃N₄ which is serving as a sign of stacking of graphitic carbon nitride layers with a distance of 0.326 nm. This is one of the major characteristic peaks of g-C₃N₄ compound³³. In the p-XRD of Zn-CN_x composite the sharpness of the peak of (002) plane of g-C₃N₄ decreases which is due to zinc doping into the g-C₃N₄ moiety. The decrease of the sharpness of the peak of (002) plane of g-C₃N₄ in the p-XRD proves that the zinc particles prevent the stacking of the layers of g-C₃N₄²⁰. A new additional broad peak at 2θ value of 13.1° has been observed in the p-XRD pattern of Zn-CN_x composite. It is the hole to hole distance of nitride pores and the characteristic peak of porous material³⁴. Therefore the presence of this broad peak proves its porous structure of Zn-CN_x composite which is also proved by FESEM and TEM measurements.

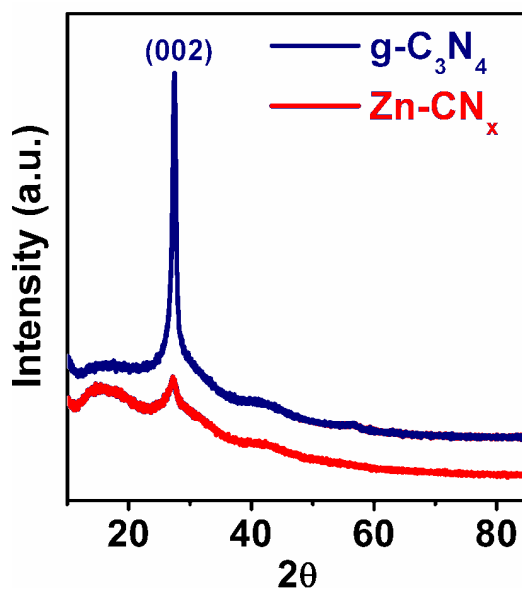


Figure 7.4. p-XRD of g-C₃N₄ and Zn-CN_x microsphere.

In the p-XRD of Zn-CN_x composite there is no characteristic peak for zinc oxide which proves that the absence of zinc oxide into the Zn-CN_x composite. The binding nature of zinc with carbon nitride moiety was studied through FT-IR spectroscopy. Figure 7.5 represents the FT-IR spectra of Zn-CN_x composite and g-C₃N₄. The FT-IR spectra of g-C₃N₄ is showing intense bands at 1213 cm⁻¹ and 1317 cm⁻¹ and 1408 cm⁻¹ correspond to the aromatic C=N stretching bands of carbon nitride moiety. The peaks at 1559 cm⁻¹ and 1616 cm⁻¹ correspond to the C=N stretching mode and 800 cm⁻¹ is the breathing mode of s-triazine unit of g-C₃N₄. After zinc doping to the g-C₃N₄ compound the intensity of the peaks decreases significantly due to the destruction of graphitic structure of carbon nitride moiety, proves the strong interaction between carbon nitride moiety and zinc particles. XPS spectra have taken to know the chemical environment of Zn doped g-CN_x microsphere and the oxidation state of zinc atom in the composite.

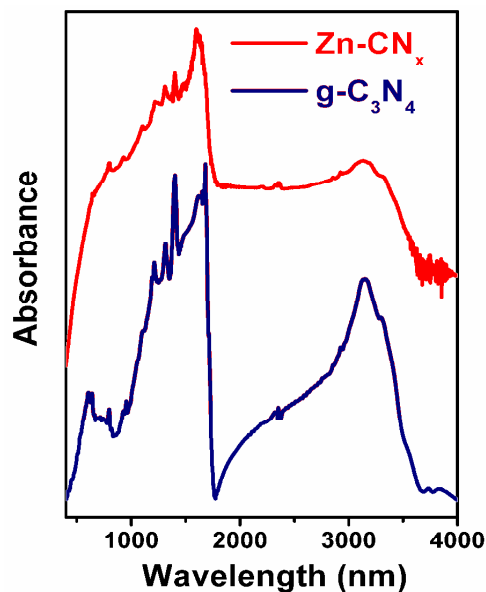


Figure 7.5. FT-IR spectra of g-C₃N₄ and Zn-CN_x microsphere.

Figure 7.6 (a) shows the survey scan of Zn doped g-CN_x microsphere proves the presence of carbon, nitrogen and zinc in the Zn doped g-CN_x microsphere. The Zn 2p XPS spectrum is presented in Figure 7.6 (b). It is well known that zero valence zinc appears at binding energy value of 1021.7 and 1045.0 eV represent the Zn 2p_{3/2} and 2p_{1/2} peaks respectively³⁵. The Zn 2p XPS spectrum of Zn doped g-CN_x microsphere exhibits a doublet at the binding energies of 1021.0 eV (2p_{3/2}) and 1044.0 eV (2p_{1/2}) corresponding to zero valence zinc with a slight lower binding energy shifting.

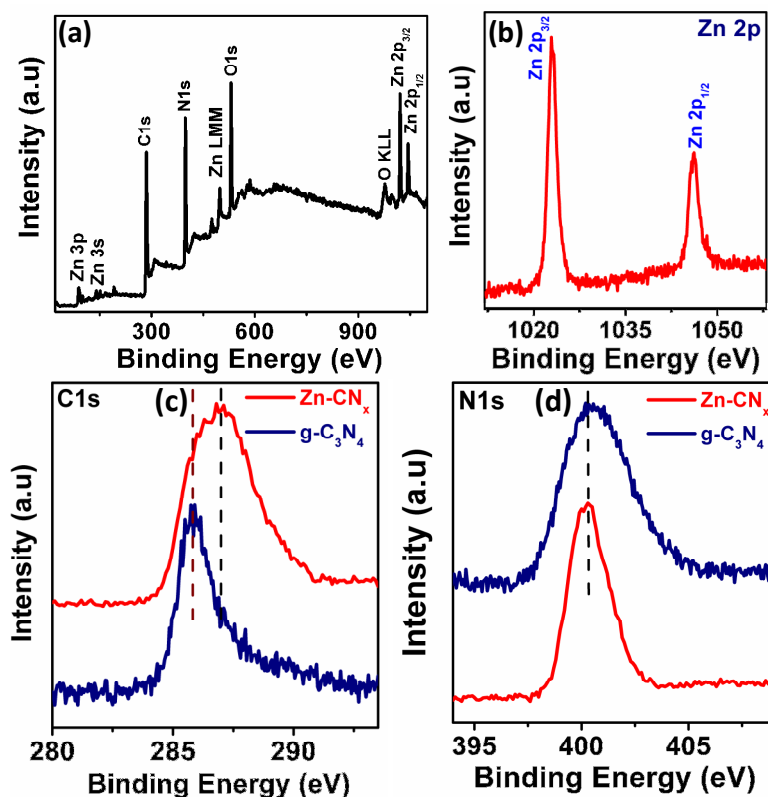


Figure 7.6. (a) XPS survey scan of Zn-CN_x microsphere. (b) XPS spectra of Zn in Zn-CN_x microsphere. (c) C1s XPS spectra of g-C₃N₄ and Zn-CN_x microsphere. (d) N1s XPS spectra of g-C₃N₄ and Zn-CN_x microsphere.

Figure 7.6 (c) shows the comparison of C1s XPS spectra between g-C₃N₄ and Zn doped g-CN_x microsphere whereas comparison of their N1s spectra is given in Figure 7.6 (d). N1s XPS spectrum of Zn doped g-CN_x microsphere was shifted towards lower binding energy compared to g-C₃N₄ suggesting interaction between Zn and nitrogen atom of g-C₃N₄. It is reported that the Zn 2p XPS spectrum of Zn-N appears at lower binding energy compare to zero valence Zn. Lower binding energy of Zn 2p XPS spectrum and negative shifting of the N1s binding energy of Zn doped g-CN_x microsphere suggested the Zn-N bond formation³⁶. In addition broadening of C1s spectrum of Zn doped g-CN_x microsphere suggesting the decrease of the graphitic nature of Zn doped g-CN_x microsphere after doping with zinc which also good agreement with the p-XRD data. In addition also presence of Zn LMM auger peak in the survey scan (Figure 7.6 (a)) also supports the strong bonding interaction between zinc and carbon nitride moiety³⁷. CHN analysis of free g-C₃N₄ and Zn doped g-CN_x microsphere was shown in Table 7.1. The Nitrogen (N):Carbon (C) ratio in Zn doped g-CN_x microsphere was 0.45 which lower than the value of free g-C₃N₄. Zinc loading in the Zn doped g-CN_x microsphere was found to be 26 wt%. We have also prepared zinc doped CN_x with various zinc loading, these porous morphologies were found when zinc loading are in between 20-40 wt%.

Table 7.1. Detailed CHN analysis of g-C₃N₄ and porous Zn-CN_x microspheres

Sample	Carbon (wt. %)	Nitrogen (wt. %)	Hydrogen (wt. %)	Oxygen (wt. %)	N/C ratio
g-C ₃ N ₄	43.13	47.3	3.79	5.78	1.1
Zn-CN _x	35	16	2.5	-	0.46

7.4. Room temperature ferromagnetic property of porous Zn-CN_x microspheres

In the chapter 3 we have shown that the g-CNQDs have ferromagnetic property at room temperature. In this chapter we have analyzed the magnetic properties of the Zn-CN_x composite. This composite also shows the ferromagnetic property at room temperature. The study of the magnetic property of this composite was done by doing the magnetic field (M-H) and temperature dependent (M-T) magnetic study. Figure 7.7 and 7.8 represent the magnetic property study of Zn-CN_x composite. Magnetic properties of the as synthesized compound was studied by measuring the Hysteresis loop i.e. magnetization (M) vs. magnetic field (H) curve at room temperature (300K) and as well as low temperature (10K). Figure 7.7 (a) shows the magnetic field dependent magnetization curve (M-H) of the Zn-CN_x composite at room temperature (300K) and at low temperature (10K). Figure 7.7 (b) represents the magnetic Hysteresis loops (M-H curve) of Zn-CN_x composite at 300K and 10K at the lower magnetic field region. The saturated magnetization values of Zn-CN_x composite are 0.0039 emu/gm at 300K temperature and 0.0062 emu/gm at 10K temperature. The coercive fields (H_c) of Zn-CN_x composite are 129.2 Oe at 300K and 50.9 Oe at 10K. The saturated magnetization (M_s) values and the coercive fields of Zn-CN_x are tabulated in Table 7.2. Therefore, at both the temperatures Zn-CN_x is showing saturated magnetization and clear hysteresis loop which prove its ferromagnetic nature at room temperature and at low temperature. FESEM image of Zn-CN_x composite reveals that it has porous structure which is responsible to create lot of defects into it which is may be origin of ferromagnetism³⁸. During measurement of Hysteresis loop when the magnetic field drops to zero, the ferromagnetic material still shows some degree of magnetization value which is called remnant magnetization (M_r). Zn-CN_x composite material are having sufficient amount of remnant magnetization at both the temperatures of 10K and 300K which are shown in Table 7.2.

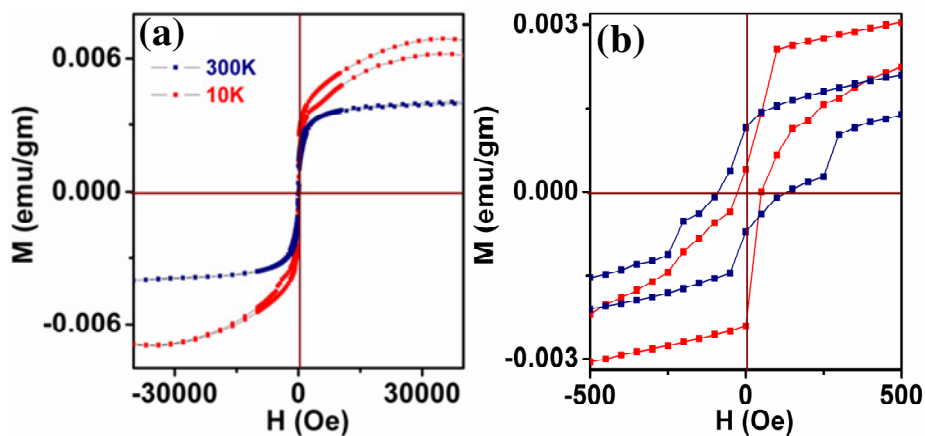


Figure 7.7. (a) Magnetic Hysteresis loops (M-H curve) of Zn-CN_x microsphere at 300K and 10K. (b) Magnetic Hysteresis loops (M-H curve) of Zn-CN_x microsphere at 300K and 10K at the lower magnetic field region.

Figure 7.8 displays the field cooled (FC)–zero field cooled (ZFC) magnetization curve Zn-CN_x composite in presence of external magnetic field of 1000 Oe. In the FC-ZFC magnetization curve of Zn-CN_x composite there is distinct splitting up to 280K which proves Curie temperature of Zn-CN_x is higher than the 280K. High Curie temperature of a magnetic material is one of the very much important criteria to be using that magnetic material in the spintronic devices. Therefore, Zn-CN_x composite can be used in the spintronic devices. The absence of any peak in the FC-ZFC magnetization curve proves that there is no magnetic phase transition in Zn-CN_x composite. In ZFC curve of Zn-CN_x composite there is no blocking temperature which proves the absence of ferromagnetic cluster in the samples. The ZFC and FC curves of Zn-CN_x composite also prove their ferromagnetic behavior with absence of Curie temperature. Usually, in ferromagnetic materials the coercive field decreases with increase of temperature whereas in

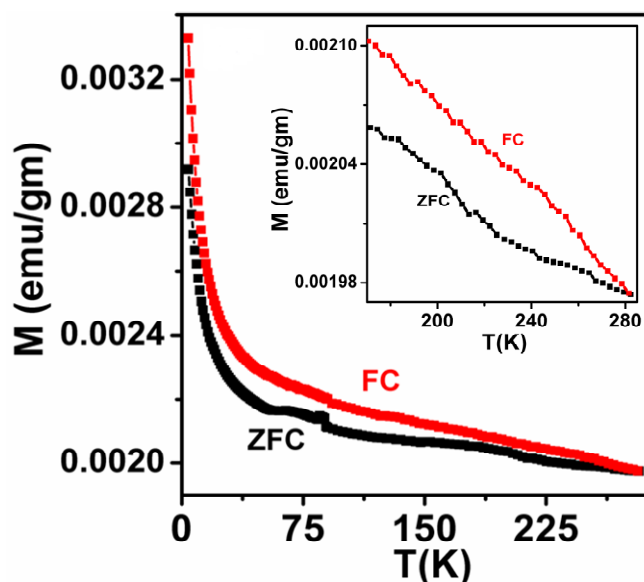


Figure 7.8. Field cooled (FC) – Zero field cooled (ZFC) magnetization curve of Zn-CN_x composite. Data measured at the external magnetic field of 1000 Oe. Insets represent the higher temperature region.

Table 7.2. Different Magnetic parameters of Zn-CN_x microspheres

M_S (emu/g)		M_R (emu/g)		Coercive field (Oe)	
<u>10K</u>	<u>300K</u>	<u>10K</u>	<u>300K</u>	<u>10K</u>	<u>300K</u>
0.0062	0.0039	0.00042	0.0012	50.9	129.2

Table 7.3. Elemental content in Zn-CN_x microspheres

Fe (ppm)	Co (ppm)	Ni (ppm)	Cr (ppm)	Mn (ppm)	Cu (ppm)
0.307	0.0704	0.0615	0.0114	0.001	0.014

Zn-CN_x composite the coercive field decreases with decrease of temperature which is an unusual behavior. A complete understanding of change of coercive field with temperature is not simple. Despite of these difficulties many scientists studied much theoretical and experimental investigation on the change of coercive field with the temperature. J. M. Guzman *et. al.*³⁹ demonstrated that for a particular thickness of FePt thin film ($35 \text{ nm} \leq d \leq 56 \text{ nm}$) the coercive field decreases with decrease of temperature, at very low temperature again the coercive field started to increases. Switching between in-plane domain and stripe domain in the disordered FePt thin film is the cause of its unusual behavior. The decrease of coercive field with decrease of temperature depends on inter magnetic particle interaction, phase transformation, different size of particles or competing magnetic anisotropy effect⁴⁰. Here the porous structure of the Zn-CN_x microspheres may be the cause of unusual dependency of coercive field on temperature. We have done atomic absorption spectroscopy (AAS) of the Zn-CN_x composite to know the amount of different metals present into the composite material which are responsible to produce the ferromagnetic signal. The metal concentrations of iron, cobalt, nickel, chromium and manganese present in the Zn-CN_x composite are shown in Table 7.3. The table represents that the all metal concentration is less than 10 ppm which this is not sufficient to produce the ferromagnetic signal into the material⁴¹. Therefore it can be concluded that ferromagnetism property of the Zn-CN_x composite does not originating from the impurity of magnetic metals; it has intrinsic ferromagnetic property. Beside this it is well known that zinc have no magnetic property, therefore zinc metal is not responsible to generate the ferromagnetism property into the Zn-CN_x microspheres. It is reported that the carbon defect, hydrogen dangling bonds due to hydrogenation and hole defect can induce the ferromagnetic property into the carbon based materials^{38, 42-43}. The CHN analysis of Zn-CN_x composite is shown into the Table 7.1. Here the

N/C ratio of Zn-CN_x microspheres is 0.46 which is less than the same of g-C₃N₄; these leading to hole defect into the Zn-CN_x microspheres. Therefore it can be concluded that the hole defect may be responsible to generate the ferromagnetic property into the Zn-CN_x microspheres. Sufficient amount of remnant magnetization value and high magnetic saturation value of Zn-CN_x composite can open a new application in magnetic memory devices and different spintonic devices.

7.5. Adsorption of metal ions on porous Zn-CN_x microspheres

7.5.1. Experimental method of metal ion adsorption by Zn-CN_x microspheres

All the metal ion adsorption studies were done at room temperature (25°C). Removal efficiency (RE) at equilibrium can be calculated from the following equation

$$RE = (C_0 - C_e) / C_0 * 100 \%$$

where C₀ and C_e are the concentrations of Cd²⁺ ions in solution at time zero and at equilibrium respectively. Adsorption isotherm plots were constructed from the batch experiment study of different metal ions separately. In batch experiment 10.0 ml aqueous solution of different initial concentration of metal ion was stirred with 5.0 mg Zn doped g-CN_x microsphere to reach the equilibration. The mixture was stirred with stirring bead throughout the adsorption process to ensure the contact between metal ions and the Zn doped g-CN_x microsphere. After reach at equilibrium the Zn doped g-CN_x microsphere was separated from the solution by centrifugation

with 16,000 rpm speed and the remaining metal ion concentration into the solution was measured by flame atomic absorption spectrophotometer (FAAS). The adsorbed metal ion on the Zn doped g-CN_x microsphere was calculated by the following equation:

$$q_e = (C_0 - C_e) * V / m$$

where q_e (mg g⁻¹) is the amount of adsorbed metal ion per unit mass of adsorbent after complete adsorption, C_0 and C_e are the initial and equilibrium concentration of metal ions respectively (mg L⁻¹), m is the weight of adsorbent (g) and V is the volume of solution (L). Adsorption kinetic study of the metal ion was done at a particular initial concentration. At different time intervals solution was taken out and measured the concentration of the metal ion present into that solution by flame atomic absorption spectrophotometer. Other experimental conditions were kept same like previous. The adsorption capacity (q_t) of the Zn-CN_x microspheres after a particular time (t) was calculated by the following equation:

$$q_t = (C_0 - C_t) \times V / m$$

where C_t represents concentration of metal ion after time t .

7.5.2. Cadmium ion adsorption study on Zn-CN_x microspheres

The Zn doped g-CN_x porous microsphere was used as an adsorbent for removal of toxic metal ions from aqueous solution. The adsorption of Cd²⁺ ions on Zn doped CN_x microspheres adsorbent was studied first. 5 mg of Zn doped g-CN_x microsphere was added in 10.0 ml aqueous

solution of Cd^{2+} ion for the adsorption study. Figure 7.9 (a) shows during adsorption the change of the concentration of Cd^{2+} ion in aqueous solution with the contact time on Zn doped g-CN_x microsphere. This contact time measurement shows the concentration of Cd^{2+} ion decreases with time and after 70 minutes decreases very slowly. After 170 minutes removal efficiency of Zn doped g-CN_x microsphere towards Cd^{2+} metal ion became $\sim 98\%$. This suggests that Zn doped g-CN_x microsphere have significant adsorptive removal efficiency towards Cd^{2+} ions from aqueous solution. Generally, the adsorption of toxic metal ions on adsorbent is strongly dependent on the pH of the solution as well as surface charge of adsorbent.

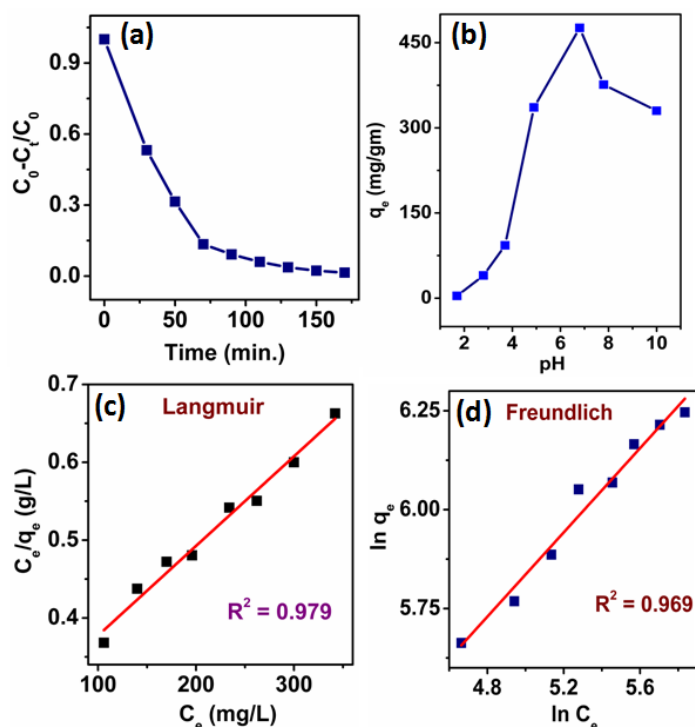


Figure 7.9. (a) Contact time effect on the adsorption of Cd^{2+} ion on Zn doped g-CN_x microsphere. (b) The effect of the pH of Cd^{2+} adsorption on Zn doped g-CN_x microsphere. Adsorption isotherm of Cd^{2+} ion on Zn doped g-CN_x microsphere after fitting with (c) Langmuir and (d) Freundlich adsorption isotherm model.

It shows highest adsorption capacity of Zn doped g-CN_x microsphere for Cd²⁺ ions at neutral pH (~6.8) and decreases the adsorption capacity with decreasing the pH of the solution. The zeta potential measurements of Zn doped g-CN_x microsphere at different pH values are shown in Figure 7.10. The zeta potential at neutral pH (6.9) is -5.0mV and increases with decreasing pH, and at pH 2, it became a positive value of 12.2mV. This suggests adsorption at acidic pH is not suitable for the removal of metal ions due to the repulsion between positively charged Zn doped g-CN_x microsphere and metal ions. Figure 7.9 (b) shows the effect the pH of Cd²⁺ adsorption on Zn doped g-CN_x microsphere. At low pH values, the adsorption capacity of Cd²⁺ ions on Zn doped g-CN_x microsphere is reduced drastically due to competitive adsorption of proton and Cd²⁺ ions.

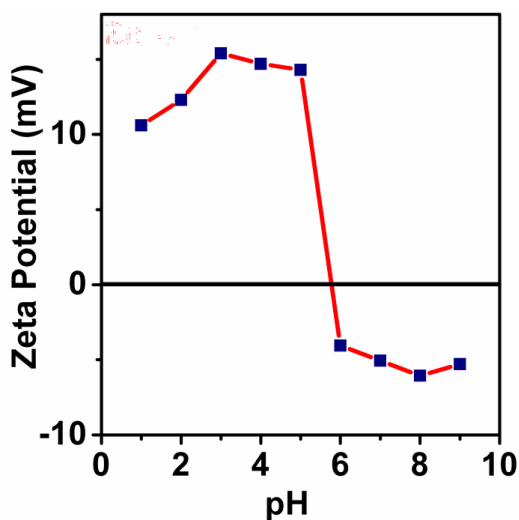


Figure 7.10. Zeta potentials of Zn-CN_x microspheres at different pH.

Therefore, we have performed all the metal ions adsorption studies on Zn doped g-CN_x microsphere at pH of 6.8. The maximum adsorption capacity (q_{max}) is an important parameter to

understand the efficiency of the adsorption. The adsorption isotherm study can provide the idea of adsorption capacity of the adsorbent. Adsorption isotherm study of Cd^{2+} metal ion on Zn doped g-CN_x microsphere was done by using batch experiment. In batch experiment, different aqueous solutions (10.0 ml) of varying Cd^{2+} ion concentrations were stirred with 5.0 mg of Zn doped g-CN_x microsphere to reach the equilibrium condition. After reaching at equilibrium, the composite was separated from the solution by centrifugation and finally, FAAS was used to find out the remaining Cd^{2+} ions concentration into the solutions. In order to find maximum adsorption capacity adsorption isotherm plots were plotted. Different adsorption isotherm models are available, such as Langmuir adsorption isotherm, Freundlich adsorption isotherm, BET model etc. Langmuir and Freundlich adsorption isotherm model is based on the heterogeneous surfaces. Langmuir adsorption assumes that there is no interaction among the adsorbent molecules. Langmuir adsorption isotherm is based on monolayer coverage of adsorbate on the adsorbent. One adsorption site of the adsorbent can take only one adsorbate molecule, it cannot take another molecule. Langmuir adsorption isotherm model is expressed by the following equation

$$\frac{C_e}{q_e} = \frac{1}{q_{\max}K_L} + \frac{C_e}{q_{\max}}$$

where q_e is the amount of metal adsorbed on adsorbent at equilibrium (mg/gm), K_L is the Langmuir constant which is related to heat of adsorption and it quantitatively represents the binding site affinity on the adsorbent, q_{\max} is the maximum adsorption capacity (mg/gm), C_e is the equilibrium concentration of metal ion in solution (mg/L)⁴⁴. If we plot C_e/q_e vs. C_e then we will get a straight line where slope will be $1/q_{\max}$ and intercept will be $1/(q_{\max} \cdot K_L)$. Therefore,

q_{\max} can be calculated from the slope and K_L can be calculated from the intercept of the straight line. Freundlich adsorption isotherm model is multilayer adsorption process and it is expressed as

$$\ln q_e = \ln K_f + \frac{1}{n} \ln C_e$$

Table 7.4. Relative parameters of adsorption isotherm of Cd^{2+} ions after fitting with Langmuir and Freundlich adsorption isotherm model

Metal ion	Langmuir constants			Freundlich constants		
	q_m (mg/g)	K_L (L/mg)	R^2	K_f	n	R^2
Cd^{2+}	869.5	0.00438	0.979	23.88	1.88	0.969

Table 7.5. Comparison of maximum adsorption capacities of Cd^{2+} metal ion adsorption with different adsorbent

Adsorbent	Method	Max. Capacity (mg/gm)	Ref.
$Cu_3(BTC)_2-SO_3H$	AAS	88.7	29
GO	FAAS	530.0	21
GO	AAS	106.3	20
PANI-PS	ICP-AES	124.0	45
3D-Graphene/ δMnO_2	ICP-OES	250.31	46
Fe_3O_4 -GS	-	27.83	47
Zn-CN _x	FAAS	869.5	this work

where K_f and n are the Freundlich fitting parameter constants. K_f (L/gm) represents the intensity of the adsorption process and $1/n$ is the measure of the adsorption intensity⁴⁸. The adsorption isotherm of Cd^{2+} metal ion on Zn doped CN_x microspheres adsorbent was studied at room temperature and at normal pH. The adsorption isotherm plots for Cd^{2+} ions on Zn doped g- CN_x microsphere was constructed from the batch adsorption experiment with aqueous solutions of different initial concentration of Cd^{2+} ions. The adsorption isotherms for Cd^{2+} ions on Zn doped CN_x microspheres are shown in Figure 7.9 (c and d). The experimental adsorption data were fitted with Langmuir and Freundlich adsorption isotherms as shown in Figure 7.9 (c and d) respectively. By using these two isotherm models, we have calculated different isotherm parameters (q_m , K_L , K_F , and n) and correlation coefficient (R^2) which were shown in Table 7.4. Based on the R^2 values, it can be concluded that the adsorption of Cd^{2+} ion on Zn doped g- CN_x microsphere adsorbent is fitted well with the Langmuir isotherm model in comparison to the Freundlich adsorption isotherm model. This suggests cadmium metal ion adsorption on Zn doped g- CN_x microsphere is monolayer type of adsorption. The maximum adsorption capacity of Cd^{2+} on Zn doped g- CN_x microsphere calculated from Langmuir isotherm was found to be 869.5 mg/gm. The Freundlich parameter (n), calculated after fitting with Freundlich adsorption isotherm model (Table 7.4) shows the value of n is higher than 1 suggesting the Cd^{2+} adsorption process is favorable on the Zn doped g- CN_x microsphere⁴⁹. Beside this, the high K_f value also represents the good Cd^{2+} metal ion adsorption property of Zn- CN_x microspheres. The comparison of maximum adsorption capacity of these Zn doped CN_x microspheres adsorbent with other reported benchmark adsorbent was tabulated in Table 7.5. The q_{max} value of Zn doped CN_x microspheres adsorbent for Cd^{2+} ion is highest among all reported carbon based adsorbents.

7.5.3. Copper and Lead ion adsorption studies on Zn doped CN_x microsphere

We have also performed adsorption of Cu²⁺ and Pb²⁺ ions on porous Zn doped g-CN_x microspheres at neutral pH solution. Like Cd²⁺ adsorption study, the batch experiment was performed to investigate the removal capacity of Cu²⁺ and Pb²⁺ ions on Zn doped g-CN_x microspheres separately. The aqueous solutions with different initial metal ion concentrations were used with 5.0 mg of Zn doped g-CN_x microsphere composite and stirred for several hours to reach the equilibrium condition to perform the batch experiment. After reach at equilibrium condition the adsorbent was separated from the solution by centrifugation and FAAS was used to find out the metal ion concentration into the solution.

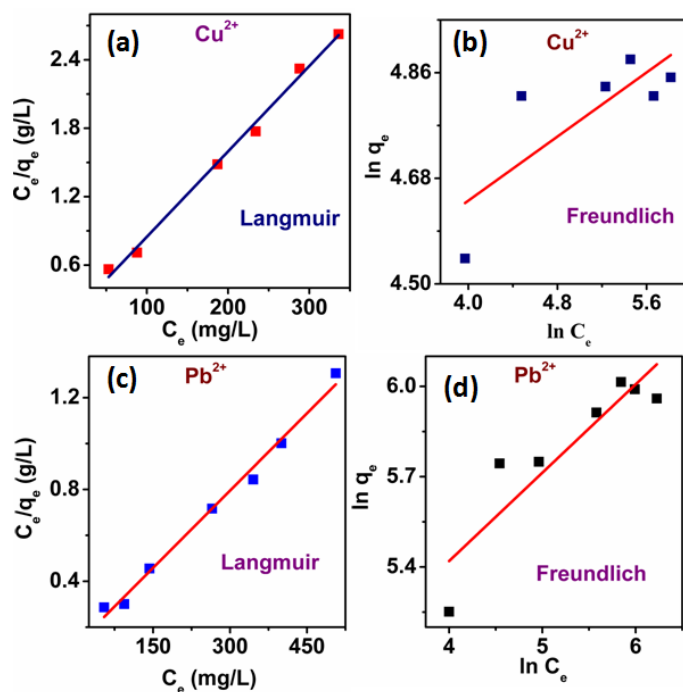


Figure 7.11. (a) Langmuir and (b) Freundlich adsorption isotherm model fitting of Cu²⁺ ion on Zn doped g-CN_x microsphere. (c) Langmuir and (d) Freundlich adsorption isotherm fitting of Pb²⁺ ion on Zn doped g-CN_x microsphere.

Table 7.6. Relative parameters of adsorption isotherm of Cu^{2+} and Pb^{2+} metal ions after fitting with Langmuir and Freundlich adsorption isotherm model

Metal ion	Langmuir constants			Freundlich constants		
	$q_m(\text{mg/g})$	$K_L (\text{L/mg})$	R^2	$K_f (\text{mg g}^{-1})$	n	R^2
Cu^{2+}	133.5	0.0758	0.994	60.1	7.32	0.546
Pb^{2+}	446.4	0.0184	0.988	69.76	3.41	0.790

Table 7.7. Comparison of maximum capacities of Cu^{2+} metal ion adsorption with different adsorbent

Adsorbent	Method	Max. Capacity (mg/g)	Ref.
(PDA)-LDH (MPL)	AAS	75.01	50
PANI-PS	ICP-AES	171	45
3D-Graphene/ δMnO_2	ICP-OES	228.46	46
GO- Fe_3O_4	AAS	18.26	51
PD/GO	ICP-OES	24.4	52
CZ-1	AAS	51.32	53
MCB	AAS	47.5	49
GO membrane	AAS	72.6	54
CuO-ZnO nanofibers	ICP-MS	27.7	55
Zn- CN_x	FAAS	133.5	this work

Table 7.8. Comparison of maximum capacities of Pb^{2+} metal ion adsorption with different adsorbent

Adsorbent	Method	Max.Capacity (mg/g)	Ref.
PS-GO	FAAS	227.92	6
MgSi/RGO	ICP-AES	416	15
ZnCl ₂ -MCM-41	AAS	479	56
GO-NH ₂	ICP-OES	96.6	57
P(AANa-co-AM)/GO	FAAS	452.3	58
Mg-silicate	ICP-AES	300	59
Zn-CN _x	FAAS	446.4	this work

The Langmuir adsorption isotherm plots for Cu^{2+} and Pb^{2+} ions are shown in Figure 7.11 (a and c) respectively whereas Freundlich adsorption isotherm plots for Cu^{2+} and Pb^{2+} ions are shown in Figure 7.11 (b and d) respectively. The isotherm parameters and correlation coefficients were summarized in Table 7.6. Both Cu^{2+} and Pb^{2+} adsorption isotherms on Zn doped g-CN_x microsphere follow the Langmuir isotherm model based on correlation coefficient values (R^2). The calculated maximum adsorption capacities (q_{max}) of Cu^{2+} and Pb^{2+} are 133.5 and 446.4 and mg/gm respectively calculated from the Langmuir isotherm model equation. The calculated maximum up take capacity of Zn doped g-CN_x microsphere for Pb^{2+} and Cu^{2+} are compared with the different reported adsorbent materials for Cu^{2+} and Pb^{2+} ions in Table 7.7 and 7.8 respectively. The maximum adsorption capacity of Zn doped g-CN_x microspheres for Cu^{2+} and

Pb²⁺ ions are comparable with the reported values. The high adsorption capacity of Zn doped CN_x microspheres towards removal of various toxic metal ions make one of best adsorbent for the purification of water.

7.5.4. Metal ion adsorption kinetic study on Zn doped CN_x microspheres

The kinetic study of metal ions adsorption on an adsorbent is important to understand adsorption mechanism. The adsorption kinetics studies of Cd²⁺ and Pb²⁺ ion on Zn doped g-CN_x microsphere were performed with initial metal concentration of 500 ppm at pH 6.8 separately. There are two different models for kinetic study of adsorption method available: one is pseudo first order kinetic model and another is pseudo second order kinetic model. The pseudo-first order kinetic model is represented as

$$\ln (q_e - q_t) = \ln q_e - K_1 t$$

where K₁ is the first order rate constant (min⁻¹) and q_e (mg g⁻¹) and q_t (mg g⁻¹) are the adsorption capacity at equilibrium and adsorption capacity at time t respectively ²⁹. The pseudo second order kinetic model represents as

$$\frac{t}{q_t} = \frac{1}{K_2 q_e^2} + \frac{1}{q_e} t$$

where K₂ is the second order rate constant (g mg⁻¹ min⁻¹)⁴⁴. The experimental kinetics data for Cd²⁺ and Pb²⁺ ion adsorption on Zn doped g-CN_x microsphere were fitted with pseudo first order kinetic model and pseudo second order kinetic model as shown in Figure 7.12 (a and b) and

Figure 7.12 (c and d) respectively. The different kinetics parameters and correlation coefficients for Cd²⁺ and Pb²⁺ ion adsorption were summarized in Table 7.9.

Table 7.9. The adsorption kinetics model parameters of metal ions after fitting with pseudo-first order and pseudo-second order kinetic model

Metal ion	Pseudo-second order			Pseudo-first order			
	q _e (mg/g) (theor.)	K ₂ X 10 ⁻⁴ (g mg ⁻¹ min ⁻¹)	R ²	q _e (mg/gm) (exp.)	K ₁ (min ⁻¹)	q _e (mg/gm) (theor.)	R ²
Cd ²⁺	684.9	0.355	0.990	590.0	0.0202	740.0	0.857
Pb ²⁺	88.5	15	0.991	90.0	0.017	35.81	0.883

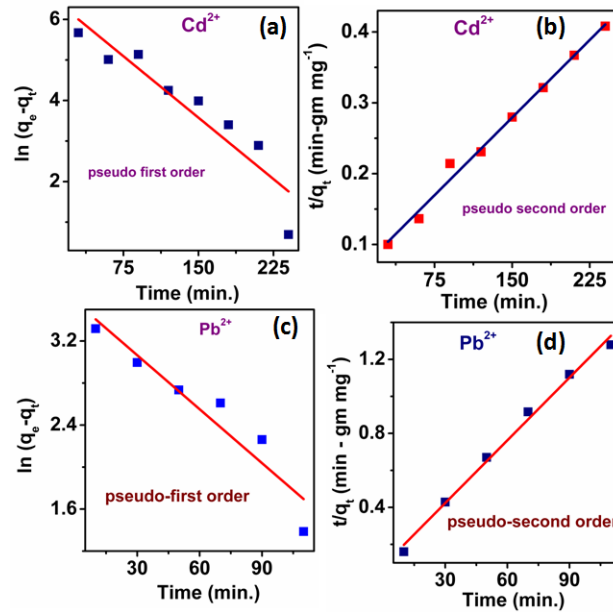


Figure 7.12. Adsorption kinetic study of Cd²⁺ ion on Zn doped g-CN_x microsphere with fitting of (a) pseudo-first order and (b) pseudo-second order kinetic model equations. Adsorption kinetic study of Pb²⁺ ion on Zn doped g-CN_x microsphere with fitting of (c) pseudo-first order and (d) pseudo-second order kinetic model equations.

The calculated correlation coefficient (R^2) for the fitting with the pseudo second order kinetic model is higher than that of pseudo first order kinetic for the both Cd^{2+} and Pb^{2+} ions adsorption kinetic studies. This suggests that adsorption of Cd^{2+} and Pb^{2+} ions on the Zn doped $g-CN_x$ microsphere follow the pseudo-second order kinetic model instead of pseudo-second first order kinetic model and rate constant (K_2) were found to be $3.5 \times 10^{-5} \text{ g mg}^{-1} \text{ min}^{-1}$ and $15 \times 10^{-5} \text{ g mg}^{-1} \text{ min}^{-1}$ for Cd^{2+} and Pb^{2+} ion respectively.

7.5.5. Determination of thermodynamic parameters during cadmium adsorption process

Thermodynamic parameters of an adsorption process which can easily be calculated from temperature dependent adsorption isotherms are important to know the spontaneity of the process and the nature of the adsorption process such as exothermic or endothermic process. The thermodynamic parameters such as change of Gibbs free energy (ΔG^0), change of enthalpy (ΔH^0) and change of entropy (ΔS^0) for the adsorption process were calculated from the following thermodynamic equations⁶⁰

$$\Delta G^0 = -RT \ln K_d$$

$$\Delta G^0 = \Delta H^0 - T \Delta S^0$$

$$\ln K_d = \Delta S^0/R - \Delta H^0/RT$$

where T is temperature in Kelvin, R is the gas constant ($8.314 \text{ J mol}^{-1} \text{ K}^{-1}$), K_d is the dimensionless distribution coefficient. K_d can be estimated from the Langmuir constant (K_L).

$$K_d = K_L \times C_w$$

C_w is water concentration ($1001900 \text{ mg L}^{-1}$)⁶¹. From this equation if we plot $\ln K_d$ vs. $1/T$, then from the slope we can find out the enthalpy change (ΔH^0) and from the intercept we can find out the entropy change (ΔS^0) of the adsorption process. The calculation of different thermodynamic parameters was done by studying the adsorption of Cd^{2+} ions onto Zn doped g- CN_x microsphere at three different temperatures (298K, 313K and 328K). The Langmuir adsorption isotherms for Cd^{2+} ions adsorption on Zn doped g- CN_x microsphere at three different temperatures are presented in Figure 7.13 (a). The maximum adsorption capacities (q_{max}) are 869.5 mg/g, 917.4 mg/g and 970.9 mg/g at temperatures of 298K, 313K and 328K respectively. Figure 7.13 (b) shows the plot of $\ln K_d$ vs $1/T$ and its linear fitting of Cd^{2+} adsorption on Zn doped g- CN_x microsphere. The calculated thermodynamic parameters were tabulated in Table 7.10 shows that the change of Gibbs free energy (ΔG) were negative values at all the temperatures (298K, 313K and 328K) suggesting that adsorption of metal ions on Zn doped porous microspheres are spontaneous (thermodynamically favourable) process at each temperatures.

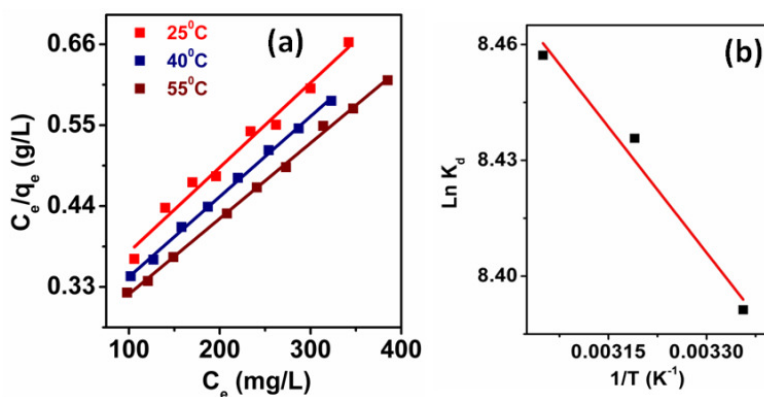


Figure 7.13. (a) Langmuir adsorption isotherm of Cd^{2+} on Zn doped g- CN_x microsphere at different temperatures. (b) van't Hoff plot of Cd^{2+} ion adsorption on Zn doped g- CN_x microsphere for the calculation of thermodynamic parameters.

The more negative ΔG values with increasing temperature suggest that metal ion adsorption on Zn doped g-CN_x microsphere at high temperatures become more favourable. The change of entropy for this adsorption process is a positive value of 75.8 J mol⁻¹ K⁻¹ is also suggesting the spontaneity of the adsorption process. The positive value of ΔS also indicates that there is increase of randomness at solid-solution interfaces. The positive value of enthalpy change (ΔH^0) indicates that the adsorption process is an endothermic process⁶². It is reported in the literature that, when ΔH value is in between 20.9 KJ mol⁻¹ and 418.4 KJ mol⁻¹, the type of adsorption is generally assumed to be a chemical adsorption processes. The small positive ΔH value (1.8 KJ mol⁻¹) for adsorption of Cd²⁺ ions on Zn doped g-CN_x microsphere suggests that adsorption is physical nature.

Table 7.10. Thermodynamic parameters of the adsorption of Cd²⁺ ions on Zn-CN_x

Temp.	Langmuir constants			Thermodynamic parameters		
	q _m (mg/gm)	K _L	R ²	ΔG^0 (KJ mol ⁻¹)	ΔH^0 (KJ mol ⁻¹)	ΔS^0 (J mol ⁻¹ K ⁻¹)
298K	869.5	0.0044	0.979	-20.79		
313K	917.4	0.0046	0.997	-21.95	1.80	75.8
328K	970.9	0.0047	0.998	-23.06		

7.5.6. Experimental method of Congo red adsorption on Zn-CN_x microspheres

The Congo red (CR) adsorption study was performed by adding 5 mg of Zn-CN_x microspheres to the 10mL solution of different concentrations of CR and stirred for 6 hours to reach adsorption equilibrium. Before adding adsorbent i.e. Zn-CN_x microspheres the pH of the CR solution was

adjusted at 3 using 0.1(M) sulfuric acid (H₂SO₄) solution. After reach at adsorption equilibrium the Zn-CN_x microspheres was separated by centrifugation at 8000 rpm for 20 minutes. After separating the adsorbent the concentration of CR in the solution was measured by UV-visible spectrophotometer. After reach at equilibrium the adsorbed CR dye was calculated by the following equation

$$q_e = (C_0 - C_e) * V / m$$

where q_e (mg/g) is the equilibrium capacity of dye on adsorbent, C_0 and C_e are the initial and equilibrium concentration of dye respectively (mg L⁻¹), m is the weight of adsorbent (g) and V is the volume of dye solution (L).

7.5.7. Effect of pH on Congo Red adsorption study by Zn-CN_x microsphere

The surface of the Zn-CN_x microspheres is positive charge at lower pH and negatively charge at higher pH which is shown in the Figure 7.11 and it is well known that Congo red is an anionic azo dye. Therefore, at neutral condition there is electrostatic repulsion between CR dye molecules and Zn-CN_x microspheres whereas at high pH there is electrostatic repulsion among OH⁻ ions, Zn-CN_x microspheres and CR dye molecules. Additionally, at high pH i.e. in basic condition the Zn-CN_x composite is not stable in solution. Due to this electrostatic repulsion there is less probability of CR dye to attach on the surface of Zn-CN_x composite at higher pH. Due to this phenomenon low pH is the suitable for the adsorption study of CR dye on the surface of Zn-CN_x microspheres. At low pH the anionic charge of the dye neutralized and then it adsorbed on the positive surface of the Zn-CN_x composite. At very low pH there is a chance of aggregation

CR dye molecules with each other. So pH was optimized at 3.0 during the experiment. The pH was adjusted by using dilute H_2SO_4 .

7.5.8. Adsorption Isotherm and kinetic study of Congo red on porous Zn-CN_x microspheres

Figure 7.14 represents the adsorption isotherm of the CR dye by Zn-CN_x microspheres. The adsorption isotherm of CR dye on Zn-CN_x composite was done at room temperature (25⁰C) and at pH 3.0. The Langmuir and Freundlich adsorption isotherm plots for CR are shown in Figure

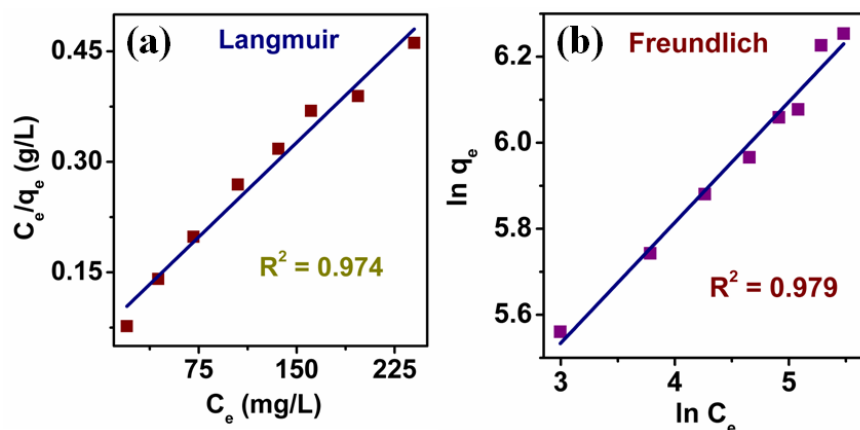


Figure 7.14. (a) Langmuir and (b) Freundlich adsorption isotherm model fitting of CR dye on Zn doped g-CN_x microsphere.

7.14 (a and b) respectively. The experimental adsorption data well fitted to both Langmuir and Freundlich isotherm models with the correlation value greater than 0.97. The Langmuir and Freundlich adsorption isotherm parameters are listed in the Table 7.11. The maximum adsorption capacity (q_{max}) of Zn-CN_x microspheres CR adsorption is 584.8 mg/g which was calculated from the linear Langmuir adsorption isotherm model equation. The calculated maximum up take

capacity of Zn-CN_x microspheres towards CR dye adsorption was compared with other different adsorbents and shown in Table 7.12. The unique porous morphology of Zn-CN_x microspheres is the key factor to adsorb the CR dye molecules on its porous spherical surface. Additionally the isotherm model parameters K_f and n were calculated from Freundlich isotherm model equation. The Freundlich constants K_f and n were calculated using the slope and intercept of the Freundlich isotherm model equation respectively. The K_f value represents the heterogeneous adsorption capacity which is sufficiently high proves the high adsorption performance of Zn-CN_x microspheres. The value of n (n = 1.88) is greater than one (n>1) proves the good adsorption of CR dye molecules on Zn-CN_x microspheres. The adsorption kinetic involves pseudo-first-order, second order, pseudo-second order and intraparticle diffusion models. The adsorption kinetic of CR dyes by Zn-CN_x microspheres is shown in the Figure 7.15 which is fitting with the pseudo-second order kinetic model equation in best way. The pseudo-second order kinetic model depends on the amount of dye adsorbed on adsorption kinetics of CR dye onto Zn-CN_x microspheres, the surface of adsorbent and amount of dye adsorbed at equilibrium.

Table 7.11. Relative parameters of adsorption isotherm of CR dye after fitting with Langmuir and Freundlich adsorption isotherm model

Langmuir constants			Freundlich constants		
q _m (mg/g)	K _L (L/mg)	R ²	K _f	n	R ²
584.8	0.02455	0.974	23.88	1.88	0.969

Table 7.12. Comparison of maximum adsorption capacities of CR adsorption with different adsorbents

Adsorbent	Max. Capacity (mg g ⁻¹)	Ref.
γ -Fe ₂ O ₃	208.33	8
(PDA)-LDH (MPL)	584.56	63
FHS	93.55	64
Zn-CN _x	584.8	this work

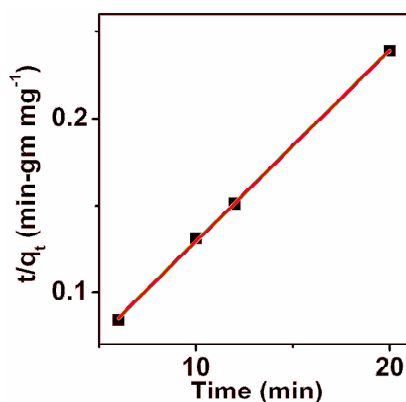


Figure 7.15. Pseudo-second order adsorption kinetics of CR dye onto Zn-CN_x composite.

Table 7.13. The adsorption kinetics model parameters of CR dye after fitting with pseudo-second order kinetic model

q _e (mg/g)	K ₂ X 10 ⁻² (g mg ⁻¹ min ⁻¹)	R ²
84.4	1.94	0.994

Figure 7.15 is the plot of t vs. t/q_t with straight line fitting. After fitting as a straight line from the slope we can find out q_e value and from this q_e value and intercept we can find out the pseudo-second order rate constant which is listed in Table 7.13.

7.5.9. Explanation on the adsorption by Zn-CN_x microsphere

In order to understand the nature of adsorption of metal ions on Zn doped g-CN_x microsphere we have done FT-IR spectroscopic measurements before and after adsorption of metal ions. To understand the mechanism of efficient adsorption of these metal ions on Zn doped g-CN_x microsphere we have done FT-IR spectroscopic measurements before and after adsorption of metal ions. Figure 7.16 (a and b) are the FT-IR spectra of Zn doped g-CN_x microsphere before and after adsorption of Cd²⁺ ion and Cu²⁺ ion respectively. There is no significant change of FT-IR spectra of the composite after metal ions adsorption suggesting a physical nature of the adsorption process.

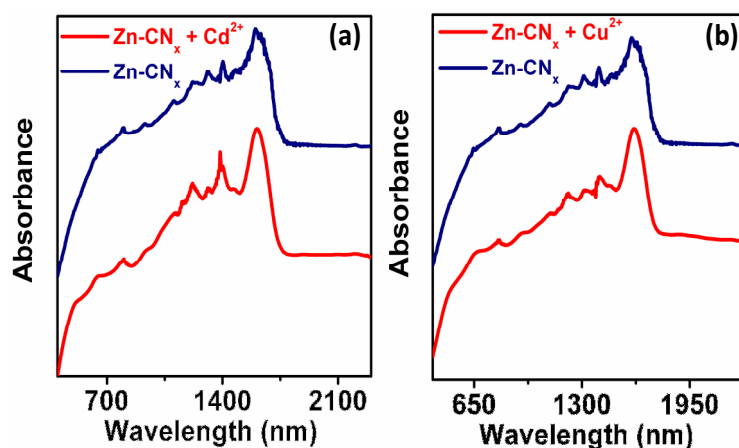


Figure 7.16. FT-IR spectra of Zn-CN_x after (a) Cd²⁺ ion adsorption (b) Cu²⁺ ion adsorption and these are compared with FT-IR spectrum of Zn-CN_x.

Furthermore, the negative zeta potential value (-5.0 mV) of this composite at neutral pH and small positive ΔH value for the adsorption proves that metal ions are physically adsorbed on Zn doped g-CN_x microsphere due to strong electro-static attraction between positively charged metals ions and negatively charged adsorbent. The superior adsorption of Zn doped g-CN_x microsphere can be attributed to porous microsphere morphology, easy dispersion of adsorbent in aqueous medium and strong electrostatic attraction between metal ions and Zn doped g-CN_x microsphere. We have tried to regenerate the adsorbent by several methods such as washing with adsorbent with de-ionized water, changing pH solution etc. However, we have unsuccessful to regenerate the adsorbent probably due to metal ions are strongly adsorbed on surface of adsorbent due to electro-static attraction.

7.6. Conclusion

In conclusion we have successfully synthesized the Zn doped CN_x porous microspheres by one pot hydrothermal method. The Zn atoms are homogeneously incorporated on the g-C₃N₄ moiety to form porous microspheres as confirmed from the FESEM and TEM analysis. Due to specific morphology of porous Zn doped CN_x composite material easy dispersion of metal ions in aqueous media make very high maximum adsorption capacities of Cd²⁺ (869.5 mg/gm), Cu²⁺ (133.5 mg/gm) and Pb²⁺ (446.4 mg/gm) ions. With increase of temperature the Gibbs free energy of the adsorption process gradually increasing that indicates the more feasibility and spontaneity of adsorption process of Cd²⁺ ion on Zn doped g-CN_x microspheres. Large maximum adsorption capacity, negative Gibbs free energy change and positive entropy change of the adsorption process by this Zn doped g-CN_x microspheres make it one of best adsorbent for water purification.

Chapter References

1. Hashim, M. A.; Mukhopadhyay, S.; Sahu, J. N.; Sengupta, B., *J. Environ. Manage.* **2011**, *92*, 2355-2388.
2. Goel, J.; Kadirvelu, K.; Rajagopal, C.; Garg, V. K., *Ind. Eng. Chem. Res.* **2006**, *45*, 6531-6537.
3. Darwish, I. A.; Blake, D. A., *Anal. Chem.* **2001**, *73*, 1889-1895.
4. Larous, S.; Meniai, A. H.; Lehocine, M. B., *Desalination* **2005**, *185*, 483-490.
5. Aydın, H.; Bulut, Y.; Yerlikaya, Ç., *J. Environ. Manage.* **2008**, *87*, 37-45.
6. Islam, A.; Ahmad, H.; Zaidi, N.; Kumar, S., *ACS Appl. Mater. Interface* **2014**, *6*, 13257-13265.
7. Chatterjee, S.; Lee, D. S.; Lee, M. W.; Woo, S. H., *Bioresource Technology* **2009**, *100*, 2803-2809.
8. Afkhami, A.; Moosavi, R., *J. Hazard. Mater.* **2010**, *174*, 398-403.
9. Skold, M. E.; Thyne, G. D.; Drexler, J. W.; Macalady, D. L.; McCray, J. E., *Environ. Sci. Technol.* **2008**, *42*, 8930-8934.
10. Chen, Y.; Pan, B.; Li, H.; Zhang, W.; Lv, L.; Wu, J., *Environ. Sci. Tech.* **2010**, *44*, 3508-3513.
11. Wu, N.; Wei, H.; Zhang, L., *Environ. Sci. Technol.* **2012**, *46*, 419-425.
12. Soyлак, M.; Unsal, Y. E.; Kizil, N.; Aydın, A., *Food Chem. Toxicol.* **2010**, *48*, 517-521.
13. Matlock, M. M.; Howerton, B. S.; Atwood, D. A., *Water Res.* **2002**, *36*, 4757-4764.
14. Ma, J.; Yu, F.; Zhou, L.; Jin, L.; Yang, M.; Luan, J.; Tang, Y.; Fan, H.; Yuan, Z.; Chen, J., *ACS Appl. Mater. Interfaces* **2012**, *4*, 5749-5760.

15. Gui, C.-X.; Wang, Q.-Q.; Hao, S.-M.; Qu, J.; Huang, P.-P.; Cao, C.-Y.; Song, W.-G.; Yu, Z.-Z., *ACS Appl. Mater. Interfaces* **2014**, *6*, 14653-14659.
16. Wang, J.; Lan, J.; Li, H.; Liu, X.; Zhang, H., *Talanta* **2017**, *162*, 380-389.
17. Garshasbi, V.; Jahangiri, M.; Anbia, M., *Appl. Surf. Sci.* **2017**, *393*, 225-233.
18. Liu, L.; Xie, Z.-H.; Deng, Q.-F.; Hou, X.-X.; Yuan, Z.-Y., *J. Mater. Chem. A* **2017**, *5*, 418-425.
19. Nagaraju, G.; Lim, J. H.; Cha, S. M.; Yu, J. S., *J. Alloys Compd.* **2017**, *693*, 1297-1304.
20. Zhao, G.; Li, J.; Ren, X.; Chen, C.; Wang, X., *Environ. Sci. Tech.* **2011**, *45*, 10454-10462.
21. Sitko, R.; Turek, E.; Zawisza, B.; Malicka, E.; Talik, E.; Heimann, J.; Gagor, A.; Feist, B.; Wrzalik, R., *Dalton Trans.* **2013**, *42*, 5682-5689.
22. Fan, L.; Luo, C.; Sun, M.; Li, X.; Qiu, H., *Colloids Surf., B* **2013**, *103*, 523-529.
23. Sitko, R.; Zawisza, B.; Talik, E.; Janik, P.; Osoba, G.; Feist, B.; Malicka, E., *Anal. Chim. Acta* **2014**, *834*, 22-29.
24. Tian, T.; Shi, X.; Cheng, L.; Luo, Y.; Dong, Z.; Gong, H.; Xu, L.; Zhong, Z.; Peng, R.; Liu, Z., *ACS Appl. Mater. Interfaces* **2014**, *6*, 8542-8548.
25. Yan, H.; Li, H.; Tao, X.; Li, K.; Yang, H.; Li, A.; Xiao, S.; Cheng, R., *ACS Appl. Mater. Interface* **2014**, *6*, 9871-9880.
26. Plaza Cazón, J.; Viera, M.; Donati, E.; Guibal, E., *J. Environ. Manage.* **2013**, *129*, 423-434.
27. Erdem, E.; Karapinar, N.; Donat, R., *J. Colloid Interface Sci.* **2004**, *280*, 309-314.
28. Senthil Kumar, P.; Ramalingam, S.; Abhinaya, R. V.; Kirupha, S. D.; Murugesan, A.; Sivanesan, S., *CLEAN – Soil, Air, Water* **2012**, *40*, 188-197.

29. Wang, Y.; Ye, G.; Chen, H.; Hu, X.; Niu, Z.; Ma, S., *J. Mater. Chem. A* **2015**, *3*, 15292-15298.
30. Kikuchi, Y.; Qian, Q.; Machida, M.; Tatsumoto, H., *Carbon* **2006**, *44*, 195-202.
31. Kumar, S.; Surendar, T.; Kumar, B.; Baruah, A.; Shanker, V., *RSC Adv.* **2014**, *4*, 8132-8137.
32. Wang, X.; Zhong, Y.; Zhai, T.; Guo, Y.; Chen, S.; Ma, Y.; Yao, J.; Bando, Y.; Golberg, D., *J. Mater. Chem.* **2011**, *21*, 17680-17687.
33. Thomas, A.; Fischer, A.; Goettmann, F.; Antonietti, M.; Muller, J.-O.; Schlogl, R.; Carlsson, J. M., *J. Mater. Chem.* **2008**, *18*, 4893-4908.
34. Goettmann, F.; Fischer, A.; Antonietti, M.; Thomas, A., *Angew. Chem. Int. Ed.* **2006**, *45*, 4467-4471.
35. Moulder, J. F.; Stickle, W. F.; E.'Sobol, P.; Bomben, K. D., *Physical Electronics Division, Perkin-Elmer Corp.* **1979**.
36. Bing, Y.; Qiuye, L.; Hideo, I.; Tetsuya, K.; Jinhua, Y., *Sci. and Tech. Adv. Mater.* **2011**, *12*, 034401.
37. Futsuhara, M.; Yoshioka, K.; Takai, O., *Thin Solid Films* **1998**, *322*, 274-281.
38. Gao, D.; Xu, Q.; Zhang, J.; Yang, Z.; Si, M.; Yan, Z.; Xue, D., *Nanoscale* **2014**, *6*, 2577-2581.
39. Guzmán, J. M.; Álvarez, N.; Salva, H. R.; Vásquez Mansilla, M.; Gómez, J.; Butera, A., *J. Magn. Magn. Mater.* **2013**, *347*, 61-67.
40. Guo, X.; Chen, X.; Altounian, Z.; Ström-Olsen, J. O., *J. Appl. Phys.* **1993**, *73*, 6275-6277.
41. Gao, D.; Shi, S.; Tao, K.; Xia, B.; Xue, D., *Nanoscale* **2015**, *7*, 4211-4216.

42. Qiu, H.; Wang, Z.; Sheng, X., *Physica B* **2013**, *421*, 46-49.
43. Xu, K.; Li, X.; Chen, P.; Zhou, D.; Wu, C.; Guo, Y.; Zhang, L.; Zhao, J.; Wu, X.; Xie, Y., *Chem. Sci.* **2015**, *6*, 283-287.
44. Vuković, G. D.; Marinković, A. D.; Čolić, M.; Ristić, M. Đ.; Aleksić, R.; Perić-Grujić, A. A.; Uskoković, P. S., *Chem. Eng. J.* **2010**, *157*, 238-248.
45. Alcaraz-Espinoza, J. J.; Chávez-Guajardo, A. E.; Medina-Llamas, J. C.; Andrade, C. A. S.; de Melo, C. P., *ACS Appl. Mater. Interfaces* **2015**, *7*, 7231-7240.
46. Liu, J.; Ge, X.; Ye, X.; Wang, G.; Zhang, H.; Zhou, H.; Zhang, Y.; Zhao, H., *J. Mater. Chem. A* **2016**, *4*, 1970-1979.
47. Guo, X.; Du, B.; Wei, Q.; Yang, J.; Hu, L.; Yan, L.; Xu, W., *J. Hazard. Mater.* **2014**, *278*, 211-220.
48. Ali, S. A.; Kazi, I. W.; Ullah, N., *Ind. Eng. Chem. Res.* **2015**, *54*, 9689-9698.
49. Luo, X.; Lei, X.; Cai, N.; Xie, X.; Xue, Y.; Yu, F., *ACS Sustainable Chem. Eng.* **2016**, *4*, 3960-3969.
50. Li, J.; Fan, Q.; Wu, Y.; Wang, X.; Chen, C.; Tang, Z.; Wang, X., *J. Mater. Chem. A* **2016**, *4*, 1737-1746.
51. Li, J.; Zhang, S.; Chen, C.; Zhao, G.; Yang, X.; Li, J.; Wang, X., *ACS Appl. Mater. Interfaces* **2012**, *4*, 4991-5000.
52. Dong, Z.; Wang, D.; Liu, X.; Pei, X.; Chen, L.; Jin, J., *J. Mater. Chem. A* **2014**, *2*, 5034-5040.
53. Wan Ngah, W. S.; Teong, L. C.; Toh, R. H.; Hanafiah, M. A. K. M., *Chem. Eng. J.* **2013**, *223*, 231-238.

54. Tan, P.; Sun, J.; Hu, Y.; Fang, Z.; Bi, Q.; Chen, Y.; Cheng, J., *J. Hazard. Mater.* **2015**, *297*, 251-260.
55. Malwal, D.; Gopinath, P., *RSC Adv.* **2016**, *6*, 115021-115028.
56. Raji, F.; Saraeian, A.; Pakizeh, M.; Attarzadeh, F., *RSC Adv.* **2015**, *5*, 37066-37077.
57. Sitko, R.; Janik, P.; Feist, B.; Talik, E.; Gagor, A., *ACS Appl. Mater. Interfaces* **2014**, *6*, 20144-53.
58. He, S.; Zhang, F.; Cheng, S.; Wang, W., *ACS Sustainable Chem. Eng.* **2016**, *4*, 3948-3959.
59. Wang, Y.; Wang, G.; Wang, H.; Liang, C.; Cai, W.; Zhang, L., *Chem. Eur. J.* **2010**, *16*, 3497-3503.
60. Liu, C.-C.; Kuang-Wang, M.; Li, Y.-S., *Ind. Eng. Chem. Res.* **2005**, *44*, 1438-1445.
61. Liu, C.-H.; Chuang, Y.-H.; Chen, T.-Y.; Tian, Y.; Li, H.; Wang, M.-K.; Zhang, W., *Environ. Sci. Technol.* **2015**, *49*, 7726-7734.
62. Mohan, D.; Singh, K. P., *Water Res.* **2002**, *36*, 2304-2318.
63. Wang, X.-K.; Li, J.; Fan, Q.; Chen, C.; Tang, Z.; Wang, X.; Wu, Y., *J. Mater. Chem. A* **2015**.
64. Wu, J.; Wang, J.; Li, H.; Du, Y.; Huang, K.; Liu, B., *J. Mater. Chem. A* **2013**, *1*, 9837-9847.